CHARACTERISATION OF THE MAJOR FACILITATOR SUPERFAMILY DOMAIN CONTAINING 1 PROTEIN (MFSD1) AND STUDY OF ITS PHYSIOLOGICAL ROLE IN THE MOUSE

DISSERTATION

In fulfilment of the requirements for the degree

'Doctor rerum naturalium (Dr. rer. nat)'

submitted to the Faculty of Mathematics and Natural Sciences

at the Christian Albrechts University of Kiel

submitted by

David Massa Lopez

Kiel, July 2018

Referee: Prof. Dr. Paul Saftig

Co-referee: Prof. Dr. Eric Beitz

Date of oral publication: 16.10.2018

Approved for publication:

Table of contents

List of abbreviations

aa	Amino acids
ALT	Alanine transaminase
AST	Aspartate transaminase
AP-1,-2,-3,-4	Adaptor protein 1,-2,-3,-4
BFR/BS	Bone formation rate/Bone surface
BMD	Bone mineral density
BS	bone surface
BSA	Bovine serum albumin
BV/TV	Bone volume/Tissue volume
CD	Cluster of differentiation
cDNA	Complementary DNA
CHAPS	3-[(3-Cholamidopropyl)dimethylammonio]-1-propanesulfonate
CHIP-seq	Chromatine immunoprecipitation DNA-sequencing
CLC	Chloride channel
CLEAR	Coordinated lysosomal expression and regulation
CLN	Ceroid lipofuscinosis
CTF	C-terminal fragment
CTX-I	C-terminal telopeptide I
DAPI	4-,6-diamidino-2-phenylindole
DMEM	Dulbecco's Modified Eagle Medium
DMSO	Dimethyl sulfoxide
FACS	Fluorescence-activated cell sorting
FBS	Fetal bovine serum
FL	Full length
Flp	Flipase
Fw	Forward
GAPDH	Glyceraldehyde 3-phosphate dehydrogenase
GFP	Green fluorescent protein
GLDH	Glutamate dehydrogenase
GLMP	Glycosylated lysosomal membrane protein
GM130	Golgin subfamily A member 2/130 kDa cis Golgi matrix protein
GO	Gene onthology
Gt	Gene-trap
HA	Hemagglutinin
H&E	Hematoxylin and eosin
HEK	Human embryonic kidney
HeLa	Henrietta Lacks
HSM	Hematopoietic stem cell
Ig	Immunoglobulin
IRES	Internal ribosome entry site
ISSD	Infantile free sialic acid storage disease
kDa	kiloDaltons
LAMP-1,-2	Lysosomal associated membrane protein 1, 2
LBPA	Lyso bis-phosphatidic acid
LC-MS/MS	Liquid chromatography-Mass spectrometry/Mass spectrometry
LDH	Lactate dehydrogenase

LIMP-1, -2	Lysosomal integral membrane protein 1, 2
LMP	Lysosomal membrane protein
LSD	Lysosomal storage disease
LSEC	Liver sinusoidal endothelial cell
LTA	Lotus Tetragonolobus lectin
MAR	Mineral apposition rate
MCH	Mean corpuscular hemoglobin
MCHC	Mean corpuscular hemoglobin concentration
MCP1	Monocyte chemoattractant protein 1
MCV	Mean corpuscular volume
µCT	Micro computed tomography
MEF	Mouse embryonic fibroblast
MFS	Major facilitator superfamily
MFSD1	Major facilitator superfamily domain containing 1
MMP	Matrix metalloproteinase
MPV	Mean platelet volume
MPO	Myeloperoxidase
mRNA	Messenger ribonucleic acid
MS/BS	Mineralization surface/Bone surface
MSC	Mesenchymal stem cell
mTORC1	Mechanistic target of rapamycin 1
NAFLD	Non-alcoholic fatty liver disease
nt	nucleotide
NTF	N-terminal fragment
OV/BV	Osteoid volume/bone volume
PAGE	Polyacrylamide gel electrophoresis
PBS	Phosphate-buffered saline
PCR	Polymerase chain reaction
PDW	Platelet distribution width
PE	Phycoerythrin
PEI	Polyethylenimine
PFA	Paraformaldehyde
P-LCR	Platelet larger cell ratio
qRT-PCR	Quantitative real-time PCR
RDW	Red cell distribution width
Rv	Reverse
S1P	Sphingosine-1-phosphate
SDS	Sodium dodecyl sulfate
SLC	Solute carrier
SMA	Smooth muscle actin
SOS	Sinusoidal obstructive syndrome
TAE	Tris-acetate-EDTA
TBS	Tris-buffered saline
TCDB	Transporter classification database
TFEB	Transcription factor EB
TGN	Trans-Golgi Network
TMD	Transmembrane domain
TMT	Tandem mass tag

UTR	Untranslated region
VODI	Veno-occlusive disease with immunodeficiency
vWF	Von Willebrand factor
WT	Wild type
WGA	Wheat germ agglutinin

Summary

The lysosome is a membrane-enclosed organelle specialized in the catabolism of macromolecules in eukaryotic cells. Catabolic products are exported to the cytosol by lysosomal membrane transporters. Some transport systems were already biochemically characterized, but generally only a few genes and proteins coding for the responsible transporters have been identified so far. Additional lysosomal metabolites with higher concentrations than in the cytosol have been described for which the importers are still unknown.

In this study, a recently identified putative lysosomal transporter, Major Facilitator Superfamily Domain containing 1 (MFSD1), was biochemically characterized and its physiological role in mice was investigated.

MFSD1 is expressed ubiquitously in mouse tissues. A dileucine-based lysosomal sorting motif necessary for the transport of MFSD1 to lysosomes was identified. GLMP, a highly glycosylated lysosomal membrane protein, was identified as an interaction partner of MFSD1. The stability of GLMP and MFSD1 depends on each other. In the absence of GLMP, the levels of MFSD1 in tissues and cells were decreased below 10 % of normal levels.

A thorough study of newly generated MFSD1-deficient mice revealed a complex phenotype, pointing towards a critical and essential role of MFSD1 in the physiology of the liver, the bone, the kidney and the immune system. MFSD1-deficient mice suffer from a liver insult characterized by loss of sinusoids, extravasation of erythrocytes, fibrosis and neocapillarization, a pathology that resembles that of human patients suffering from sinusoidal obstructive syndrome (SOS). SOS patients with genetic mutations in the transcription factor sp110 show an immunodeficiency. Interestingly, MFSD1-konockout mice are also immunodeficient due to impaired maturation of B lymphocytes, suggesting a possible role of MFSD1 in the pathology of SOS patients with immunodeficiency. Additionally, the mineralization ability of MFSD1-deficient osteoblasts in vertebrae is impaired, leading to decreased bone mineral density. Furthermore, the absence of MFSD1 also leads to an increase of the size of lysosomes in the proximal tubules of the kidney, suggesting a potential accumulation of the substrate(s) normally transported by MFSD1. A prove of the interdependence between MFSD1 and GLMP is that the phenotype of GLMP-deficient mice is a phenocopy of MFSD1 knockout mice.

Zusammenfassung

Das Lysosom ist ein membranumschlossenes Zellorganell, das auf den Katabolismus von Makromolekülen in eukaryontischen Zellen spezialisiert ist. Die dabei entstehenden Abbauprodukte werden über lysosomale Membrantransporter aus dem Lysosom in das Zytosol der Zelle exportiert. Einige wenige dieser Transportproteine wurden bereits biochemisch charakterisiert, wohingegen bisher nur wenige Gene identifiziert wurden, welche für diese verantwortlichen Membrantransporter codieren. Zudem wurden weitere lysosomale Metabolite identifiziert, von denen angenommen wird, dass sie keine Produkte aus dem lysosomalen Abbauprozess sind. Für diese Metabolite sind die Importer, die diese Metabolite in das Lysosom transportieren, noch weitestgehend unbekannt.

In dieser Studie wurde ein neu identifizierter lysosomaler Transporter, Major Facilitator Superfamily Domain containing 1 (MFSD1), biochemisch charakterisiert und seine physiologische Rolle in der Maus anhand einer neu erzeugten MFSD1-defizienten Mauslinie untersucht.

MFSD1 wird ubiquitär in Mausgeweben exprimiert. Im Rahmen der Arbeit wurde ein dileucinbasiertes lysosomales Transportmotiv, welches für den Transport von MFSD1 zu den Lysosomen notwendig ist, identifiziert. Weiterhin wurde GLMP, ein hochglykosyliertes lysosomales Membranprotein, als Interaktionspartner von MFSD1 identifiziert. Die Stabilität von MFSD1 und GLMP ist hierbei stark voneinander abhängig. In Abwesenheit von GLMP lag MFSD1 sowohl in Mausgewebe, als auch in kultivierten Zellen, um bis zu 90 % reduziert vor.

Die MFSD1-defizienten Mäuse zeigten einen sehr komplexen Phänotyp auf, der auf eine essentielle Rolle von MFSD1 in der Physiologie der Leber, der Knochen, der Niere und des Immunsystems hindeutet. MFSD1-defiziente Mäuse leiden an einer Leberschädigung, die durch den Verlust von Sinusoiden, Extravasation von Erythrozyten, Fibrose und Neokapillarisation gekennzeichnet ist, eine Pathologie, die der von Patienten mit sinusoidalen obstruktiven Syndrom (SOS) ähnelt. Weiterhin besitzen SOS-Patienten mit einer Mutationen im Transkriptionsfaktor sp110 eine Immunschwäche, welche interessanterweise auch bei MFSD1-defiziente Mäuse auftritt, da bei ihnen die Reifung der B-Lymphozyten beeinträchtigt ist. Dies deutet auf eine mögliche Rolle von MFSD1 in der Pathologie von SOS-Patienten mit Immunschwäche hin. Zusätzlich ist die Mineralisierungsfähigkeit von MFSD1-defizienten Osteoblasten in der Wirbelsäule beeinträchtigt, was zu einer verminderten Knochenmineraldichte führt. Darüber hinaus führt der Verlust von MFSD1 auch zu einer

Vergrößerung der Lysosomen in den proximalen Tubuli der Niere. Ein solcher Anstieg könnte auf eine mögliche Akkumulation des (der) normalerweise von MFSD1 transportieren Substrat(en) zurückzuführen sein. Zudem ist der Phänotyp von GLMP-defizienten Mäuse identisch mit dem der MFSD1-Knockout-Mäuse, was die starke Abhängigkeit der beiden Proteine weiter verdeutlicht.

1 Introduction

1.1 The lysosome

The functional unit of eukaryotic organisms, the cell, is formed by several organelles that are orchestrated to fulfil its needs and respond to environmental challenges. The lysosome is a membrane-enclosed organelle, which is found in all animal cells with the exception of erythrocytes. Christian De Duve used for the first time the word lysosome in 1955, differentiating it from other organelles due to its richness in hydrolytic enzymes (de Duve et al. 1955). The richness in hydrolytic enzymes allows the lysosome to carry out one of its main function, the degradation and recycling of macromolecules. Both intracellular and extracellular components are degraded in lysosomes. Intracellular components include soluble proteins, aggregated proteins, organelles and macromolecular complexes, that reach the lysosome through autophagy. Extracellular substrates comprise bacteria, erythrocytes or extracellular matrix components, that can reach the lysosome by endocytosis or phagocytosis. Beside degradation processes, lysosomes also play a pivotal role in other biological functions, such as plasma membrane repair, nutrient sensing, cell signalling, cholesterol metabolism, cell death and immune response (Goberdhan, Wilson, and Harris 2016; Saftig and Klumperman 2009; Settembre et al. 2015; Yamayoshi et al. 2009).

Lysosomes are generated by the fusion of endocytic vesicles with vesicles from the biosynthetic pathway, and are characterized by a pH of 4.5 - 5. The lysosome needs two kind of proteins to fulfil its functions, soluble hydrolases and integral membrane proteins, which are synthetized in the endoplasmic reticulum, and transported to the lysosome by different means.

1.1.1 Lysosomal soluble proteins

Hydrolases catalyse the hydrolytic cleavage of specific substrates. More than 60 lysosomal enzymes with high affinities to different substrates have been described, including proteases, sulfatases, glycosidases, phosphatases, lipases, and nucleases. Lysosomal enzymes are synthetized in the ER and are transported via the secretory pathway to the lysosome, most of them by mannose-6-phosphate receptor dependent transport, where they become active due to the acidic pH of the lysosomal lumen (Braulke and Bonifacino 2009).

1.1.2 Lysosomal membrane proteins

The lysosomal membrane is a 7-10 nm thick phospholipid bilayer plus a glycoprotein coat of 5-12 nm thickness that delimit the numerous luminal hydrolases from the cytosol (Wilke, Krausze, and Büssow 2012). Besides its obvious isolating function, the lysosomal membrane integrates proteins that are required for other functions like fusion, acidification or transport of substrates among others (Figure 1). Lysosomal Associated Membrane Proteins type 1 and 2 (LAMP-1 and LAMP-2) are the most abundant membrane proteins in lysosomes, and they have been suggested, together with Lysosomal Integral Membrane Protein type 1 and 2 (LIMP-1 and LIMP-2), to represent more than 50% of the total lysosomal membrane proteins (LMP) (Marsh et al. 1987). They are highly glycosylated, like the vast majority of the LMPs, contributing to the formation of a lysosomal glycocalyx, which is thought to protect membrane proteins from luminal lysosomal proteases (Peters and von Figura 1994).

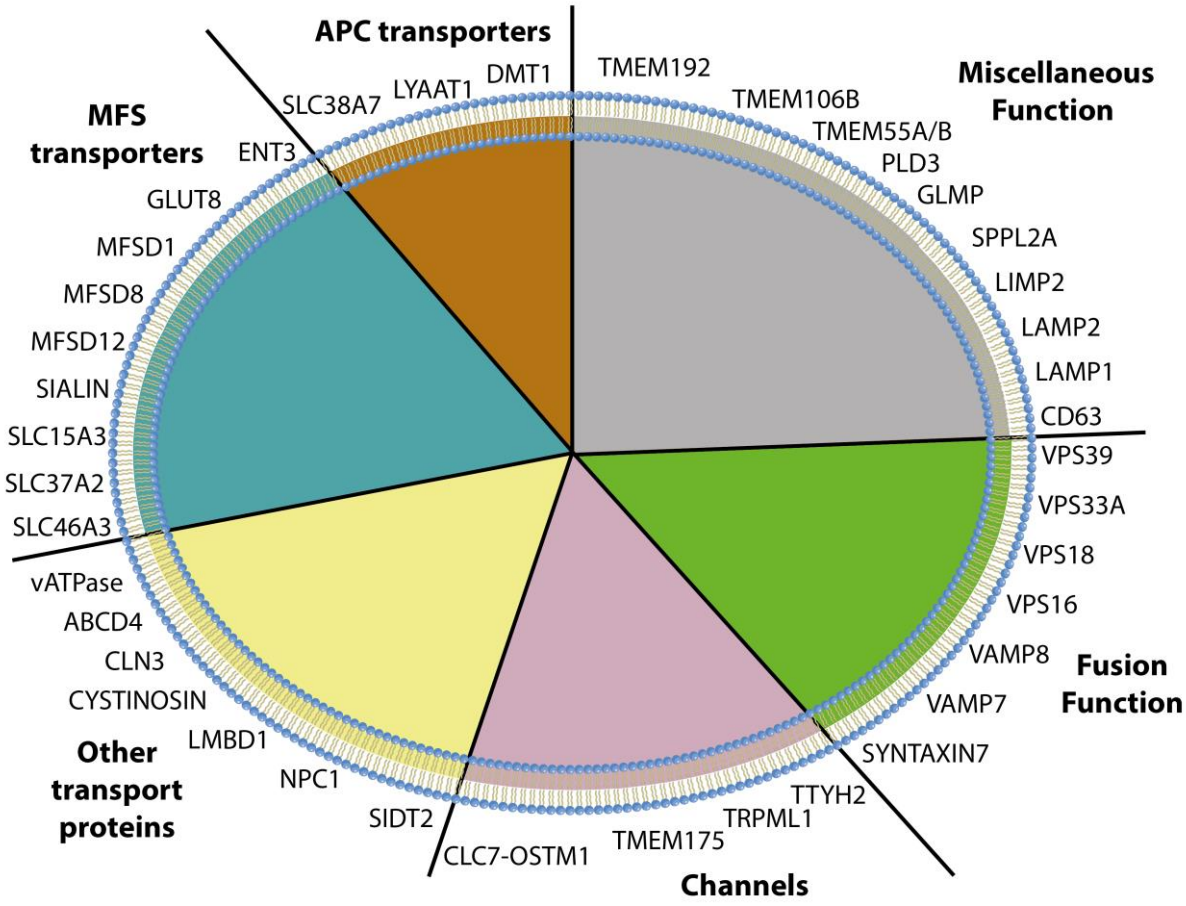

Figure 1. Scheme of selected endo-lysosomal membrane proteins.

The transport of ions and small molecules through the lysosomal membrane is important to preserve the acidic pH, the electrochemical gradient and for the recycling of degradation products. These functions are fulfilled by pumps, channels and transporters, which are described in more detail in chapter 1.21.1.2.2.

1.1.2.1 Trafficking of lysosomal membrane proteins

Lysosomal membrane proteins bear sorting signals in the cytosolic domains, that mediate the lysosomal targeting and/or endocytosis from the cell surface. The lysosomal targeting motifs of membrane proteins are usually localized proximal to the transmembrane domain, and the most common have a consensus sequence YXXØ, where Ø is a bulky hydrophobic residue, and [D/E]XXXL[L/I] (Bonifacino and Traub 2003). Lysosomal membrane proteins reach lysosomes by two different paths. The so-called direct pathway, where membrane proteins are transported from the Trans-Golgi Network (TGN) to endosomes and further to lysosomes, and the indirect pathway, where membrane proteins are first transported from the TGN to the plasma membrane and afterwards they are endocytosed to reach lysosomes (Figure 2).

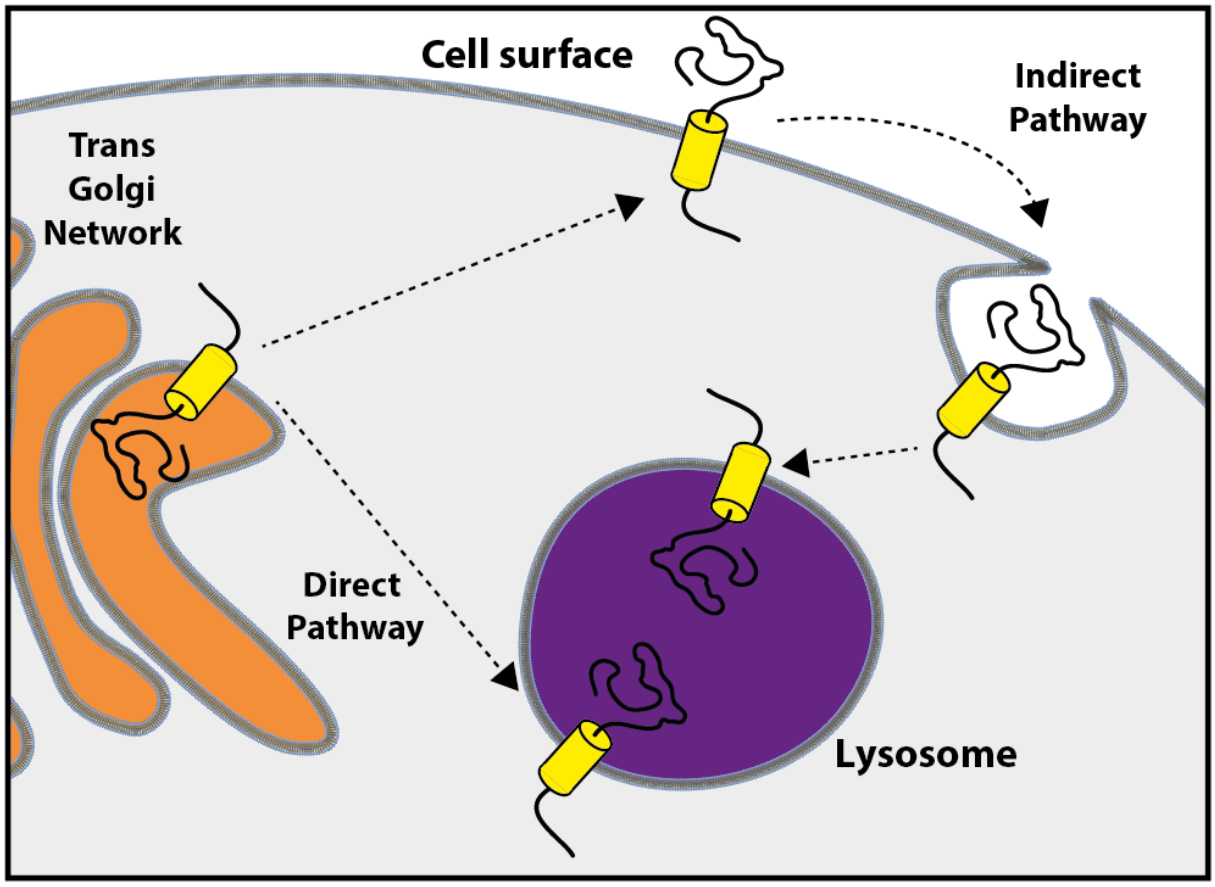

Figure 2. Scheme of the two main lysosomal transport pathways of membrane proteins.

YXXØ and [D/E]XXXL[L/I] sequences are recognized by adaptor protein (AP) complexes AP-1 and AP-2 that are formed by four subunits. AP-1 is localized to the TGN and endosomes and is responsible for the direct transport pathway. AP-2 is localized to the plasma membrane and is responsible for the endocytosis of proteins bearing those motifs. YXXØ and [D/E]XXXL[L/I] can be recognized by AP-3 and AP-4 complexes. The recognition of both motifs by AP is complex. Modifications in the X amino acids or the amino acid previous to the Y and D/E of YXXØ and [D/E]XXXL[L/I] motifs, respectively, can lead to the recognition by one or other AP complex (Bonifacino and Traub 2003).

1.1.2.2 Lysosomal transport systems

The recognition of the lysosomal transport systems started in 1982, when Gahl et al. and Jonas et al. demonstrated that the accumulation of cystine in cystinosis patients was caused by a defect of the cystine export out of the lysosome (Gahl et al. 1982; Jonas et al. 1982). By the end of the 90s, the study of lysosomes from fibroblasts, leukocytes or rat liver cells among other tissues led to the demonstration of more than 20 lysosomal transport systems of numerous low molecular weight metabolites (Table 1) (Gahl et al. 1982; Jonas et al. 1982; Mancini, Havelaar, and Verheijen 2000; Pisoni and Thoene 1991).

Many functions of the lysosome require or involve the transport of ions and molecules across the lysosomal membrane. These transport processes are carried out by pumps, channels and transporters. To date, some of the transporter proteins responsible for the lysosomal transport systems have been identified. For instance, a multimeric proton pump, the vacuolar H^+-ATPase (v-ATPase), contribute to the acidification of the lysosomal lumen (Forgac 1999). The acidification of the lysosomal lumen involves the generation of a transmembrane voltage that is compensated by channels that import the negatively charged ion chloride, like Clc-7 channel, and by channels that release positively charged ions, like the Ca^{2+}, Fe^{2+} and Zn^{2+} permeable channel TRPML1 (Dong et al. 2008) or the K^+ channel TMEM175 (Cang et al. 2015). The acidification of the lysosomal lumen allows the hydrolases to become active and produce catabolic products that need to be exported to the cytosol. The acidic pH of the lysosome is also important for the transport of some molecules across the lysosomal membrane, as many transporters use the proton gradient to couple the cotransport of a second molecule against the gradient.

A number of lysosomal transporter proteins responsible for amino acid transport have been described. The lysosomal cystine transporter was identified as cystinosin (Kalatzis et al. 2001); LYAAT-1 was characterized as a small neutral amino acid exporter that requires the lysosomal pH gradient to be active (Sagné et al. 2001); PQLC2 was characterized as a cationic amino acid transporter (B. Liu et al. 2013) and recently, SLC38A9 has been identified as a transporter of essential amino acids, like leucine, phenylalanine or methionine, that activates mTORC1 (Wyant et al. 2017).

Sialin, a member of the MFS superfamily of transporters, acts as a transporter for sialic acid and anionic sugars (Verheijen et al. 1999). GLUT8 is an hexose transporter predominantly expressed in brain and testis. It is found in endosomal and lysosomal membranes, but also in membranes of the ER (Schmidt, Joost, and Schurmann 2009). No lysosomal transporters for N-acetylated hexoses have been identified. Some additional proteins have been suggested to act as lysosomal transporters. LMBD1 and ABCD4 are predicted to transport cobalamin (Coelho et al. 2012; Rutsch et al. 2009), and there is good evidence that NPC1 transports cholesterol.

The transporter proteins responsible for many of the lysosomal transport systems are still unknown, and in the meanwhile, proteomics analysis have identified additional lysosomal substrates that are not thought to be a lysosomal catabolic product, such as taurine, choline, creatine and multiple species of carnitines, suggesting that a transporter is needed to import such substrates across the membrane of lysosomes (Abu-Remaileh et al. 2017).

Transport systems	Substrate	Transport type	Source
Amino acids			
(c) cationic	L-Lys, Arg	Secondary active?	Fibroblasts
(d) anionic	L-Glu, Asp	Passive	Fibroblasts
(e) small neutral	L-Ala, Ser, Thr	Passive	Fibroblasts
(f) small neutral	L-Pro (major route), Ala	Passive	Fibroblasts
(p) Small neutral	L-Pro (minor route)	Passive	Fibroblasts
(h) Large neutral	L-Tyr, Leu, Ileu, Trp, Phe, His, Val, Met	Passive	Rat thyroid cells
(l) Bulky bipolar	L-Leu, Val	Passive	Fibroblasts
(t) Aromatic	L-Trp, Phe	Passive	Fibroblasts
Cystine	L-Cystine, selenocysteine	Passive?	Leukocytes, rat liver
Cysteine	L-Cysteine	Secondary active?	Fibroblasts
Cysteamine	Cysteamine	Secondary active?	Fibroblasts
Taurine	Taurine	Secondary active?	Rat liver
Dipeptides	Gly-Gln	Secondary active?	Rat liver

Sugars			
Acidic sugars	Nau5Ac, GlcA	Secondary active	Rat liver, fibroblasts, lymphoblasts
Neutral monohexoses	D-Glucose	Passive	Rat liver, fibroblasts
N-Acetylated hexoses	N-Acetylglucosamine, N-Acetlgalactosamine	Passive	Rat liver
Nucleosides	Purines, pyrimidines	Passive	Fibroblasts
Inorganic ions			
H+ pump/ATPase	Protons	Primary active	Rat liver
Chloride channel	Cl^-	Channel	Rat liver
Phosphate ion	HPO_4^{2-}	Passive	Fibroblasts
Sulphate ion	SO_4^{2-}	Secondary active?	Rat liver
Calcium ion	Ca^{2+}	Passive	Fibroblasts
Heavy metal ions	Ag^+	Primary active	Rat liver
Vitamins			
Folypolyglutamates		Passive	S180 cells
Cobalamin (B12)	Cyanocobalamin	Secondary active	Fibroblasts
Unknown mechanism			
Cholesterol			
Iron ion			

Table 1. List of lysosomal transport systems. The lysosomal transport systems on the list were identified using isolated lysosomes from different tissues and cells. Uptake studies and methyl ester loading techniques were used for the identification of the transport systems. Adapted from Mancini et. al., 2000**.**

1.2 Transport proteins

The presence of impermeable membranes that act as barriers between the extracellular and intracellular space and between the cytosol and the lumen of different organelles requires transport proteins to allow the uptake of nutrients, extrusion of deleterious compounds and in general the exchange of metabolites between the two sides of the membrane. Even the transport of small molecules like water or glycerol, whose translocation across the membrane was thought to take place merely by free diffusion, can be regulated by transport proteins (Agre 2006). The diversity of transport proteins and their high substrate specificity provide the cell with a regulated barrier between the cytosol and the extracellular space or organelles lumen.

Transport proteins can be divided in channels and transporters. A channel is a protein that mediates the diffusion of substrates, typically ions, down their electrochemical gradient. They are characterized by a substrate binding site that is accessible from the two sides of the membrane (Pohorille et al., 2005).

In contrast, transporters can transport a substrate against their electrochemical gradient. They have two gates that can not be open simultaneously. Transporters can be divided into primary active transporters, secondary active transporters or facilitators. Primary active transporters use metabolic energy to transport substrates across the membrane, while secondary active transporters exploit the electrochemical potential generated during the cotransport of an ion or solute in the same direction (symporter) or in the opposite direction (antiporter) as the main substrate (Sadée, Drübbisch, and Amidon 1995). Facilitators are also called uniporters, and are able to transport a substrate only down its electrochemical gradient.

1.2.1 Major Facilitator Superfamily of transporters

Three major classification systems have been proposed for transporters. The HUGO Gene Nomenclature Committee (HGNC) classifies genes that code for human transporters excluding channels, ABC transporters and ion pumps and uses the solute carrier system to organize them; the protein families database (Pfam) analyses sequences of all organisms and classifies them according to domain-structure; the Transport Classification Database (TCDB) classifies transporters from all species based on transport mechanism, phylogenetic relations and substrates (Yan 2015).

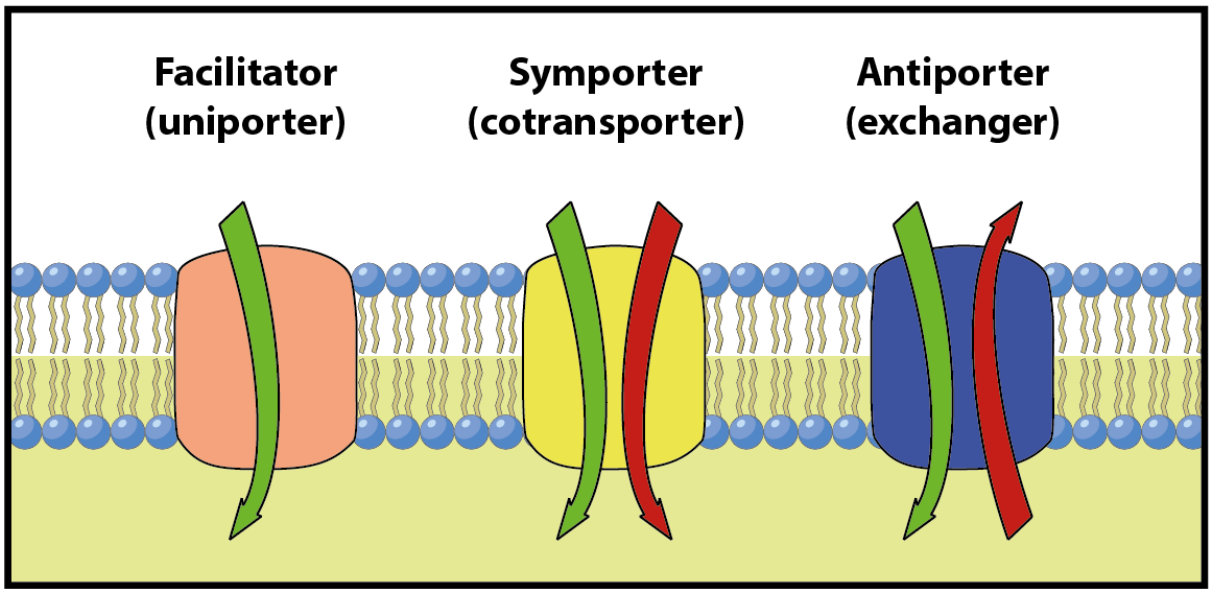

Figure 3. Schematic illustration of secondary active transporters and facilitators.

In 1993, bioinformatic analysis revealed that several families of secondary transporters with different substrates had a common structural motif of 12 transmembrane spanning α-helical

segments. They were grouped in the Major Facilitator Superfamily (MFS) of transporters (Marger and Saier 1993). MFS transporters include facilitators, symporters and antiporters (Figure 3) and have a broad range of substrates including monosaccharides, oligosaccharides, amino acids, peptides, vitamins, nucleosides, nucleotides, organic and inorganic ions and lipids.

In 2003 the first crystal structures of MFS transporters were reported, and to date more than 40 crystal structures of different MFS transporters have been described (Abramson et al. 2003; Yan 2015). The study of the crystal structures of MFS protein members has shown that MFS transporters share the same structural fold, containing a structural core with 12 transmembrane helices (the MFS domain) (Figure 4) . The structural core is organized in two domains with six transmembrane domains (TMD), the C-terminal domain and the N-terminal domain, which exhibit a certain degree of symmetry between them (Pao, Paulsen, and Saier 1998; Quistgaard et al. 2016). Within each domain, the six TMD are organized into two inverted repeats of three helices. The first helix of each three helix bundle (TMD1, TMD4, TMD7 and TMD10) is localized in the centre of the protein generating the transport pore and enclosing the substrate binding site (Yan 2015). In addition to the core MFS domain, some members of the MFS superfamily have additional domains. For instance, all the members of the drug:H antiporters 2 family have 14 TMD (Law, Maloney, and Wang 2009).

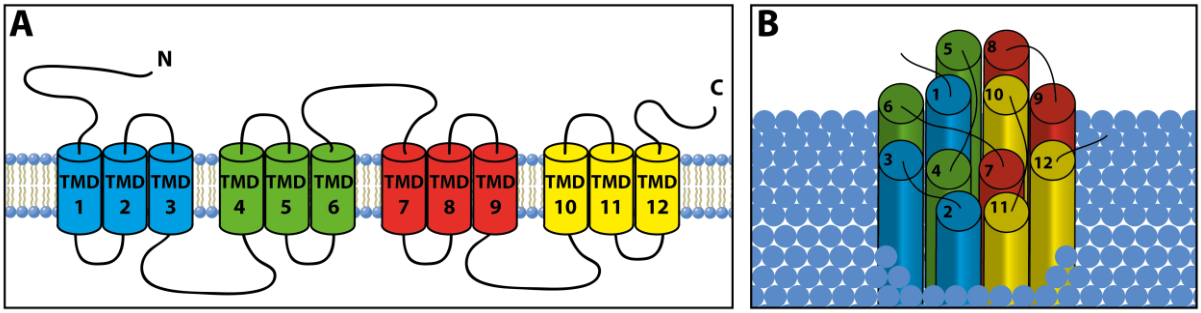

Figure 4. Schematic illustration of the MFS domain containing 12 transmembrane domains (TMD) in 2D (A) and 3D (B).

An alternate access model was proposed already in 1966 as a possible mechanism by which transport proteins transfer substrates across the membrane (Jardetzky 1966). This model suggest that the substrate transport requires the binding of the substrate to the centrally located binding site followed by a conformational change of the transporter that enables the

release of the substrate to the other side of the membrane. The structure determination of the same MFS transporter in both inward- and outward-facing conformations supports this alternate access model transport (Quistgaard et al. 2016; Yan 2015).

1.3 Lysosomal storage diseases

The malfunction of lysosomal proteins can lead to lysosomal storage diseases (LSD), which are a group of inherited diseases characterized by the deposition of low molecular weight metabolites in lysosomes, and they are usually classified according to the accumulated material. Despite each form of LSD is individually rare, they have altogether an incidence of approximately one in every 5000 births (Fuller et al. 2006). More than 50 LSD have been described so far, and the clinical symptoms and age of onset can vary. These variabilities depend on the functionality of the protein affected, on the material accumulated in lysosomes and on the cell types affected by the lysosomal accumulation (Platt, Boland, and van der Spoel 2012).

The substrate storage in multiple organs lead to several clinical manifestations in each LSD, with some overlap among different disorders. The age of onset is variable and the diseases progress and evolve over time. Most of the LSD present with neurological symptoms. Many LSD patients suffer from splenomegaly, like Gaucher disease and Niemann Pick disease patients (Vom Dahl and Mengel 2010; Platt, Boland, and van der Spoel 2012). Skeletal abnormalities are common features of patients suffering from several LSD, such as Gaucher or mucopolysaccharidosis (Malm, 2001; Platt et al., 2012). Patients suffering from some LSD have a dysfunctional immune system, like Gaucher, Niemann Pick C or α-mannosidosis patients (Castaneda et al. 2008). Additional organs may be affected in LSD patients (Parenti, Andria, and Ballabio 2015)

While most of the LSDs are caused by defects in lysosomal enzymes involved in the degradation of different substrates, defects in LMPs and accessory proteins also can lead to LSD.

1.3.1 LSD can be caused by loss of function of lysosomal membrane proteins

Mutations in genes coding for different types of lysosomal membrane proteins involved in functions like transport of small molecules, ion flux across the membrane or autophagy are responsible for the development of some cases of LSDs. A few cases of LSDs are caused by

mutations in genes that code for lysosomal membrane proteins which function has not yet been unravelled, like CLN3 or CLN7 (Brandenstein et al. 2016; Kovacs and Pearce 2015).

1.3.1.1 Danon disease is caused by autophagy defects

Mutations of the gene encoding for LAMP-2, a highly glycosylated lysosomal type I transmembrane protein, cause Danon disease (Nishino et al. 2000). Danon disease is characterized by increased number and size of cytoplasmic vacuoles containing autophagic material and glycogen in skeletal and cardiac muscle (Danon et al. 1981). The study of LAMP2-deficient mouse tissues and cells revealed that the lack of LAMP-2 leads to defects on autophagosomes maturation (Tanaka et al. 2000). Additionally, fibroblasts deficient for the expression of LAMP-1 and LAMP2 accumulate cholesterol in endo-lysosomes. This endo-lysosomal cholesterol accumulation can be rescued by the reintroduction of LAMP2, suggesting a role of LAMP2 in the lysosomal export of cholesterol (Eskelinen et al. 2004).

1.3.1.2 Sanfilippo syndrome C is caused by defective degradation of heparin sulphate

Sanfilippo syndrome C is caused by mutations in *HGSNAT*, a gene that codes for Heparan-Alpha-Glucosaminide N-Acetyltransferase, and is characterized by lysosomal accumulation of heparan sulphate due to its defective lysosomal degradation (Fan et al. 2006; Hřebíček et al. 2006; Kresse, Von Figura, and Klein 1978). HGSNAT catalyses the transmembrane acetylation of heparan sulphate, acting simultaneously as a N-acetyltransferase and as a AcetylCoA transporter (Bame and Rome 1985; Rome et al. 1983).

1.3.1.3 Niemann Pick Type C is caused by defective lysosomal cholesterol transport

In Niemann-Pick type C disease the cholesterol export from late endosomes is impaired and unesterified cholesterol and other lipids accumulate in lysosomes. The disease is caused by mutations in the *NPC1* or *NPC2* genes (Carstea et al. 1997), and is clinically characterized by neurodegeneration and hepatosplenomegaly. NPC1 is a glycosylated polytopic transmembrane protein localized in late endosomes (Higgins et al. 1999; Neufeld et al. 1999) necessary for the cholesterol export. However, the direct cholesterol transport by NPC1 has not yet been shown.

1.3.1.4 LSDs caused by impaired lysosomal export of small molecules

The first LSD caused by impaired lysosomal metabolite export identified was cystinosis, which is characterized by lysosomal cystine accumulation (Gahl et al. 1982; Jonas et al. 1982). Patients suffering from cystinosis have renal failure and photophobia due to crystals in the cornea, but additionally, the widespread accumulation of cystine in diverse organs leads to diverse clinical manifestations, such as mental deterioration, muscle wasting or pulmonary dysfunction (Ivanova et al. 2014). Mutations in *CTNS* gene were shown to cause cystinosis (Town et al. 1998). *CTNS* gene codes for cystinosin, a seven transmembrane domain protein localized in late endosomes and lysosomes responsible for the export of cystine from lysosomes (Kalatzis et al. 2001). The study of cystinosin-deficient mice revealed an accumulation of cystine in all organs, ranging from tenfold cystine accumulation in spleen to 350-fold cystine accumulation in liver of cystinosin-deficient mice compared to wild-type mice (Cherqui et al. 2002).

Impaired export of free sialic acid from the lysosome is the cause of Salla disease and Infantile sialic storage disorder (ISSD). Both are neurodegenerative diseases with different degrees of severity. Salla disease is the mildest phenotype and is accompanied by psychomotor retardation and slow developmental progress. ISSD, the more severe phenotype, is characterized by severe developmental delay, hepatosplenomegaly and skeletal changes among other characteristics (Adams and Gahl 1993; Froissart et al. 2005). They are caused by mutations in *SLC17A5* gene, which codes for sialin, a lysosomal membrane protein member of the Major Facilitator Superfamily of transporters (MFS) responsible for the export of sialic acid out of the lysosome (Morin, Sagné, and Gasnier 2004; Verheijen et al. 1999).

Cobalamin F-type disease (CblF) and cobalamin J-type disease (CblJ) are LSDs characterized by the accumulation of cobalamin (synonymously known as vitamin B_{12}) in lysosomes (Rosenblatt et al. 1985). Common clinical signs of the patients are malnutrition and developmental delay, and they are identified by elevated homocysteine and methylmalonic acid concentrations in blood or urine samples. Mutations in *LMBRD1* gene, that codes for the lysosomal transmembrane protein LMBD1, cause CblF and mutations in *ABCD4* gene, that codes for the lysosomal transmembrane protein member of the ATP-Binding Cassette superfamily of transporters (ABC), ABCD4, cause CblJ (Coelho et al. 2012; Rutsch et al. 2009). Despite no transport assay has shown the direct transport of cobalamin across the lysosomal membrane, reintroduction of *LMBRD1* or *ABCD4* in fibroblasts of CblF patients or CblJ patients,

respectively, rescues the cytosolic cobalamin cofactor synthesis to wild-type levels, suggesting the implication of both proteins in lysosomal cobalamin release (Coelho et al. 2012; Rutsch et al. 2009). Since ABCD4 belongs to the well characterized ABC transporters superfamily, it is likely that ABCD4 is the responsible for the direct export of vitamin B_{12} from lysosomes. Additionally, LMBD1 and ABCD4 interact physically with each other and the lysosomal localization of ABCD4 depends on LMBD1 (Fettelschoss et al. 2017; Kawaguchi et al. 2016).

1.3.1.5 LSDs caused by defective ion flux across the lysosomal membrane

Mutations in the *CLCN7* and *OSTM1* genes cause osteopetrosis, a disease characterized by increased bone mineral density due to a decreased activity of the bone degrading cells, the osteoclasts. Some patients with severe forms of osteopetrosis also suffer from retinal atrophy and neurodegeneration due to lysosomal storage (Frattini et al. 2003; Kasper et al. 2005; Kornak et al. 2001; Pangrazio et al. 2006). *CLCN7* codes for chloride channel protein 7 (Clc-7), a Cl^-/H^+ exchanger localized in late endosomes. Despite Clc-7 is involved in the acidification of lysosomes in some cell types, it is not essential for lysosomal acidification. *In vivo*, other membrane transporters/channels contribute to the generation of the voltage shunt necessary for the H^+ pumping carried out by the vATPase (Graves et al. 2008; Kornak et al. 2001; Lange et al. 2006; Steinberg et al. 2010). Clc-7 is also present in the specialized cell membrane of osteoclasts, the ruffled border, where it plays a critical role in the acidification of the resorption lacuna, the space formed between the ruffled border and the bone where bone degradation takes places. Loss of function of Clc-7 in humans and mice cause impaired bone degradation that leads to osteopetrosis (Kornak et al. 2001). *OSTM1* codes for a lysosomal type I transmembrane protein, also named Ostm1 that is localized in lysosomes and in the ruffled border of osteoclasts. Ostm1 is the accessory subunit of Clc-7 and is necessary for the transport activity of Clc-7. Additionally, the stability of Clc-7 depends on Ostm1 and Ostm1 requires co-expression of Clc-7 to be directed to lysosomes. Mutations in *OSTM1* cause a severe form of osteopetrosis with neuronal involvement, and mice deficient for Ostm1 have a phenotype strikingly similar to the phenotype of Clc-7 deficient mice, strengthening the relationship between the two proteins *in vivo* (Lange et al. 2006; Pangrazio et al. 2006).

Mucolipidosis type IV is a LSD caused by mutations in *MCOLN1* gene that affects the nervous system with mental retardation, ophthalmologic abnormalities and lipid storage in lysosomes (Bassi et al. 2000; Berman et al. 1974; Sun et al. 2000). *MCOLN1* codes for TRPML1, a channel

localized in late endosomes-lysosomes that has been shown to be permeable to Na^+, K^+, Ca^{2+} and Fe^{2+} (Bach 2005; Cantiello et al. 2005; Laplante et al. 2002). Mice deficient for *MCOLN1* closely replicate the phenotype observed in patients suffering from mucolipidosis type IV (Venugopal et al. 2007).

1.3.1.6 LSDs caused by mutations in lysosomal membrane genes with unknown function

Batten disease is the most common juvenile form of neuronal ceroid lipofuscinosis (NCL), clinically characterized by vision loss, childhood progressive neurodegeneration and eventually death in the second or third decade of life. A common characteristic of NCL is the accumulation of autofluorescent lipofuscin in neurons (Cotman and Staropoli 2012). The disease is caused by mutations in the *CLN3* gene, that codes for a transmembrane protein localized in endosomes and lysosomes. CLN3 has a domain structure consistent with members of the major facilitator superfamily (MFS) of transporters, suggesting that it might have a transport function. Mice deficient for CLN3 have a phenotype that resembles the phenotype observed in NCL human patients (Mitchison et al. 2000). CLN3 has been suggested to transport arginine and to regulate post-Golgi transport, but its precise molecular function remains still unknown (Cotman and Staropoli 2012; Munroe et al. 1997; Ramirez-Montealegre and Pearce 2005).

Mutations in the *CLN7* gene cause a late infantile variant of NCL characterized by the accumulation of autofluorescent storage material in neurons. The *CLN7* gene encodes MFSD8, a transmembrane protein member of MFS superfamily of transporters that is mainly localized in lysosomes (Aiello et al. 2009; Kousi et al. 2009; Siintola et al. 2007; Stogmann et al. 2009). Mice deficient for MFSD8 expression have a phenotype that resembles the phenotype of CLN7 patients with lysosomal dysfunction, suggesting lysosome/autophagy defects in brain with neurodegeneration at a late stage (Brandenstein et al. 2016; Damme et al. 2014). Despite the efforts made in the study of MFSD8-deficient mice, the substrate/s transported by MFSD8 and its function remain unknown.

Altogether ten different LSDs are known to be caused by mutations in genes that code for lysosomal transmembrane proteins. Eight of those LSD are caused by mutations in genes that code for a transport protein or a protein predicted to be a transporter, highlighting the importance of lysosomal transport proteins in lysosome homeostasis.

Human disease	Causative gene	Protein name	Protein size, # of transmembrane domains (TMD)
Cystinosis	*CTNS*	Cystinosin	367 aa, 7 TMD
Salla disease ISSD	*SLC17A5*	Sialin	495 aa, 12 TMD
Cobalamin F-type Cobalamin J type	*LMBRD1* *ABCD4*	LMBRD1 ABCD4	540 aa, 9 TMD 606 aa, 6 TMD
Neuronal ceroid lipofuscinosis, late variant	*MFSD8*	MFSD8 (CLN7)	518 aa, 12 TMD
Neuronal ceroid lipofuscinosis, juvenile form	*CLN3*	BATTENIN (CLN3)	438 aa, 6 TMD
Malignant infantile osteopetrosis	*CLCN7* *OSMT1*	CLC-7 OSTM1	805 aa; 18 TMD 338 aa; 1 TMD
Mucolipidosis IV	*MCOLN1*	TRPML1	580 aa, 6 TMD
Mucopolysaccharidosis type IIIC	*HGSNAT*	HGSNAT (TMEM76)	663 aa, 11 TMD
Niemann-Pick type C	*NPC1*	NPC1	1278 aa, 11 TMD
Danon disease	*LAMP2*	LAMP2	410 aa, 1 TMD

Table 2. List of lysosomal storage diseases with causative genes coding for lysosomal transmembrane proteins (Adapted from (Ruivo et al. 2009))

1.4 MFS transporters and lysosomes

MFS transporters are found in a variety of cell organelles, like in the plasma membrane, endoplasmic reticulum, Golgi apparatus, lysosomes or other vesicles. The general knowledge about the structure and transport mechanism of MFS superfamily members has rapidly increased and the substrate/s transported by some members of MFS superfamily are well characterized (Yan 2015). To name some examples of MFS transporters with known substrates in different compartments: GLUT5 and FLVCR1, which are fructose and heme transporters, respectively, are localized in the plasma membrane (Burant 1992; Quigley et al. 2004). MFSD2A and MFSD2B, which transport essential omega-3 fatty acid docosahexaenoic acid and sphingosine-1-phosphate, respectively, are also localized at the plasma membrane (Nguyen et al. 2014a; Vu et al. 2017). GLUT1, a glucose transporter and SLC33A1, an acetyl-CoA transporter are found in the endoplasmic reticulum (ER) (Hirabayashi, Nomura, and Nomura 2013; Takanaga and Frommer 2010). SLC2A13 is a myo-inositol transporter localized in the Golgi apparatus (Di Daniel et al. 2009). SLC18A3 and SLC17A7 are responsible of transporting acetylcholine and glutamate in synaptic vesicles, respectively, while sialin exports the sialic acid produced after degradation process in the lysosome (Aihara et al. 2000; Erickson et al. 1994; Verheijen et al. 1999).

Although the substrate for a number of MFS transporters has been identified, such as glucose for GLUT1, GLUT2 and GLUT3, sialic acid for SIALIN or docosahexaenoic acid for MFSD2A, the majority of MFS members are still orphan transporters, like HIATL, SLC2A6, MFSD8, MFSD9 or MFSD14A (www.tcdb.org) (Nguyen et al. 2014a; Pao, Paulsen, and Saier 1998; Verheijen et al. 1999). The process of deorphanization, or unravelling of the substrates transported, of MFS transporters is a major challenge for the understanding of this superfamily.

A wide range of potential substrates of MFS transporters are found in the lysosome that need to be exported to the cytosol in order to be reused. The identification of substrates in the lysosomal lumen that are not thought to be a product of the degradation process, such as taurine, choline or creatine, suggest that lysosomal transporters are involved in the import of those substrates from the cytosol to the lysosome lumen (Abu-Remaileh et al. 2017).

46 novel potentially lysosomal transporters were identified in a semi-quantitative proteomic analysis of rat liver lysosome-enriched and lysosome-nonenriched membranes (Chapel et al. 2013). Three of the identified potential lysosomal transporters are members of the MFS superfamily, slc46a3, sclo2b1 and MFSD1.

1.4.1 Major Facilitator Superfamily Domain containing 1 (MFSD1)

To date, very little is known about MFSD1. The *MFSD1* gene is evolutionary conserved. It has homologues to the human gene in *Mus musculus*, *Gallus gallus*, *Danio rerio* and two different orthologues in *Drosophila melanogaster*. No orthologues are present in *Caenorhabditis elegans.* An initial quantitative real-time PCR analysis in different tissues showed that MFSD1 is expressed ubiquitously at the transcript level (Sreedharan et al. 2011). Phylogenetic studies related MFSD1 to the facilitative nucleoside transporter family SLC29 and to other transporters like SLC2A8, SLC16A10 or SLC19A2 (Perland, Bagchi, et al. 2017; Perland, Hellsten, et al. 2017).

Human *MFSD1* gene was identified as a target of the CLEAR (Coordinated Lysosomal Expression And Regulation) network in a combination of genomic approaches in HeLa cells, including ChIP-seq analysis, profiling of TFEB-mediated transcriptional induction, genome-wide mapping of TFEB target sites and recursive expression meta-analysis of TFEB targets (Palmieri et al., 2011). Later on, MFSD1 protein was identified in a proteomic screen using rat

liver enriched lysosomes. Additionally, MFSD1 localized in lysosomes of HeLa cells after transfection of a plasmid coding for MFSD1 tagged to GFP (Chapel et al. 2013).

A study about MFSD1 expression and localization at endogenous level was performed by others using a commercial antibody. The detection of a protein at a similar molecular weight to the predicted molecular weight of MFSD1 by Western blotting was interpreted as a sign of specificity of the antibody used (Perland, Hellsten, et al. 2017). Such study claimed that MFSD1 expression is affected by altered nutrient intake.

Initial experiments performed in our lab revealed that MFSD1 is localized to LAMP2 positive vesicles in HeLa cells after overexpression of a plasmid coding for mouse MFSD1 fused to an HA tag. Additionally, treatment of HeLa cells transfected with a plasmid coding for mouse MFSD1 fused to an HA tag at the C-terminus with PNGase and EndoH glycosidases demonstrated that MFSD1 is, uncommon for a lysosomal membrane protein, not N-glycosylated (Figure 5).

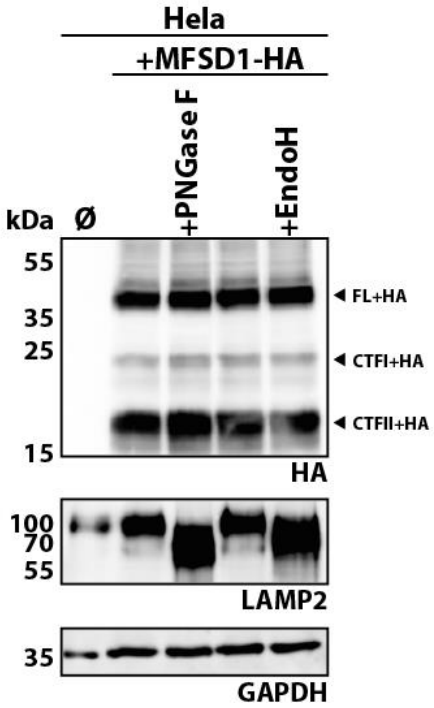

Figure 5. MFSD1 is not glycosylated. HeLa cells transfected with a plasmid coding for MFSD1-HA were collected and the lysate was treated with PNGaseF or EndoH and analysed by Western Blotting with anti-HA, anti-LAMP2 and anti GAPDH antibodies.

1.5 Aim of the study

Lysosomes are membrane-enclosed organelles responsible for the degradation of macromolecules in eukaryotic cells. The degradation products are exported by lysosomal membrane transporters and recycled in the cytosol. Despite a few transporters have been identified, many of the proteins responsible for the export of lysosomal degradation products are still unknown. The described higher concentrations of some metabolites in lysosomes than in the cytosol suggest the involvement of lysosomal transporters in the import of such metabolites. An aim of this study was to increase the knowledge about the undescribed lysosomal membrane transporters. Major Facilitator Superfamily Domain containing 1 (MFSD1) was recently identified as a putative lysosomal transporter. Since very little is known about MFSD1, this thesis aimed to perform a profound biochemical characterization of MFSD1 by analysing its topology, its subcellular localization, the transport to its subcellular localization, the tissue protein expression and finally decipher its function *in vivo*.

The main aim of this dissertation was to generate a MFSD1-deficient mouse model and use it as a tool to investigate the physiological role of MFSD1 in mouse tissues and to unravel the potential substrate(s) transported by it. In order to understand how the lack of MFSD1 affects the physiology of the mouse, a thorough investigation of the phenotype developed by MFSD1 knockout mice in different tissues was performed. Additionally, this thesis aimed to identify potential changes in the lysosomal proteome of MFSD1-deficient mice. Proteomics analysis of lysosomal enriched fraction of MFSD1-deficient liver should elucidate whether the level of lysosomal proteins is changed in the absence of MFSD1.

2 Material and methods

2.1 Material

2.1.1 Biochemicals

All chemicals were purchased with the purity grade ''pro analysis'' (p.a.) from Sigma-Aldrich, Carl Roth, AppliChem or Merck, unless stated otherwise.

2.1.2 Mouse strains

Mouse strain	Mouse strain (full name)	Source	Reference
MFSD1 KO	-	Generated during the course of this study	-
GLMP KO	-	Prof. Dr Winnie Eskild (University of Oslo)	(Kong et al. 2014)
Flipase	-	Dr. Bernd Schröder (University of Dresden)	(Rodríguez et al. 2000)
Cre	B6.C-Tg(CMV-cre)1Cgn/J	Dr. Bernd Schröder (University of Dresden)	(Schwenk, Baron, and Rajewsky 1995)
Tie2 cre	B6.Cg-Tg(Tek-cre)12Flv/J	Dr. Dirk Schmidt-Arras (University of Kiel)	(Koni et al. 2001)
Rosa EYFP	B6.129X1-Gt(ROSA)26Sortm1(EYFP)Cos/J	Dr. Dirk Schmidt-Arras (University of Kiel)	(Srinivas et al. 2001)

Table 3. List of transgenic mouse strains.

2.1.3 Cell lines

Cell line	Description	Reference
MEF MFSD1$^{wt/wt}$	Mouse embryonic fibroblasts, SV40 Large T antigen-immortalised	Generated in the course of this thesis
MEF MFSD1$^{tm1a/tm1a}$	Mouse embryonic fibroblasts, SV40 Large T antigen-immortalised	Generated in the course of this thesis
MEF GLMP$^{wt/wt}$	Mouse embryonic fibroblasts	Winnie Eskild (University of Oslo)
MEF GLMP$^{gt/gt}$	Mouse embryonic fibroblasts	Winnie Eskild (University of Oslo)
HeLa	Cervical carcinoma cells (Henrietta Lacks)	DMSZ, stablished cell line
293T	Human embryonic kidney cells, adenovirus immortalised	ATTC, Stablished line

Table 4. List of cell lines.

2.1.4 Bacteria

The amplification of plasmids was performed using *Escherichia Coli* XL1-blue (Agilent Technologies)

Genotype: *recA1 endA1 gyrA96 thi-1 hsdR17 supE44 relA1 lac* [*F´proAB lacqZΔM15* Tn*10* (Tet^{r})]

2.1.5 Cell culture media and additives

Material	Reference
Bafilomycin A1	Calbiochem
Dulbecco´s modified eagle medium (DMEM) supplemented with L-Glutamine	Life-Technologies
E64D	Enzo Life Sciences
Fetal bovine serum (FBS)	Biochrom
Leupeptin	Enzo Life Sciences
Penicillin-Streptomycin	Life-Technologies
Polyethylenimin Max MW 40,000 (PEI)	Polysciences
Trypsin/EDTA	Sigma Aldrich

Table 5. List of cell culture media and additives.

2.1.6 Antibodies

2.1.6.1 First antibodies

Antigen	Clonality	Host	Relevant dilution	Reference
Actin, TR-phalloidin	-	-	1:300 (IF)	Life Technologies #T7471
aSMA	Polyclonal	Rabbit	1:100 (IF)	GeneTex #GTX100034
CD3e	Monoclonal	Armenian Hamster	1:500 (IF)	Biolegend #145-2C11
CD31	Monoclonal	Rat	1:100 (IF)	BD Biosciences #MED 13.3
CD41	Monoclonal	Rat	1:1000 (IF)	Biolegend #MWReg30
CD45R	Monoclonal	Rat	1:500 (IF)	Immunotools RA3-6B2
CD45R-FITC	Monoclonal	Rat	1:500 (FC)	eBioscience RA3-6B2
CD63	Polyclonal	Rabbit	1:250 (IF)	Eurogentec
CD68	Monoclonal	Rat	1:500 (IF)	Biolegend #FA-11
F4/80	Monoclonal	Rat	1:500 (IF)	Austyn and Gordon 1981
GAPDH	Polyclonal	Rabbit	1:1000 (WB)	Santa Cruz Biotechnology #sc-25778
GLMP	Polyclonal	Rabbit	1:500 (WB)	Pineda
GM130	Monoclonal	Mouse	1:500 (IF)	BD Biosciences #35/GM130
HA	Monoclonal	Rat	1:1000 (WB) 1:500 (IF)	Roche #3F10
HA-PE	Monoclonal	Mouse	1:400 (FC)	Biolegend #16B12
KDEL	Monoclonal	Mouse	1:500 (IF)	Enzo Life Sciences #10C3
Ki67	Monoclonal	Rat	1:500 (IF)	Ebioscience #SolA15
LAMP1	Monoclonal	Rat	1:1000 (WB) 1:500 (IF)	DSHB #1D4B
hLAMP2	Monoclonal	Mouse	1:500 (IF)	DSHB #H4B4
LBPA	Monoclonal	Mouse	1:50 (IF)	Gift Jean Gruenberg #6C4
Limp2	Polyclonal	Rabbit	1:1000 (WB)	Pineda # L2T2
MFSD1	Polyclonal	Rabbit	1:10000 (WB)	Pineda #T2
MFSD1	Polyclonal	Rabbit	1:2500 (IF)	Pineda #T3
MPO	Polyclonal	Rabbit	1:400 (IF)	Millipore #07-496-I
Na^+/K^+ ATPase	Monoclonal	Mouse	1:1000 (WB)	Millipore #C464.6
Tubulin	Monoclonal	Mouse	1:1000 (WB)	DSHB #E7
vWF	Polyclonal	Rabbit	1:300 (IF)	DAKO #A0082

Table 6. List of primary antibodies. Dilution factors are presented for flow cytometry (FC), immunofluorescence (IF) or Western blotting (WB).

2.1.6.2 Secondary antibodies

Antibody	Coupled to	Host	Dilution	Reference
Anti-mouse	HRP	Goat	1:10000	Dianova 115-035-166
Anti-rabbit	HRP	Goat	1:10000	Dianova 111-035-144
Anti-rat	HRP	Goat	1:10000	Dianova 112-035-143
Anti-Armenian Hamster	Alexa Fluor 594	Goat	1:500	Cell Signalling Technology
Anti-mouse	Alexa Fluor 488	Goat	1:500	Cell Signalling Technology
Anti-mouse	Alexa Fluor 594	Goat	1:500	Cell Signalling Technology
Anti-mouse	Alexa Fluor 647	Goat	1:500	Cell Signalling Technology
Anti-rabbit	Alexa Fluor 488	Goat	1:500	Cell Signalling Technology
Anti-rabbit	Alexa Fluor 594	Goat	1:500	Cell Signalling Technology
Anti-rabbit	Alexa Fluor 647	Goat	1:500	Cell Signalling Technology
Anti-rat	Alexa Fluor 488	Goat	1:500	Cell Signalling Technology
Anti-rat	Alexa Fluor 594	Goat	1:500	Cell Signalling Technology
Anti-rat	Alexa Fluor 647	Goat	1:500	Cell Signalling Technology

Table 7. List of secondary antibodies.

2.1.7 Plasmids

Plasmid	Resistance	Reference
pcDNA3.1/H$^+$	Ampicillin/hygromycin	(Huang, Morielli, and Peralta 1993)
pEGFP-N1	Kanamycin/neomycin	(T. T. Yang et al. 1998)

Table 8. List of plasmids.

Construct	Encoded protein	Tag	Source
GLMP-pcDNA3.1/H$^+$	GLMP	-	Self-produced
GLMP-HA-pcDNA3.1/H$^+$	GLMP	HA	Self-produced
GLMP Y400A-HA-pcDNA3.1/H$^+$	GLMP Y400A	HA	Self-produced
GGL-HA-pcDNA3.1/H$^+$	Chimera GLMP-LAMP1	HA	Lea Kählau
GLG-HA-pcDNA3.1/H$^+$	Chimera GLMP-LAMP1	HA	Lea Kählau
GLL-HA pcDNA3.1/H$^+$	Chimera GLMP-LAMP1	HA	Lea Kählau
LGG-HA-pcDNA3.1/H$^+$	Chimera GLMP-LAMP1	HA	Lea Kählau
LGL-HA-pcDNA3.1/H$^+$	Chimera GLMP-LAMP1	HA	Lea Kählau
LLG-HA-pcDNA3.1/H$^+$	Chimera GLMP-LAMP1	HA	Lea Kählau
LAMP1-pcDNA3.1/H$^+$	LAMP1	-	Self-produced
LAMP1-HA-pcDNA3.1/H$^+$	LAMP1	HA	Lea Kählau
MFSD1-pcDNA3.1/H$^+$	MFSD1	-	Self-produced
MFSD1-pEGFP-N1	MFSD1	GFP	Arne Linhorst
MFSD1-HA-pcDNA3.1/H$^+$	MFSD1	HA	Arne Linhorst
HA-MFSD1-pcDNA3.1/H$^+$	MFSD1	HA	Arne Linhorst
MFSD1-TD1-HA-TD2-pcDNA3.1/H$^+$	MFSD1	HA	Self-produced
MFSD1 LL/AA-pEGFP-N1	MFSD1 LL11,12AA	GFP	Arne Linhorst
MFSD1 LL/AA-TD1-HA-TD2-pcDNA3.1/H$^+$	MFSD1 LL11,12AA	HA	Self-produced

Table 9. List of expression constructs.

2.1.8 Oligonucleotides

Oligonucleotide name	Sequence 5´→3
Cre Fw	ATGCGCTGGGCTCTATGGCTTCTG
Cre Rv	TGCACACCTCCCTCTGCATGCACG
CSD-MFSD1-F	TATGGACTCTGCCCACAGTGTTACG

CSD-MFSD1-R	AATGGCCAAAGACAGGCAGAAATGG
CSD-MFSD1-ttR	ACTCAGCCCTTTTCTGTCTCCTACG
CSD-neoF	GGGATCTCATGCTGGAGTTCTTCG
Flp Fw	GTCACTGCAGTTTAAATACAAGACG
Flp Rv	GTTGCGCTAAAGAAGTATATGTGCC
Rosa26-EYFP Fw	GGAGCGGGAGAAATGGATATG
Rosa26-EYFP Fw insert	AAGACCGCGAAGAGTTTGTC
Rosa26-EYFP Rv	AAAGTCGCTCTGAGTTGTTAT

Table 10. List of oligonucleotides for genotyping.

Gene			Sequence´5´→3	UPL#
CD31	NM_001032378.2	Left	gctggtgctctatgcaagc	64
		Right	atggatgctgttgatggtga	
F8	NM_001161373.1	Left	agatacacttaccctgttcccatt	2
		Right	accccaagacccatagacct	
GLMP	NM_020003.1	Left	agtgaacgaacggaactcca	11
		Right	tggagaagagccccataaca	
MFSD1	NM_025813.3	Left	tcgaagggatacttgctgct	76
		Right	gcacggttcaccaagtacag	
MMP2	NM_008610.3	Left	aactttgagaaggatggcaagt	29
		Right	tgccacccatggtaaacaa	
MMP9	NM_013599.4	Left	acgacatagacggcatcca	19
		Right	gctgtggttcagttgtggtg	
TIMP1	NM_001044384.1	Left	gcaaagagctttctcaaagacc	76
		Right	agggatagataaacagggaaacact	
vWF	NM_011708.4	Left	gagaatgcagacccaccttt	98
		Right	ggggacactcttttgcactc	
CXCL1	NM_008176.3	Left	gactccagccacactccaac	83
		Right	tgacagcgcagctcattg	
CCL2 (MCP1)	NM_011333.3	Left	catccacgtgttggctca	62
		Right	gatcatcttgctggtgaatgagt	
CD34	NM_001111059.1	Left	gggtagctctctgcctgatg	84
		Right	tccgtggtagcagaagtcaa	

Table 11. List of oligonucleotides and hydrolysis probes (UPL, Roche) used for qRT-PCR.

Analysis of GAPDH was performed with pre-designed probe and primer set from Abcam (#4352932E).

Name	Sequence 5´→3´
GLMP HindIII Fw	gtataagcttatgtttcgctgttggggacct
GLMP XbaI C-HA Rv	gatctctagattaagcgtagtctgggacgtcgtatgggtagtttatggactggtactcaga
GLMP XhoI Rv	gatcctcgagtcagtttatggactggtact
GLMP Y400A XhoI Rv	gatcctcgagtcagtttatggactgggcct
LAMP1 HindII Fw	gatcaagcttatggcggcccccggcgcccgg
LAMP1 XbaI Rv	gatctctagactagatggtctgatagccggc
MFSD1 HindIII Fw	gtataagcttatggaggacgaggatggggaa
MFSD1 XhoI Rv	aagactcgagttactctggatgagagagct
MFSD1 LL/AA HindIII Fw	aagaaagcttatggaggacgaggatggggaagatcgggcggcggctggg
MFSD1 (TD1-HA-TD2) Rv	agcgtagtctgggacgtcgtatgggtagtcccgtttcacctgagtct
MFSD1 (TD1-HA-TD2) Fw	tacccatacgacgtcccagactacgctatgcaagtgaacaccacgaa

Table 12. List of oligonucleotides used for cloning.

2.1.9 Enzymes

DreamTaq DNA Polymerase	Thermo Fisher Scientific
Phusion High-Fidelity DNA Polymerase	Thermo Fisher Scientific
HindIII restriction enzyme	Thermo Fisher Scientific
XbaI restriction enzyme	Thermo Fisher Scientific
XhoI restriction enzyme	Thermo Fisher Scientific
T4 DNA Ligase	Thermo Fisher Scientific
Proteinase K	Roche

2.1.10 Substrate for β-hexosaminidase activity measurement

p-nitrophenyl N-acetyl-β-D-glucosaminide	Sigma-Aldrich

2.1.11 Radioactive amino acids

Amino acid	Reference
L-Glutamine, [2,3,4-^{3}H]	0149A, American Radiolabelled Chemicals
L-Glycine, [2-^{3}H]	MT 885, Hartmann Analytic
L-[^{35}S] Methionine/cysteine mix (Methionine 70 %, Cysteine 20 %)	SCIS-103, Hartmann Analytic
L-Proline, [2,3,4,5-^{3}H]	0475, American Radiolabelled Chemicals
L-Threonine, [3-^{3}H]	0330, American Radiolabelled Chemicals
L-Valine, [^{3}H]	MT 1654, Hartmann Analytic
L-Amino Acid Mixture [^{3}H] (Alanine 8 %, Arginine 7 %, Aspartic Acid 8 %, Glutamic Acid 12.5 %, Glycine 4 %, Histidine 1.5 %, Isoleucine 5 %, Leucine 14 %, Lysine 6 %, Phenylalanine 8 %, Proline 5 %, Serine 4 %, Threonine 5 %, Tyrosine 4 %, Valine 8 %)	0328, American Radiolabelled Chemicals

Table 13. List of radioactive amino acids used.

2.1.12 Protein and DNA standards

PageRuler Plus Prestained Protein Ladder	Thermo Fisher Scientific
GeneRuler 100bp Plus DNA Ladder	Thermo Fisher Scientific

2.1.13 Ready-made reagents collections and kits

PureYield Plasmid Midiprep System	Promega
GeneJet Plasmid Miniprep kit	Thermo Fisher Scientific
NucleoSpin RNA Plus kit	Macherey-Nagel
RevertAid First Strand cDNA Synthesis Kit	Thermo Fisher Scientific
Pierce BCA Protein Assay kit	Thermo Fisher Scientific

ECL Ultra (TMA-6)	Lumigen
RatLaps™ (CTX-I) EIA immunoassay	IDS

2.1.14 Frequently used buffers and aqueous solutions

LB medium:	1 % (w/v)	Trypton/Pepton
	0.5 % (w/v)	Yeast extract
	1 % (w/v)	NaCl
		pH 7.0
LB agar:	1.5 % (w/v)	Agar-agar
	in	LB medium
Phosphate buffer (0.1 M):	77.4 mM	Na_2HPO_4
	22.6 mM	NaH_2PO_4
Phosphate-buffered saline (PBS) (10x):	100mM	Na_2HPO_4
	18 mM	KH_2PO_4
	1.37 M	NaCl
	27 mM	KCl
		pH 6.8
Mounting medium:	1x	PBS pH 7.4
	17 % (w/v)	Mowiol 4-88
	33 % (v/v)	Glycerol
	20 mg/ml	1,4-diaza-bicyclo-2,2,2-octane (DABCO)

2.1.15 Devices

2720 thermal cycler	Applied Biosystems
Branson Sonifier 450	Emerson Industrial Automation
Centrifuge 5415R	Eppendorf
Centrifuge 5424	Eppendorf
FACSCanto II	BD Biosciences
FlexCycler^2	Analytik Jena
FV1000 confocal laser	Olympus Life Science Solutions
Gel Jet Imager	Intas
Glass homogeniser (type 853202)	B.Braun

Heracell 150 CO_2 incubator	Thermo Fisher Scientific
ImageQuant LAS 4000	GE Healthcare
Light Cycler 480 Instrument II	Roche
Optima LE-80K Ultracentrifuge	Beckmann Coulter
Optima TLX Ultracentrifuge	Beckmann Coulter
Precellys homogeniser	Bertin Instruments
Skyscan 1172 model micro-CT	Bruker micro-CT, Kontich
SM 2000 R sliding microtome	Leica Microsystems
Synergy HT microplate reader	Biotek
Thermomixer 5436	Eppendorf
TriCarb 2910 TR liquid scintillation counter	PerkinElmer

2.1.16 Statistic

Unless stated otherwise, the statistic calculations were performed using GraphPad Prism. Two-tailed unpaired Student's t-test was applied and the significance was stated from $p < 0.05$. The error bars are exposed as standard error of the mean (SEM).

2.2 Methods

2.2.1 Molecular biological methods

2.2.1.1 PCR

The polymerase chain reaction (PCR) is a cyclic method that allows the amplification of DNA fragments *in vitro.* A DNA-polymerase, dNTPs a DNA template and two specific oligonucleotides (primers) spanning the DNA sequence to be amplified are necessary. Every cycle of the PCR reaction has a denaturing phase, an annealing phase and an elongation phase. During the denaturing phase, at high temperature (96º), the double strand DNA template is separated into single strand DNA. Next, the primers and its complementary single strand DNA hybridize in the annealing phase at a temperature usually 3-5 ºC below the melting point of both primers. Finally, during the elongation phase the DNA-polymerase synthesises the complementary DNA strand in a direction 5'→3' at the optimal temperature for its performance, 72ºC. The mentioned cycle is repeated usually between 30 and 45 times. For cloning purposes, Phusion High Fidelity DNA polymerase with proofreading activity (Thermo Fisher Scientific) was used. For genotyping purposes, DreamTaq DNA polymerase (Thermo Fisher Scientific) was used.

2.2.1.2 PCR-driven overlap extension

PCR-driven overlap extension is a three step PCR method that is used to introduce insertions or deletions into a protein, or for mutagenesis. Initial PCRs generate overlapping gene segments that are used as a DNA template for another PCR to create the desired chimeric sequence. In two single PCR reactions, the external forward primer is incubated with the internal reverse primer including the insertion, and *vice-versa* the internal forward primer including the insertion is incubated with the external reverse primer. Two overlapping PCR products are generated and incubated in the same PCR reaction with the external forward and reverse primers (fusion PCR). The PCR product is a DNA fragment including the desired insertion. In this thesis this technique was used to introduce a sequence coding for HA tag between the TD1 and TD2 of MFSD1. A scheme of the PCR-driven overlap extension technique is shown in Figure 6.

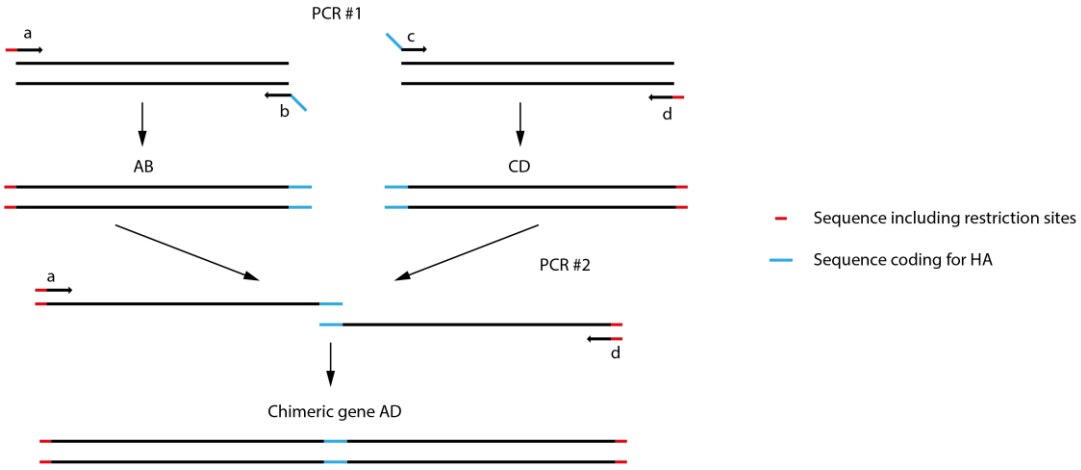

Figure 6. Scheme of PCR-driven overlap extension strategy.

2.2.1.3 Cloning experiments: Restriction enzyme digestion and DNA ligation

Several cDNA constructs were used for overexpression studies. Insertions on the cDNA were introduced by PCR-driven overlap extension (See 2.2.1.2). For cloning of a specific PCR product into a plasmid, the insert and the vector (2 µg) were digested with the corresponding restriction enzyme (Thermo Fisher Scientific). Restriction enzymes cut specific palindromic DNA-sequences, and their activity varies depending on the buffer used for the reaction. The amount of enzyme and the buffer used for each reaction was chosen according to the suggestions of the `DoubleDigest Calculator´ on the Thermo Fisher Scientific webpage (https://www.thermofisher.com/de/de/home/brands/thermo-scientific/molecular-biology/thermo-scientific-restriction-modifying-enzymes/restriction-enzymes-thermo-

scientific/double-digest-calculator-thermo-scientific.html). The digestion products were separated in an agarose gel, purified (See 2.2.1.9) and the concentration of the samples was determined (See 2.2.1.5). For ligation of the insert and the vector, 40 ng of digested vector were incubated with x ng of the digested DNA insert, being x=3*(plasmid bp/insert bp)*40, 1 µl of T4-ligase 1 µl of 10x T4 DNA ligase buffer, filled up to 10 µl with distilled water and incubated at 16°C for 16 hours followed by deactivation of the ligase 10 minutes at 60°C.

2.2.1.4 Amplification and purification of expression vectors in *Escherichia Coli*

For amplification of expression plasmids or for retransformation of established expression vectors, 0.5 µg of plasmid DNA were added into chemically-competent *E.Coli* and incubated for 15 minutes at 4°C. The bacteria were incubated for 1 minute at 42°C in a thermoblock and cooled down 5 minutes on ice. Afterwards 200 µl of LB medium were added to the cell suspension and further incubated for 30 minutes at 37°C shaking. The cell suspension was plated on LB agar plates containing selection antibiotic (50 µg/ml ampicillin or 30 µg/ml kanamycin) and the plates were inverted and incubated at 37°C overnight. The next day single colonies were picked and grown in 3 ml or 200 ml LB medium with antibiotics (50 µg/ml ampicillin or 30 µg/ml kanamycin) at 37°C overnight in a shaking incubator.
The DNA was isolated and purified using the GeneJet Plasmid miniprep kit or the PureYield Plasmid Midiprep System for small and large volumes, respectively. The plasmid isolation was performed according to the manufacturers protocols.

2.2.1.5 Determination of nucleic acid concentration

The DNA and RNA concentration was measured using a Synergy HT microplate reader (Biotek). The maximum peak of absorption of both DNA and RNA, 260 nm, was measured. An optical density (OD) of 1 at 260nm corresponds to a concentration of 50 µg/ml and 40 µg/ml for doubled stranded DNA and RNA, respectively. Additionally, the maximum absorption peak of proteins at 280nm was measured in order to test for protein contamination of the samples. The ratio A_{260}/A_{280} should be between 1.8 and 2.

2.2.1.6 Total RNA extraction

Total RNA was isolated using Nucleospin RNA plus kit (Macherey-Nagel) following the manufacturer´s instructions. Cells were scrapped, centrifuged at 300xg for 5 minutes at 4°C and the pellet was lysed. For homogenisation of liver samples, small pieces of the organ and

ceramic beads (Precellys) were added to 350 µl of lysis buffer provided by the kit and lysed using a Precellys homogeniser (Bertin instruments) with two cycles at 6,000 rpm for 30 seconds. The quality of the RNA was tested by agarose gel electrophoresis (See 2.2.1.9).

2.2.1.7 cDNA synthesis

The synthesis of complementary DNA (cDNA) was performed using the RevertAid First Strand Synthesis kit according to the manufacturer´s instructions. 2 µg of total RNA (2.2.1.6) and random hexamer primers (Thermo Fisher Scientific) were used for the transcription.

2.2.1.8 Quantitative real-time PCR (qRT-PCR)

The mRNA transcripts levels of different genes were analysed by qRT-PCR using the Universal Probe Library (UPL) System Technology (Roche). The oligonucleotides and UPL probes used for every gene were designed using the Assay Design Center (Roche) (See 2.1.8). Hydrolysis probes contain the reporter fluorescein at their 5' end and a dark quencher dye at their 3' end. During the amplification process, the probe hybridises with the mRNA target and the polymerase cleaves the quencher, resulting in an increase of the fluorescence signal in every cycle that can be quantified.

Samples containing 0.5 µl of cDNA (See 2.2.1.7), 4.5 µl LightCycler 480 Probes Master (Roche), 0.1 µM hydrolysis probe and 0.3 µM of each oligonucleotide in a final volume of 10 µl were analysed in a Light Cycler 480 Instrument II (Roche) containing FastStart Taq DNA Polymerase, reaction buffer, a mixture of dNTPs and Mg Cl_2. All the assays were performed in technical duplicates for each sample.

Serial cDNA dilutions of a mixture of samples cDNA was used to calculate the primer efficiency ($E=10^{-1/slope}$). ΔCp (crossing point) for each sample and gene was calculated normalizing the Cp of each assay to the Cp of the reference gene GAPDH of the same sample and assay. The primer efficiency of each gene was used to calculate ΔΔCp ($\Delta\Delta Cp=E^{-\Delta^{Cp}}*100$). The results are presented relative to the values of WT samples.

2.2.1.9 Agarose gel electrophoresis

Separation of DNA and RNA was performed using agarose gel electrophoresis. The samples were prepared by addition of 6x DNA gel loading dye (Thermo Fisher Scientific) and loaded on an agarose gel. Agarose gels were cast in 1x TAE buffer with a final concentration of 1.5% (w/v) and 500 ng/ml of agarose and ethidium bromide, respectively. Electrophoresis was performed

at 120 V in 1x TAE buffer, and the size of the samples was compared to the size standard GeneRuler 100 bp Plus DNA ladder (Thermo Fisher Scientific). The detection of the nucleic acids was performed using the Gel Jet Imager (Intas) at a wavelength of 312 nm. For cloning, DNA-fragments were cut out of the gel and purified according to instructions of the kit manual (High Pure PCR-Purification Kit, Roche).

2.2.2 Cell biological methods

2.2.2.1 Maintenance of cell lines

All cells were kept in a sterile incubator at 37°C and 5% CO_2. The cells were cultivated in DMEM containing 4.5 g/L of D-glucose, L-glutamine (Thermo Fisher Scientific) supplemented with 10% FBS (v/v) and 1% Penicillin/Streptomycin (v/v). The handling of the cells was performed in sterile conditions under a laminar flow clean bench. The cell lines were passaged twice per week at a 100% confluence by trypsin digestion. Shortly, the cells were washed with PBS, incubated with trypsin/EDTA (0.5 mg/ml/0.22 mg/ml in PBS) for approximately 3 minutes in the incubator until they were detached. Next, cells were recovered with culture media and diluted 1:10 or 1:25 for HeLa or MEFs cells, respectively.

2.2.2.2 Isolation of mouse embryonic fibroblasts (MEFs)

Embryos from female mice sacrificed 13.5 days *post coitum* were used to isolate mouse embryonic fibroblasts. After the mice were sacrificed, the uterine horns were extracted, placed in a Petri dish with PBS and the embryos were separated from the placenta and the embryonic sac. The head of the embryos was removed and used for genotyping. All red organs, like liver and spleen, were dissected and the remaining embryo tissue was washed with PBS and placed in a Petri dish with 2 ml of trypsin/EDTA (0.5 mg/ml/0.22 mg/ml in PBS). The tissue was minced with a sterile razor blade and incubated for 15 minutes at 37°C. The cells were collected with culture medium and centrifuged at 300xg for 5 minutes at room temperature. The pellet was resuspended in 10 ml of culture medium and plated in a 10 cm culture dish.

2.2.2.3 Splenocytes isolation

Erylysis buffer:	150 mM	NH_4Cl
	15 mM	Na_2CO_3
	0.1 mM	EDTA

MACS buffer:	1x	PBS
	EDTA	2 mM
	BSA	0.5 % (w/v)

To obtain a cell suspension, the spleen was perforated with a needle and passed through a 100 µm cell strainer located on top of a 50 ml Falcon with the help of a syringe. 5 ml of MACS buffer were poured over the cell strainer in order to collect the cells. Splenocytes were collected by centrifuging 5 minutes at 210 x g at 4°C. In order to lyse the erythrocytes, the cell pellet was resuspended in 1 ml erylysis buffer and incubated 10 minutes at room temperature. Next. 19 ml of culture medium were added and the cell suspension was centrifuged 5 minutes at 210 x g at 4°C. Finally, the cell pellet was resuspended in 2.5 ml of MACS buffer.

2.2.2.4 Isolation of primary B cells

MACS buffer:	1x	PBS
	EDTA	2 mM
	BSA	0.5 % (w/v)

$B220^+$ B cells from spleen were isolated using magnetic activated cell sorting system (MACS) from Miltenyi Biotec. After splenocytes isolation (see 2.2.2.3), $3x10^7$ cells were centrifuged 5 minutes at 210 x g at 4°C, resuspended in 370 µl of MACS buffer, 30 µl of B220 Microbeads were added and the cell suspension was incubated for 20 minutes at 4°C. 3 ml of MACS buffer were added to the cell suspension, it was further centrifuged 5 minutes at 210 x g at 4°C and resuspended in 500 µl of MACS buffer. A LS column was inserted into the MACS separator and equilibrated with 3 ml of MACS buffer. The 500 µl of cell suspension was added to the column and unlabelled cells were collected. The columns were washed with 3 ml of MACS buffer for three times. After removal of the column from the MACS separator, magnetically labelled cells were flushed out with 5 ml of MACS buffer by applying a plunger. The cells obtained were prepared for electron microscopy analysis (See 2.2.2.6)

2.2.2.5 Isolation of primary T cells

MACS buffer:	1x	PBS
	2 mM	EDTA
	0.5 % (w/v)	BSA

T lymphocytes from spleen were isolated by negative selection using MACS and Mojosort Mouse CD3 T Cell Isolation Kit from Biolegend. After splenocytes isolation (see 2.2.2.3), 10^7 cells were incubated with 5 µl of biotin-antibody cocktail containing anti-Ly6C (Gr-1), CD45R, CD49b, CD19, CD11b, CD24 and TER-119 for 15 minutes on ice. 4 ml MACS buffer were added to the cell suspension and centrifuged 5 minutes at 210 x g at 4°C. The pellet was resuspended in 100 µl of MACS buffer and 2 µl of streptavidin-conjugated nanobeads were added and incubated for 15 minutes on ice. A LD column was inserted into the MACS separator and equilibrated with 3 ml of MACS buffer. 500 µl of MACS buffer were added to the cell suspension and the mix was added to the column. Unlabelled cells, corresponding to T lymphocytes were collected and prepared for electron microscopy analysis (See 2.2.2.6).

2.2.2.6 Cell fixation for electron microscopy analysis

Polymerization buffer:	0.1 M	Phosphate buffer pH 7.4
	1.5 % (w/v)	PFA
	1.25 % (v/v)	Glutaraldehyde
	6 % (w/v)	Bovine serum albumin (BSA)

Isolated B or T lymphocytes (See 2.2.2.4 and 2.2.2.5) were washed with 1x PBS, centrifuged for five minutes at 220 x g and 4°C and resuspended in 0.5 ml of 0.1 M phosphate buffer (pH 7.4). 0.5 ml of 5 % (v/v) glutaraldehyde in 0.1 M phosphate buffer (pH 7.4) were added and the sample was incubated one hour at room temperature and overnight at 4°C. Next, the sample was centrifuged for five minutes at 220 x g and 4°C. The pellet was resuspended in 25 µl of polymerization solution, prepared immediately before use, and incubated for one hour at room temperature. The polymerized pellet was stored in 2.5 % (v/v) glutaraldehyde in 0.1 M phosphate buffer at 4°C.

2.2.2.7 Cryo-preservation of cell lines

The cell lines were preserved as cryo-cultures in liquid nitrogen. The cells were detached from the dishes using trypsin, centrifuged at 210 x g for 5 minutes at room temperature, resuspended in 1 ml of DMEM containing 20% (v/v) FBS and 10% (v/v) DMSO and frozen at -80°C. For long-term storage, the cryo-cultures were transferred to the gas phase of a liquid nitrogen tank.

The cryo-cultures were thawed with nine ml of pre-warmed medium, centrifuged at 210 x g for 5 minutes at room temperature, resuspended in new culture medium and seeded in a 10 cm dish.

2.2.2.8 Transfection of mammalian cells

The introduction of nucleic acids into eukaryotic cells is the so-called transfection. All the transfections in this thesis were performed using polyethylenimine (PEI). PEI condenses DNA into positively charged particles that bind to anionic cell surface residues and is further endocytosed. Inside the vesicle, the amines from PEI are protonated resulting in an influx of counter-ions and osmotic swelling, which leads to the vesicle burst and release of the content. High concentrations of PEI are toxic.

For transfection of HeLa cells 1 µg of DNA was incubated with 2.5 µl of PEI in 300 µl of DMEM only (without antibiotics nor FBS), and for transfection of MEF cells 5 µg of DNA were incubated with 12.5 µl of PEI in 300 µl of DMEM only for 15 minutes at room temperature. The mix was applied to a 10 cm dish with the cells, and after ~6 hours the media was exchanged. The transfected cells were analysed 24-48 hours post-transfection.

2.2.2.9 Indirect immunofluorescence labelling of cells

Quenching solution:	1x	PBS pH 7.4
	0.2 % (w/v)	Saponin
	0.12 % (w/v)	Glycine
Blocking solution:	1x	PBS pH 7.4
	0.2 % (w/v)	Saponin
	10 % (v/v)	FBS

The subcellular localization of proteins was analysed by indirect immunofluorescence using specific first antibodies and secondary antibodies coupled to fluorophores.

Cells were grown over glass coverslips until a confluence of approximately 80%. After washing three times with PBS, the cells were fixed for 20 minutes with 4% (w/v) paraformaldehyde (PFA) followed by three additional washing steps. Cells were permeabilized with 0.2% (w/v) saponin in PBS for 5 minutes. The samples were quenched with quenching solution for 10 minutes and washed with 0.2% (w/v) saponin in PBS. In order to reduce unspecific binding of the antibodies, the samples were incubated with blocking solution for one hour at room temperature. Next, the samples were incubated with primary antibodies diluted in blocking

solution overnight at 4°C. The coverslips were washed 4 times in 0.2% (w/v) saponin in PBS and incubated for 90 minutes with AlexaFluor dye-conjugated secondary antibodies diluted (1:500) in blocking solution. Finally, the coverslips were washed 4 times in 0.2% (w/v) saponin in PBS, two times in distilled water and mounted on microscope slides with mounting medium including 1 µl/ml of DAPI (4-,6-diamidino-2-phenylindole) to visualize the cell nuclei. For visualization of the samples an FV1000 confocal laser scanning microscope (Olympus Life Science Solutions) using a U Plan S-Apo 100x oil immersion objective (NA=1.40) was used. For Image acquisition and process the Olympus FluoView Software was used.

2.2.2.10 Indirect immunofluorescence labelling of cells using selective permeabilization

The selective permeabilization of the plasma membrane was performed following the protocol in section 2.2.2.9 exchanging all the steps containing 0.2% (w/v) saponin in PBS by 0.001% (w/v) digitonin in PBS.

2.2.2.11 Labelling of surface molecules for flow cytometry

MACS buffer:		
	1x	PBS
	EDTA	2 mM
	BSA	0.5 % (w/v)

Surface protein expression of transfected HeLa cells and isolated splenocytes (See 2.2.2.3) was analysed by flow cytometry. Approximately 10^6 cells were pipetted in 96 well round bottom tissue cultures plates and centrifuged at 210 x g for 5 minutes at 4°C. The samples were incubated with specific antibodies coupled to phycoerythrin (PE) or fluorescein-5-isothiocyanate (FITC) diluted in MACS buffer (See 2.1.6.1) for 45 minutes on ice in dark conditions. Next the samples were centrifuged at 210 x g for 5 minutes at 4°C and washed with MACS buffer. The process was repeated and the cells were resuspended in 200 µl of MACS buffer for further analysis on a FACSCanto II (BD Biosciences) device using the FACSDiva software. Positive and negative controls were used for every dye. No compensation of spectral overlap was performed as only one dye was analysed at the same time.

2.2.2.12 Radioactive amino acid uptake assay

Krebs-Ringer Buffer:	146 mM	NaCl
	3 mM	KCl
	1 mM	$CaCl_2$
	10 mM	KH_2PO_4/K_2HPO_4 (pH 7.5/6.2/5.5)

HEK cells were transfected with the plasmid of interest (See 2.2.2.8). 7 hours post transfection, approximately $5x10^4$ transfected or untransfected cells were seeded on p12 culture plates previously coated overnight with poly-L-lysine. 24 hours post-transfection the cells were washed twice with KR buffer (pH 7.4) and incubated for 15 minutes with KR buffer (pH 5.5) containing 100 µM of cold amino acids and 0.5 µCi of H^3 or S^{35} labelled amino acids. The cells were washed twice with cold KR buffer (pH 7.4) on ice, lysed with 0.5 ml of 0.1 M NaOH and collected in a 2 ml tube. The wells were washed with additional 0.5 ml of 0.1 M NaOH and added to the tube. 1 ml of 0.2 M KR buffer (pH 6.2) was added to the mix containing the lysed cells in order to neutralize the pH. 0.2 ml of the cell lysates were used for protein quantification (See 2.2.3.4). 1.8 ml of the cell lysates were mixed with 8 ml of Ultima Gold™ liquid scintillation cocktail (PerkinElmer) and the disintegrations per unit (DPM) were measured in a TriCarb 2910 TR liquid scintillation counter (PerkinElmer). The radioactivity measurements were corrected by the protein concentrations.

2.2.3 Protein biochemical methods

2.2.3.1 Generation of cell lysates for protein extraction

Lysis buffer:	1x	PBS
	1x	Complete inhibitor
	1 % (w/v)	Triton X-100

Cells grown on culture dishes were washed twice with PBS and 600 µl of PBS supplemented with 1x complete Protease inhibitor cocktail (Roche) were added to the plate for harvesting the cells using a cell scraper. The cell suspension was centrifuged for 8 minutes at 1,000 x g at 4°C. The pellet was resuspended in lysis buffer, sonicated twice for 20 seconds at 4°C using a Branson Sonifier 450 (level 7 in a cup horn, Emerson Industrial Automation) and lysed on ice for approximately 60 minutes (the samples were homogenised using a vortex every 15 minutes). The cell suspension was centrifuged at 16,000 x g for 15 minutes at 4°C and the

supernatants containing the extracted proteins were kept in a new tube for protein concentration determination (2.2.3.4).

2.2.3.2 Preparation of tissue homogenates

Lysis buffer:	1x	PBS
	1x	Complete inhibitor
	1 % (w/v)	Triton X-100

For mouse tissue homogenisation, the tissues were prepared in 20 volumes of lysing buffer and homogenised with 10-20 strokes at 1,000 rotation per minute using a Glass homogeniser (B.Braun type 853202). The lysates were sonicated twice for 20 seconds at 4°C using a Branson Sonifier 450 (level 7 in a cup horn, Emerson Industrial Automation) and lysed on ice for approximately 60 minutes (the samples were homogenised using a vortex every 15 minutes). The lysates were centrifuged at 16,000 x g for 15 minutes at 4°C and the supernatants containing the extracted proteins were kept in a new tube for protein concentration determination (2.2.3.4).

2.2.3.3 Membrane protein preparation of mouse tissues and cells

Homogenisation buffer:	1x	PBS pH 7.4
	1x	Complete inhibitor
	250 mM	Saccharose
	10 mM	Tris HCl

Mouse tissues were prepared in 10 volumes homogenisation buffer and homogenised with 10-20 strokes at 1,000 rotation per minute using a Glass homogeniser (B.Braun type 853202). The lysates were centrifuged for 10 minutes at 1,000 x g at 4°C, and the post nuclear supernatant was collected (PNS).

Cells were grown in culture dishes, washed twice with PBS and collected in 600 µl of PBS supplemented with 1x complete Protease inhibitor cocktail (Roche) using a cell scraper. The cell suspension was centrifuged for 10 minutes at 1,000 x g at 4°C, and the pellet was resuspended in homogenisation buffer.

The PNS and cell suspensions were sonicated twice for 20 seconds at 4°C using a Branson Sonifier 450 (level 7 in a cup horn, Emerson Industrial Automation) and three cycles of freeze/thaw were applied. The samples were placed into a polypropylene tube with snap-on cap (Beckmann Coulter) and ultracentrifuged at 186,000 x g in an Optima TLX Ultracentrifuge

(Beckmann Coulter) using a TLA-55 rotor (Beckmann Coulter) for one hour at 4°C. The pellet was resuspended in 2% SDS in PBS and the protein concentration was determined (2.2.3.4)

2.2.3.4 Determination of protein concentration

The protein concentration determination was performed using the Pierce BCA Assay kit (Thermo Fisher Scientific) according to the manufacturer's instructions. This method combines the reduction of Cu^{2+} to Cu^{1+} by proteins in an alkaline medium (biuret reaction) and the chelation of Cu^{1+} by bicinchonic acid (BCA) that results in a complex with a strong absorption at 562 nm that is nearly linear with increasing protein concentrations. The samples were diluted and incubated with the assay mixture for 30 minutes at 37°C and the absorbance at 562 nm was measured using a Synergy HT (BioTek) microplate reader. A calibration curve based on bovine serum albumin (BSA) standard concentrations ranging from 0 to 2.0 mg/ml was used to determine the protein concentration of the samples.

2.2.3.5 Co-immunoprecipitation (Co-IP)

Immunoprecipitation buffer:	1x	PBS pH 7.4
	1x	Complete inhibitor
	120 mM	NaCl
	50 mM	Tris HCl
	2,5 mM	$CaCl_2$
	2,5 mM	$MgCl_2$
	1% (w/v)	CHAPS (Alternative detergents used: Brij35, Brij78, Brij96, BrijS20, or Triton X-100)
Lammli buffer (1x):	125 mM	Tris/HCl pH 6.8
	1 % (w/v)	SDS
	10 % (v/v)	Glycerol
	1 % (v/v)	β-mercaptoethanol
	Traces of	Bromophenol blue

In order to check for protein-protein interaction, Co-IP assay was performed. HeLa cells were transfected with plasmids coding for the desired proteins. 48 hours post-transfection, cells were washed twice with PBS and collected in 600 µl of PBS supplemented with 1x complete Protease inhibitor cocktail (Roche) using a cell scraper. The cell suspension was centrifuged for 8 minutes at 1,000 x g at 4°C, and the pellet was resuspended in the immunoprecipitation buffer containing the desired detergent. The cell suspension was sonicated twice for 20

seconds at 4°C using a Branson Sonifier 450 (level 7 in a cup horn, Emerson Industrial Automation) and lysed on ice for approximately 60 minutes (the samples were homogenised using a vortex every 15 minutes). The cell suspension was centrifuged at 16,000 x g for 15 minutes at 4°C and the supernatants containing the extracted proteins were kept in a new tube for protein concentration determination (2.2.3.4). 300-1,000 µg of protein were incubated with 1.5 µl of anti-MFSD1 antibody overnight at 4°C in a rotor. At the same time, 50 µl/sample of Dynabeads protein G for Immunoprecipitation (Thermo Fisher Scientific) were blocked with 3% BSA. Next day, the beads were incubated with the lysate/antibody mixture for 2 hours at room temperature in a rotor. The samples were washed with 1 ml immunoprecipitation buffer using a magnetic separator and incubated 15 minutes at room temperature for three times. The supernatants were discarded. In a final step, the beads were incubated with 40 µl of 1x lammli buffer, and incubated for 10 minutes at 55°C or 95°C depending on the protein to be detected. Finally, the Co-IP samples were analysed by SDS-PAGE and immunoblotting (See 2.2.3.6 and 2.2.3.7).

2.2.3.6 SDS polyacrylamide gel electrophoresis (SDS-PAGE)

Sample buffer (5x):	625 mM	Tris/HCl pH 6.8
	50% (v/v)	Glycerol
	5 % (w/v)	SDS
	5 % (v/v)	B-mercaptoethanol
	Traces of	Bromophenol blue
Separating gel buffer:	1.5 M	Tris/HCl pH 8.8
	0.4 % (w/v)	SDS
Stacking gel buffer:	0.5 M	Tris/HCl pH 6.8
	0.4 % (w/v)	SDS
SDS gel electrophoresis running buffer (10x):	0.25 M	Tris
	0.2 M	Glycine
	1 % (w/v)	SDS

Proteins can be separated according to their size and independent of their charge by sodium dodecyl polyacrylamide gel electrophoresis (SDS-PAGE). Proteins were prepared in sample buffer to a final concentration of 1% SDS, 1% β-mercaptoethanol and traces of bromophenol blue and were denatured for 10 minutes at 55°C or 95°C depending on the hydrophobicity of

the sample and its running behaviour. The samples were loaded together with a protein-size standard (Thermo Fisher Scientific) in 7.5-12.5 % self-made polyacrylamide separating gels combined with a 4.5% polyacrylamide stacking gel (Table 14). The gel was exposed to constant voltage (80-120 V) in 1x running buffer.

		Separating gel			Stacking gel
	Units	7.5 %	10 %	12.5 %	5.25 %
Separating/Stacking buffer	[ml]	2.6	2.6	2.6	1.35
30 % (w/v) Acrylamide/bisacrylamide Rotiphorese Gel 30 (37, 5:1)	[ml]	2.5	3.3	4.2	1.75
H_2O	[ml]	4.8	4	3.1	6.85
10 % (w/v) ammonium persulfate	[µl]	60	60	60	60
Tetramethylethylenediamine (TEMED)	[µl]	30	30	30	30

Table 14. Composition of SDS polyacrylamide gels.

2.2.3.7 Western blotting

Transfer buffer (1x):	25 mM	Tris pH 8.3
	0.2 M	Glycine
	20 % (v/v)	Methanol

In order to detect proteins with antibodies after the separation by SDS-PAGE, the proteins were transferred from the polyacrylamide gels into nitrocellulose membranes (GE Healthcare) by the TANK-blot system. The membrane, the whatman-filter paper and the fibre pads used were equilibrated in transfer buffer. The gel and the membrane were placed between a couple of whatman-filter paper, those between a couple of fibre pads and all those inside a cassette. The membrane was located close to the anode and the gel close to the cathode. The cassette was placed in a TANK-blotting chamber (Bio-Rad) filled with 1x blotting buffer and an ice block and subjected to constant electric current of 800 mA for 2 hours in a 4°C room.

2.2.3.8 Incubation with antibodies and stripping of the immunoblots

TBS-T buffer:	20 mM	Tris/HCl pH 7.0
	150 mM	NaCl
	0.1 % (w/v)	Tween® 20
Detection solution A:	0.1 M	Tris/HCl pH 8.6
	0.025 % (w/v)	luminol
Detection solution B:	0.11 % (w/v)	p-Coumaric acid
	In	DMSO

In order to reduce unspecific binding of antibodies, after western blotting (2.2.3.7) the membranes were incubated in 5% (w/v) milk powder in 1x TBS-T buffer for one hour at room temperature. Next, the membranes were incubated with the antibody diluted (2.1.6.1) in 5% (w/v) milk powder in 1x TBS-T buffer overnight at 4°C. Next day, the membranes were washed in 1x TBS-T buffer three times for 10 minutes at room temperature followed by incubation with the respective secondary antibody coupled to horseradish peroxidase (HRP) (2.1.6.2) diluted in 5% (w/v) milk powder in 1x TBS-T buffer for two hours at room temperature. Following three further washing steps in 1x TBS-T buffer for 10 minutes, horseradish peroxidase activity was detected by using an ImageQuant LAS 4000 (GE Healthcare). Hereby the membranes were covered with a mixture of ECL Ultra TMA-6 (Lumigen) (100 µl of each), 1 ml detection solution A, 100 µl of detection solution B and 4.5 µl of H_2O_2. The intensity of the signal was quantified using Image J software. Before incubation with new antibodies, the membranes were stripped using 0.2 M NaOH. Incubations of 5 minutes at room temperature and gentle shaking were done in distilled water, followed by 0.2 M NaOH, rinsing with distilled water, 0.2 M NaOH distilled water, and TBS-T. Next, the membranes were incubated in 5% (w/v) milk powder in 1x TBS-T buffer for one hour at room temperature followed by incubation with first antibody.

2.2.3.9 Purification of tritosomes

Lysosomes usually have a comparable density to mitochondria, and those organelles can not be separated by buoyant density centrifugation. Fractions highly enriched in lysosomes can be isolated by the method developed by Wattiaux through differential centrifugation (Wattiaux et al. 1963). After injection of Triton WR-1339 (tyloxapol), the lipoprotein-lipase activity is inhibited, which leads to an increase of VLDL in plasma (Hayashi et al., 1981). The VLDL are recognized by LDL–receptors of liver cells and are endocytosed and further transported to lysosomes, decreasing their density (Hayashi et al., 1982).

3 days after the intraperitoneal injection of tyloxapol into mice (See 2.2.5.6), the liver was collected and homogenised in 4 ml of 0.25 M saccharose with 5 strokes at 1,000 rotation per minute using a Glass homogeniser (B.Braun type 853202) and centrifuged at 1,140 x g for 10 minutes at 4°C. The supernatant was kept and the nuclear pellet was resuspended in 4 ml of 0.25 M saccharose and centrifuged at 1,140 x g for 10 minutes at 4°C. Both supernatants were pooled in a Ti-70 centrifuge tube and centrifuged in an Optima LE-80K Ultracentrifuge

(Beckmann Coulter) with a Ti-70 rotor for seven minutes at 56,500 x g at 4°C. The supernatant was collected and the pellet was resuspended in 8.5 ml of 0.25 M saccharose and a centrifugation for seven minutes at 56,500 x g at 4°C was repeated. The supernatant was discarded, and the pellet, containing the mitochondrial and lysosomal fractions, was carefully resuspended in 2.5 ml of ρ 1.21 saccharose and overlaid by a discontinuous saccharose gradient of 2.5 ml ρ 1.15 saccharose, 2.5 ml ρ 1.14 saccharose and 2 ml ρ 1.06 saccharose. The tubes were centrifuged for 150 minutes at 110,000 x g at 4°C and the different fractions were collected (Figure 7). Fraction F2, which is enriched in lysosomes was used for further proteomics and immunoblotting analysis.

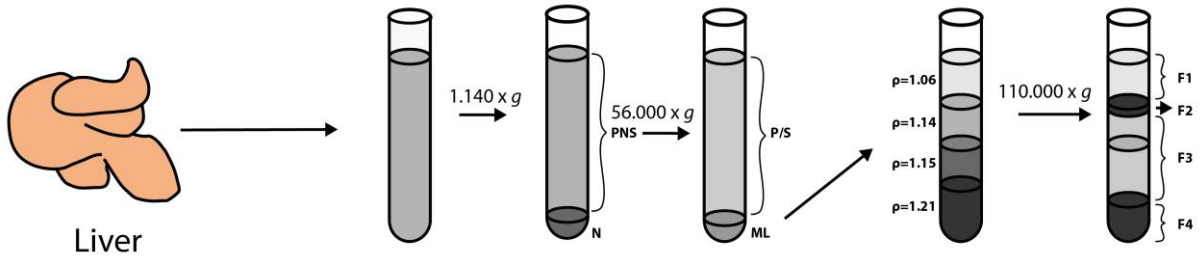

Figure 7. Schematic representation of tritosomes preparation.

2.2.3.10 Percoll gradient of tissues

Buffer I:	0.25 M	Saccharose
	20 mM	Imidazole pH 7.4
Buffer I:	90 % (v/v)	Percoll
	250 mM	Saccharose

Liver and kidney subcellular fractionation was performed by density gradient centrifugation using colloidal silica particles of 15-30 nm of diameter coated with polyvinylpyrrolidone, named as Percoll.

The tissue was homogenised with 9 volumes of buffer I with 10 strokes at 150 rotations per minute using a Glass homogeniser (B.Braun type 853202) and centrifuged for 5 minutes at 1,000 x g and 4°C. 0.9 ml of the supernatant were carefully mixed with 3 ml of buffer P and 5.1 ml of buffer I and added to type 70 Ti centrifuge tubes. The samples were centrifuged for 90 minutes at 30,000 x g at 4°C using an Optima LE-80K Ultracentrifuge (Beckmann Coulter) with a Ti-70 rotor.

The gradient was separated in 13 fractions of approximately 700 µl each. The fractions were sonicated for 20 seconds twice, and the β-hexosaminidase of the fractions was measured (See 2.2.3.11).

2.2.3.11 In vitro measurement of lysosomal hydrolase activity

Substrate buffer:	0,1 M	Sodium citrate pH 4.6
	0,2 % (w/v)	BSA
	0,04 % (w/v)	Sodium azide
Stop solution:	0,4 M	NaOH pH 10.4
	0,4 M	Glycine

The artificial substrate p-nitrophenyl-β-D-glucosaminide (Sigma-Aldrich) was used to assess the enzymatic activity of β-hexosaminidase. At an acidic pH, beta-hexosaminidase hydrolyse the substrate the glucose and the p-nitrophenol are freed. A basic solution stops the reaction, the p-nitrophenol become fully protonated leading to a yellow colour shift. The intensity of the colour shift can be quantified by analysing the absorbance of the samples at 405 nm.
In this thesis, Percoll fractions of liver and kidney (See 2.2.3.10) were analysed for beta-hexosaminidase activity. 10 µl of the sample were mixed with 90 µl of H2O and 100 µl of 10mM p-nitrophenyl N-acetyl-β-D-glucosaminide in substrate buffer and were incubated for 2 hours at 37°C. The reaction was stopped by adding 500 µl of stop solution. 200 µl of the mixture were pippeted into a 96 well plate and the absorbance at 405 nm was measured using a Synergy HT (BioTek) microplate reader. In Equation 1 the formula to calculate the enzymatic activity is shown.

$$Activity\left[\frac{mU}{ml}\right] = \frac{\Delta E \times 10^6}{\varepsilon\left[\frac{l}{mol \times cm}\right] \times d[cm] \times t[\min]} \times \frac{V_{test\ volume}[\mu l]}{V_{sample\ volume}[\mu l]} \times F_{dil.\ Sample}$$

Equation 1. Calculation of the enzymatic activity. $\Delta E = E_{Sample} - E_{blank}$; Test volume = Volume of the reaction after stopping the reaction; Sample volume = Volume of the sample analysed; F = dilution factor of the sample; ε = Extinction coefficient; t = time; d = thickness of the cuvette.

2.2.3.12 Enzyme-linked immunosorbent assay (ELISA) for CTX-I

The serum concentration of the C-terminal telopeptide of type I collagen (CTX-I), which is released into circulation during renewal of the skeleton bone matrix, was analysed using the

RatLaps™ (CTX-I) ELISA (ids). ELISA assays base the quantification of the concentration of specific proteins in the use of specific antibodies and detection of an enzymatic activity proportional to the protein concentration. The RatLaps™ ELISA is based upon competitive binding of a soluble polyclonal antibody to immobilized antigens or to soluble antigens (in the samples). The assay was performed according to the manufacturer's instructions.

2.2.3.13 Antibody generation

Antibodies against mouse MFSD1 and mouse GLMP were produced by Pineda Antibody-Service. Rabbits were immunized with an amino acid sequence of MFSD1 (NH_2-EDEDGEDRALLGGRREAD-COOH) or GLMP (NH_2-CQAFSRSGRPAQPPRLLH-COOH). The serum of the rabbits immunized with MFSD1 or GLMP sequences was extracted 120 days and 220 days post-immunization, respectively. In both cases, the serum was affinity purified using columns with immunization peptides coupled to beads. The resulting affinity purified antibodies were used for analysis.

2.2.4 Histological methods

2.2.4.1 Preparation of semi-thin cryosections

After mouse perfusion and post-fixation in 4 % PFA (See 2.2.5.8), the fixative was removed and the tissues were washed with 0.1 M phosphate buffer. Subsequently, the tissues were incubated in 30 % (w/v) saccharose in 0.1 M phosphate buffer for 24 hours at 4 °C. Semi-thin sections (35 µm) were prepared using a Leica SM 2000 R sliding microtome (Leica Microsystems) and dry-ice cooling. The samples were stored in 0.1 M phosphate buffer containing 0.02 % (w/v) sodium azide.

2.2.4.2 Immunofluorescence staining of semi-thin sections

Blocking solution:	0.1 M	Phosphate Buffer pH 7.4
	4 % (v/v)	Goat serum
	0.5 % (w/v)	Triton X-100
Washing buffer:	0.1 M	Phosphate Buffer pH 7.4
	0.25 % (w/v)	Triton X-100

Indirect immunofluorescence stainings were performed on semi-thin cryosections (See 2.2.4.1) in order to detect specific proteins. The sections were washed with 0.1 M phosphate

buffer in order to remove remaining sodium azide. To reduce unspecific binding, the sections were incubated in blocking solution for two hours at room temperature and shaking. Subsequently, three washing steps with washing buffer were applied followed by incubation with the primary antibodies diluted (See 2.1.6.1) in blocking solution overnight at 4°C. After three washing steps with washing buffer, the sections were incubated with AlexaFluor dye-conjugated secondary antibodies diluted (1:500) in blocking solution for two hours at room temperature under conastant shaking. Finally, the samples were rinsed with washing buffer and embedded using mounting medium including 1 µl/ml of DAPI to stain the cell nuclei.

2.2.4.3 X-Gal staining of β-galactosidase in mouse tissues

Permeabilizing solution:	0.01 % (w/v)	Na-deoxycholat
	0.02 % (w/v)	NP-40
	In	PBS
X-Gal solution:	5 mM	K3Fe(CN)6
	5 mM	K4Fe(CN)6
	2 mM	MgCl2
	1 mg/ml	X-Gal in PBS

Semi-thin cryosections were washed in PBS for 10 minutes shaking and incubated for 10 minutes in permeabilizing solution. After a washing step in PBS, the samples were incubated for 3 hours in X-Gal solution at 37°C with gentle shaking. The sections were washed twice in PBS and embedded in mounting medium.

2.2.4.4 High-resolution microCT

High resolution micro computed tomography (µCT) is x-ray imaging in 3D. Consecutive cross-sections are recorded and using computer software they are stacked, and 3D morphometric parameters can be measured. Vertebras L5 and femurs were extracted and incubated in 4 % (w/v) PFA in PBS for three days at room temperature, and kept in 70 % (v/v) ethanol until analysis. µCT analysis was performed on vertebra L5 and femur using a Skyscan 1172 model micro-CT (Bruker micro-CT, Kontich). Both were imaged with an X-ray tube voltage of 50 kV, a current of 200 µA with a 0.5 mm aluminium filter. The scanning angular rotation was 180° and the angular increment was 0.70°. The voxel size was 4.49 µm isotropically. Image reconstructions were performed with NRecon (version 1.6.9). The trabecular bone in the vertebral body was selected for analysis starting at a distance of 4.5 µm

caudal of the lower end of the pedicles and extending a longitudinal distance of 225 µm in the caudal direction. The femur trabecular bone proximal to the distal growth plate was selected for analysis excluding the cortical bone, starting at a distance of 786 µm from the growth plate and extending a longitudinal distance of 135 µm in the distal direction. The cortical measurements of the femur were performed in the midshaft diaphyseal region starting at a distance of 5.4 mm proximal from the distal growth plate and extending a longitudinal distance of 135 µm in the distal direction.

2.2.5 Animal experimentation

2.2.5.1 Animal housing

The mice were kept in a specific pathogen free environment by housing in individually ventilated cages (IVC). The room temperature was kept constant at 21 °C (± 5 °C) with a humidity of 45 – 60 %. Cycles of 12 hours lighting and 12 hours darkness were applied. The animals had access to water and food *ad libitum*. The animal handling and care were performed in agreement with the German animal welfare law according to the guidelines of the Christian Albrechts University of Kiel. Experiments involving animals were approved by the Ministery of Energy, Agriculture, the Environment and Rural Areas Schleswig-Holstein under the reference number V312-72241.121-3.

2.2.5.2 MFSD1 'knockout-first' allele (tm1a) strategy

The new MFSD1-deficient mouse strain used was based in a 'knockout-first' allele (tm1a) strategy. The tm1a allele is formed by a FRT sequence followed by an IRES:lacZ trapping cassette that contains an acceptor splicing site. The LacZ cassette is followed by a loxP sequence, a neo cassette, a FRT sequence, a loxP sequence, the exon 2 of *MFSD1* and a last loxP sequence (Figure 8). The tm1a allele was inserted into the second *MFSD1* gene intron of an embryonic stem (ES) cell that was injected into a host blastocysts and gave rise to chimeric mice.

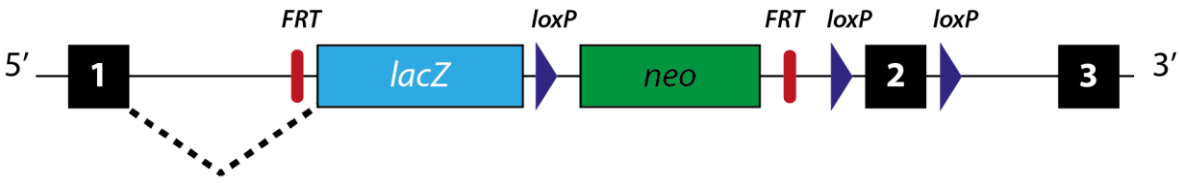

Figure 8. Scheme of 'knock-out first' tm1a allele.

The breeding of mice containing MFSD1 tm1a allele with flipase expressing mice leads to recombination between the FRT sequences that result in a tm1c allele coding for MFSD1 WT protein (Figure 9A). Further breeding of mice containing tm1c allele with cre expressing mice induces the recombination between the loxP sequences that results in a tm1d allele which has a deletion of the exon 2, leading to a frameshift mutation, a new STOP codon in exon 3 and a truncated MFSD1 protein (Figure 9B).

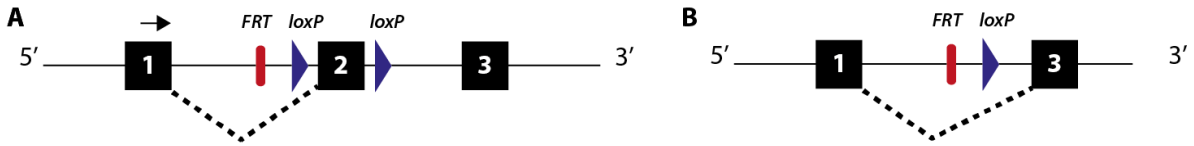

Figure 9. Scheme of tm1c allele (A) and tm1d allele (B).

2.2.5.3 Analysis of Tie2-Cre-EYFP reporter mice

During the course of this study a conditional MFSD1 knockout mouse line was established using a *Cre/loxP* recombination system with mice expressing Cre recombinase under the control of *Tie2* promotor. *Tie2* is expressed in endothelial cells and cells from the hematopoietic lineage (Schlaeger et al. 1997; Tang et al. 2010). In order to evaluate the *Tie2* promoter activity, *Tie2-Cre* mice were bred with a *Rosa26-EYFP* reporter strain (Srinivas et al. 2001).

These reporter mice contain a genomic insertion coding for the enhanced yellow fluorescent protein (EYFP) in the ubiquitously expressed locus Rosa26. The insertion contains a STOP codon cassette flanked by *loxP* upstream of the EYFP coding region. Upon cre-mediated recombination EYFP is expressed, which can be visualized (Figure 10A). In Figure 10B the breeding strategy used between Tie2-Cre and Rosa-EYFP mice is shown. The immunofluorescence analysis of liver sections with anti-CD31, anti-F4/80 or Texas red phalloidin to identify liver sinusoidal endothelial cells (LSECs), macrophages and hepatocytes, respectively, revealed that both LSECs and macrophages from Tie2-Reporter mice expressed EYFP (Figure 10C). The analysis of spleen and thymus sections revealed the expression of EYFP in the tissues of Tie2-Reporter mice (Figure 10D).

These results indicate that Tie2 promoter is active in LSECs and Kupffer cells in liver and in splenocyte and thymocyte populations, but not in hepatocytes.

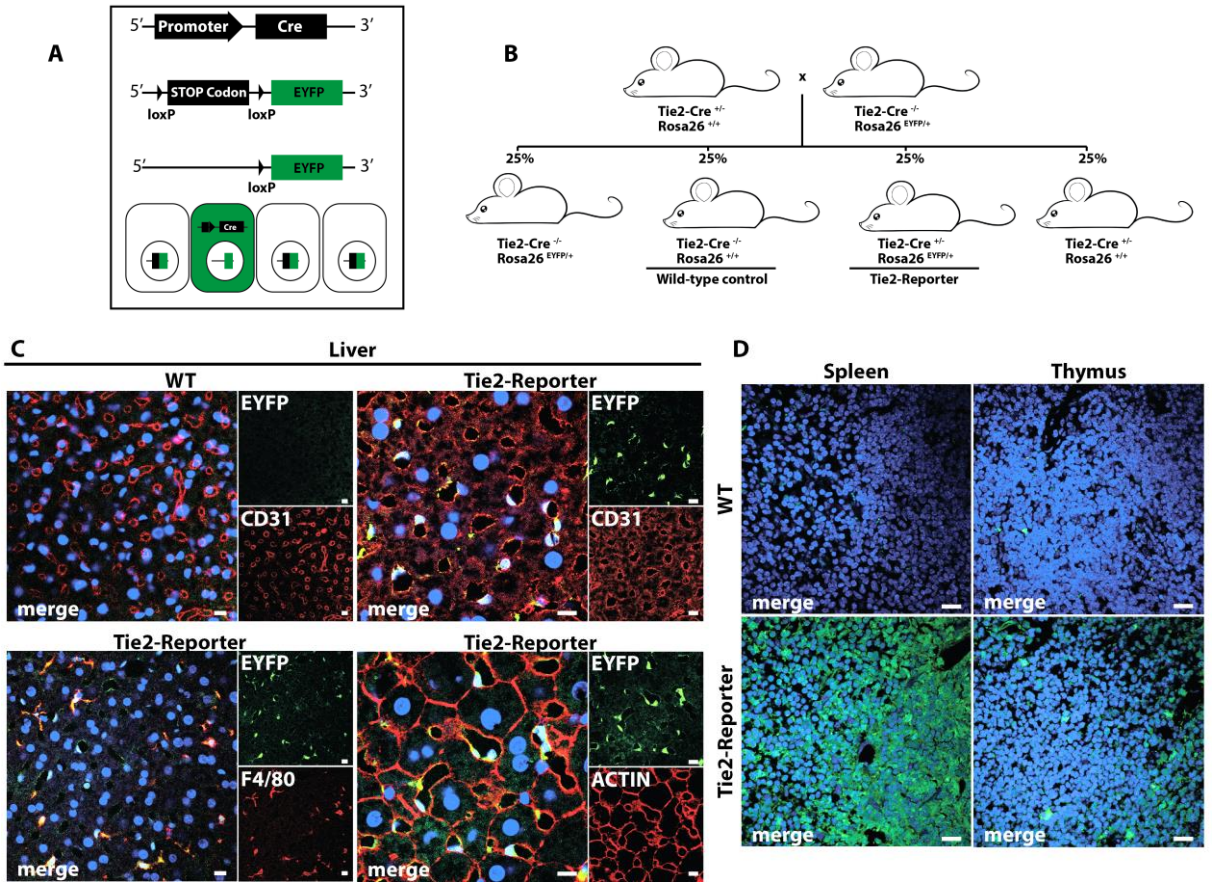

Figure 10. Tie2 promoter is active in LSECs, Kupffer cells, spleen and thymus. (A) Scheme of *Rosa26-EYFP* reporter gene. (B) Breeding strategy between Tie2-Cre and Rosa-EYFP mice. (C) Wild-type and Tie2-Reporter mice liver sections were prepared after mice perfusion with 4% PFA and were stained with antibodies against CD31 and F4/80 and with TR-phalloidin. (D) Wild-type and Tie2-Reporter mice spleen and thymus sections were prepared after mice perfusion with 4% PFA.

2.2.5.4 Tail biopsy and isolation of genomic DNA

In order to determine the genotype of mice and mouse embryos, tail biopsies from mice at three to four weeks of age and embryo tissues were collected for genomic DNA isolation. The tissues were digested in DirectPCR Lysis Reagent Tail (Peqlab) 0.3 mg/ml of proteinase K overnight at 55°C with vigorous shaking. The proteinase K was inactivated for 45 minutes at 85°C and the samples were centrifuged at 13,000 x g for 1 minute. The supernatant was used as template for genotyping (See 2.2.5.5)

2.2.5.5 Genotyping by polymerase chain reaction

The genotype of mice and derived mouse embryonic fibroblasts was analysed by PCR (See 2.2.1.1). The following PCRs (Table 15 and Table 16) were used to differentiate the MFSD1 alleles WT, tm1a, tm1c and tm1d, and the insertion of cre, flp or EYFP-Stop alleles.

	Flp	Cre	Rosa26	MFSD1
Primer Forward	1 µl	1 µl	1 µl	0,5 µl
Primer Reverse	1 µl	1 µl	1 µl	0,5 µl
dNTP mix (2 mM each)	5 µl	2.5 µl	2.5 µl	2.5 µl
10x DreamTaq™ buffer	5 µl	2.5 µl	2.5 µl	2.5 µl
DMSO	2.5 µl	0 µl	0 µl	0.325 µl
Template DNA	2 µl	1 µl	1 µl	2 µl
Betain 5M	0 µl	0 µl	0 µl	6.5 µl
DreamTaq™ Pol. (5U/µl)	0.5 µl	0.25 µl	0.5 µl	0.2 µl
H_2O	33 µl	16.75 µl	16.5 µl	9.975 µl

Table 15. Pipetting scheme for PCR-based genotyping.

Flp/Cre/Rosa26			
Step	Temp. [°C]	Time [s]	
Initiation	95	300	
Cycle	95	30	35 x
	55	30	
	72	60	
Elongation	72	420	
Hold	4	∞	

MFSD1			
Step	Temp. [°C]	Time [s]	
Initiation	95	300	
Cycle	95	15	10 x
	65 (-1°C/cycle)	30	
	72	40	
Cycle	95	15	30x
	55	30	
	72	40	
Elongation	72	300	
Hold	4	∞	

Table 16. PCR conditions applied for genotyping.

The PCR products were separated by agarose gel electrophoresis (See 2.2.1.9). In Table 17 the expected length of the PCR products is detailed.

PCR	Primers	Product length (bp)
Cre	Cre Fw, Cre Rv	250
Flp	Flp Fw Flp Rv	480
MFSD1 WT	CSD-MFSD1-F CSD-MFSD1-ttR	426
MFSD1 tm1a	CSD-neoF CSD-MFSD1-ttR	570
MFSD1 tm1c	CSD-MFSD1-F CSD-MFSD1-ttR	557
MFSD1 tm1d	CSD-MFSD1-F CSD-MFSD1-R	583
Rosa WT	Rosa26-EYFP Fw Rosa26-EYFP Rv	600
Rosa EYFP	Rosa26-EYFP insert Fw Rosa26-EYFP Rv	250

Table 17. Product length of the genotyping-PCR used.

2.2.5.6 Treatment for tritosomes isolation

In order to isolate tritosomes from mouse liver, mice were treated with 17% (v/v) Triton WR-1339 (tyloxapol) in 0.9 % (w/v) NaCl. Four µl of tyloxapol solution per gram of body weight were injected intraperitoneally three days prior to mice preparation.

2.2.5.7 Mouse anaesthesia

In order to anaesthetize the mice, 168 mg/kg body weight ketamine (HFW Heinrich Fromme) and 22.4 mg/kg body weight xylazine (Rompun, Bayer) solved in saline phosphate buffer were injected intraperitoneally. After several minutes, the paws were pressed in order to assess the anaesthetic depth. When the mice did not respond to the paw stimulation, perfusion or blood extraction was performed.

2.2.5.8 Mouse perfusion

Anaesthetized mice were perfused from the left ventricle with 30 ml of phosphate buffer (PB) followed by 30 ml of 4 % (w/v) paraformaldehyde (PFA) in PB at 1.5 ml/min using a Model '11' Plus Syringe Pump (Harvard apparatus). The organs were collected and either post-fixed for 3 h in 4% PFA at 4°C for histological and immunofluorescence analysis or kept in 3 % (v/v) of glutaraldehyde at 4°C for electron microscopy analysis.

2.2.5.9 Blood extraction and serum preparation

Blood was extracted from the caudal vena cava using a 27G needle and collected in a centrifuge tube. The blood was coagulated for 30 minutes at 4°C, centrifuged for 15 minutes at 2,000 x g at 4°C and the supernatant containing the serum was collected and frozen at -20°C.

2.2.5.10 Blood extraction and plasma preparation

Blood was extracted from the caudal vena cava using a 27G needle and a syringe containing heparin (Heparin-Natrium-25000, Ratiopharm), collected in a centrifuge tube and centrifuged for five minutes at 15,700 x g at 4°C. The supernatant containing the plasma was collected and frozen at -20°C.

2.2.5.11 Euthanasia of mice

Experimental animals were sacrificed for organ harvesting by cervical dislocation.

3 Results

3.1 Characterization of MFSD1

3.1.1 Bioinformatic analysis of MFSD1

The gene coding for murine *Mfsd1* is encoded on chromosome three and its genomic locus is composed of sixteen exons. The mRNA contains 2978 nucleotides (nt), and consists of a 51 nt 5'-UTR (untranslated region), a 1395 nt coding sequence and the remaining 3'-UTR (NCBI Reference Sequence: NM_025813.3).

The amino acid (aa) sequence of MFSD1 protein has 464 residues with a predicted molecular mass of approximately 51kDa (UniProtKB, accession number: Q9DC37) (Figure 11A).

A

```
1   MEDEDGEDRALLGGRREADSAVHGAPRALSALCDPSRLAHRLVVLSLMCF
51  LGFGSYFCYDNPAALQTQVKRDMQVNTTKFMLLYAWYSWPNVVLCFLGGF
101 LIDRIFGIRWGTVIFSCFVCIGQVIFALGGIFNAFWLMELGRFVFGIGGE
151 SLAVAQNTYAVSWFKGKELNLVFGLQLSMARIGSTVNMNLMGWLYGKIEA
201 LLGSAGHMTLGVTLMIGCITCIFSLICALALAYLDRRAEKILHKEQGKTG
251 EVIKLRDIKDFSLPLILVFVICVCYYVAVFPFIGLGKVFFMEKFRFSSQS
301 ASAINSIVYIISAPMSPLFGLLVDKTGKNIIWVLYAVAATLVSHMMLAFT
351 FWNPWIAMCLLGFSYSLLACALWPMVAFIVPEHQLGTAYGFMQSIQNLGL
401 AVIAILAGMILDSKGYLLLEVFFIACVSLSLLAVVCLYLVNRAQGGNLNY
451 SAKQRERMKLSHPE
```

B

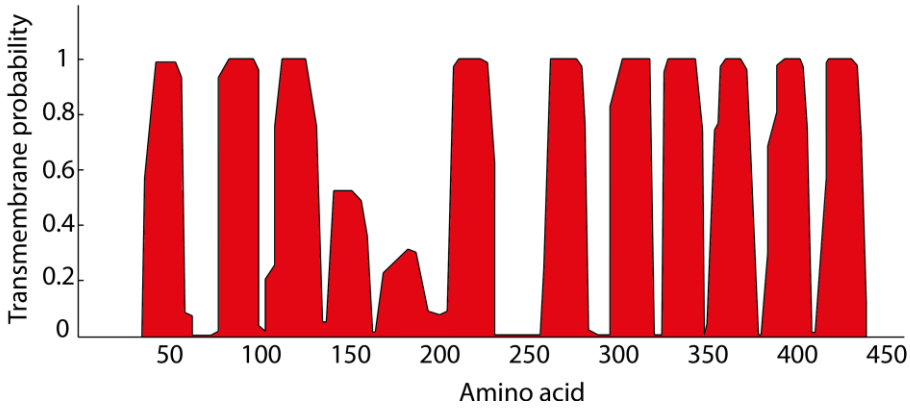

Figure 11. MFSD1 consists of 464 aa and 12 potential TMD. (A) MFSD1 aa sequence with two potential lysosomal sorting motifs represented with italic and gray letters, 10 TMD represented in green, and two aa sequences with a probability between 30 and 50% of being TMD are represented in red. (B) A graphic showing the transmembrane domain prediction of MFSD1 adapted from TMHMM Server, v.2.0-CBS/DTU.

The bioinformatics analysis (TMHMM Server,v.2.0-CBS/DTU) predicts 10 transmembrane domains (TMD), and two additional domains with a probability of approximately 50% and 30% of being TMDs (Figure 11B). Therefore, considering the TMD number and the possible

orientations towards the membrane, there are eight different possible MFSD1-topologies (Figure 12).

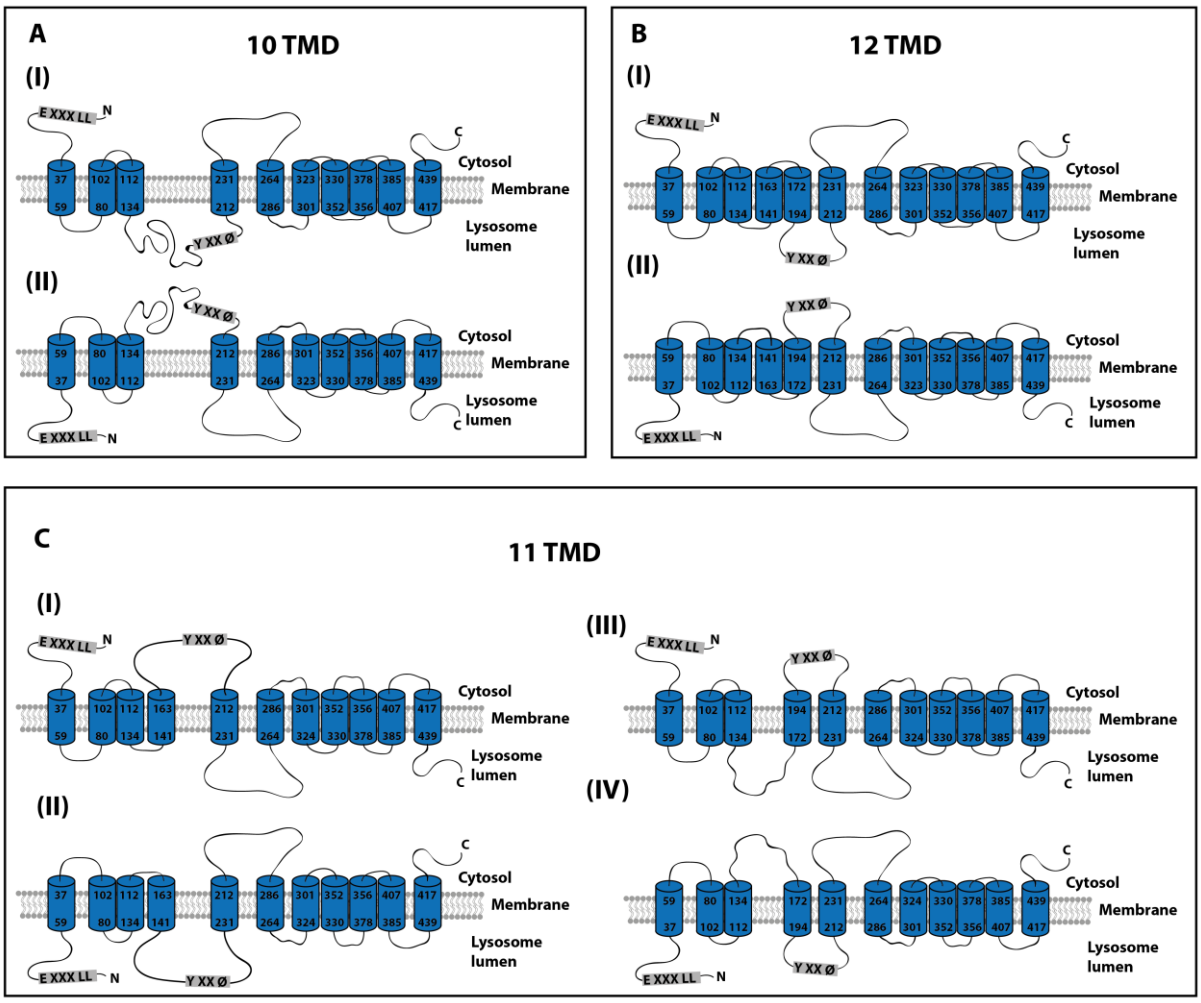

Figure 12. Scheme of the eight possible MFSD1 topologies according to TMD prediction. (A) MFSD1 represented with 10 TMD and its N-terminus and C-terminus facing the cytosol (I) or the lysosomal lumen (II). (B) MFSD1 represented with the typical MFS topology with 12 TMD and its N-terminus and C-terminus facing the cytosol (I) or the lysosomal lumen (II). (C) MFSD1 represented having 11 TMD with aa 141-163 as TMD and aa 172-192 as soluble domain with its N-terminus facing the cytosol (I) or the lysosome lumen (II), or with aa 141-163 as soluble domain and aa 172-192 as TMD and its N-terminus facing the cytosol (III) or the lysosome lumen (IV).

The prediction of the tertiary structure of mMFSD1 using Phyre2 software with GLUT3, which has 12 TMD, as a model displayed a 12 TMD protein (Figure 13).

MFSD1 contains two putative N-glycosylation sites (N76 and N449) with the consensus sequence NxS/T and harbours two potential lysosomal targeting signals (Figure 11A). The N-terminal fragment contains a dileucine-based ([E/D]XXXL[L/I]) lysosomal targeting motif with EDRALL (aa 7-12) and the second third of the protein sequence contains a tyrosine-based

(YXXØ) lysosomal targeting motif with YGKI (aa 195-198). These data suggest that MFSD1 is a multispanning protein that might be localized at the lysosome.

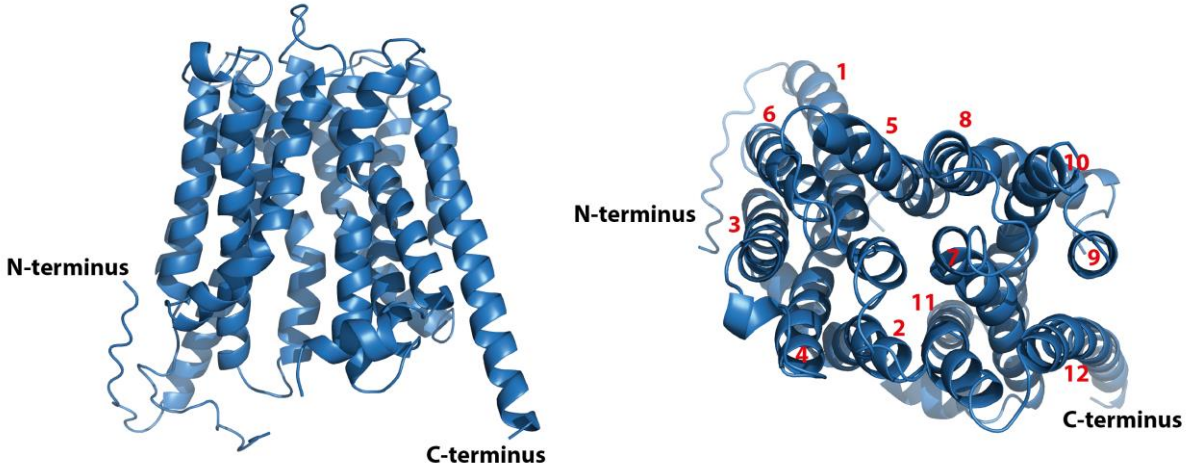

Figure 13. Structure prediction of mMFSD1 using Phyre2 software with GLUT3 as a model. The prediction covers mMFSD1 aa sequence from S20 to S451. Numbers in red represent the transmembrane domains.

3.1.2 C-terminus HA-tagged MFSD1 is localized in HeLa lysosomes

In order to validate the lysosomal localization of MFSD1, mouse *Mfsd1* cDNA fused to a human influenza hemagglutinin (HA) tag coding sequence (protein sequence: YPYDVPDYA) at the C-terminus (MFSD1-HA) or at the N-terminus (HA-MFSD1) was cloned into pcDNA3.1 expression vector. Both constructs were expressed in HeLa cells, and the lysates were analysed by Western blotting using an antibody directed against HA tag, showing in both cases a prominent band of approximately 37 kDa. HA-MFSD1 displayed an additional signal of approximately 25 kDa corresponding to an N-terminal fragment (NTF-HA), while MFSD1-HA revealed two additional C-terminal fragments at approximately 24 kDa (CTFI-HA) and 17 kDa (CTFII-HA) (Figure 14B), all of them fused to HA. It has been previously shown that membrane protein migration in SDS-PAGE gels usually does not correlate with the predicted molecular weight due to hydrophobicity and detergent binding (Rath et al, 2007). Therefore, it is likely that the prominent band of 37 kDa corresponds to full length MFSD1 protein fused to HA (FL-HA). The intensity of the fragments bands is less than 30% of the total intensity of HA signals.

The analysis of HeLa cells transfected with MFSD1-HA by immunofluorescence using an anti-HA antibody and an antibody against LAMP2, an established lysosomal membrane marker,

revealed that MFSD1-HA is mainly localized to lysosomes (Figure 14AIII). No co-localization of MFSD1 was found with the ER marker KDEL, but a partial co-localization was found with the cis-Golgi marker GM130, which could be a consequence of the overexpression.

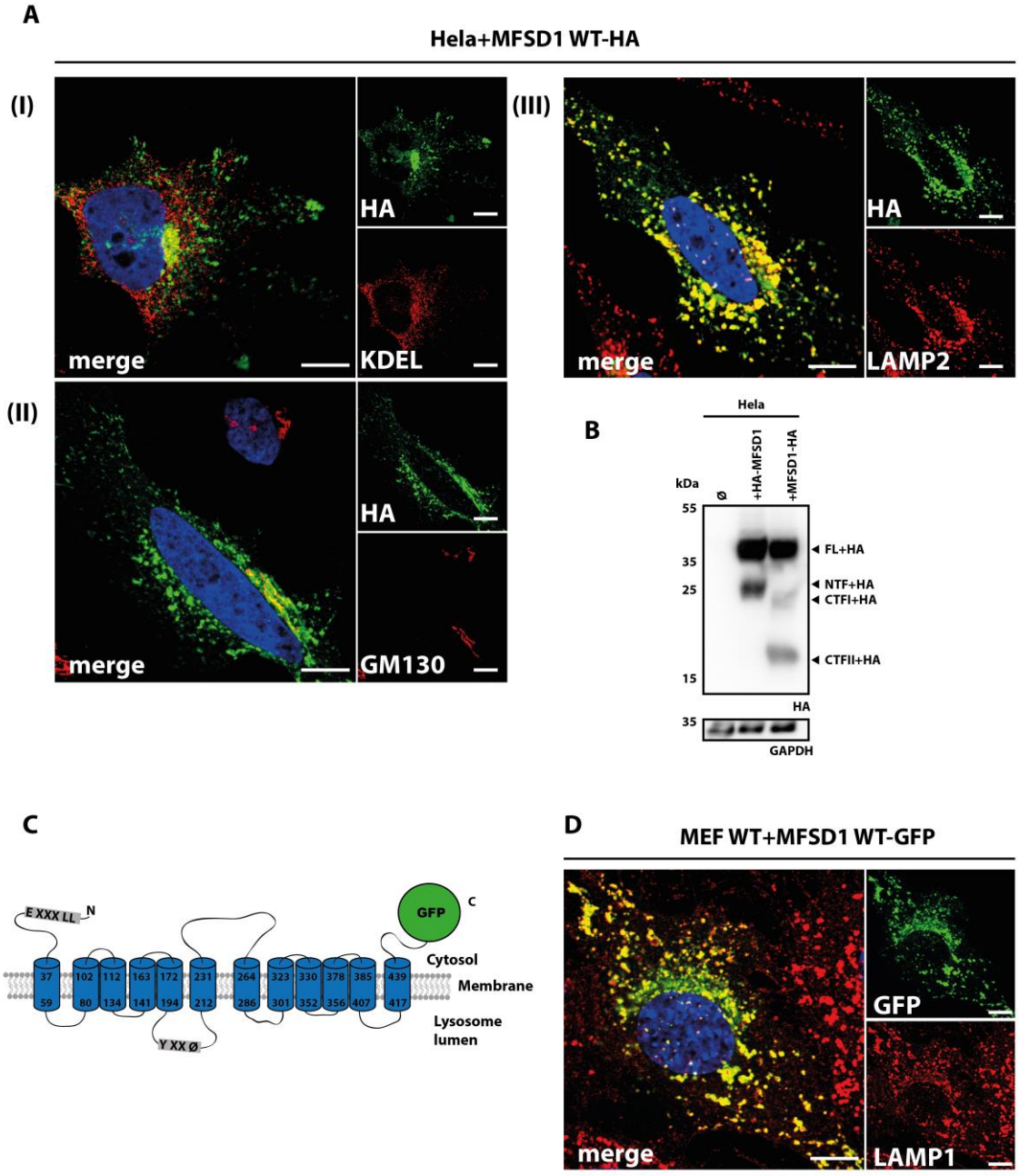

Figure 14. MFSD1 overexpression results in its lysosomal localization in HeLa and MEF cells. (A) HeLa cells were transiently transfected with a plasmid coding for MFSD1-HA, fixed 24 hours post-transfection, permeabilized and stained by indirect immunofluorescence using an anti-HA antibody. KDEL (I), GM130 (II) and LAMP2 (III) antibodies were used to stain ER, Golgi apparatus and lysosomes respectively. (B) Non transfected HeLa cells and HeLa cells transiently transfected with a plasmid coding for MFSD1-HA or HA-MFSD1 were collected 24 hours post-transfection and their lysates were analysed by Western blotting using anti-HA antibody, and anti-GAPDH antibody as loading control. (C) Scheme of MFSD1 with GFP fused at its C-terminus (MFSD1-GFP). (D) MEFs were transiently transfected with a plasmid coding for MFSD1-GFP, fixed 24 hours post-transfection, permeabilized and stained by indirect immunofluorescence using an anti-LAMP1 antibody. Scale bars, 10 µm.

Additionally, the lysosomal localization of MFSD1 was investigated in a different cell line using a different tag. MFSD1 gene was cloned with a Green Fluorescence Protein (GFP) coding sequence tag at the C-terminus using pEGFPN1 plasmid (MFSD1-GFP) (Figure 14C). This construct was expressed in mouse embryonic fibroblasts (MEF) and the cells were immunostained with an antibody raised against the lysosomal protein LAMP1. The images showed the presence of MFSD1-GFP in LAMP1 positive compartments (Figure 14D). These results confirm the lysosomal localization of MFSD1 after overexpression using two different tags and in two different cell lines.

3.1.3 Analysis of MFSD1 topology

Most of the proteins belonging to the MFS superfamily span the membrane twelve times (Reddy et al. 2013). According to the TMD number prediction of MFSD1 and depending on its orientation, the protein could have eight different topologies (Figure 12). In order to differentiate whether the MFSD1 N-terminus and C-terminus face the cytosol or the lysosomal lumen, a selective permeabilization assay was performed overexpressing MFSD1-HA or HA-MFSD1 in HeLa cells. As an example, on Figure 15AII the two possible topologies of a hypothetical MFSD1 spanning the lysosomal membrane 12 times with an HA tag at its N-terminus are depicted. The H4B4 monoclonal antibody recognizes an epitope within the lysosomal lumen of human LAMP2 (Figure 15AI). Digitonin is a non-ionic detergent that, at a determined concentration, permeabilizes the plasma membrane selectively without affecting the inner organelles membranes of the cells (Koltzscher et al. 2003), while saponin, being also a non-ionic detergent, permeabilizes all the cell membranes. After permeabilization of the cells with digitonin, the antibodies recognizing an epitope located at the lysosomal lumen, like H4B4, can't bind its epitope. On the other hand, the use of saponin, allows that the antibodies that recognize an epitope in the lysosomal lumen, like H4B4, can reach their epitopes (Figure 15BII).

In order to discriminate whether the N-terminus and C-terminus of MFSD1 are faced towards the cytosol or towards the lysosomal lumen, HeLa cells were transfected with HA-MFSD1 or MFSD1-HA, permeabilized with either saponin or digitionin, and analysed by co-immunofluorescence using anti-HA and H4B4 antibodies. The analysis of the samples revealed HA signal after HA-MFSD1 transfection, independent of the permeabilization method. The

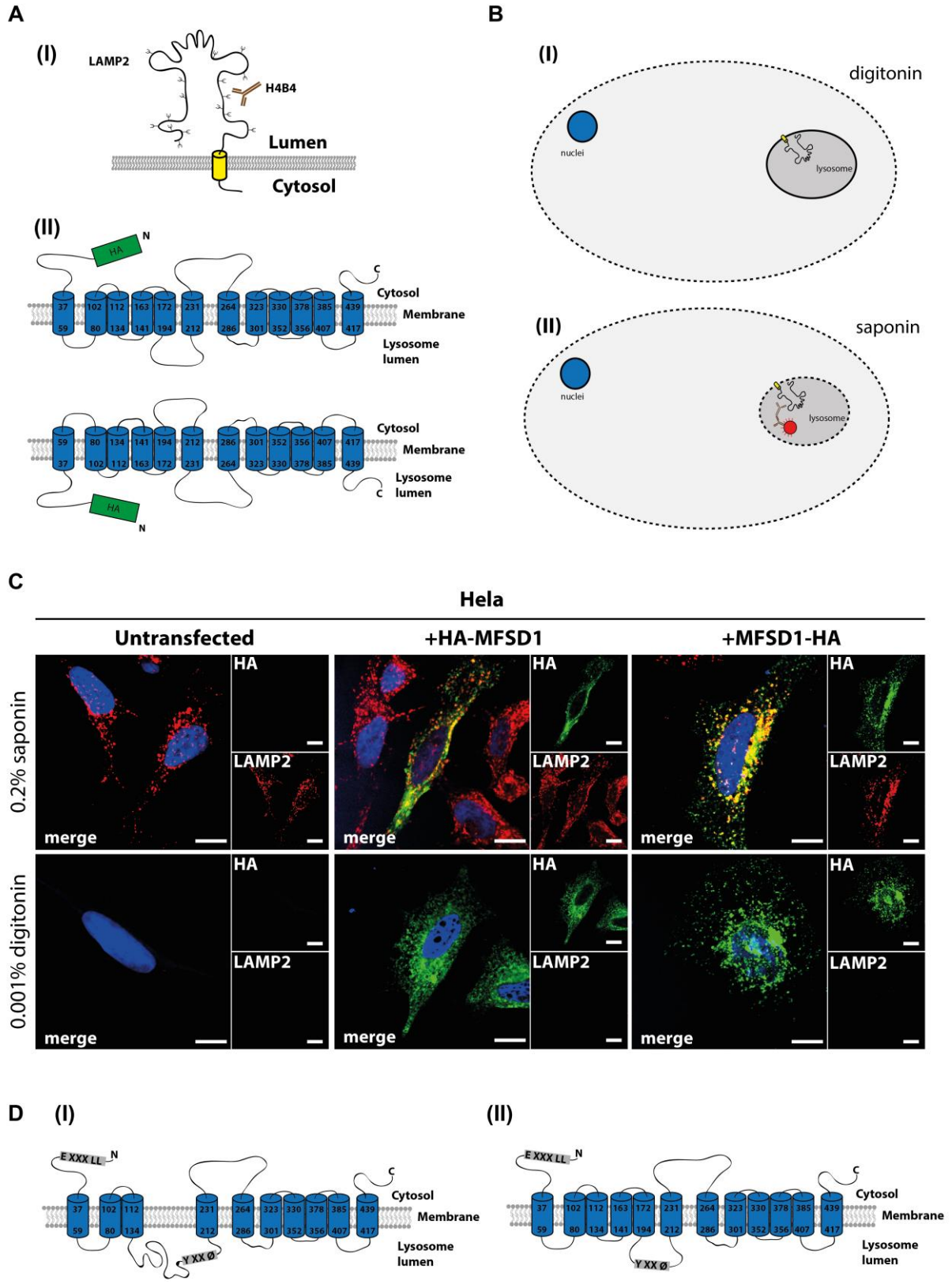

Figure 15. C and N-terminus of MFSD1 face the cytosol. (A) Scheme of LAMP2 protein and the epitope recognized by H4B4 antibody (I). The two possible topologies of a hypothetical MFSD1 with 12 TMD fused to an HA tag at the N-terminus (II). (B) Scheme of the cell membrane and lysosome permeabilized either with digitonin (I) or saponin (II). (C) HeLa cells were transfected with a plasmid coding for HA-MFSD1 or MFSD1-HA, fixed 24 hours post-transfection, permeabilized with saponin or digitonin and stained for HA and LAMP2 with H4B4 antibody. (D) MFSD1 possible topologies left. Scale bars, 10 µm.

same result was observed when HA was fused at the MFSD1 C-terminus. H4B4 staining displayed fluorescence signal only when the cells were permabilized with saponin (Figure 15C). These results indicate that both N and C-terminus of MFSD1 are faced towards the cytosol, and that MFSD1 should contain either ten or twelve TMD. Therefore, out of the eight initial potential topologies, there are just two possible topologies of MFSD1 left (Figure 15D). As most MFS superfamily members have 12 TMD, MFSD1 is represented in the following schemes as a 12 TMD protein.

3.1.4 The dileucine based motif in N-terminus of MFSD1 is required for a lysosomal localization

As mentioned, bioinformatic analysis predicted 2 putative lysosomal targeting motifs in the MFSD1 aa sequence. The two possible topologies of MFSD1 described in Figure 15D suggest that the dileucine based signal is facing the cytosol, being accessible to the adaptor proteins that mediate sorting of membrane proteins. In contrast, the tyrosine based motif is facing the lumen in both suggested topologies, being unlikely for it to be used for the transport of MFSD1 to the lysosome. To analyse the use of the dileucine based sequence, EDRALL, for the lysosomal transport of MFSD1, the two leucines at positions 11 and 12 from MFSD1-GFP were exchanged by alanines using site directed mutagenesis, obtaining a plasmid coding for MFSD1 LL/AA-GFP (Figure 16A). After expression of the construct in MEF cells, co-immunofluorescence analysis with the lysosomal marker LAMP1 did not reveal a lysosomal localization of MFSD1 LL/AA-GFP, but instead cell plasma membrane localization was observed (Figure 16B). This result demonstrates that the dileucine based motif is necessary for the transport of MFSD1 to the lysosome.

In order to obtain quantitative data about MFSD1 LL/AA cell surface expression, plasmids coding for MFSD1 and MFSD1 LL/AA with an HA tag between the TMD1 and TMD2 in both cases (MFSD1 TMD1-HA-TMD2 and MFSD1 LL/AA TMD1-HA-TMD2) were designed (Figure 17AI,II). In both cases, if the protein is localized in the lysosome the HA tag faces the lysosomal lumen, and if the protein is localized in the cell surface the HA tag faces the extracellular space. The expression of the fusion proteins was tested in HeLa cells transiently transfected with plasmids coding for MFSD1 TMD1-HA-TMD2 or MFSD1 LL/AA TMD1-HA-TMD2. Western blotting analysis of both cell lysates using an anti-HA antibody showed a band at an approximate molecular weight of 37 kDa, similar to the band observed in HeLa cells

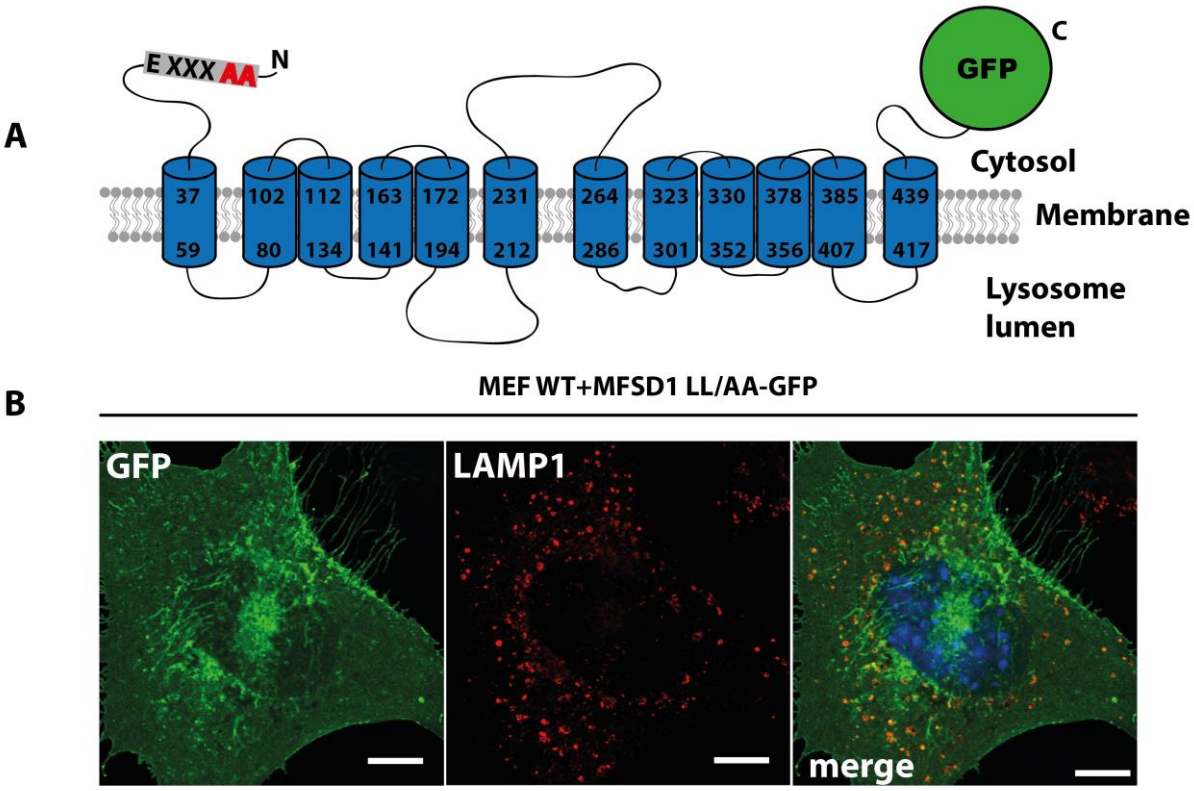

Figure 16. MFSD1 has a dileucine based motif at its N-terminus necessary for the transport to lysosomes. (A) Scheme of MFSD1 with EDRALL motif mutated into EDRAAA fused to GFP (MFSD1 LL/AA-GFP) with two alanine in position 11 and 12 instead of leucine. (B) MEF cells were transfected with a plasmid coding for MFSD1 LL/AA-GFP, fixed 24 hours post-transfection, permeabilized and stained with an anti-LAMP1 antibody. Scale bars, 10 µm.

transfected with a plasmid coding for MFSD1 with an HA tag fused to the C-terminus (Figure 17BI). Additionally, quantification of the expression of the two constructs in HeLa cells revealed that MFSD1 TMD1-HA-TMD2 and MFSD1 LL/AA TMD1-HA-TMD2 were expressed to comparable amounts (Figure 17BII). Immunofluorescence analysis of HeLa cells transfected with plasmids coding for MFSD1 TMD1-HA-TMD2 or MFSD1 LL/AA TMD1-HA-TMD2 using anti-HA and anti-LAMP2 antibodies revealed a lysosomal and cell surface localization, respectively. Untransfected HeLa cells and HeLa cells transfected with plasmids coding for MFSD1 TMD1-HA-TMD2 or MFSD1 LL/AA TMD1-HA-TMD2 were analysed by flow cytometry using an HA antibody coupled to PE. MFSD1 was localized at the cell surface membrane in approximately 20% and 3% of the cells transfected with MFSD1 LL/AA TMD1-HA-TMD2 MFSD1 or MFSD1 TMD1-HA-TMD2, respectively.

These results show that the dileucine motif of MFSD1 is crucial for MFSD1 lysosomal localization, and that the mutation of the two leucine to alanine leads to the cell surface mislocalization of MFSD1.

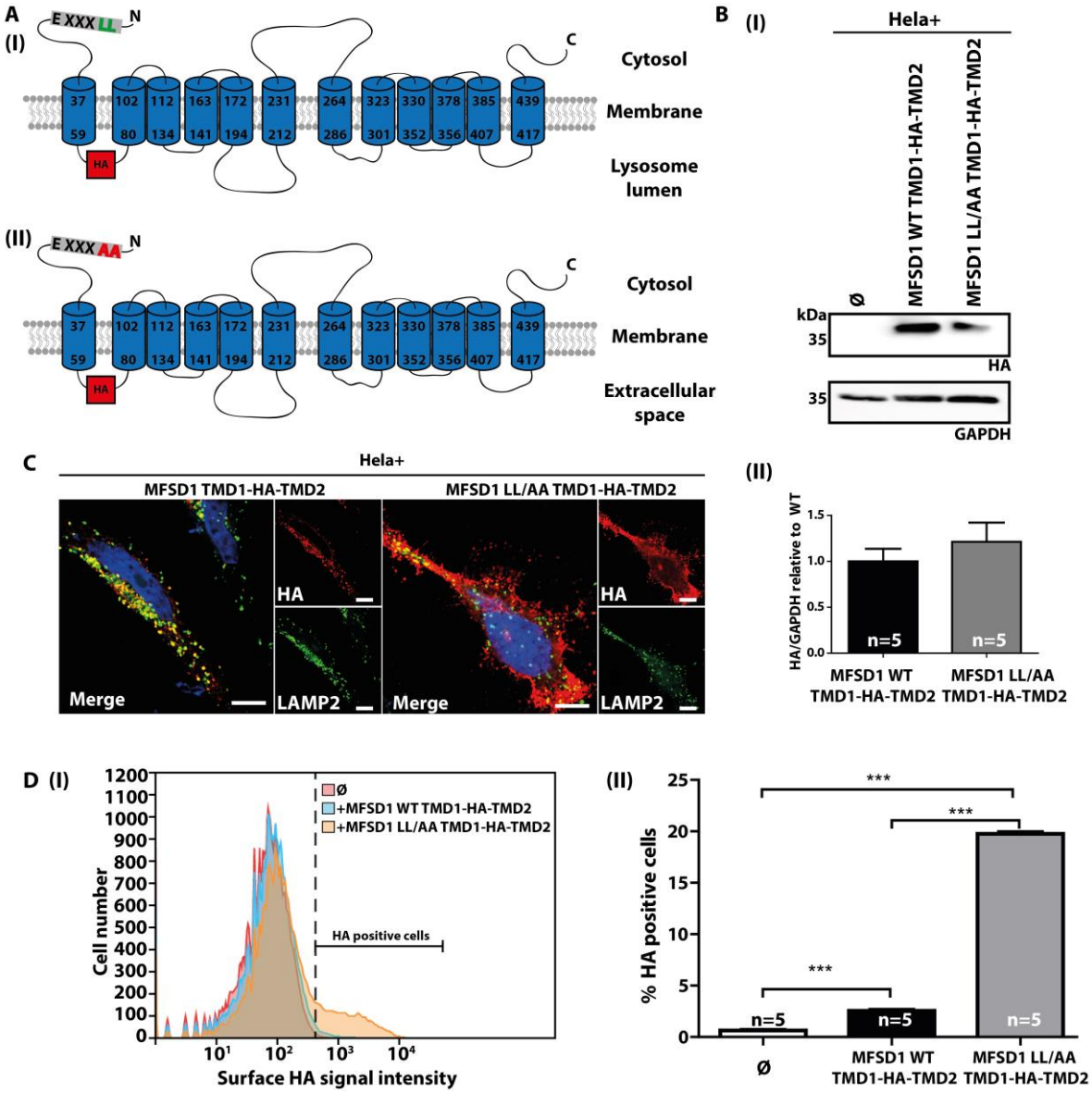

Figure 17. Mutation of the dileucine motif of MFSD1 leads to a plasma membrane localization. (A) Scheme of MFSD1 (I) and MFSD1 with EDRALL motif mutated into EDRAAA (II) with an HA tag fused between TMD1 and TMD2. (B) HeLa cells were transiently transfected with plasmids coding for MFSD1 TMD1-HA-TMD2 or MFSD1 LL/AA TMD1-HA-TMD2, collected 24 hours after transfection and the lysates were analysed by Western Blotting using anti-HA and anti-GAPDH antibodies (I) and densiometric quantification of the signals was performed (II). (C) HeLa cells were transfected with a plasmid coding for MFSD1 TMD1-HA-TMD2 or MFSD1 LL/AA TMD1-HA-TMD2, fixed 24 hours post-transfection, permeabilized and stained for LAMP2 and HA. (D) HeLa cells were transfected with a plasmid coding for MFSD1 TMD1-HA-TMD2 or MFSD1 LL/AA TMD1-HA-TMD2, collected 24 hours after transfection and analysed without permeabilization by flow cytometry with an HA antibody coupled to phycoerythrin (PE)(I). The percentage of HA positive cells was quantified (II). Scale bars, 10 µm.

3.1.5 Endogenous MFSD1 is localized at the lysosome of MEF cells

In order to study the expression and localization of MFSD1 in different cell types and organs at an endogenous level, a polyclonal antibody was raised in rabbits. Shortly, rabbits were

immunized with an eighteen aa long peptide derived from the N-terminus of MFSD1 (aa 2-19) (indicated in Figure 18A). The serum was collected at day 120 after immunization and affinity purified (anti-MFSD1 antibody).

In order to validate the specificity of the newly generated anti-MFSD1 antibody, MEF cells deficient for MFSD1 expression were prepared. MFSD1 deficient MEF (MEF MFSD1$^{tm1a/tm1a}$) were isolated from 14 day old embryos after breeding of mice heterozygotes for *MFSD1* (See 2.2.2.2).

The anti-MFSD1 antibody was used to analyse the protein expression of HA-MFSD1 and MFSD1-HA after transfection in HeLa cells and of endogenous MFSD1 in MEFs (MEF) by immunoblotting and immunofluorescence. The analysis of MEFs MFSD1$^{tm1a/tm1a}$ allowed the specificity determination of anti-MFSD1 antibody.

Immunoblotting analysis with the anti-MFSD1 antibody revealed an unspecific signal in MEF lysates at around 39 kDa, but it also displayed a signal in MFSD1$^{wt/wt}$ MEF lysate at a slightly lower molecular weight as compared to the HA-tagged version under overexpression conditions that is not present in MFSD1$^{tm1a/tm1a}$ MEF lysate (FL) (Figure 18B). Apart from the full length protein, no additional signals were detected in MFSD1$^{wt/wt}$ MEF lysates using anti-MFSD1 antibody.

The immunofluorescence study of HeLa cells transfected with MFSD1-HA after co-staining with anti-HA and anti-MFSD1 antibodies showed a complete co-localization of both antibodies (Figure 18C). Immunofluorescence analysis of MFSD1$^{wt/wt}$ MEF and MFSD1$^{tm1a/tm1a}$ MEF after incubation with the anti-MFSD1 antibody showed a signal in MFSD1$^{wt/wt}$ MEF that was missing in MFSD1$^{tm1a/tm1a}$ MEF. Co-staining with either anti-LAMP1 or anti-GM130 determined a co-localization of MFSD1 with the lysosomal marker LAMP1, but no co-localization with the cis-Golgi marker GM130 (Figure 18D). These results demonstrate that MFSD1 antibody detects specifically MFSD1 and confirms its lysosomal localization at the endogenous level in MEF cells.

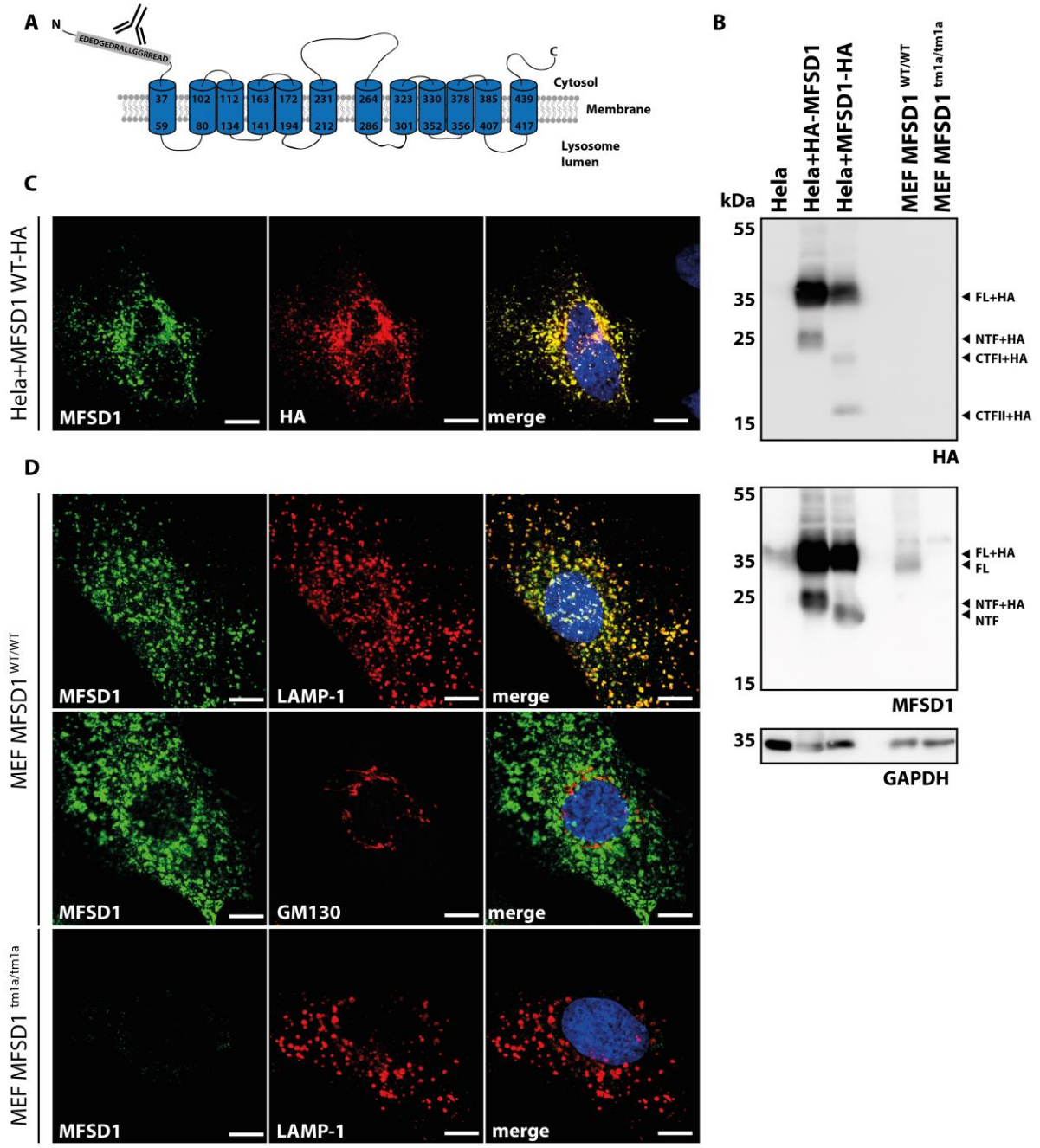

Figure 18. Endogenous MFSD1 is localized in lysosomes of MEF$^{wt/wt}$ cells. (A) Scheme of MFSD1 protein showing the peptide sequence used to immunize the rabbits for the antibody generation. (B) HeLa cells were transiently transfected with plasmids coding for MFSD1-HA or HA-MFSD1, collected 24 hours after transfection and the lysates were analysed by Western Blotting in parallel with MEF MFSD1$^{wt/wt}$ and MEF MFSD1$^{tm1a/tm1a}$ lysates using anti-HA, anti-MFSD1 and anti-GAPDH antibodies. (C) HeLa cells were transfected with a plasmid coding for MFSD1-HA, fixed 24 hours post-transfection, permeabilized and stained for MFSD1 and HA. (D) MEF MFSD1$^{wt/wt}$ and MEF MFSD1$^{tm1a/tm1a}$ were fixed, permeabilized and stained for MFSD1 and LAMP1. Additionally, MFSD1$^{wt/wt}$ were stained for MFSD1 and GM130. FL, full length; FL+HA, full length fused to HA; NTF, N-terminal fragment; NTF+HA, N-terminal fragment fused to HA; CTFI+HA, C-terminal fragment I fused to HA; CTFII+HA, C-terminal fragment II fused to HA. Scale bars, 10 µm.

3.2 Study of MFSD1 expression in mouse tissues

After a basic biochemical characterization of MFSD1 *in cellulo*, our aim was to analyse MFSD1 tissue distribution in the major murine organs and investigate its endogenous subcellular distribution in tissues.

3.2.1 MFSD1 is expressed ubiquitously in mouse tissues

A MFSD1-deficient mouse strain was generated in order to decipher the function of MFSD1 in lysosomes. Briefly, a 'knockout-first' allele (tm1a) containing an IRES:lacZ trapping cassette was inserted into the second *MFSD1* gene intron of an ES cell that was injected into host blastocysts and gave rise to chimeric mice. The generation of chimeric mice was done by Irm Hermans-Borgmeyer (ZMNH, UKE Hamburg) . After breeding of the chimeric mice, PCR analysis of genomic tail DNA confirmed the heterozygous presence of the *MFSD1* tm1a allele in the litters (See 2.2.5.5). As a result of heterozygote breedings, 263 mice were born with an outcome of 57 MFSD1$^{wt/wt}$, 142 MFSD1$^{wt/tm1a}$ and 64 MFSD1$^{tm1a/tm1a}$ mice. These numbers correlate with the expected percentages according to Mendelian inheritance, demonstrating a lack of elevated embryonic lethality of homozygous MFSD1$^{tm1a/tm1a}$ mice. After birth, MFSD1$^{tm1a/tm1a}$ mice were indistinguishable from MFSD1$^{wt/wt}$, and no obvious behavioural differences were observed.

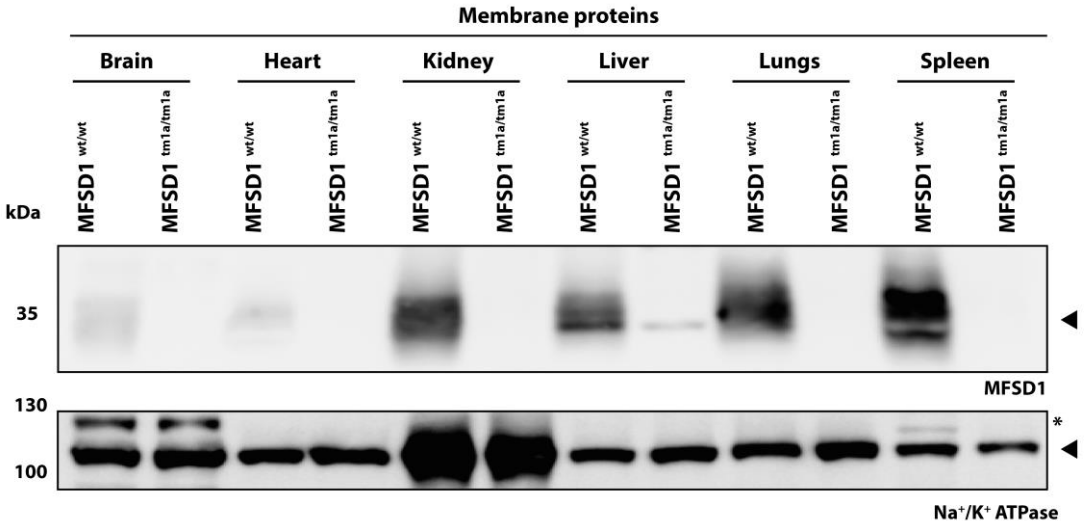

Figure 19. MFSD1 is ubiquitously expressed in mice. (A) The indicated tissues from MFSD1$^{wt/wt}$ and MFSD1$^{tm1a/tm1a}$ mice were collected and the membrane proteins were separated from the soluble proteins using ultracentrifugation. The membrane proteins were analysed by Western blotting with an anti-MFSD1 antibody and an anti-Na^+/K^+-ATPase as a loading control for membrane fractions.

In order to validate the deficiency of MFSD1 in MFSD1$^{tm1a/tm1a}$ mice, the main tissues of MFSD1$^{wt/wt}$ and MFSD1$^{tm1a/tm1a}$ mice were collected, the membrane proteins were separated from soluble proteins using ultracentrifugation, and the membrane proteins were further analysed by Western blotting using the anti-MFSD1 antibody. Full length MFSD1 was detected in all tissue membrane fractions analysed of MFSD1$^{wt/wt}$ mice at an approximate size of 35 kDa, and it was completely absent in all the MFSD1$^{tm1a/tm1a}$ tissue membrane fractions. Highest protein levels were found in kidney, liver, lung and spleen, whereas low MFSD1 levels were detected in brain and heart (Figure 19A).

In order to investigate whether the tm1a cassette contained the IRES:lacZ trapping cassette, X-gal stainings from MFSD1$^{wt/wt}$ and MFSD1$^{wt/tm1a}$ tissue sections were performed. No differences on the staining of liver, kidney and spleen were found between MFSD1$^{wt/wt}$ and MFSD1$^{wt/tm1a}$ mice due to high endogenous β-galactosidase activity in MFSD1$^{wt/wt}$ mice (data not shown). The results of X-gal staining of brain sections revealed a turquoise signal in MFSD1$^{wt/tm1a}$ samples limited to the hippocampus area that was absent in MFSD1$^{wt/wt}$ brain (Figure 20).

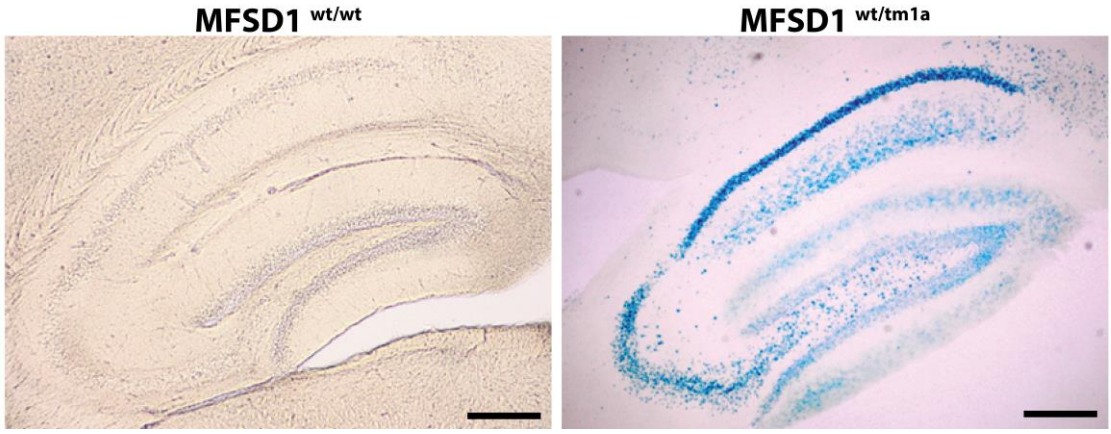

Figure 20.MFSD1 is expressed in the hippocampus in brain. MFSD1$^{wt/tm1a}$ and MFSD1$^{wt/wt}$ brain sections were prepared after tissue perfusion with 4% PFA and sections were with X-gal. Scale bars, 100 µm.

Altogether, these results confirmed the complete loss of MFSD1 expression, the presence of the IRES:lacZ trapping cassette in MFSD1$^{tm1a/tm1a}$ mice and revealed the ubiquitous expression of MFSD1.

3.2.2 MFSD1 subcellular distribution

With the aim to investigate the subcellular distribution of MFSD1 in tissues, Percoll density fractionation of liver and kidney from MFSD1$^{wt/wt}$ mice was performed using

ultracentrifugation. The activity of the lysosomal acidic hydrolase β-hexosaminidase in the fractions was evaluated and the fractions were analysed by Western blotting with the anti-MFSD1 antibody. The liver results demonstrated a basal β-hexosaminidase activity (>6%) through fractions F3-F13, with a β-hexosaminidase activity peak in fractions F12 and F13 (Figure 21AI). Similar to β-hexosaminidase activity, MFSD1 had a basal expression pattern through F3-F12 fraction, with the highest expression at fraction F12 (Figure 21BI). The kidney

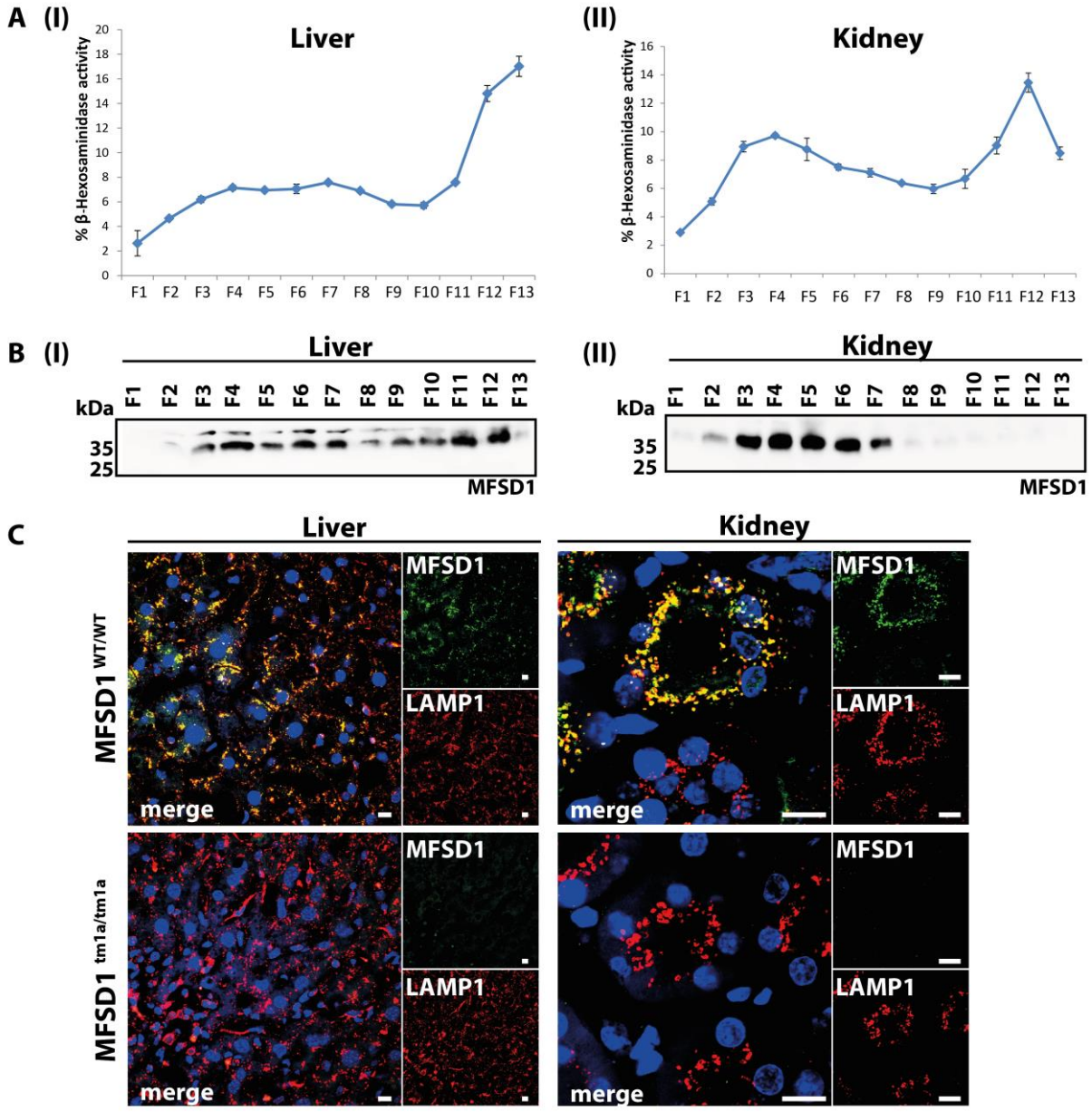

Figure 21. MFSD1 highest expression in liver and kidney is found in fractions with a high β-hexosaminidase activity. Liver and kidney fractions were prepared by Percoll density centrifugation. (A) The enzymatic activity of the lysosomal hydrolase β-hexosaminidase in the Percoll density fraction of liver (I) and kidney (II) was analysed using *p*-nitrophenyl-β-D-glucosaminide as a substrate at a pH of 4.6. (B) The Percoll density fractions (F) of liver (I) and kidney (II) were analysed by Western blotting using an anti-MFSD1 antibody. (C) MFSD1$^{tm1a/tm1a}$ and MFSD1$^{wt/wt}$ liver and kidney sections were prepared after tissue perfusion with 4% PFA, sections were stained with anti-MFSD1 and anti-LAMP1 antibodies. Scale bars, 10 µm.

fractions also had a basal β-hexosaminidase activity (>6%) through fractions F3-F13, and two activity peaks were present in fractions F4 and F12 (Figure 21AII). Interestingly, Western blotting analysis of the kidney fractions showed the detection of MFSD1 through fractions F2-F7, with the highest expression in fraction F4, and the absence of detection in fraction F12, where β-hexosaminidase activity is highest in kidney (Figure 21BII). Tissue sections of both liver and kidney from MFSD1$^{wt/wt}$ and MFSD1$^{tm1a/tm1a}$ mice were evaluated by immunofluorescence using the anti-MFSD1 antibody and an anti-LAMP1 antibody. The results revealed a specific signal of MFSD1 in MFSD1$^{wt/wt}$ (absent in MFSD1$^{tm1a/tm1a}$) that co-localized with the lysosomal marker LAMP1, confirming the presence of endogenous MFSD1 in lysosomes of both liver (in hepatocytes, macrophages and sinusoidal endothelial cells) and kidney (in cells from the proximal convoluted tubules) (Figure 21C).

3.3 MFSD1$^{tm1a/tm1a}$ mice phenotype study

Mutations in genes coding for lysosomal transporters often lead to accumulation of the substrates in the lysosomes. For instance, mice deficient for cystinosin, a lysosomal cystine transporter, accumulate cystine in the lysosomes of liver, kidney and heart, among other tissues (Cherqui et al. 2002). Also Salla disease patients with mutations in *SLC17A5* gene, that is coding for the lysosomal sialic acid transporter sialin, exhibit accumulation of sialic acid in the lysosomes of fibroblasts (Renlund et al. 1986). After confirming the complete absence of MFSD1 in MFSD1$^{tm1a/tm1a}$ mice, our aim was to use the MFSD1-deficient mice as a tool to learn more about the function of MFSD1 and its possible transport substrate/s.

3.3.1 MFSD1 deficiency leads to enlarged lysosomes in kidneys

One might hypothesize that if MFSD1 is a lysosomal exporter, the deficiency of MFSD1 would lead to the accumulation of its substrate/s in the lysosome, and as a consequence the size and number of lysosomes would increase.

In order to test this hypothesis, the organs with highest expression of MFSD1 (kidney, liver, lung and spleen) were collected and analysed by Western blotting using several antibodies directed against lysosomal proteins. The results revealed no changes in the protein levels of the lysosomal proteins LAMP1 and LIMP2 in liver, lung or spleen of MFSD1$^{tm1a/tm1a}$ mice compared to the same tissues of MFSD1$^{wt/wt}$ mice (data not shown). However, in kidney the

levels of LAMP1 were increased twofold in MFSD1$^{tm1a/tm1a}$ mice compared to MFSD1$^{wt/wt}$ mice, while no change in the levels of LIMP2 was observed (Figure 22A).

Since overall LAMP1 levels were increased in kidney, a more detailed analysis was performed.

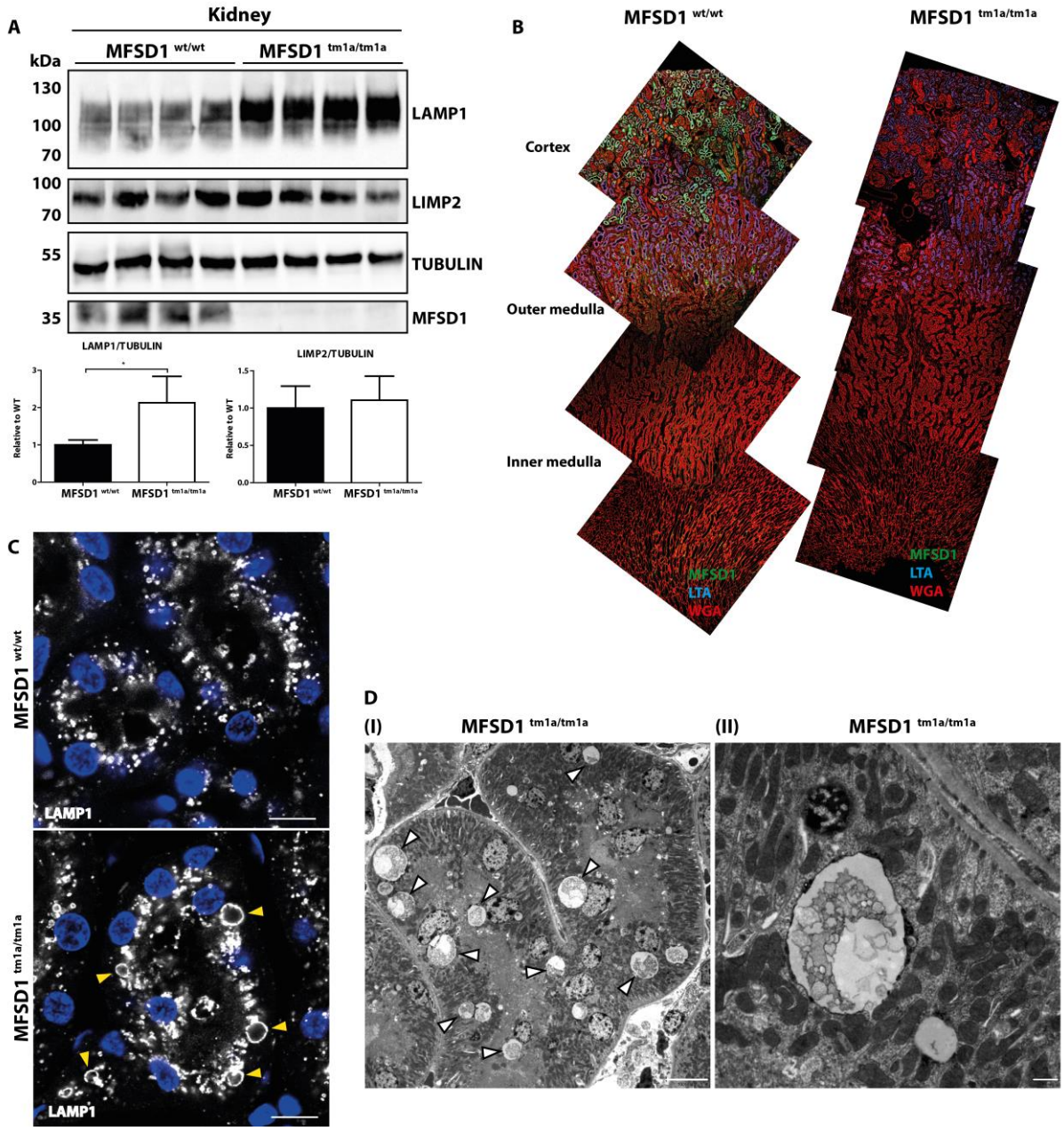

Figure 22. The deficiency of MFSD1 leads to the accumulation of material in vesicles of the proximal tubules of kidney. (A) Kidneys of MFSD1$^{tm1a/tm1a}$ and MFSD1$^{wt/wt}$ were collected, lysed and analysed by Western blotting using antibodies against LAMP1, LIMP2, TUBULIN and MFSD1. (B) MFSD1$^{tm1a/tm1a}$ and MFSD1$^{wt/wt}$ kidney sections were prepared after mice perfusion with 4% PFA and were stained with anti-MFSD1, anti-LTA and anti-WGA antibodies. (C) MFSD1$^{tm1a/tm1a}$ and MFSD1$^{wt/wt}$ kidney sections were prepared after mice perfusion with 4% PFA and were stained with anti-LAMP1 antibody. Scale bars, 10 µm. (D) MFSD1$^{tm1a/tm1a}$ and MFSD1$^{wt/wt}$ kidneys were collected and fixed with 3% glutaraldehyde and sections for electron microscopy analysis were prepared. White arrows show enlarged vesicles with accumulated material. Scale bar (I), 10 µm; Scale bar (II), 1 µm. Analysis of MFSD1 expression through major structures of kidney was performed by C. Meyer-Schwesinger. Electron microscopy was performed by R. Lüllmann-Rauch and D. Niemeier.

The expression of MFSD1 through cortex, outer medulla and inner medulla of the kidney was analysed in collaboration with C. Meyer-Schwesinger (Institute for Cellular and Integrative Physiology, UKE Hamburg) by immunofluorescence using the anti-MFSD1 antibody. Lotus tetragonolobus lectin (LTA) and Wheat germ agglutinin lectin (WGA) were used to identify the proximal convoluted tubule and the distal convoluted tubule, respectively, as they bind monosaccharides of the mentioned structures. MFSD1 was only detected in the cortex of MFSD1$^{wt/wt}$ kidneys, while no MFSD1 signal was detected in MFSD1$^{tm1a/tm1a}$ kidneys (Figure 22B). The highest MFSD1 expression was found in the proximal convoluted tubules and the juxtaglomerular apparatus, while low MFSD1 levels were detected in the distal convolutes tubules and no specific staining for MFSD1 was detected in the glomerulus (data not shown). Immunofluorescence analysis were performed in order to investigate the size of LAMP1 positive lysosomes in MFSD1$^{tm1a/tm1a}$ kidneys. Kidney sections were stained with the anti-LAMP1 antibody, revealing enlarged lysosomes (up to 3-4 µm) in the proximal convoluted tubules of MFSD1$^{tm1a/tm1a}$ kidneys that could hardly be found in MFSD1$^{wt/wt}$ kidney (Figure 22C, yellow arrows). Potential substrate/s transported by MFSD1 might be accumulated in the enlarged LAMP1 positive vesicles found in the proximal convoluted tubulues of MFSD1$^{tm1a/tm1a}$ kidneys. Therefore, the kidneys of MFSD1$^{tm1a/tm1a}$ mice and MFSD1$^{wt/wt}$ mice were analysed by electron microscopy (EM) together with R. Lüllmann Rauch and D. Niemeier. Despite variability between the samples, the EM images revealed the presence of polymorphic material in vesicles of the proximal convoluted tubules of MFSD1$^{tm1a/tm1a}$ mice (Figure 22D).
Also liver sections were analysed by electron microscopy, but no consistent vesicle enlargement was observed in MFSD1$^{tm1a/tm1a}$ samples compared to MFSD1$^{wt/wt}$ samples (data not shown).

3.3.2 MFSD1$^{tm1a/tm1a}$ mice have an abnormal liver morphology

The study of young MFSD1$^{tm1a/tm1a}$ mice five weeks after birth showed no macroscopically detectable phenotype on the major organs with the exception of the spleen, whose size was increased twofold compared to age matched MFSD1$^{wt/wt}$ mice (Figure 23BII). At three months of age the absence of MFSD1 resulted, in addition to splenomegaly (Figure 23AII), in an abnormal appearance of the liver with large nodules on the surface (Figure 23AI). The death rate of MFSD1$^{tm1a/tm1a}$ mice at older age (>1 year) was comparable to the death rate of MFSD1$^{wt/wt}$ mice, the macroscopic liver appearance did not worsen and splenomegaly was still

present (Figure 23BII). The enzymatic activity in serum of hepatic proteins was measured in collaboration with D. Wiegmann (Clinical chemistry, UKE Hamburg), revealing a significant increase in alanine transaminase (ALT), aspartate transaminase (AST) and glutamate dehydrogenase (GLDH) activity in MFSD1$^{tm1a/tm1a}$ serum at 3 months of age when compared to MFSD1$^{wt/wt}$ serum, while no difference on lactate dehydrogenase (LDH), albumin and

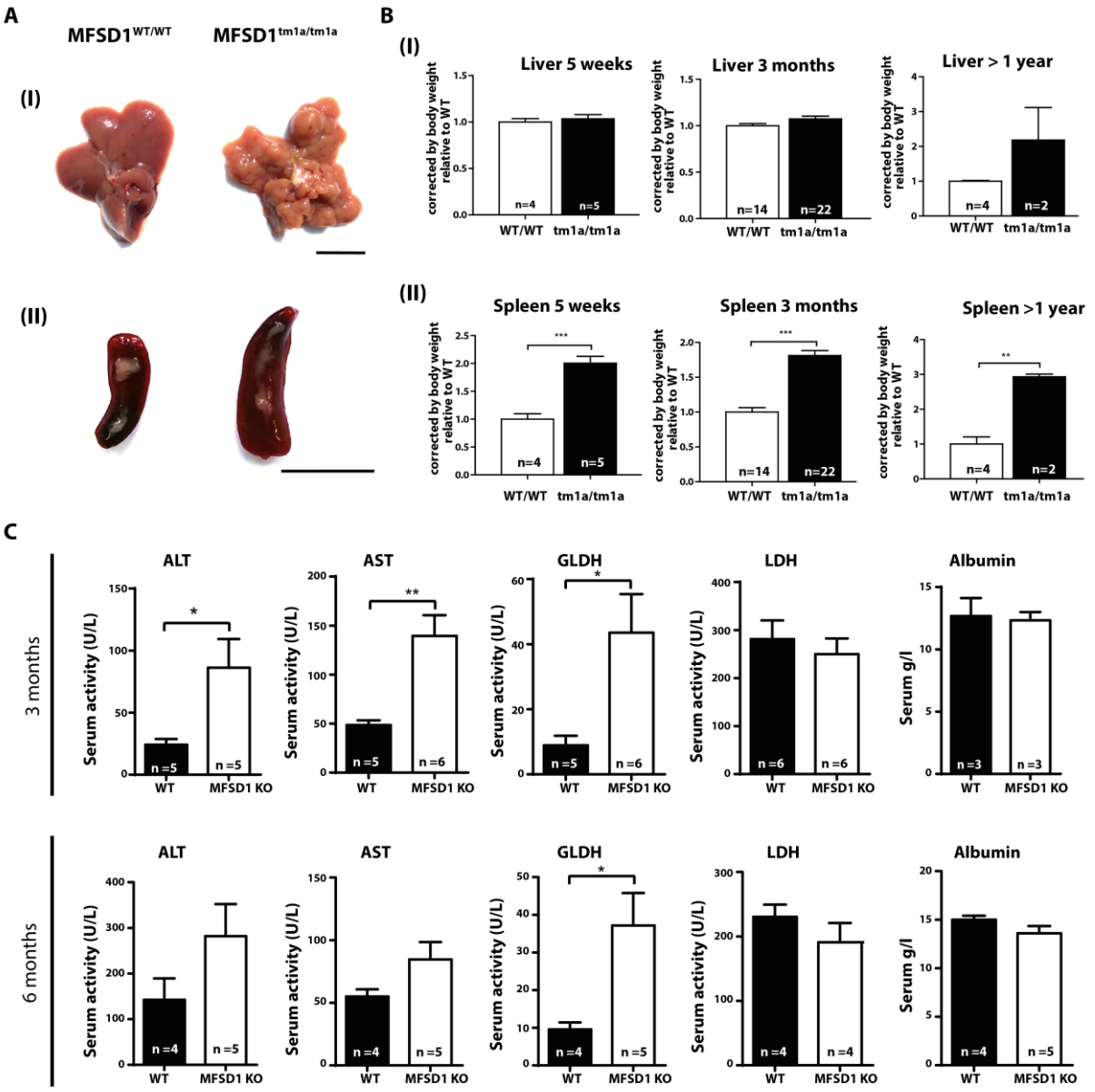

Figure 23. MFSD1$^{tm1a/tm1a}$ mice have splenomegaly and suffer of a liver insult. (A) Representative pictures of MFSD1$^{wt/wt}$ and MFSD1$^{tm1a/tm1a}$ liver (I) and spleen (II) of 3 months old mice. (B) MFSD1$^{wt/wt}$ and MFSD1$^{tm1a/tm1a}$ mice were sacrificed 5 weeks, 3 months or more than one year after birth and their livers (I) and spleens (II) were weighted. The tissue weight values were normalized to the body weight. (C) Serum from 3 and 6 month old mice was collected, the enzymatic activity for ALT, AST, GLDH and LDH was assayed and the albumin levels were measured. The enzymatic activities were analysed by D. Wiegmann (Clinical chemistry, UKE Hamburg). Values are given as mean±SEM. Asterisks indicate statistically significant differences between the two groups (*p<0.05; **p<0.01; ***p<0.005). Scale bars, 1cm.

bilirubin levels was found between the two genotypes. At six months of age, ALT, AST and GLDH enzymatic activity levels in MFSD1$^{tm1a/tm1a}$ serum were still higher than the levels found in MFSD1$^{wt/wt}$ serum, but the differences in ALT and AST activity levels between the two genotypes did not reach significance (Figure 23C). These results show that the lack of MFSD1 at three months of age leads to hepatocyte damage, that the liver phenotype does not worsen afterwards and suggest that MFSD1$^{tm1a/tm1a}$ mice livers might slightly recover from the liver insult.

3.3.2.1 Sinusoids obstruction and hepatocyte atrophy in MFSD1$^{tm1a/tm1a}$ mice liver

Since the previous results suggested that the liver insult was acute at three months of age, a more detailed analysis of mice liver sections at this age was performed. All the data that will be presented has been obtained from the analysis of three months old mice, if not stated otherwise.

Hematoxylin and eosin (H&E) staining of the liver revealed an heterogeneous liver histology in MFSD1$^{tm1a/tm1a}$ mice, where some areas were comparable to MFSD1$^{wt/wt}$ liver while other areas were affected by sinusoidal obstruction and hepatocyte atrophy (Figure 24, empty arrowheads).

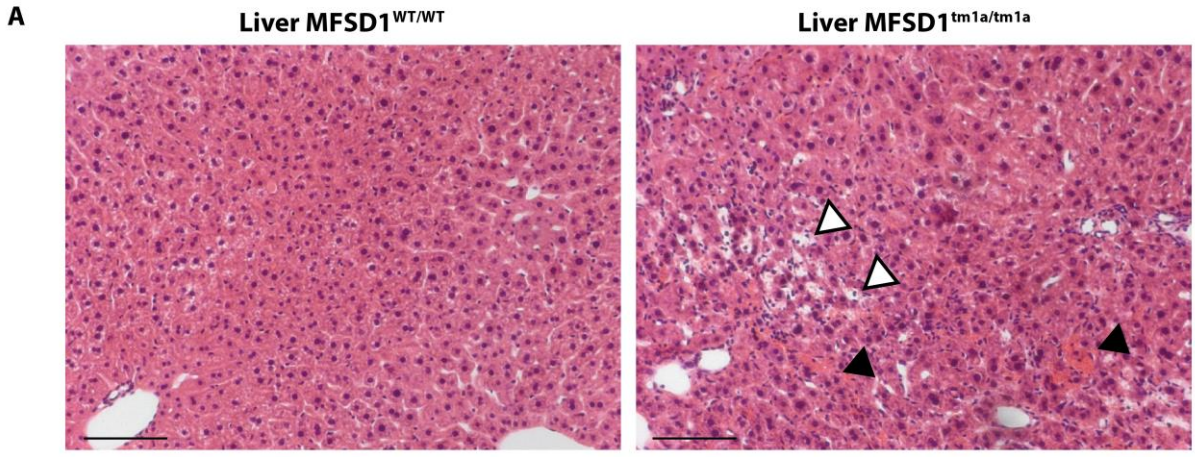

Figure 24. MFSD1$^{tm1a/tm1a}$ livers have sinusoidal obstruction and erythrocyte extravasation. MFSD1$^{tm1a/tm1a}$ and MFSD1$^{wt/wt}$ liver sections of three months old mice were prepared after mice perfusion with 4% PFA and were stained with haematoxylin and eosin. Red arrow show sinusoid obstruction and hepatocyte atrophy. Black arrows show erythrocytes extravasation. Scale bars, 100 µm. H&E stainings were performed by R. Lüllmann-Rauch and D. Niemeier.

Additionally, extravasation of erythrocytes through the space of Disse was observed (Figure 24, black arrowheads) and infiltration of mononuclear cells in the same affected areas of MFSD1$^{tm1a/tm1a}$ liver tissue was detected (Figure 24). Toluidine blue staining of liver sections

confirmed the obstruction of sinusoids, the atrophy of hepatocytes (Figure 25, red arrows) and the presence of erythrocytes in the space of Disse (Figure 25, black arrow) as observed by H&E staining in MFSD1$^{tm1a/tm1a}$ mice.

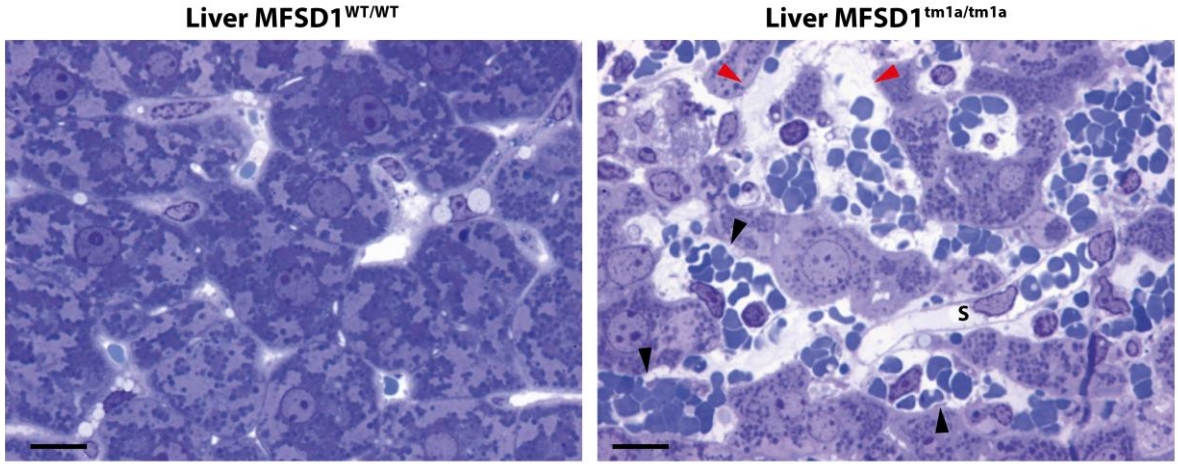

Figure 25. MFSD1$^{tm1a/tm1a}$ livers have hepatocyte atrophy and erythrocyte extravasation. MFSD1$^{tm1a/tm1a}$ and MFSD1$^{wt/wt}$ liver sections were prepared after mice perfusion with 4% PFA and were stained with toluidine blue. Black arrows show erythrocytes extravasation. Red arrows show hepatocyte atrophy. Scale bars, 10 µm. Toluidine blue stainings were performed by R. Lüllmann-Rauch and D. Niemeier.

3.3.2.2 Infiltration of blood cells in liver tissue of MFSD1$^{tm1a/tm1a}$ mice

The analysis of H&E stainings of liver sections suggested an infiltration of mononuclear cells in MFSD1$^{tm1a/tm1a}$ tissues. Therefore, immunofluorescence analysis of the samples using antibodies against different mononuclear cell markers was performed. Antibodies against CD68, myeloperoxidase (MPO), B220 and CD3e were used to identify macrophages, neutrophils, B lymphocytes and T lymphocytes, respectively. The analysis of the stainings revealed an increase in the number of macrophages, neutrophils, B lymphocytes and T lymphocytes in MFSD1$^{tm1a/tm1a}$ liver when compared to MFSD1$^{wt/wt}$ liver (Figure 26A). Also an increase of autofluorescent material and augmented levels of the proliferation marker ki67 were found in the affected areas of MFSD1$^{tm1a/tm1a}$ livers when compared to MFSD1$^{wt/wt}$ livers (Figure 26A). Macrophages, lymphocytes and neutrophils are known to be inflammatory cells (Susca et al. 2001), so the mRNA levels of proinflammatory cytokines in liver were investigated by real-time quantitative PCR (qRT-PCR). The results of the analysis revealed an increment of CXCL1 and MCP1 mRNA levels in MFSD1$^{tm1a/tm1a}$ compared to MFSD1$^{wt/wt}$ samples (Figure 26B). These results suggest an inflammatory state and an increase in cell proliferation in the affected areas of the MFSD1$^{tm1a/tm1a}$ liver.

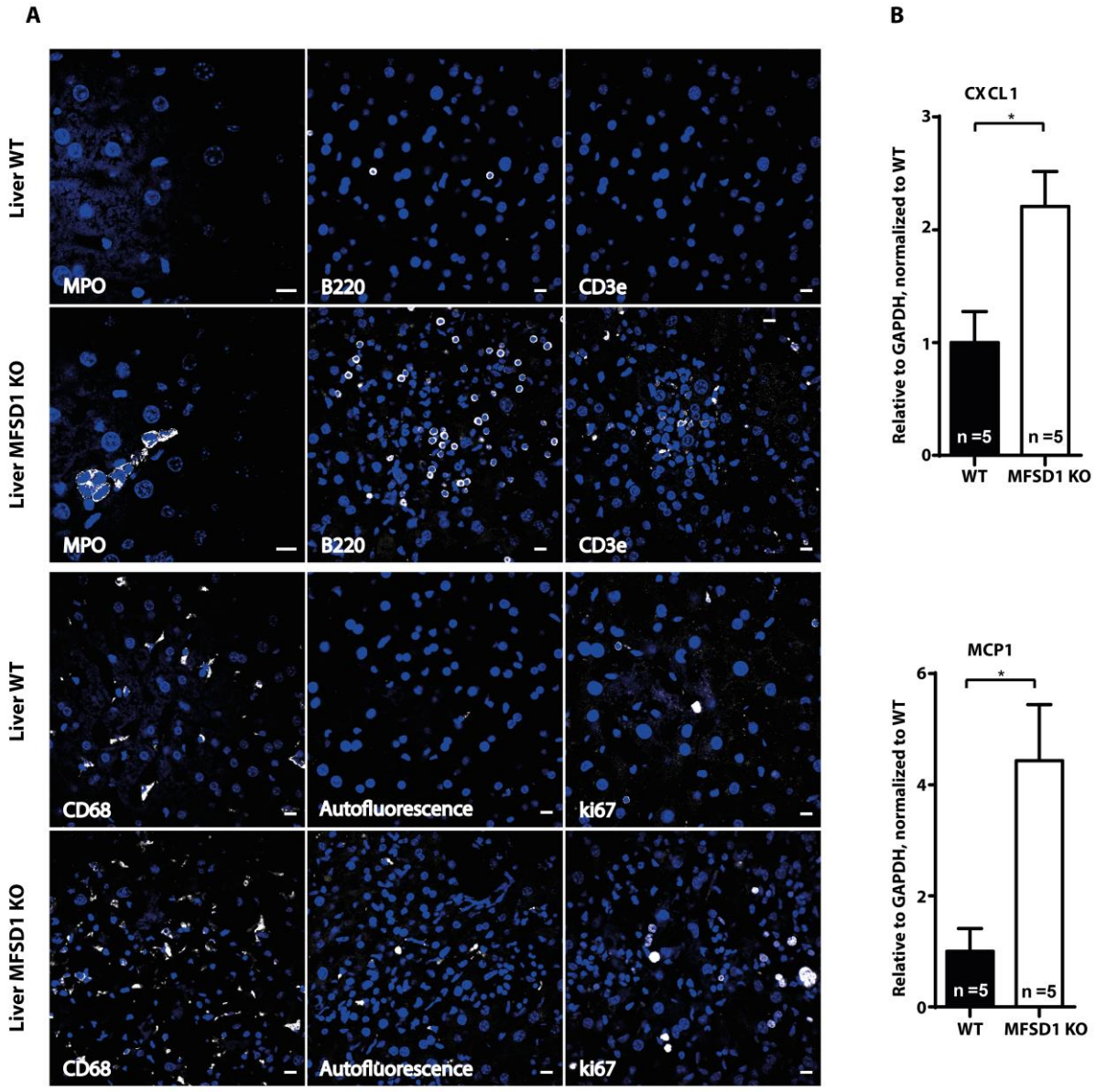

Figure 26. Infiltration of inflammatory cells in MFSD1$^{tm1a/tm1a}$ livers. (A) MFSD1$^{tm1a/tm1a}$ and MFSD1$^{wt/wt}$ liver sections were prepared after mice perfusion with 4% PFA and were stained with antibodies against myeloperoxidase (MPO), B220, CD3e, CD68 and ki67. (B) MFSD1$^{tm1a/tm1a}$ and MFSD1$^{wt/wt}$ livers were collected, the total RNA was extracted and it was used to generate cDNA, which afterwards was used to analyse the transcription of CXCL1 and MCP1 genes by qRT-PCR. Scale bars, 10 µm. Values are given as mean±SEM. Asterisks indicate statistically significant differences between the two groups (*p<0.05).

3.3.2.3 Liver fibrosis and angiogenesis in MFSD1$^{tm1a/tm1a}$ liver

Fibrosis is an ubiquitous response of the liver to acute or chronic injury (Bataller and Brenner 2005), and damaged liver sinusoidal endothelial cells (LSECs) are reported to play a key role contributing to hepatic complications like fibrosis (Poisson et al. 2017).

Since our results demonstrate that MFSD1$^{tm1a/tm1a}$ mice suffer a liver insult, and that the sinusoids are affected, the liver fibrotic state was investigated using different methods. The

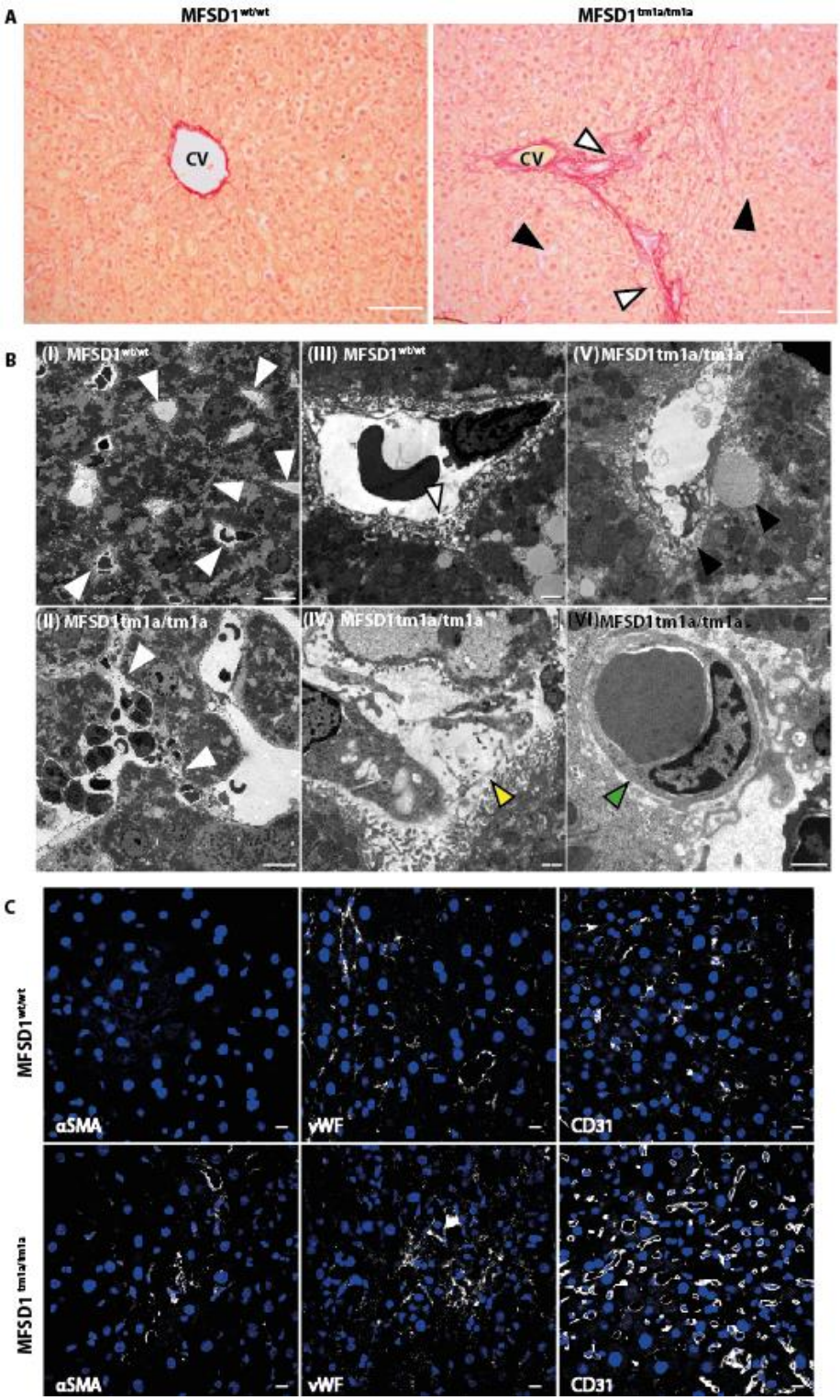

Figure 27. MFSD1$^{tm1a/tm1a}$ liver suffer fibrosis and loss of LSECs. (A) MFSD1$^{tm1a/tm1a}$ and MFSD1$^{wt/wt}$ liver sections were prepared after mice perfusion with 4% PFA and were stained with Sirius red. Black arrows show sinusoids obstruction; empty arrows show collagen deposition. Scale bars, 100 µm. (B) MFSD1$^{tm1a/tm1a}$ and MFSD1$^{wt/wt}$ livers were collected and fixed with 3% glutaraldehyde and sections for electron microscopy analysis were prepared. White arrows show sinusoids; empty arrow shows LSECs fenestrae; yellow arrow shows the absence of LSECs endothelium; green arrow shows capillary. Scale bars (I) and (II), 10 µm; scale bars (III)-(VI), 1 µm. (C) MFSD1$^{tm1a/tm1a}$ and MFSD1$^{wt/wt}$ liver sections were prepared after mice perfusion with 4% PFA and were immunostained using anti-αSMA, anti-vWF and anti-CD31 antibodies. Scale bars, 10 µm. Electron microscopy was performed by R. Lüllmann-Rauch and D. Niemeier.

examination of liver sections stained with Sirius red provided evidence of collagen deposition in MFSD1$^{tm1a/tm1a}$ livers (Figure 27A, arrowheads) and confirmed the obstruction of sinusoids in the affected areas (Figure 27A, black arrows). The analysis of the liver by electron microscopy supported the presence of collagen fibres in MFSD1$^{tm1a/tm1a}$ samples (Figure 27BV, black arrows) observed by Sirius red staining. It also revealed the sinusoidal structures in MFSD1$^{wt/wt}$ (Figure 27BI, white arrow), while those structures were lost in MFSD1$^{tm1a/tm1a}$ liver (Figure 27BII, white arrows). Higher magnification images allowed to identify the sinusoidal fenestrae of MFSD1$^{wt/wt}$ LSECs (Figure 27BIII, empty arrow), while in MFSD1$^{tm1a/tm1a}$ livers LSECs were not detected in many areas (Figure 27BIV, yellow arrow). Finally, the electron microscopy analysis of the samples revealed the pathological presence of capillaries in MFSD1$^{tm1a/tm1a}$ samples, rarely seen in MFSD1$^{wt/wt}$ (Figure 27B, green arrow).

Immunofluorescence analysis of liver sections provided evidence of a high α-smooth muscle actin (SMA) expression, that has been shown to be characteristic of activated hepatic stellate cells in liver (Boers et al. 2006; Friedman 2008), in MFSD1$^{tm1a/tm1a}$ livers compared to MFSD1$^{wt/wt}$ (Figure 27C), confirming the presence of activated hepatic stellate cells. Von Willebrand Factor (vWF), an adhesive glycoprotein expressed and stored in Weibel-Palade bodies of LSECs (Turner and Moake 2015), is observed as vesicle like structures by immunofluorescence in healthy liver (Knittel et al. 1995). The analysis of liver sections stained with an anti-vWF antibody, revealed an accumulation of vWF in the injured areas of the MFSD1$^{tm1a/tm1a}$ liver sections (Figure 27C). Furthermore, immunostaining with an anti-CD31 antibody demonstrated an increased staining in the MFSD1$^{tm1a/tm1a}$ liver in comparison to MFSD1$^{wt/wt}$ liver, suggesting the generation of new capillaries in MFSD1$^{tm1a/tm1a}$ livers (Figure 27C).

Gene expression analyses using qRT-PCR revealed a significant increase of the transcript levels of proteins involved in matrix remodelling like TIMP1, MMP2 and MMP9 in MFSD1$^{tm1a/tm1a}$ liver in comparison to MFSD1$^{wt/wt}$ liver (Figure 28A). qRT-PCR analysis also confirmed the transcript levels increase of *Vwf* and *Pecam1* genes, and revealed the expression increase of *Cd34* gene, involved in new capillarization process in liver (Fina et al. 1990; Wisse et al. 1985), in MFSD1$^{tm1a/tm1a}$ liver compared to MFSD1$^{wt/wt}$ liver (Figure 28A). The transcripts levels of the gene coding for Factor VIII, *F8*, a specific marker of LSECs (Fahs et al. 2014; Shahani et al. 2014),

were decreased in MFSD1$^{tm1a/tm1a}$ liver in comparison to MFSD1$^{wt/wt}$ samples, therefore supporting the loss of LSECs in MFSD1$^{tm1a/tm1a}$ mice (Figure 28A).

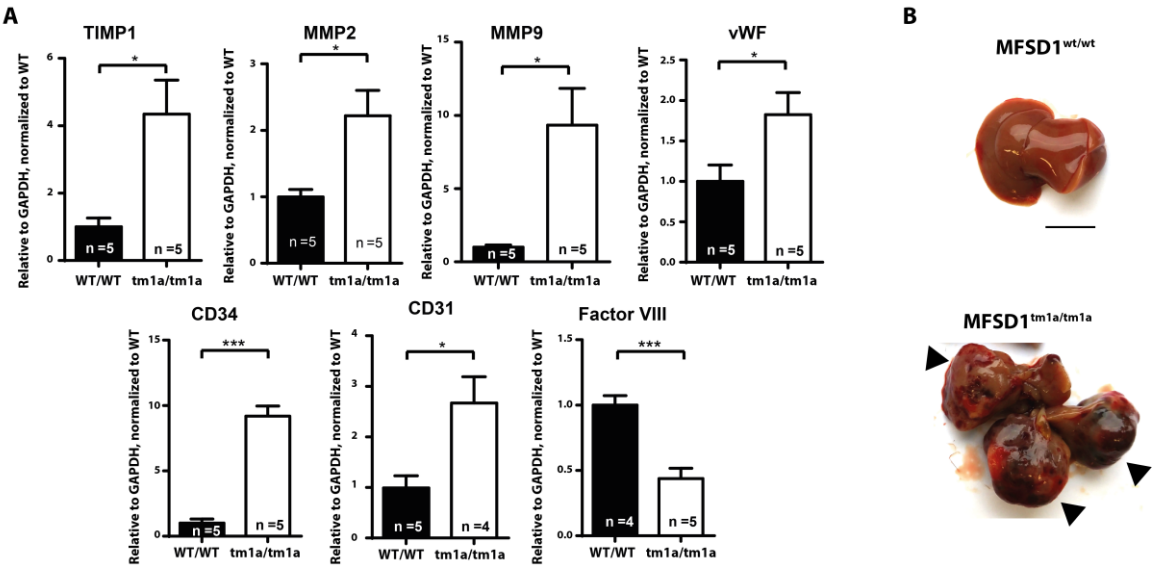

Figure 28. MFSD1$^{tm1a/tm1a}$ liver have increased matrix remodelling and capillarization genes expression and decreased expression of LSEC genes. (A) Livers of MFSD1$^{tm1a/tm1a}$ and MFSD1$^{wt/wt}$ mice were collected, the total RNA was extracted and reverse transcribed to cDNA, which afterwards was used to analyse the transcript levels of the mentioned genes. (B) Representative liver pictures of mice at one and a half years of age. Arrows show tumors. Scale bar, 1 cm. Asterisks indicate statistically significant differences between the two groups (*p<0.05; **p<0.01; ***p<0.005).

A common end-stage of chronic liver disease is cancer (Hernandez-Gea and Friedman 2011; Pinzani, Rosselli, and Zuckermann 2011). The study of mice at an old age (>18 months) revealed a statistically significant increase in the frequency of liver tumours in MFSD1$^{tm1a/tm1a}$ mice (6 mice out of 9 had liver tumours) when compared to MFSD1$^{wt/wt}$ mice (3 mice out of 17 had liver tumours) applying Fisher´s exact test. A representative picture of the tumours found in MFSD1 $^{tm1a/tm1a}$ liver is shown in Figure 28B.

Altogether, these results suggest the damage of LSECs, a process of new capillarization and fibrogenesis in MFSD1$^{tm1a/tm1a}$ liver, that would develop into cancer in a late stage. It has been shown that all forms of liver cirrhosis are characterized by a defenestrated sinusoidal endothelium (Bhunchet and Fujieda 1993; Martinez-Hernandez and Martinez 1991; Mori et al. 1993). Therefore, the lack of MFSD1 in LSECs leads to LSECs cell damage and defenestration of the sinusoids, triggering the process of neo-capillarization and fibrogenesis.

3.3.2.4 Tie2 promoter-driven MFSD1 conditional knockout mice have an abnormal liver morphology

In order to test the hypothesis that the lack of MFSD1 in LSECs is the trigger of the liver phenotype, we aimed to generate a conditional LSEC-specific MFSD1 knockout mouse strain.

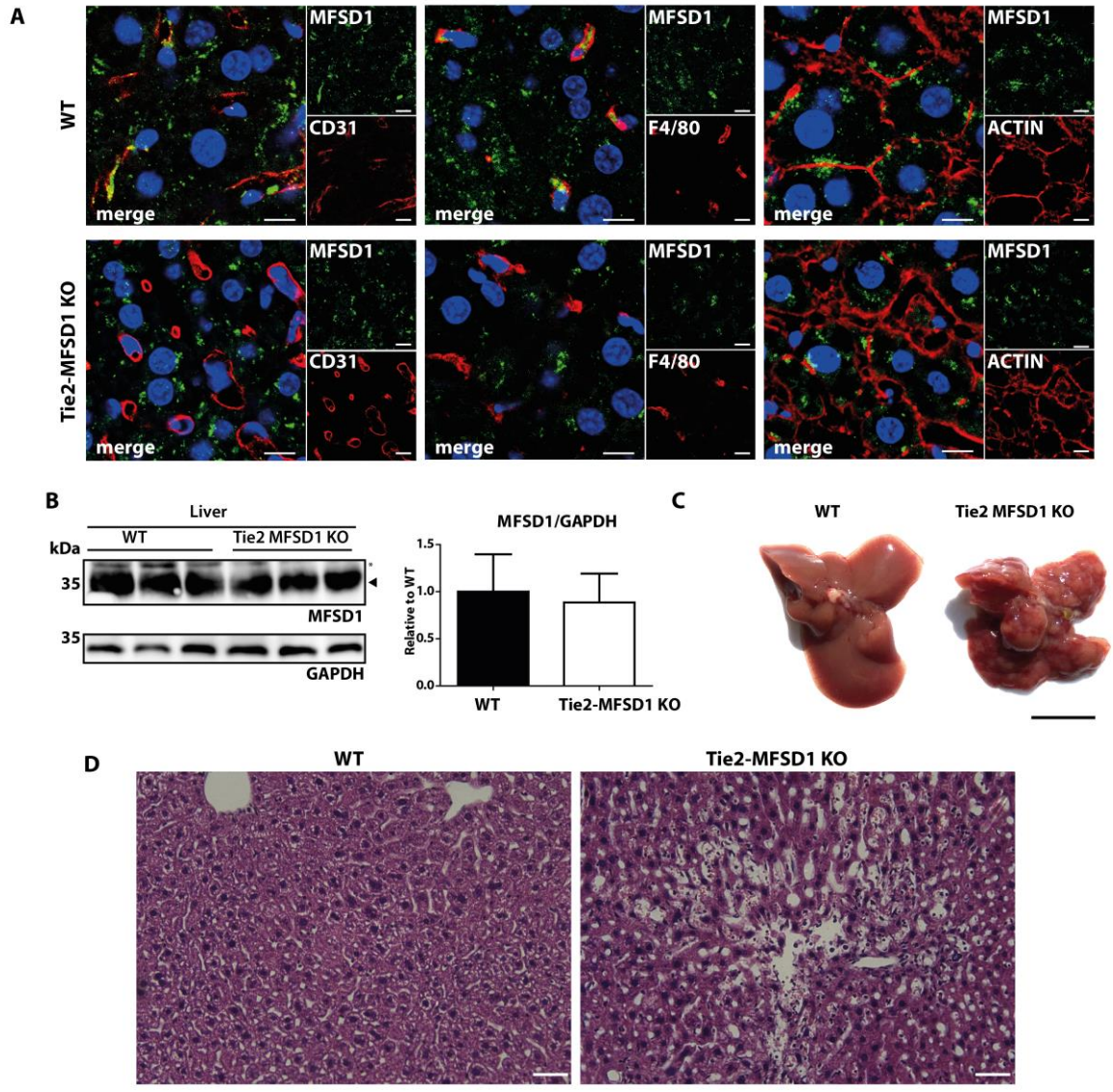

Figure 29. Tie2 promoter driven MFSD1 knockout mice have an abnormal morphology. (A) MFSD1$^{tm1c/tm1c}$ Tie2-cre$^{wt/wt}$ and MFSD1$^{tm1c/tm1c}$ Tie2-cre$^{+/wt}$ liver sections were prepared after perfusion with 4% PFA and were immunostained using the anti-MFSD1 antibody in combination with anti-CD31, anti-F4/80 antibodies or Texas red phalloidin, which recognizes actin. Scale bars, 10 µm (B) Livers from MFSD1$^{tm1c/tm1c}$ Tie2-cre$^{wt/wt}$ and MFSD1$^{tm1c/tm1c}$ Tie2-cre$^{+/wt}$ mice were collected five weeks after birth, the lysates were analysed by Western blotting with the anti-MFSD1 antibody and an anti-GAPDH antibody as a protein loading control (I) for the quantification of MFSD1 expression (II). (C) Representative picture of livers form MFSD1$^{tm1c/tm1c}$ Tie2-cre$^{wt/wt}$ and MFSD1$^{tm1c/tm1c}$ Tie2-cre$^{+/wt}$ mice at 3 months of age. Scale bar, 10 cm. (D) Liver sections of three months old mice were prepared after mice perfusion with 4% PFA and were stained with haematoxylin and eosin. Scale bars, 50 µm. H&E stainings were performed by R. Lüllmann-Rauch and D. Niemeier.

Most endothelial specific promoters used to express cre are also active in hematopoietic cells (Fahs et al. 2014). Tie2 promoter-driven cre expressing mice were used to produce a mouse strain with MFSD1 deficiency in endothelial cells and Kupffer cells (Figure 29A and see 2.2.5.3). Shortly, the breeding of MFSD1$^{tm1a/tm1a}$ with flipase expressing mice generated MFSD1$^{tm1c/wt}$ mice. *Mfsd1 tm1c* gene corresponds to the wild type *MFSD1* gene with 2 loxP sequences flanking exon 2. Cre enzyme catalyses a recombination between the two loxP sequences (Sternberg 1981) that results in the deletion of the exon 2 of MFSD1, and the mRNA generated harbours a frameshift mutation that leads to a premature stop codon. The litters generated from breeding MFSD1$^{tm1c/tm1c}$ Tie2-cre$^{wt/wt}$ females and MFSD1$^{tm1c/tm1c}$ Tie2-cre$^{+/wt}$ males consisted of 50% of MFSD1$^{tm1c/tm1c}$ Tie2-cre$^{wt/wt}$ and 50% MFSD1$^{tm1c/tm1c}$ Tie2-cre$^{+/wt}$ mice. MFSD1$^{tm1c/tm1c}$ Tie2-cre$^{wt/wt}$ mice (WT mice) expressed MFSD1 ubiquitously, while MFSD1$^{tm1c/tm1c}$ Tie2-cre$^{+/wt}$ mice (Tie2-MFSD1 KO mice) were mosaic for MFSD1 expression, with MFSD1 expression in the cells where Tie2 promoter is inactive and MFSD1 absent in the cells where Tie2 promoter is active.

MFSD1 expression of different cell types from the liver was analysed by immunofluorescence. Liver sections of WT and Tie2-MFSD1 KO mice were co-immunostained with the anti-MFSD1 antibody and with anti-CD31, anti-F4/80 antibodies or Texas red phalloidin, which recognizes actin, in order to detect LSECs, macrophages and hepatocytes, respectively. The results revealed that LSECs and macrophages had lost MFSD1 expression, while hepatocytes still expressed MFSD1 in Tie2-MFSD1 KO mice (Figure 29A). The MFSD1 expression in Tie2-MFSD1 KO liver was investigated by Western blotting using the anti-MFSD1 antibody. MFSD1 expression in Tie2-MFSD1 KO liver was indistinguishable from that of WT liver (Figure 29B). Despite a high variability, at three months of age the absence of MFSD1 in the Tie2 expressing cells resulted in an abnormal appearance of the liver with large nodules on the surface similar to MFSD1 full knockout mice (MFSD1$^{tm1a/tm1a}$) (Figure 29C). H&E analysis of liver sections revealed the presence of areas affected by sinusoidal obstruction, hepatocyte atrophy and erythrocytes extravasation in Tie2-MFSD1 KO mice (Figure 29D). These results indicate that the expression of MFSD1 in hepatocytes is not sufficient to prevent LSECs death and hepatocyte integrity loss. They also suggest that the lost of MFSD1 expression in LSECs (and eventually Kupffer cells) might be triggering the liver phenotype observed in MFSD1$^{tm1a/tm1a}$ mice.

3.3.2.5 Platelets levels are decreased in serum and increased in liver of MFSD1$^{tm1a/tm1a}$ mice

Since the loss of MFSD1 expression is leading to LSECs damage, abnormally exposing the hepatocytes to the blood circulation, the recruitment of platelets to the affected areas of MFSD1$^{tm1a/tm1a}$ liver was investigated by immunofluorescence staining using an anti-CD41 antibody. The results revealed an increase of CD41 signal in the affected areas of MFSD1$^{tm1a/tm1a}$ when compared to MFSD1$^{wt/wt}$ livers (Figure 30A). This staining also revealed the presence of large CD41 positive cells, which appear to be megakaryocytes, in MFSD1$^{tm1a/tm1a}$ livers that were not observed in MFSD1$^{wt/wt}$ liver (Figure 30A).

Since the platelet levels in MFSD1$^{tm1a/tm1a}$ liver were abnormal, the platelet numbers in blood of MFSD1$^{tm1a/tm1a}$ mice were investigated together with the following platelet parameters in collaboration with D. Wiegmann (Clinical chemistry, UKE Hamburg): mean platelet volume (MPV), platelet distribution width (PDW) and platelet large cell ratio (P-LCR). The results revealed that the thrombocyte levels in serum were significantly decreased in MFSD1$^{tm1a/tm1a}$ samples in comparison to MFSD1$^{wt/wt}$ samples (Figure 30B). Additionally, the mean platelet volume (MPV), platelet distribution width (PDW) and platelet large cell ratio (P-LCR) values were higher in MFSD1$^{tm1a/tm1a}$ platelets compared to MFSD1$^{wt/wt}$ platelets (Figure 30B), which could be interpreted as a sign of platelet activation (Budak, Polat, and Huysal 2016).

The spleen is one of the major organs where megakaryocytopoiesis takes places in mice. Therefore, the spleen of MFSD1$^{tm1a/tm1a}$ and MFSD1$^{wt/wt}$ mice was analysed. Immunofluorescence staining of spleen sections with an anti-CD41 antibody revealed an increased staining, suggesting a higher megakaryocyte number, of the MFSD1$^{tm1a/tm1a}$ spleens when compared to MFSD1$^{wt/wt}$ spleens (Figure 30C). H&E staining of spleen sections and counting of megakaryocytes confirmed the increase of the megakaryocyte number in MFSD1$^{tm1a/tm1a}$ spleen in comparison to MFSD1$^{wt/wt}$ spleen (Figure 30DI,II).

The interpretation of these results suggests that the sinusoidal damage of MFSD1$^{tm1a/tm1a}$ liver leads to a consumption of platelets in the damaged sinusoids, even recruiting megakaryocytes to the liver and causing decreased platelet levels in serum. Significantly higher number of megakaryocytes were found in MFSD1$^{tm1a/tm1a}$ spleen, which might be a sign of an attempt to compensate the decreased platelet numbers found in serum. As the spleen is one of the major immune organs in the mice, we aimed to investigate in more detail the immune status of MFSD1$^{tm1a/tm1a}$ mice.

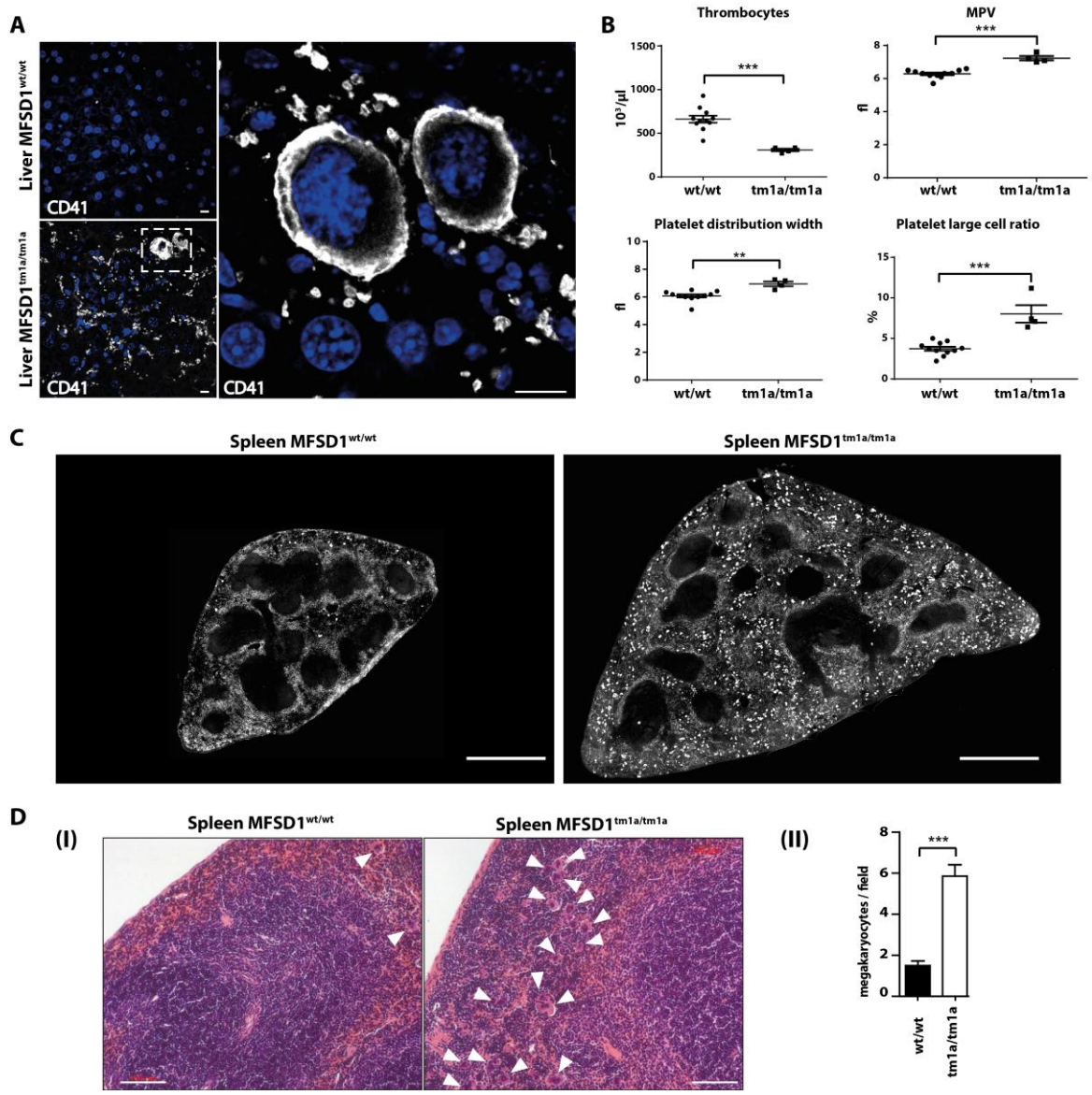

Figure 30. MFSD1$^{tm1a/tm1a}$ mice have increased platelets in liver, increased megakaryocytes in spleen and decreased platelets in serum compared to MFSD1$^{wt/wt}$ mice. (A) MFSD1$^{tm1a/tm1a}$ and MFSD1$^{wt/wt}$ liver sections were prepared after perfusion with 4% PFA and were immunostained using anti-CD41 antibody. (B) The serum of MFSD1$^{tm1a/tm1a}$ and MFSD1$^{wt/wt}$ mice was collected and the thrombocyte number was analysed. The platelet values indicated were also analysed. (C) MFSD1$^{tm1a/tm1a}$ and MFSD1$^{wt/wt}$ spleen sections were prepared after mice perfusion with 4% PFA and were immunostained using anti-CD41 antibody. (D) MFSD1$^{tm1a/tm1a}$ and MFSD1$^{wt/wt}$ spleen sections were prepared after mice perfusion with 4% PFA and were stained with H&E (I). The number of megakaryocytes per field was counted (II). Scale bars (A), 10 µm; scale bars (C), 1mm; scale bars (D), 100 µm. Asterisks indicate statistically significant differences between the two groups (*p<0.05; **p<0.01; ***p<0.005). H&E stainings were performed by R. Lüllmann-Rauch and D. Niemeier. The platelet values were analysed by D. Wiegmann (Clinical chemistry, UKE Hamburg).

3.3.3 Deficiency of MFSD1 leads to immunodeficiency

The spleen, one of the main tissues involved in the immune competent system of the mouse, was increased in size (Figure 23B) and had higher number of megakaryocytes in MFSD1$^{tm1a/tm1a}$ mice in comparison to MFSD1$^{wt/wt}$ mice (Figure 30C). Additionally, the liver of MFSD1$^{tm1a/tm1a}$ mice was affected by sinusoidal obstruction and infiltration of immune cells. The phenotype resembled that of sinusoidal obstructive syndrome (SOS) in human patients and experimental animal models. SOS is a liver disease where the sinusoids are obstructed. Patients suffering from SOS have thrombocytopenia (Mohty et al. 2015) and some patients have immunodeficiency (C. Q. Fan and Crawford 2014). Therefore, the expression of MFSD1 in immune organs and immune cells, and the immune status of MFSD1$^{tm1a/tm1a}$ mice were investigated in more detail.

3.3.3.1 MFSD1 is expressed in immune organs

First, the expression of MFSD1 in the immune organs and cells was evaluated by Western blotting and immunofluorescence analysis.

Western blotting analysis of bone marrow, spleen and thymus lysates from MFSD1$^{tm1a/tm1a}$ and MFSD1$^{wt/wt}$ mice using the anti-MFSD1 antibody revealed a high expression of MFSD1 in the three MFSD1$^{wt/wt}$ organs, with highest expression in bone marrow (Figure 31A). Spleen and thymus sections of MFSD1$^{tm1a/tm1a}$ and MFSD1$^{wt/wt}$ mice were analysed by immunofluorescence with anti-MFSD1 and anti-LAMP1 antibodies. The results revealed that MFSD1 co-localized with the lysosomal marker LAMP1 in the two tissues of MFSD1$^{wt/wt}$ mice, and that MFSD1 signal was absent in MFSD1$^{tm1a/tm1a}$ mice (Figure 31B). The expression of MFSD1 in B cells and T cells isolated from blood was investigated by Western blotting analysis with the anti-MFSD1 antibody. The results revealed that MFSD1 was expressed in both cell types, with the highest expression in B cells (Figure 31C). Spleen sections of MFSD1$^{wt/wt}$ mice were stained with anti-MFSD1 antibody and anti-B220 or anti CD3e antibodies as B lymphocyte and T lymphocyte markers, respectively. The analysis of the stainings revealed that all the B220 positive cells and the CD3e positive cells expressed MFSD1 (Figure 31D).

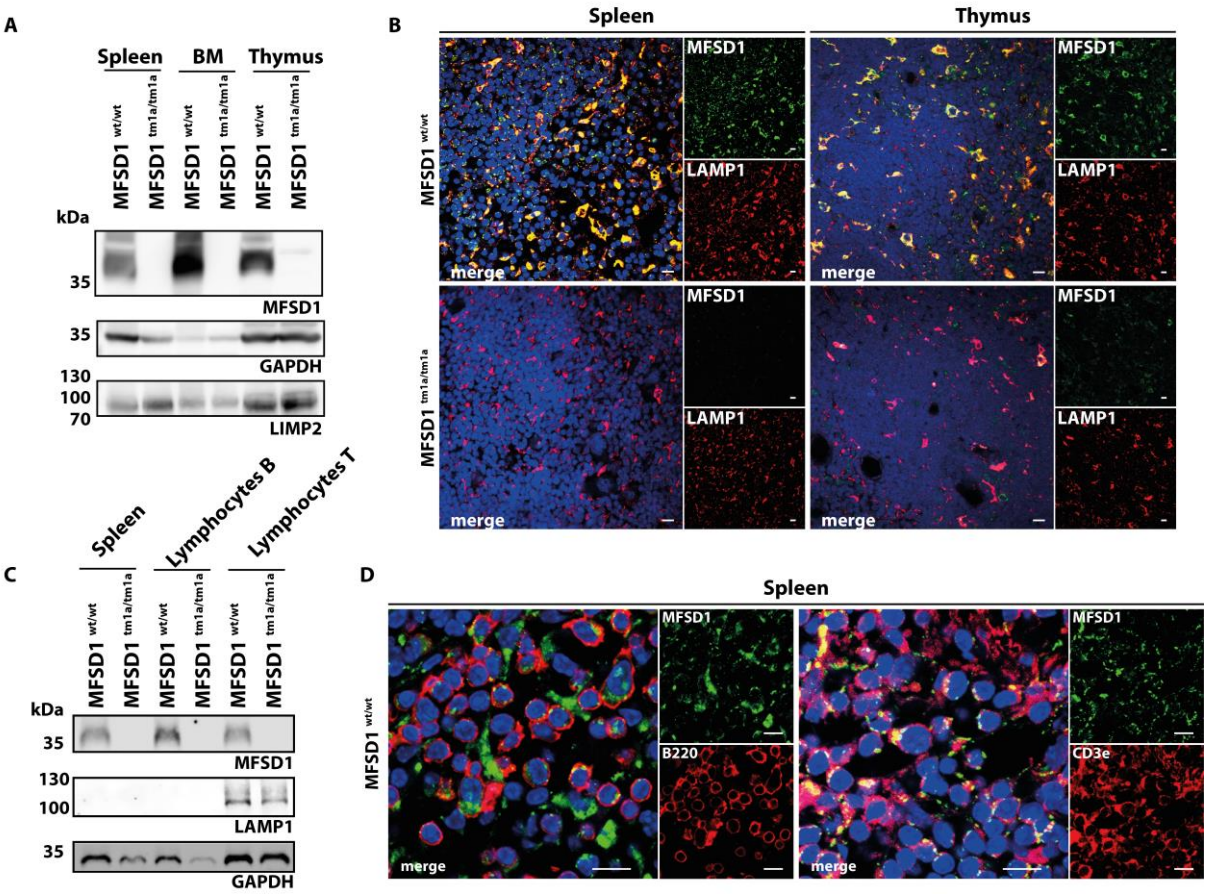

Figure 31. MFSD1 is expressed by B and T lymphocytes in spleen. (A) The indicated tissues from MFSD1$^{tm1a/tm1a}$ and MFSD1$^{wt/wt}$ mice were collected and their lysates were analysed by Western blotting with anti-MFSD1 antibody and anti-GAPDH and anti-LIMP2 antibodies as loading controls. (B) MFSD1$^{tm1a/tm1a}$ and MFSD1$^{wt/wt}$ spleen and thymus sections were prepared after mice perfusion with 4% PFA and were immunostained using anti-MFSD1 and anti-LAMP1 antibodies. (C) Lysates of spleen and B and T lymphocytes isolated from from MFSD1$^{tm1a/tm1a}$ and MFSD1$^{wt/wt}$ mice were analysed by Western blotting using the anti-MFSD1 antibody and anti-GAPDH and anti-LIMP2 antibodies as loading control. (D) MFSD1$^{wt/wt}$ spleen sections were prepared after mice perfusion with 4% PFA and were immunostained using anti-MFSD1, anti-B220 and anti-CD3e antibodies. Scale bars, 10 µm.

3.3.3.2 MFSD1$^{tm1a/tm1a}$ mice exert reduced lymphocyte numbers and immunodeficiency

As MFSD1 was expressed in both B and T lymphocytes, the lymphocyte distribution in spleen was investigated by immunofluorescence using antibodies against B220 and CD3e. The results revealed that MFSD1$^{tm1a/tm1a}$ spleen had reduced number of B220 positive cells in the red pulpa area when compared to MFSD1$^{wt/wt}$ spleen, while no difference in the staining of CD3e was observed between the spleen of the two genotypes analysed (Figure 32A).

In order to have quantitative data about the percentage of B220 positive cells, the splenocytes of MFSD1$^{wt/wt}$ and MFSD1$^{tm1a/tm1a}$ mice were analysed by flow cytometry with the anti-B220 antibody. The analysis showed that MFSD1$^{tm1a/tm1a}$ spleen had significantly reduced

percentage of B220 positive cells when compared to MFSD1$^{wt/wt}$ spleen (Figure 32B). Since the lymphocyte levels were changed in spleen, the leukocyte numbers in serum were analysed in collaboration with D. Wiegmann (Clinical chemistry, UKE Hamburg). The results revealed a significant decrease in total leukocyte numbers in MFSD1$^{tm1a/tm1a}$ serum compared to MFSD1$^{wt/wt}$ serum. Lymphocytes in MFSD1$^{tm1a/tm1a}$ serum were reduced to less than half of the number in MFSD1$^{wt/wt}$ serum (Figure 32C). Because the lymphocyte number was reduced in spleen and serum, the immunoglobulin levels were investigated. The immunoglobulin G (IgG) levels in spleen were analysed by Western blotting using an anti-IgG antibody. The results revealed that the IgG levels in MFSD1$^{tm1a/tm1a}$ spleens were reduced to approximately 25% of MFSD1$^{wt/wt}$ spleen IgG levels (Figure 32D). However, 5 weeks after birth the IgG levels in spleen were unchanged (Figure 32F). The serum immunoglobulin levels were analysed in collaboration with K. Dittmann (Institute for Cellular and Molecular Immunology, University of Göttingen), revealing that levels of IgG1, IgG2a, IgG2b and IgG3 in MFSD1$^{tm1a/tm1a}$ serum were significantly reduced to 16%, 12.1%, 21.4% and 17%, respectively, of the levels found in MFSD1$^{wt/wt}$ serum (Figure 32E). Also the IgA levels in MFSD1$^{tm1a/tm1a}$ serum were reduced to 50% of the levels found in MFSD1$^{wt/wt}$ serum. Interestingly, no decrease in the IgM values in MFSD1$^{tm1a/tm1a}$ serum compared to MFSD1$^{wt/wt}$ serum was detected (Figure 32E).

In order to investigate the ultrastructure of lymphocytes, B cells and T cells of MFSD1$^{wt/wt}$ and MFSD1$^{tm1a/tm1a}$ spleen were isolated with magnetic cell isolation kits using positive and negative selection, respectively, and further analysed by electron microscopy. The results revealed no obvious difference in the cellular structure, including vesicles, between B or T lymphocytes of WT spleen and B or T lymphocytes of MFSD1 deficient spleen (data not shown).

The histology of the bone marrow, which can function as a lymphoid organ in mouse (Tripp et al. 1997; Zhao et al. 2012), was analysed by H&E staining. When collecting the bones for analysis, a paler color of the femur and tibias from MFSD1$^{tm1a/tm1a}$ mice compared to those of MFSD1$^{wt/wt}$ mice was observed (Figure 32G, black arrows). H&E stainings revealed a different morphology of MFSD1$^{tm1a/tm1a}$ bone marrow in comparison to MFSD1$^{wt/wt}$ bone marrow, finding a high number of adipocytes in MFSD1$^{tm1a/tm1a}$ samples (Figure 32HI). The number of adipocytes in the bone marrow was quantified, demonstrating that MFSD1$^{tm1a/tm1a}$ bone marrow had significantly more adipocytes than MFSD1$^{wt/wt}$ bone marrow (Figure 32HII).

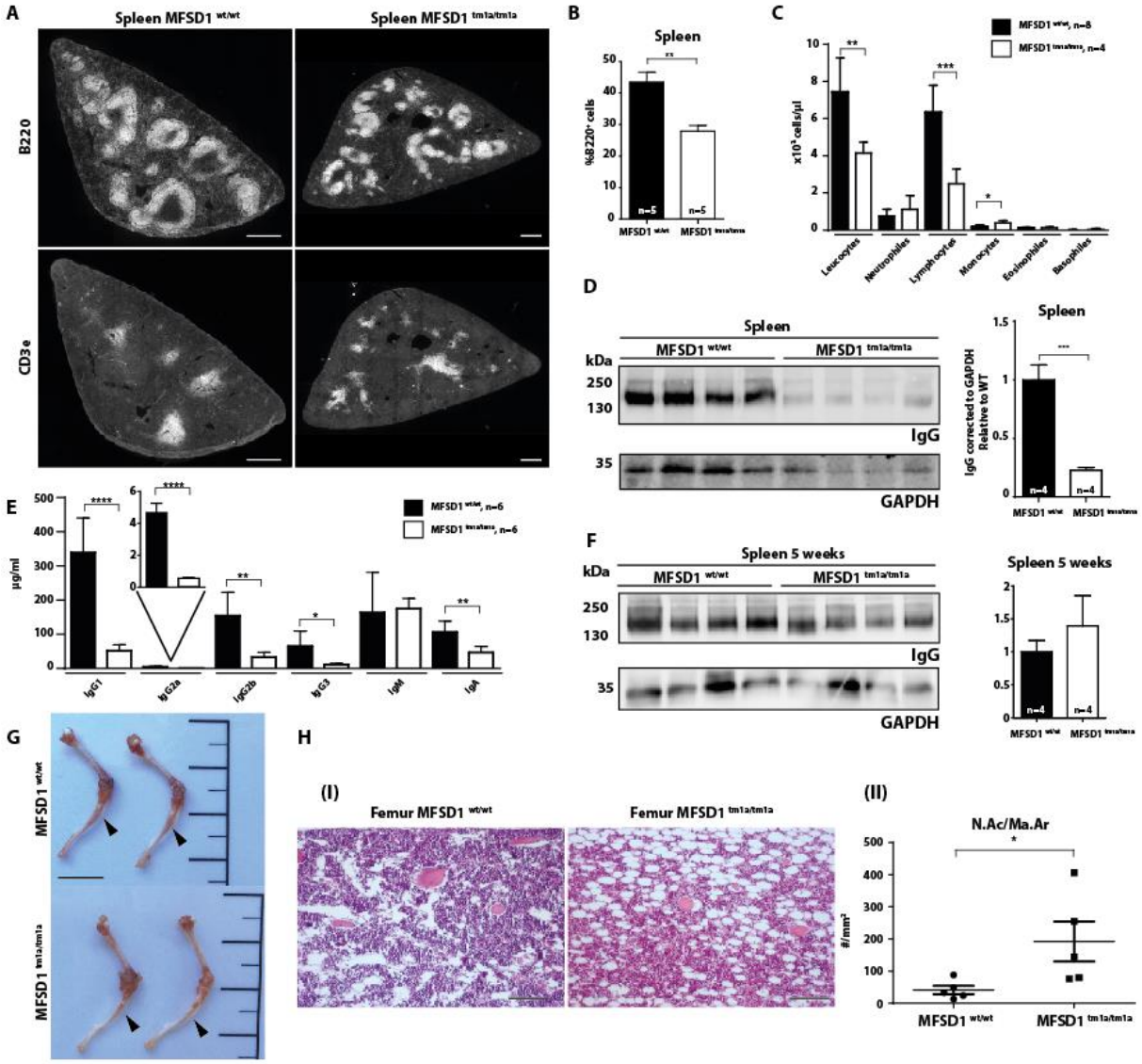

Figure 32. MFSD1$^{tm1a/tm1a}$ mice have decreased B220 positive cells and immunodeficiency. (A) MFSD1$^{tm1a/tm1a}$ and MFSD1$^{wt/wt}$ spleen sections were prepared after mice perfusion with 4% PFA and were stained with anti-B220 and anti-CD3e antibodies. (B) Splenocytes were isolated from MFSD1$^{tm1a/tm1a}$ and MFSD1$^{wt/wt}$ spleens, stained for the cell marker B220 and analysed by flow cytometry. (C) Serum from MFSD1$^{tm1a/tm1a}$ and MFSD1$^{wt/wt}$ mice was collected and leukocyte levels were analysed. (D) Spleens were isolated and the lysates were analysed by Western blotting in non-denaturing conditions using an anti-IgG antibody. (E) Serum from MFSD1$^{tm1a/tm1a}$ and MFSD1$^{wt/wt}$ mice was collected and the immunoglobulin levels were analysed. (F) Representative picture of freshly isolated femur and tibia from MFSD1$^{tm1a/tm1a}$ and MFSD1$^{wt/wt}$ mice. (G) MFSD1$^{tm1a/tm1a}$ and MFSD1$^{wt/wt}$ femurs sections were prepared after mice perfusion with 4% PFA and were stained with H&E (I) and the number of adypocytes (N.Ac/Ma.Ar) was quantified (II). Scale bars (A), 500 µm; scale bars (F), 1 cm; Scale bars (G), 100 µm. Values are given as mean±SEM. Asterisks indicate statistically significant differences between the two groups (*p<0.05; **p<0.01; ***p<0.005). The serum immunoglobulins analysis were performed by K. Dittmann (Institute for Cellular and Molecular Immunology, University of Göttingen). The leukocyte values were analysed by D. Wiegmann (Clinical chemistry, UKE Hamburg).

3.3.3.3 MFSD1$^{tm1a/tm1a}$ mice show signs of anemia

Bone marrow and spleen, organs where hematopoiesis takes places, from MFSD1$^{tm1a/tm1a}$ mice were altered and MFSD1$^{tm1a/tm1a}$ mice had decreased number of hematopoietic cells in serum, like thrombocytes and leukocytes, compared to MFSD1$^{wt/wt}$ mice. Therefore, the erythrocyte levels in serum were analysed in collaboration with D. Wiegmann (Clinical chemistry, UKE Hamburg). A decrease in number of erythrocytes, hemoglobin and hematocrit, and an increase in the cellular sizes of erythroid cells (RDW) in MFSD1$^{tm1a/tm1a}$ in comparison to MFSD1$^{wt/wt}$ were observed indicating anemia (Table 18).

	Units	WT(n=8)	tm1a/tm1a (n=4)
Erythrocytes	X10^9/µl	11.22±0.16	10.52±0.21*
Hemoglobin	g/dl	16.50±0.14	15.05±0.25***
Hematocrit	%	58.55±0.67	54.03±0.80**
Mean Corspuscular Volume (MCV)	fl	52.20±0.21	51.35±0.59
Mean Corspuscular Hemoglobin (MCH)	pg	14.70±0.11	14.30±0.09*
Mean Corspuscular Hemoglobin Concentration (MCHC)	g/dl	28.18±0.12	27.85±0.15
Red cell distribution width (RDW)	fl	31.05±0.23	35.33±0.53***

Table 18. MFSD1$^{tm1a/tm1a}$ mice have decreased erythrocytes, hemoglobin and hematocrit. Serum from MFSD1$^{tm1a/tm1a}$ and MFSD1$^{wt/wt}$ mice was collected and the shown parameters were analysed. The analysis were performed by D. Wiegmann (Clinical chemistry, UKE Hamburg).

These results indicate that MFSD1 deficiency leads to a decreased number of B lymphocytes in spleen and lymphocytes in serum, which causes a significant decrease in the IgGs and IgA levels in spleen and serum, but does not affect the IgM levels, suggesting that the B lymphocyte maturation is impaired. Additionally, the bone marrow cell composition from femurs is changed, with increased number of adipocytes in MFSD1 deficient mice, and decreased erythrocyte numbers in serum.

3.3.4 MFSD1$^{tm1a/tm1a}$ mice have decreased BMD in vertebra and decreased osteoblast activity

Mice with osteopetrosis have increased bone thickness, which causes a paler appearance of the bones. Hematopoietic stem cells (HSM), that give rise to osteoclasts, and mesenchymal stem cells (MSC), that give rise to osteoblasts and osteocytes, reside in the bone marrow and are closely related (Yin and Li 2006). Since MFSD1$^{tm1a/tm1a}$ mice had paler femur and tibia color when compared to MFSD1$^{wt/wt}$ mice, and also the cellular composition of the bone marrow

was altered, the status of the cortical and trabecular bones of MFSD1$^{tm1a/tm1a}$ mice three months after birth was investigated.

3.3.4.1 Bone volume and bone mineral density of cortical bone from MFSD1$^{tm1a/tm1a}$ femurs is unchanged

Femurs from MFSD1$^{wt/wt}$ and MFSD1$^{tm1a/tm1a}$ mice were analysed by micro-computed tomography (µCT) in collaboration with U. Lerner, P. Henning and V. Lionikaite (Department of Internal Medicine, University of Gothenburg). The results demonstrated unaltered bone mineral density (BMD) of the cortical and trabecular bone from MFSD1$^{tm1a/tm1a}$ femurs (Figure 33B). Also the cortical cross-sectional thickness, cortical porosity, trabecular thickness and trabecular bone volume/total volume ratio (BV/TV) were unchanged in MFSD1$^{tm1a/tm1a}$ mice femurs compared to MFSD1$^{wt/wt}$ femurs (Figure 33B). The femurs of a different set of animal was analysed by Von Kossa/van Gieson staining in collaboration with T. Schinke (Institute for Osteology and Biomechanic, UKE Hamburg), also revealing no differences between the two genotypes. Representative pictures of femurs stained with von Kossa/van Gieson are shown in Figure 33A.

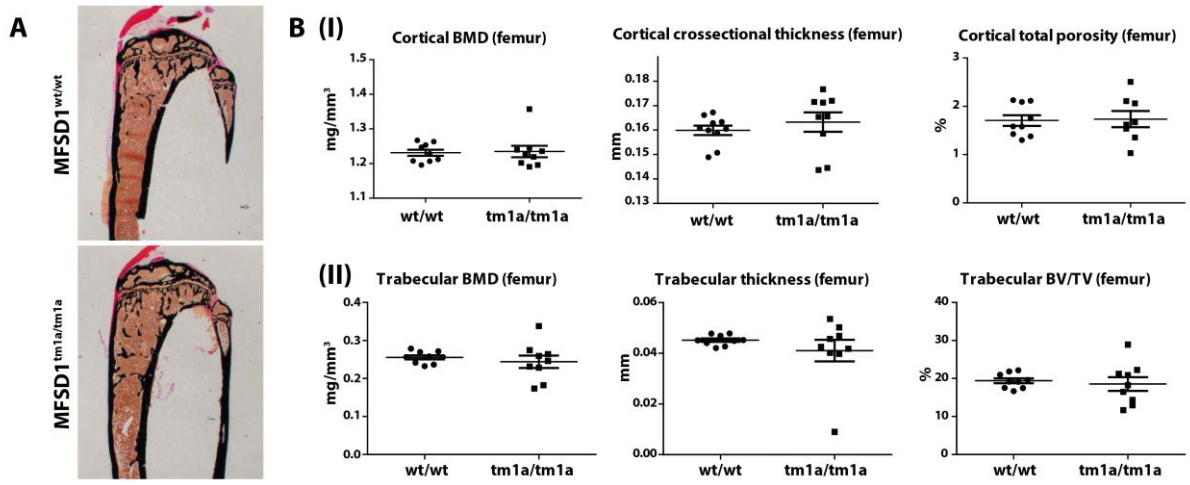

Figure 33. Femur bone values analysed by µCT are not altered in MFSD1$^{tm1a/tm1a}$ mice. (A) MFSD1$^{tm1a/tm1a}$ and MFSD1$^{wt/wt}$ mice were fixed with 4% PFA and the femurs were stained with VonKossa/van Gieson. (B) Femurs from MFSD1$^{tm1a/tm1a}$ and MFSD1$^{wt/wt}$ mice were isolated, fixed with 4% PFA and the mentioned measurements of cortical bone (I) and the trabecular bone (II) were performed by µCT. Values are given as mean±SEM. VonKossa/Gieson stainings were performed by T. Schinke and M. Neven.

3.3.4.2 Trabecular bone of MFSD1$^{tm1a/tm1a}$ vertebrae show decreased bone volume and decreased bone formation rate

Vertebrae from MFSD1$^{wt/wt}$ and MFSD1$^{tm1a/tm1a}$ mice were also analysed by µCT. The results revealed that the trabecular bone of vertebrae in MFSD1$^{tm1a/tm1a}$ mice had decreased BMD and decreased BV/TV ratio compared to MFSD1$^{wt/wt}$ vertebrae (Figure 34A). Also MFSD1$^{tm1a/tm1a}$ vertebrae had reduced trabecular number in comparison to MFSD1$^{wt/wt}$ vertebrae (Figure 34A). Representative reconstruction of the µCT images of vertebrae is shown in Figure 34B. In order to validate those results by an alternative method, Von Kossa/van Gieson staining was applied in vertebrae of a different set of mice. The results confirmed the decreased trabecular BV/TV ratio and decreased trabecular number in MFSD1$^{tm1a/tm1a}$ vertebrae (Figure 35B). Additionally, MFSD1$^{tm1a/tm1a}$ vertebrae had an increased separation of trabeculae in comparison to MFSD1$^{wt/wt}$ vertebrae (Figure 35B). Representative pictures of the Von Kossa/van Gieson stainings of vertebrae from the two genotypes are shown in Figure 35A. The samples were also used to perform histomorphometric quantification of the different bone cell types in the vertebrae. MFSD1$^{tm1a/tm1a}$ vertebrae had increased number of osteoblast and osteocytes compared to

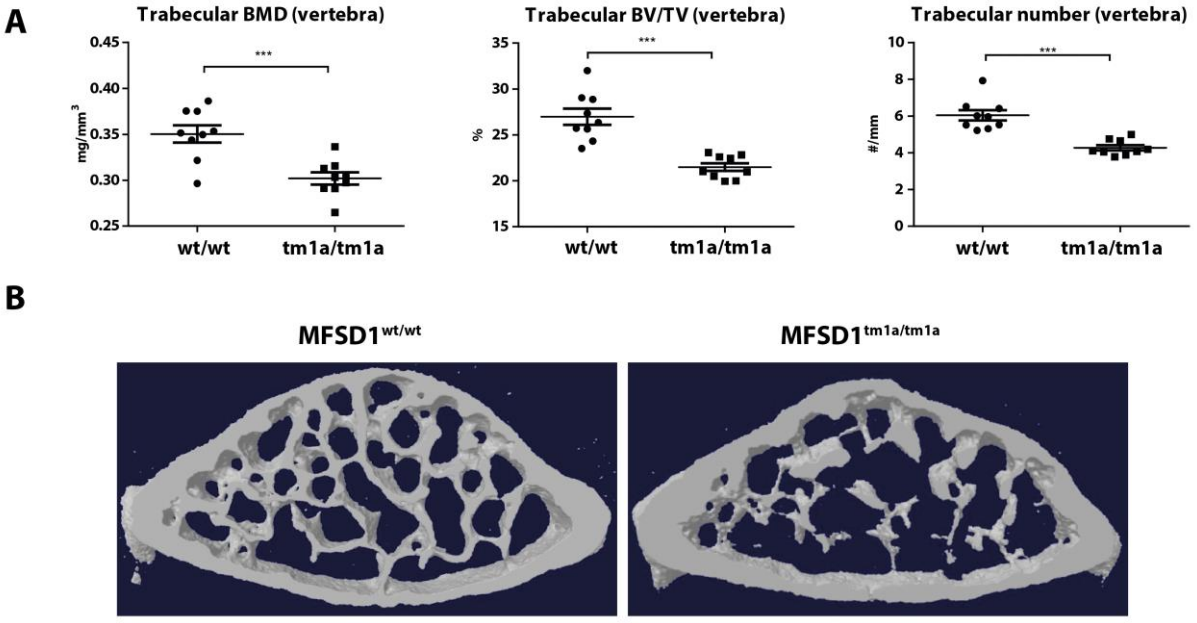

Figure 34. Vertebra of MFSD1$^{tm1a/tm1a}$ has decreased trabecular BMD, BV/TV and trabecular number. (A) Vertebrae from MFSD1$^{tm1a/tm1a}$ and MFSD1$^{wt/wt}$ mice were fixed with 4% PFA and the mentioned measurements from trabecular bone were performed. (B) Representative reconstructions of µCT images. Values are given as mean±SEM. Asterisks indicate statistically significant differences between the two groups (*p<0.05; **p<0.01; ***p<0.005).

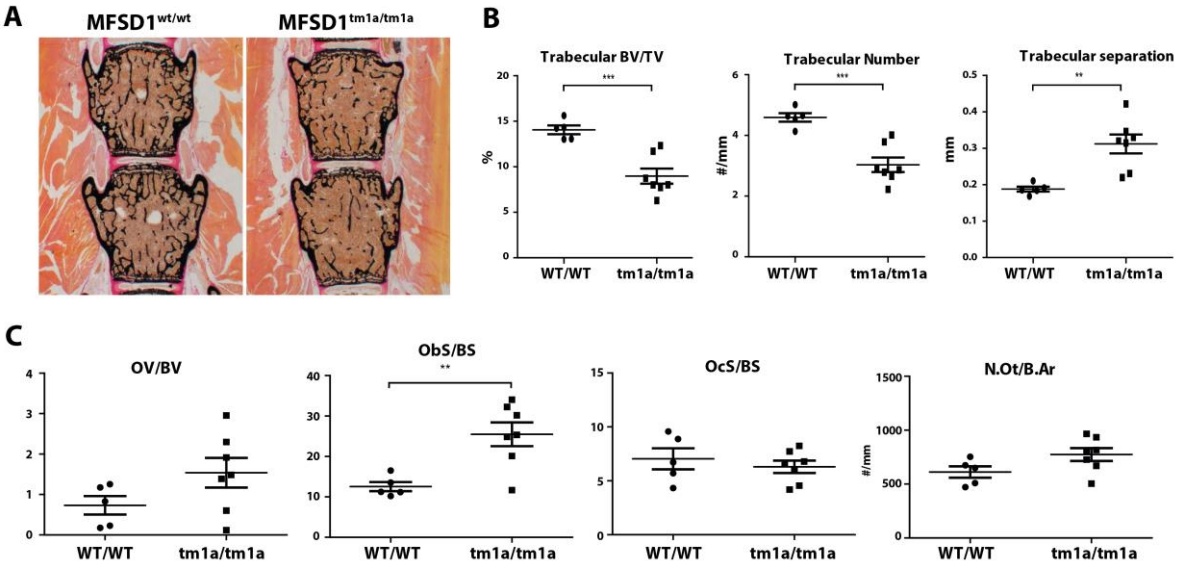

Figure 35. Osteoblast number is increase in vertebrae of MFSD1$^{tm1a/tm1a}$. (A) MFSD1$^{tm1a/tm1a}$ and MFSD1$^{wt/wt}$ mice were fixed with 4% PFA and the vertebrae were stained with Von Kossa/van Gieson. (B) Histomorphometric quantification of the trabecular bone volume, trabecular number and trabecular separation in MFSD1$^{tm1a/tm1a}$ and MFSD1$^{wt/wt}$ vertebrae. (C) Histomorphometric quantification of osteoid volume (OV/BV), osteoblast surface (ObS/BS), osteoclast surface (OcS/BS) and osteocyte number (N.Ot/B.Ar) in MFSD1$^{tm1a/tm1a}$ and MFSD1$^{wt/wt}$ vertebrae. Values are given as mean±SEM. Asterisks indicate statistically significant differences between the two groups (*p<0.05; **p<0.01; ***p<0.005). Histomorphometric analysis was performed by T. Schinke and M. Neven.

MFSD1$^{wt/wt}$ vertebrae, but the differences did not reach statistical significance for the osteocyte number. Also the osteoid volume was increased in MFSD1$^{tm1a/tm1a}$ mice vertebrae compared to MFSD1$^{wt/wt}$ vertebrae, but the difference also failed to reach statistical significance. No differences were detected in the number of osteoclasts between the two genotypes (Figure 35C). Surprisingly, the bone volume of MFSD1$^{tm1a/tm1a}$ vertebrae was decreased compared to MFSD1$^{wt/wt}$ vertebrae, but the number of osteoblast was higher in the MFSD1$^{tm1a/tm1a}$ vertebrae. In order to investigate whether the osteoblast activity in MFSD1$^{tm1a/tm1a}$ vertebrae was impaired, the bone apposition rate of MFSD1$^{tm1a/tm1a}$ mice in vertebrae was analysed by double calcein labeling. Briefly, mice were injected intraperitoneally with calcein nine and two days prior to the day of sacrifice. Representative images of the calcein labelling in vertebrae of MFSD1$^{tm1a/tm1a}$ and MFSD1$^{wt/wt}$ mice showing decreased number of calcein-labeled surface in MFSD1$^{tm1a/tm1a}$ compared to MFSD1$^{wt/wt}$ are shown in Figure 36A. The histomorphometric quantification of the mineralizing surface, the bone formation rate and the mineral apposition rate revealed that all three parameters were decreased in MFSD1$^{tm1a/tm1a}$ vertebrae compared to MFSD1$^{wt/wt}$ vertebrae, indicating that the osteoblast activity in MFSD1$^{tm1a/tm1a}$ vertebrae was decreased (Figure 36B).

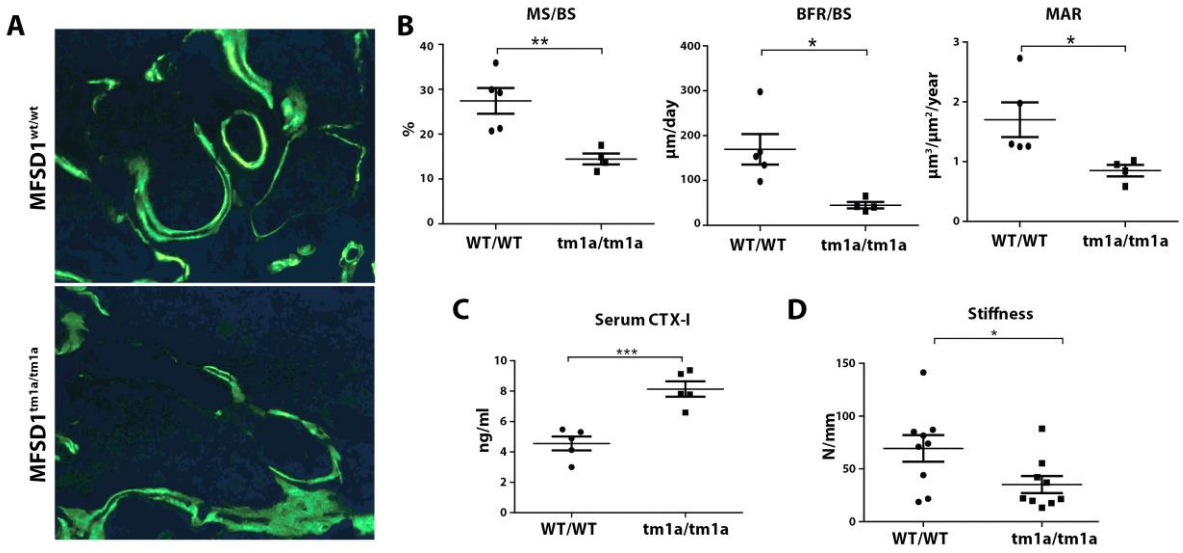

Figure 36. Osteoblast activity is decreased in vertebrae of MFSD1$^{tm1a/tm1a}$ mice. (A) MFSD1$^{tm1a/tm1a}$ and MFSD1$^{wt/wt}$ mice were injected with calcein 9 and 2 days prior to sacrifice, and the vertebrae were analysed by confocal microscopy. A representative image is shown. (B) Histomorphometric quantification of the mineralization surface (MS/BS), bone formation rate (BFR/BS) and matrix apposition rate (MAR). (C) Serum from MFSD1$^{tm1a/tm1a}$ and MFSD1$^{wt/wt}$ mice was collected and the C-terminal telopeptide I (CTX-I) was analysed by ELISA. (D) The stiffness of vertebrae from MFSD1$^{tm1a/tm1a}$ and MFSD1$^{wt/wt}$ mice was analysed by compression test. Values are given as mean±SEM. Asterisks indicate statistically significant differences between the two groups (*p<0.05; **p<0.01; ***p<0.005). Histomorphometric analysis was performed by T. Schinke and M. Neven. Compression test was performed by J. Tuukkanen.

Additionally, the osteoclast activity in MFSD1$^{tm1a/tm1a}$ mice was investigated by analysing the serum levels of the C-terminal telopeptide I (CTX-I), which is a collagen degradation product produced by osteoclast activity and is commonly used as a biomarker for bone turnover (Kuo and Chen 2017; Rosen et al. 2000). The results revealed that CTX-I levels in MFSD1$^{tm1a/tm1a}$ serum were increased compared to MFSD1$^{wt/wt}$ serum (Figure 36C), indicating that the osteoclast activity was increased in MFSD1$^{tm1a/tm1a}$ mice.

Finally, in order to investigate how the decreased BMD and BV/TV of MFSD1$^{tm1a/tm1a}$ vertebra were affecting its mechanical quality, a compression test was performed in collaboration with J. Tuukkanen (University of Oulu). The results showed that MFSD1$^{tm1a/tm1a}$ vertebrae had decreased stiffness compared to MFSD1$^{wt/wt}$ vertebrae (Figure 36D).

Altogether these results indicate that the lack of MFSD1 affects bone homeostasis in the vertebrae but not long bones. MFSD1 deficiency also leads to a decreased osteoblastic activity in vertebrae and increased osteoclast activity, resulting in decreased BMD and BV/TV of the vertebrae affecting its stiffness.

3.4 Proteomics analysis of MFSD1$^{tm1a/tm1a}$ liver and tritosomes

The study of MFSD1-deficient mice revealed that the lack of MFSD1 in mice leads to LSECs damage, immunodeficiency, decreased osteoblast activity in trabecular bone from vertebrae, and increased osteoclast activity. The complexity of the phenotype observed in MFSD1$^{tm1a/tm1a}$ mice makes it difficult to interpret whether all the phenotypes observed are a primary consequence of the MFSD1 deficiency.

In order to gather more hints leading to the function of MFSD1, we aimed to study how the lack of MFSD1 would affect the total liver and lysosomal liver proteome. To answer this question, whole liver lysates and lysosome-enriched fractions (F2) from liver after tyloxapol injection in MFSD1$^{tm1a/tm1a}$ and MFSD1$^{wt/wt}$ mice were prepared and further analysed by liquid chromatography tandem-mass spectrometry (LC-MS/MS) in collaboration with M. Thelen. Briefly, the samples were differentialy labeled with tandem mass tags (TMT), mixed in equal ratios, fractionated by liquid chromatography and further analysed by tandem mass spectrometry. The simultaneous analysis of all the samples together with the use of TMT allowed the differential quantification of the liver proteome or the lysosomal proteome.

The proteomic analysis of whole liver lysates revealed changes in the levels of 79 proteins out of more than 1400 proteins identified between MFSD1$^{tm1a/tm1a}$ liver lysates compared to MFSD1$^{wt/wt}$ liver lysates and *vice-versa* in a 1.5 fold or higher ratio with a *p-value* ≥0.05 after a two-tailed Student´s t test (Figure 37). The levels of 69 proteins of the altered proteins were increased in MFSD1$^{tm1a/tm1a}$ liver lysates compared to MFSD1$^{wt/wt}$ liver lysates. The genes coding for those proteins were submitted to Gene Ontology Enrichment analysis for biological process (http://geneontology.org/page/go-enrichment-analysis).

GO term	Description	P-value
GO:0071593	Lymphocyte aggregation	$1.36E^{-04}$
GO:0030168	Platelet aggregation	$4.72E^{-09}$
GO:0030168	Platelet activation	$6.56E^{-08}$
GO:0030199	Collagen fibril organization	$1.07E^{-05}$
GO:0030198	Extracellular matrix organization	$7.09E^{-09}$
GO:0090303	Positive regulation of wound healing	$6.33E^{-04}$
GO:1903921	Regulation of protein processing in phagocytic vesicle	$5.46E^{-05}$

Table 19. Selection of gene ontology enriched proteins in MFSD1$^{tm1a/tm1a}$ livers

The results revealed an over-representation in MFSD1$^{tm1a/tm1a}$ liver lysates of genes involved in regulation of protein processing in phagocytic vesicle, lymphocyte aggregation, platelet

aggregation, platelet activation, collagen fibril organization, extracellular matrix organization and positive regulation of wound healing among other processes (Table 19). These results supported the described liver insult in MFSD1$^{tm1a/tm1a}$ mice, but did not provide obvious hints towards the function of MFSD1.

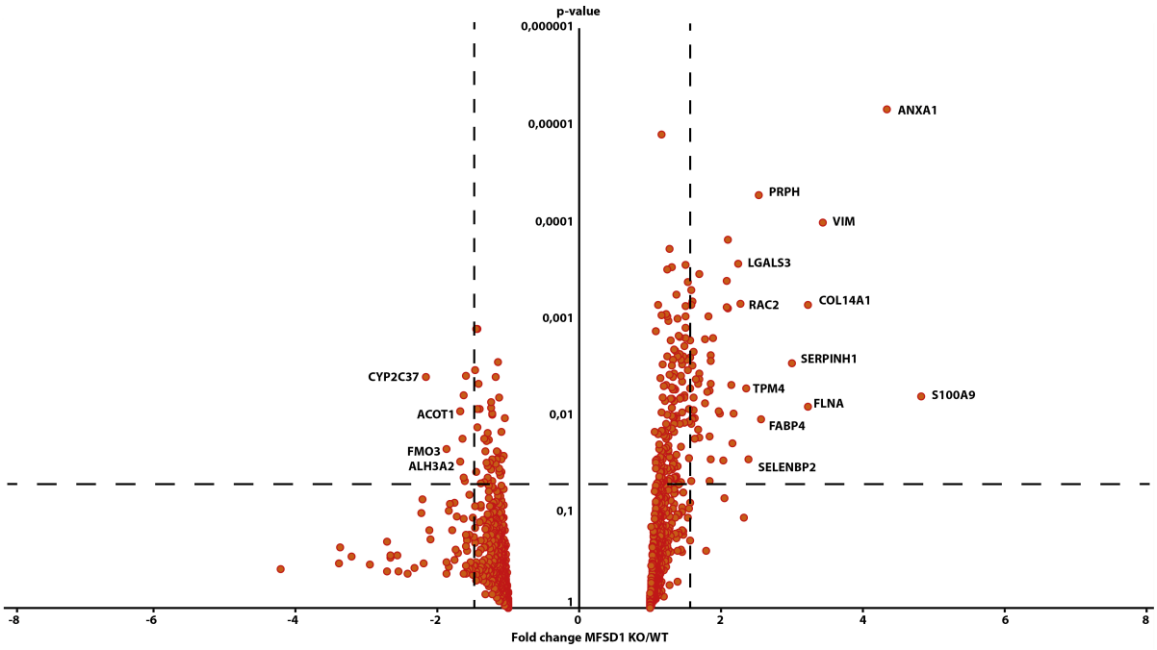

Figure 37. Proteins involved in wound healing, fibrosis, leukocyte and platelet aggregation are increased in MFSD1$^{tm1a/tm1a}$ liver. Liver lysates of MFSD1$^{tm1a/tm1a}$ and MFSD1$^{wt/wt}$ mice were analysed by liquid chromatography tandem-mass spectrometry (LC-MS/MS). All the proteins found to have statistically changed levels between MFSD1$^{tm1a/tm1a}$ and MFSD1$^{wt/wt}$ mice are represented in Supplementary Table 1. The analysis was performed by M. Thelen (Institute for Biochemistry and Molecular Biology, University of Bonn).

The analysis of lysosome enriched fractions revealed altered levels of 17 proteins out of 1000 proteins identified between MFSD1$^{tm1a/tm1a}$ liver lysosomes compared to MFSD1$^{wt/wt}$ liver lysosomes and *vice-versa* in a two-fold or higher ratio with a *p-value* ≥0.05 after a two-tailed Student´s t test. MFSD1 levels in MFSD1$^{tm1a/tm1a}$ liver lysosomes was eight fold reduced compared to MFSD1$^{wt/wt}$ samples. The observed ratio for MFSD1 is probably due to co-isolation interference, causing a distortion of the results due to additional peptides present in the respective measure window. Since there are not many peptide spectral matches of MFSD1, probably due to the hydrophobicity of its numerous membrane domains, this effect is quite distinct. Upon manual inspection there were also spectra devoid of any signal for the MFSD1 knockout samples, proving the absence of MFSD1 peptides. The change in the levels of some proteins with immune system functions suggests that those changes are due to the

immune phenotype observed in MFSD1$^{tm1a/tm1a}$ mice, like the decrease of the immunoglobulin subunits, IGKV6-17 and IGHMAC38, or the increase in the subunit of the classic complement pathway C1R in MFSD1$^{tm1a/tm1a}$ mice compared to MFSD1$^{wt/wt}$ mice. The change in some other proteins might be related to the liver stress of MFSD1$^{tm1a/tm1a}$ mice, like the increase of SOD3 and DCN levels in MFSD1$^{tm1a/tm1a}$ mice compared to MFSD1$^{wt/wt}$ mice. But among all the proteins detected with different levels in MFSD1$^{tm1a/tm1a}$ samples compared to MFSD1$^{wt/wt}$ samples, one protein stood out above the rest, GLMP, that was reduced almost seven fold in MFSD1$^{tm1a/tm1a}$ lysosomes compared to MFSD1$^{wt/wt}$ lysosomes (Figure 38A). Western blotting analysis of F2 fractions from MFSD1$^{tm1a/tm1a}$ and MFSD1$^{wt/wt}$ mice using a newly developed anti-GLMP antibody (See 2.2.3.13) was performed in order to validate the proteomic data. The results confirmed the almost complete absence of GLMP in MFSD1$^{tm1a/tm1a}$ lysosomal fractions (Figure 38B).

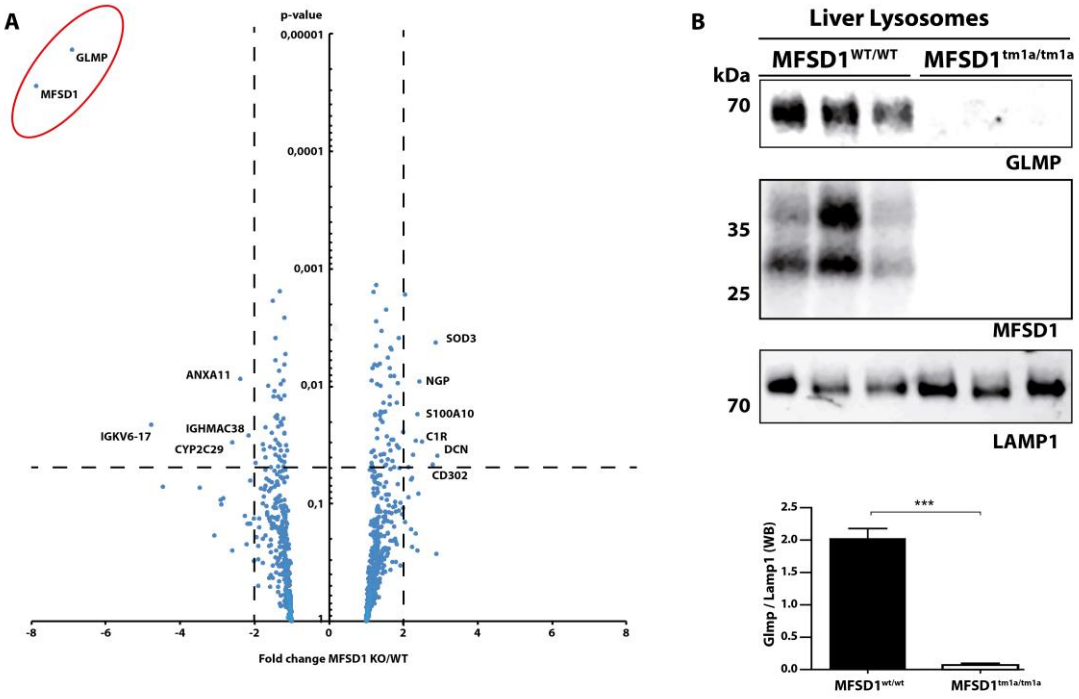

Figure 38. GLMP protein levels are strikingly reduced in MFSD1$^{tm1a/tm1a}$ liver lysosomes. (A) Liver lysosomes were isolated after intraperitoneal injection of tyloxapol into MFSD1$^{tm1a/tm1}$ and MFSD1$^{wt/wt}$ mice and further analysed by liquid chromatography tandem-mass spectrometry (LC-MS/MS). All the proteins with statistically changed levels between MFSD1$^{tm1a/tm1a}$ and MFSD1$^{wt/wt}$ mice are represented in Supplementary Table 2 (B) Liver lysosomes from MFSD1$^{tm1a/tm1}$ and MFSD1$^{wt/wt}$ mice were analysed by Western blotting using anti-GLMP, anti-MFSD1 and anti-LAMP1 antibodies. Values are given as mean±SEM. Asterisks indicate statistically significant differences between the two groups (*p<0.05; **p<0.01; ***p<0.005). Proteomics analysis was performed by M. Thelen (Institute for Biochemistry and Molecular Biology, University of Bonn).

3.5 Study of MFSD1-GLMP interaction

GLMP, previously named NCU-G1, was initially described as a nuclear protein serving as a transcription factor as well as a nuclear receptor co-activator (Steffensen et al. 2007). However, later studies demonstrated that GLMP is a highly glycosylated type I transmembrane protein localized at the lysosome, with a tyrosine based motif at the C-terminus (YQSI) that is critical for its transport to lysosomes (Figure 39A), but its function remained elusive (Schieweck et al. 2009). Due to the dramatic decrease of GLMP levels in MFSD1$^{tm1a/tm1a}$ liver lysosomes compared to MFSD1$^{wt/wt}$ liver lysosomes, the nature of the relationship between MFSD1 and GLMP was studied in more detail.

3.5.1 Study of MFSD1-GLMP interaction *in cellullo*

3.5.1.1 GLMP and MFSD1 co-localize in lysosomes of HeLa cells after transfection

In order to confirm the lysosomal localization of GLMP (Schieweck et al. 2009) and the specificity of the newly raised anti-GLMP antibody, mouse *GLMP* cDNA alone (GLMP) or fused to an HA coding sequence at the C-terminus (GLMP-HA) was cloned into pcDNA3.1 plasmid. HeLa cells were transfected with plasmids coding for GLMP-HA or GLMP and analysed by Western blotting using an anti-HA antibody and the newly generated anti-GLMP antibody. The results revealed that the migration pattern of GLMP and GLMP-HA in the polyacrylamide gel was similar, and several bands of approximately 70 kDa were detected in both cases (Figure 39B). HeLa cells transfected with a plasmid coding for GLMP-HA were analysed 24 hours post-transfection by immunofluorescence using anti-HA and anti-LAMP2 antibodies. The results confirmed the lysosomal localization of GLMP in HeLa cells (Figure 39B). Double transfection of HeLa cells with GLMP-HA plasmid and MFSD1 WT plasmid was performed in order to investigate whether GLMP and MFSD1 were localized in the same subcellular compartments. GLMP and MFSD1 were detected in the same LAMP2 positive vesicles after immunofluorescence analysis of the transfected cells using anti-MFSD1, anti-HA and anti-LAMP2 antibodies (Figure 39C).

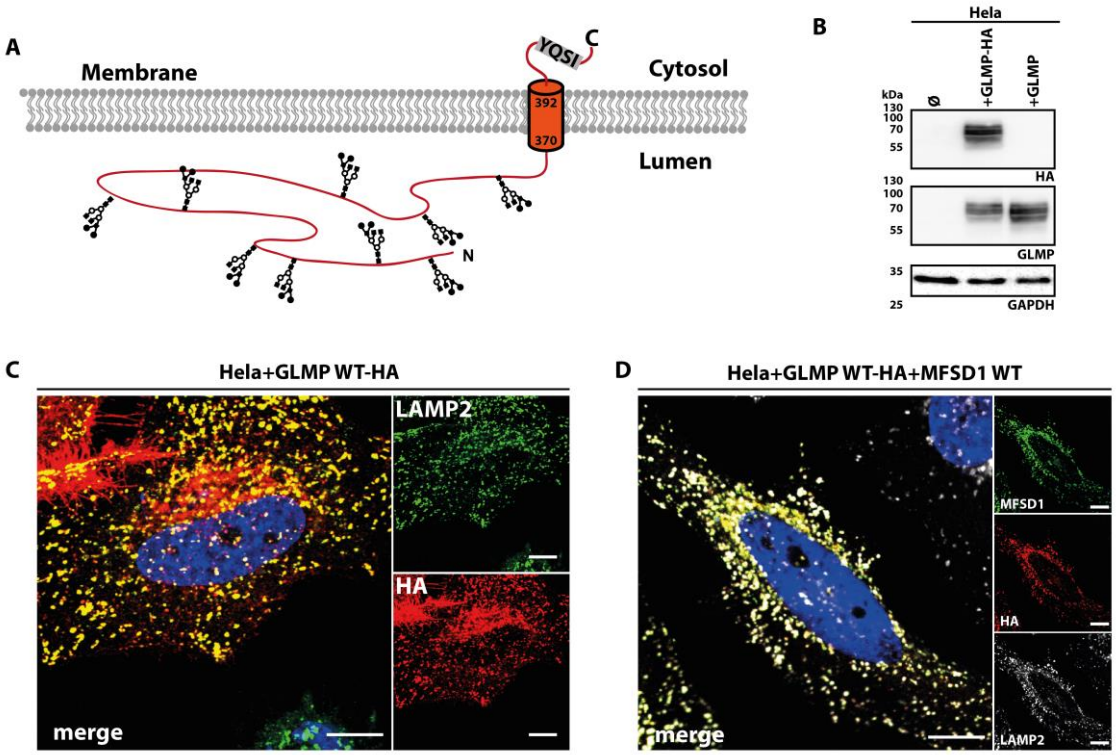

Figure 39. GLMP and MFSD1 co-localize in lysosomes. (A) Scheme of GLMP protein. (B) HeLa cells were transiently transfected with a plasmid coding for GLMP-HA or GLMP, collected 24 hours post-transfection and analysed by Western blotting using anti-HA, anti-GLMP and anti-GAPDH antibodies. (C) HeLa cells were transiently transfected with a plasmid coding for GLMP-HA, fixed 24 hours post-transfection, permeabilized and stained by indirect immunofluorescence using anti-HA and anti-LAMP2 antibodies. (D) HeLa cells were transiently transfected with plasmids coding for GLMP-HA and MFSD1 WT, fixed 24 hours post-transfection, permeabilized and stained by indirect immunofluorescence using anti-HA, anti-MFSD1 and anti-LAMP2 antibodies. Scale bars, 10 µm.

3.5.1.2 MFSD1 deficiency in MEFs leads to dramatic decrease of GLMP levels and *vice-versa*

After having confirmed the co-localization of GLMP with MFSD1 in lysosomes after overexpression, the endogenous levels of GLMP in MFSD1$^{tm1a/tm1a}$ MEFs and the endogenous MFSD1 levels in GLMP deficient MEFs (GLMP$^{gt/gt}$ MEFs, kindly provided by Winnie Eskild (University of Oslo)) were analysed by Western blotting using the anti-GLMP antibody. MFSD1$^{wt/wt}$, MFSD1$^{tm1a/tm1a}$ and GLMP$^{gt/gt}$ MEFs were collected and the membrane proteins were separated from soluble proteins using ultracentrifugation. The membrane proteins were further analysed by Western blotting using the anti-MFSD1 antibody, the anti-GLMP antibody and an anti-Na^+/K^+ATPase antibody as a loading control for membrane fractions. The results confirmed the complete absence of MFSD1 in MFSD1$^{tm1a/tm1a}$ MEFs and the complete absence of GLMP in GLMP$^{gt/gt}$ MEFs (Figure 40AI). In accordance with the proteomics results obtained in liver lysosomes (Figure 38), GLMP was not detected in MFSD1$^{tm1a/tm1a}$ MEFs. Unfortunately,

the newly generated anti-GLMP antibody did not detect endogenous GLMP in MEF cells by immunofluorescence analysis. MFSD1 levels were decreased in GLMP$^{gt/gt}$ MEFs to less than 20% of the levels found in MFSD1$^{wt/wt}$ MEFs (Figure 40AI and II).

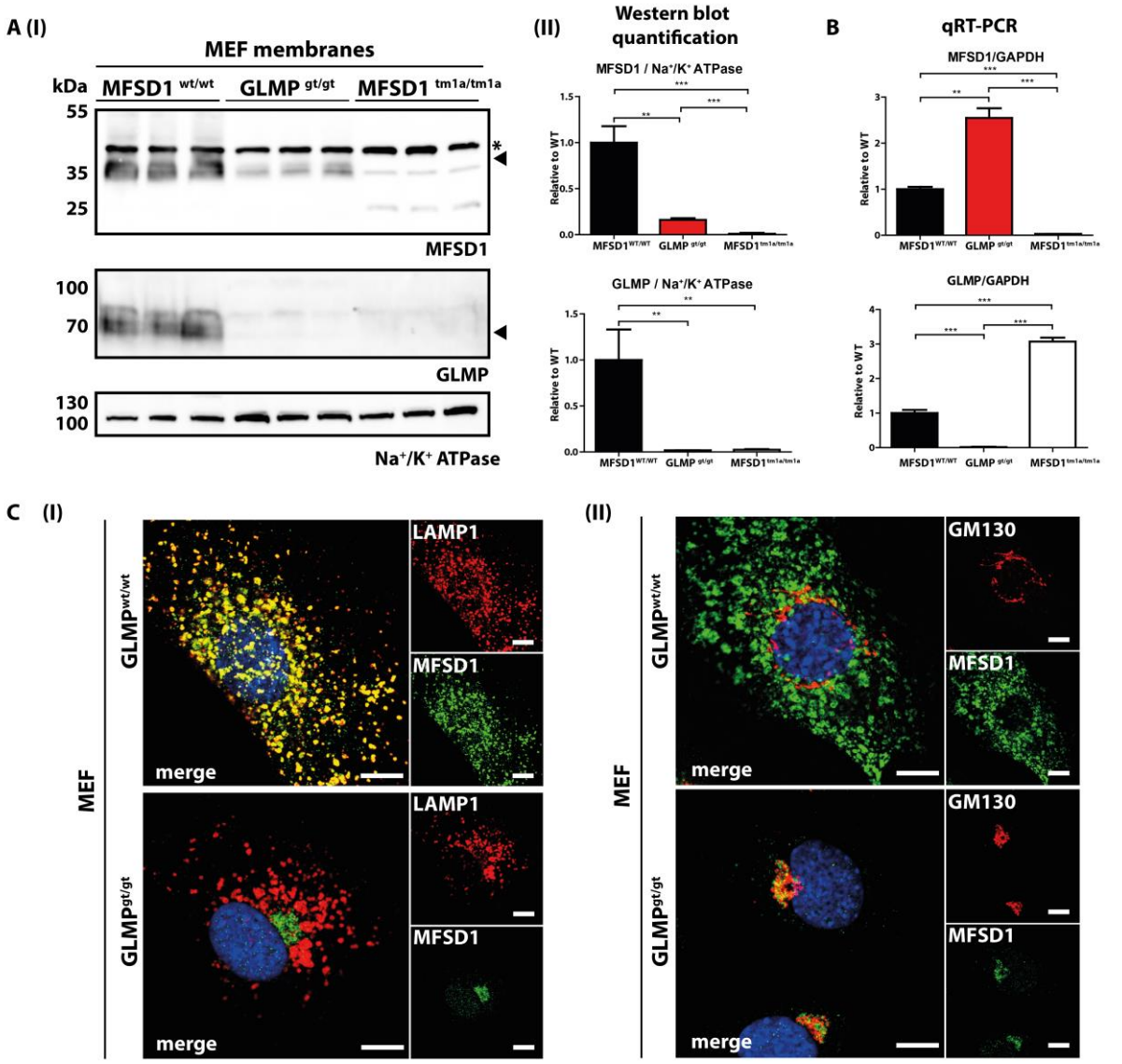

Figure 40. Residual levels of MFSD1 are found in the Golgi apparatus of GLMP$^{gt/gt}$ MEFs. (A) MFSD1$^{wt/wt}$, MFSD1$^{tm1a/tm1a}$ and GLMP$^{gt/gt}$ MEFs were collected and the membrane proteins were separated from the soluble proteins using ultracentrifugation. Triplicates of the membrane proteins were analysed by Western blotting with anti-MFSD1 antibody, anti-GLMP antibody and anti-Na^+/K^+-ATPase as a loading control for membrane fractions (I), and the signals were quantified (II). (B) MFSD1$^{wt/wt}$, MFSD1$^{tm1a/tm1a}$ and GLMP$^{gt/gt}$ MEFs were collected, the total RNA was extracted and reverse transcribed to cDNA, which afterwards was used to analyse the transcripts levels of *MFSD1* and *GLMP* genes by qRT-PCR. (C) GLMP$^{wt/wt}$ and GLMP$^{gt/gt}$ MEFs were fixed, permeabilized and stained by indirect immunofluorescence using anti-MFSD1 and anti-LAMP1 antibodies (I) or anti-MFSD1 and anti-GM130 antibodies (II). Scale bars, 10 µm.

In order to investigate whether the decrease of MFSD1 and GLMP levels in GLMP$^{gt/gt}$ and MFSD1$^{tm1a/tm1a}$ MEFs, respectively, was due to decreased mRNA levels, qRT-PCR analysis of

MFSD1 and GLMP mRNA in MFSD1$^{wt/wt}$, MFSD1$^{tm1a/tm1a}$ and GLMP$^{gt/gt}$ MEFs was performed. In contrast to the protein levels, the MFSD1 mRNA levels in GLMP$^{gt/gt}$ MEFs were increased more than two-fold in comparison to the levels detected in MFSD1$^{wt/wt}$ MEFs, while the GLMP mRNA levels in MFSD1$^{tm1a/tm1a}$ MEFs were increased three-fold compared to the mRNA levels detected in MFSD1$^{wt/wt}$ MEFs (Figure 40B). The increased levels of MFSD1 mRNA and GLMP mRNA found in GLMP$^{gt/gt}$ MEFs and MFSD1$^{tm1a/tm1a}$ MEFs, respectively, could be interpreted as an attempt of the cells to compensate the low protein levels of the correspondent proteins.
Since GLMP was absent in liver lysosomes of MFSD1$^{tm1a/tm1a}$ mice (Figure 38), the subcellular localization of MFSD1 in GLMP$^{gt/gt}$ MEFs was investigated by immunofluorescence. The immunostaining analysis of GLMP$^{wt/wt}$ and GLMP$^{gt/gt}$ MEFs using anti-MFSD1 and anti-LAMP1 antibodies revealed that while MFSD1 was localized in lysosomes of GLMP$^{wt/wt}$ MEFs, the remaining MFSD1-protein did not co-localize with LAMP1 positive lysosomes in GLMP$^{gt/gt}$ MEFs (Figure 40CI). The co-immunostaining of GLMP$^{wt/wt}$ and GLMP$^{gt/gt}$ MEFs using anti-MFSD1 antibody and an antibody recognizing the Golgi apparatus-marker GM130 demonstrated that MFSD1 was localized in the Golgi apparatus of GLMP$^{gt/gt}$ MEFs, while no co-localization of MFSD1 with GM130 was observed in GLMP$^{wt/wt}$ MEFs (Figure 40CII).

3.5.1.3 Transfection of GLMP into GLMP$^{gt/gt}$ MEFs rescues lysosomal MFSD1

In order to rule out the possibility that the lack of MFSD1 in the lysosome of GLMP$^{gt/gt}$ MEFs was due to clonal differences of MEF cells, a plasmid containing GLMP-HA or a plasmid containing LAMP1-HA, another highly glycosylated lysosomal membrane protein, as a negative control, were transfected into GLMP$^{gt/gt}$ MEFs and analysed by immunofluorescence 48 hours post-transfection using anti-MFSD1, anti-HA and anti-LAMP1 antibodies. The results revealed that the reintroduction of GLMP-HA into GLMP$^{gt/gt}$ MEFs rescued the localization of MFSD1 in lysosomes, while the transfection with LAMP1-HA, did not change the localization of MFSD1 in GLMP$^{gt/gt}$ MEFs (Figure 41).

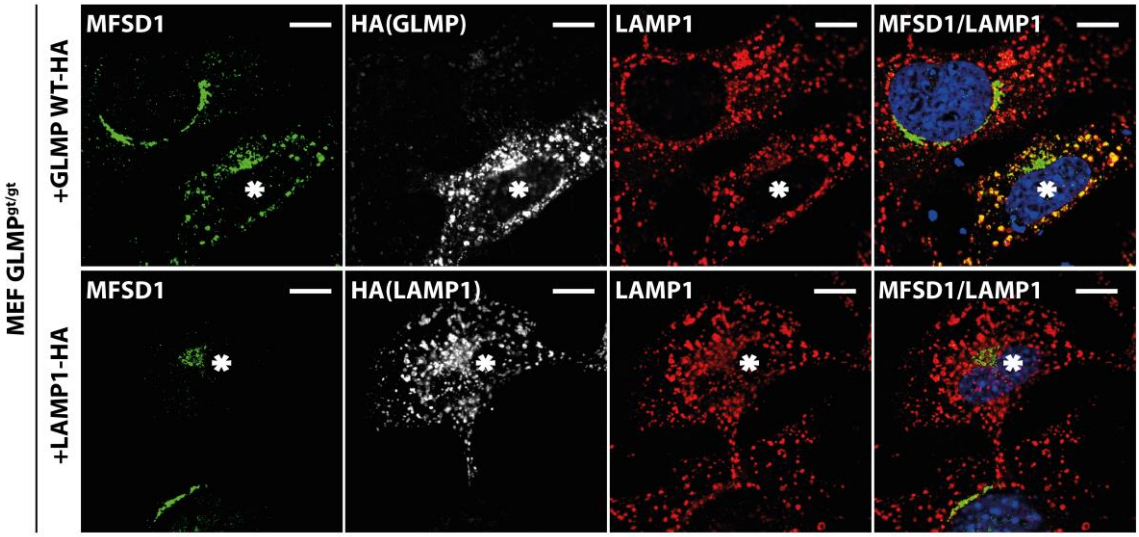

Figure 41. Transfection of GLMP-HA into GLMP deficient MEFs rescues MFSD1 at the lysosome. GLMP$^{gt/gt}$ MEFs cells were transiently transfected with a plasmid coding for GLMP-HA or a plasmid coding for LAMP1-HA, fixed 48 hours post-transfection, permeabilized and stained by indirect immunofluorescence using anti-MFSD1, anti-HA and anti-LAMP1 antibodies. White asterisks show the transfected cells. Scale bars, 10 µm.

3.5.1.4 MFSD1 and GLMP interact directly

The previous experiments raised the question whether the rescue of the lysosomal localization of MFSD1 in GLMP$^{gt/gt}$ MEFs after the reintroduction of GLMP involved a direct physical interaction between GLMP and MFSD1. In order to answer that question, a possible interaction between GLMP and MFSD1 was analysed by a co-immunoprecipitation assay.

The detergent used for the solubilization of membranes can irreversibly denature the membrane proteins and can affect their function, like the interaction with other proteins (Garavito and Ferguson-Miller 2001). Nonionic and zwitterionic detergents are able to solubilize membrane proteins with retention of function (Kalipatnapu and Chattopadhyay 2005). Therefore, co-immunoprecipitation assays were performed using several non-ionic detergents (Brij35, BrijS20, Brij96 and Triton X-100) and a zwitterionic detergent (CHAPS) for solubilizing the membranes of HeLa cells after transfection with plasmids coding for MFSD1 and GLMP-HA. Anti-MFSD1 antibody was used to immunoprecipitate MFSD1, and afterwards the immunoprecipitates were analysed by Western blotting with an anti-HA antibody.

The results revealed that GLMP was co-immunoprecipitated with MFSD1 after solubilization of the samples with the zwitterionic detergent CHAPS, but not after solubilization with the non-ionic detergents Brij35, BrijS20, Brij96 or Triton X-100 (Figure 42A). GLMP-HA was also

co-immunoprecipitated with MFSD1 when solubilizing the membranes with the non-ionic detergent Brij78, but it was not co-immunoprecipitated when solubilizing the samples with the zwitterionic detergent Fos-choline-12 (data not shown).

In order to test whether the interaction between MFSD1 and GLMP was specific, co-immunoprecipitation assays using CHAPS as solubilizing detergent were performed with HeLa cells transfected with plasmids coding for MFSD1 and GLMP-HA and immunoprecipitating the samples with the anti-MFSD1 antibody raised in rabbit or an antibody raised in rabbit against PLD3, an unrelated lysosomal membrane protein. Additionally, HeLa cells were transfected with plasmids coding for MFSD1 and LAMP1-HA and were immunoprecipitated with the anti-MFSD1 antibody. The immunoprecipitates were analysed by Western blotting using the anti-HA antibody, revealing that GLMP-HA was co-immunoprecipitated with MFSD1 while LAMP1-HA was not co-immunoprecipitated with MFSD1 (Figure 42B).

Lysates of HeLa cells transfected with plasmids coding for MFSD1 and GLMP-HA were used for immunoprecipitation using an anti-HA antibody. Surprisingly, MFSD1 was not detected in the immunoprecipitate after analysis by Western blotting using the anti-MFSD1 antibody (data

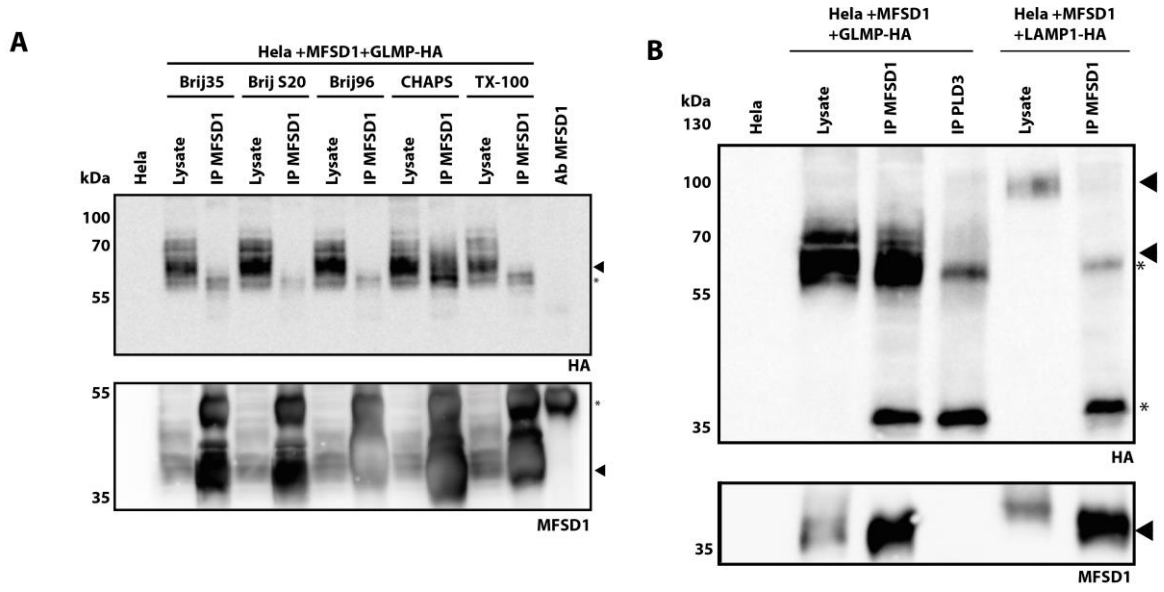

Figure 42. GLMP-HA is co-immunoprecipitated with MFSD1 after solubilisation of the membranes with CHAPS.
(A) HeLa cells were transiently transfected with plasmids coding for MFSD1 and GLMP-HA, collected 24 hours after transfection, solubilized with the mentioned detergents, immunoprecipitated using the anti-MFSD1 antibody and analysed by Western blotting using an anti-HA antibody. (B) HeLa cells were transiently transfected with plasmids coding for MFSD1 and GLMP-HA or LAMP1-HA, collected 24 hours after transfection, solubilized with CHAPS, immunoprecipitated using the anti-MFSD1 or an antibody against PLD3, an unrelated lysosomal protein, and analysed by Western blotting using an anti-HA antibody.

not shown). The explanation for the detection of MFSD1-GLMP interaction in only one direction is not fully understood and will be a matter of discussion. However, the results indicate that MFSD1 and GLMP-HA specifically interact, and demonstrate how critical the detergent used for the solubilization of the samples is in order to preserve the interaction between the two proteins.

3.5.1.5 MFSD1 can reach lysosomes in the absence of GLMP and *vice-versa*

The previous results suggest that GLMP and MFSD1 physically interact. They also revealed that GLMP protein levels are strikingly reduced in liver lysosomes in the absence of MFSD1 (Figure 38) and that MFSD1 does not localize in lysosomes in the absence of GLMP in MEFs (Figure 40C). The interaction between MFSD1 and GLMP could be necessary for the transport to the lysosome, for the stability of both proteins, for the transporter activity/function of MFSD1 or for several of these assumptions.

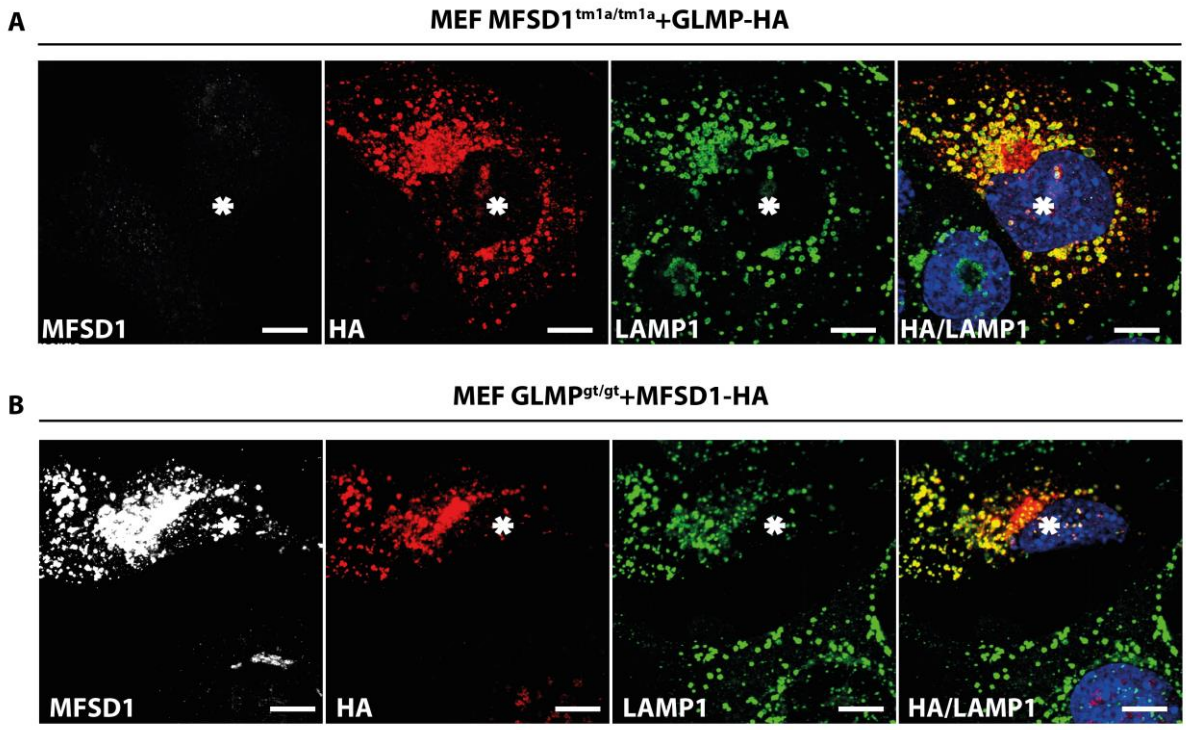

Figure 43. GLMP and MFSD1 are transported to lysosomes independent of each other. (A) MFSD1$^{tm1a/tm1a}$ MEFs were transiently transfected with a plasmid coding for GLMP-HA, fixed 24 hours after transfection, permeabilized and stained by indirect immunofluorescence using anti-MFSD1, anti-HA and anti-LAMP1 antibodies. (B) GLMP$^{gt/gt}$ MEFs cells were transiently transfected with a plasmid coding for MFSD1-HA, fixed 24 hours post-transfection, permeabilized and stained by indirect immunofluorescence using anti-MFSD1, anti-HA and anti-LAMP1 antibodies. Asterisks show transfected cells. Scale bars, 10 µm.

In order to investigate whether MFSD1 and GLMP could reach the lysosome in the absence of each other, GLMP knockout MEF cells, GLMP$^{gt/gt}$ MEFs, were transfected with a plasmid containing MFSD1-HA and MFSD1-deficient MEFs, MFSD1$^{tm1a/tm1a}$ MEFs, were transfected with a plasmid containing GLMP-HA and were evaluated by immunofluorescence using anti-MFSD1, anti-HA and anti-LAMP1 antibodies. Surprisingly, after expression of GLMP-HA in MFSD1$^{tm1a/tm1a}$ MEFs, GLMP-HA was present in lysosomes co-localizing with LAMP1 (Figure 43A), and after expression of MFSD1-HA in GLMP$^{gt/gt}$ MEFs, MFSD1-HA also co-localized with LAMP1 (Figure 43B).

These results indicate that both MFSD1 and GLMP can be transported to lysosomes even in the absence of each other, suggesting that the interaction between MFSD1 and GLMP is not essential for the transport to the lysosomes.

3.5.1.6 GLMP protects MFSD1 from lysosomal proteases in MEF cells

The interaction between GLMP and MFSD1 might be important for the stability of both proteins. The lysosomal lumen is characterized by an acidic pH between 4.5 and 5 containing high concentrations of active proteases that are responsible for the degradation of proteins (Saftig and Klumperman 2009). The great majority of lysosomal membrane proteins are glycosylated in their luminal domains, and it is thought that glycosylation plays a role in the protection against lysosomal proteases. Having demonstrated that GLMP and MFSD1 are interacting, that MFSD1 is transported to lysosomes even in the absence of GLMP, and taking in account that GLMP is a highly glycosylated protein and MFSD1 is not glycosylated, it is tempting to speculate that GLMP protects MFSD1 from proteolytic degradation in lysosomes. In order to test this hypothesis, GLMP$^{wt/wt}$ MEFs and GLMP$^{gt/gt}$ MEFs were treated with lysosomal inhibitors like Bafilomycin A1, a specific inhibitor of the vATPase and therefore, an indirect inhibitor of lysosomal proteolysis, E64D, a calpain and cathepsin inhibitor or leupeptin, a cysteine, serine and threonine peptidase inhibitor. After 24 hours of treatment, the cells were collected and analysed by Western blotting using the anti-MFSD1 and an anti-tubulin antibody as a loading control. The results revealed an increase of MFSD1 protein levels in all the samples treated with the different inhibitors, except of GLMP $^{wt/wt}$ MEFs treated with leupeptin (Figure 44A). Interestingly, MFSD1 protein levels of GLMP $^{gt/gt}$ MEFs after treatment with Bafilomycin or E64D were comparable to MFSD1 levels of untreated GLMP $^{wt/wt}$ MEFs (Figure 44B).

These results indicate that when the lysosomal proteolytic activity is inhibited in the absence of GLMP, MFSD1 levels recover to the MFSD1 levels found in WT MEFs, suggesting that MFSD1 is protected from lysosomal proteolysis by the interaction with GLMP.

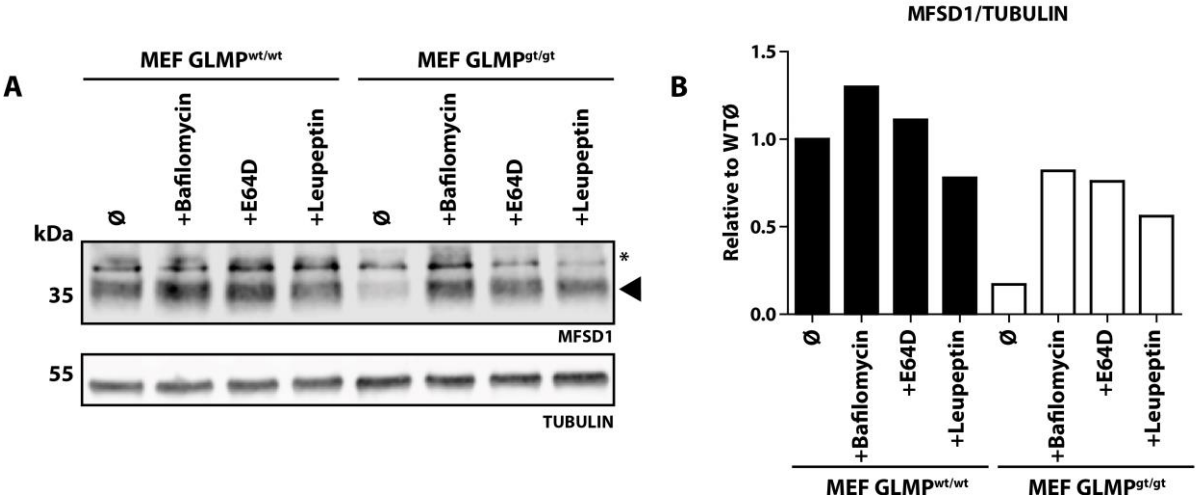

Figure 44. Inhibition of lysosomal activity in GLMP$^{gt/gt}$ MEFs leads to recovery of MFSD1 levels. (A) GLMP$^{wt/wt}$ MEFs and GLMP$^{gt/gt}$ MEFs were treated with the inhibitors of lysosomal proteolysis Bafilomycin A1 (100 nM), E64D (50 µM) or leupeptin (50 µM) for 24 hours. The cells were collected and the lysates were analysed by Western blotting using anti-MFSD1 and anti-TUBULIN antibodies. (B) The intensity of the MFSD1 signal was quantified. The results are shown relative to the untreated WT sample.

3.5.1.7 The luminal domain of GLMP is sufficient to rescue MFSD1 at lysosomes of GLMP$^{gt/gt}$ MEFs

To this end, the results have demonstrated that MFSD1 and GLMP are interaction partners and that GLMP is protecting MFSD1 from lysosomal degradation in MEFs. In order to investigate which GLMP domain/s are involved in the rescue of MFSD1 expression in lysosomes in GLMP$^{gt/gt}$ MEFs, cDNA chimeras of GLMP and LAMP1 were generated combining the three domains (cytosolic, transmembrane and luminal) of both proteins.

Both GLMP and LAMP1 are lysosomal type I transmembrane proteins, whose structure is defined by a large glycosylated luminal domain, a transmembrane domain and a short cytosolic C- terminus. Chimeras exchanging each of GLMPs domains by the same domain (luminal, transmembrane or cytosolic) of LAMP1 were designed. The cDNA of the six chimera was cloned and fused to a HA coding sequence at the C-terminus (Figure 45A) into a pcDNA3.1 plasmid by Lea Kählau (Bachelor thesis, 2016). The overexpression of the constructs in MEF cells and the analysis of the lysates by Western blotting using an anti-HA antibody revealed that the chimeric proteins were expressed, and a difference of molecular weight between the chimeras containing the luminal domain of LAMP1, LGG, LGL and LLG, and the chimeras

containing the luminal domain of GLMP, GGL, GLG, and GLL, was observed (Figure 45B). The difference of the molecular weight corresponds to the higher glycosylation of LAMP1 luminal domain compared to GLMP. Immunofluorescence analysis of GLMP$^{gt/gt}$ MEFs 48 hours after

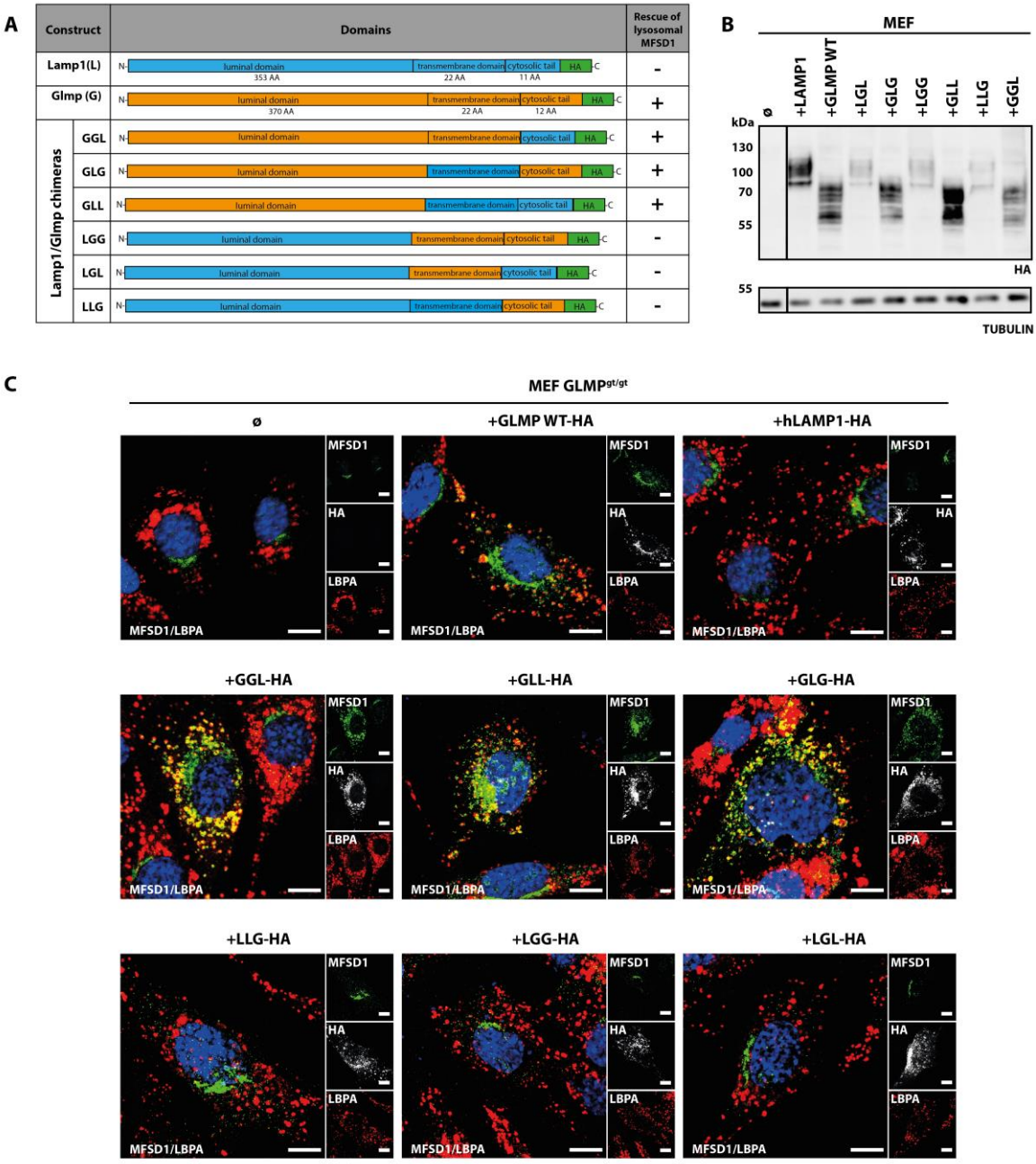

Figure 45. The luminal domain of GLMP is sufficient to rescue MFSD1 at the lysosome of GLMP $^{gt/gt}$ MEFs. (A) Scheme of GLMP, LAMP1 and the six GLMP-LAMP1 chimeras generated. (B) MEF cells were transiently transfected with plasmids coding for the constructs depicted in (A), harvested 24 hours post-transfection and analysed by Western blotting using anti-HA and anti-TUBULIN antibodies. (C) GLMP $^{gt/gt}$ MEFs were transfected with plasmids coding for GLMP-HA, LAMP1-HA or one of the six GLMP-LAMP1 chimeras. The cells were fixed 48 hours post-transfection, permeabilized and analysed by immunofluorescence with anti-MFSD1, anti-HA and anti-LBPA antibodies. Scale bars, 10 µm.

transfection with plasmids coding for either GLMP-HA, LAMP1-HA or one of the six different GLMP-LAMP1 chimeras using anti-MFSD1, anti-HA and anti-LBPA antibodies revealed that all the chimeras were localized in LBPA positive vesicles, corresponding to late endosomes (Kobayashi et al., 1998). The results also revealed that the transfection of GLMP$^{gt/gt}$ MEFs with plasmids coding for GGL-HA, GLG-HA and GLL-HA, the three chimeras containing the GLMP luminal domain, were sufficient to rescue the lysosomal localization of MFSD1 in GLMP$^{gt/gt}$ MEFs.

In contrast, the transfection of GLMP$^{gt/gt}$ MEFs with the constructs containing the luminal part of LAMP1-HA, LGG-HA, LGL-HA and LLG-HA, was not able to rescue the localization and expression of MFSD1 in lysosomes (Figure 45C). Altogether, these results indicate that the highly glycosylated luminal domain of GLMP is essential and sufficient to rescue the expression of MFSD1 in lysosomes of GLMP$^{gt/gt}$ MEFs. They also suggest that the luminal domain of GLMP interacts with MFSD1, and that the glycosylation of GLMP luminal domain protects MFSD1 from the lysosomal proteases.

To further investigate the role of GLMP glycosylation in the protection of MFSD1, a plasmid containing GLMP cDNA with the nine asparagine residues possibly being glycosylated mutated to alanine was generated and used to transfect GLMP$^{gt/gt}$ MEFs. Non-glycosylated GLMP was not detected in lysosomes but in the ER, most likely due to improper folding (data not shown). A scheme of the hypothetical interaction between MFSD1 and GLMP is shown in Figure 46. It should be noted that the stoichiometry MFSD1:GLMP might be other than 1:1.

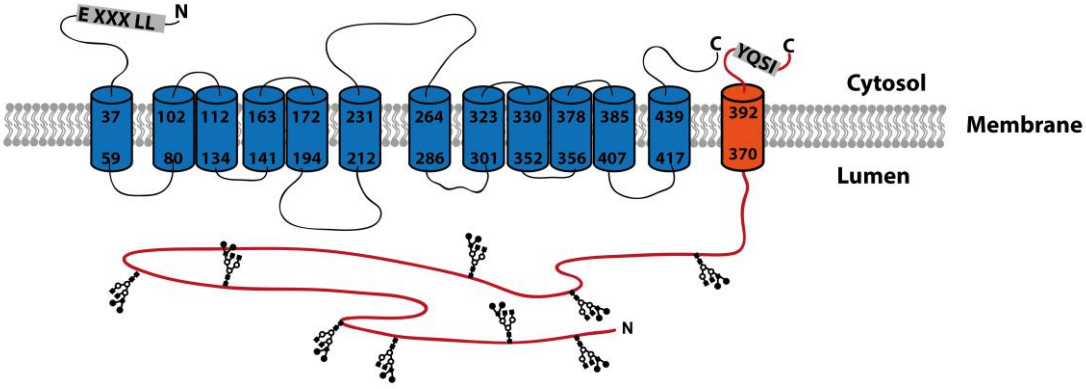

Figure 46. Scheme of the possible interaction between MFSD1 and GLMP.

3.5.1.8 The MFSD1-GLMP interaction rescues the lysosomal localization of GLMP Y400A and MFSD1 LL/AA

The interaction between a lysosomal protein and its interaction partner can be necessary for the co-transport of both proteins to the lysosome. This is the case for Clc-7, a lysosomal chloride transporter, and OSTM1, its β subunit. The transient transfection of fibroblasts with Ostm1 lead to an ER-like distribution, while if Ostm1 was co-transfected with Clc-7, the staining pattern of Ostm1 was observed in lysosomes (Lange et al. 2006). MFSD1 and GLMP have lysosomal transport motifs, dileucine based and tyrosine based, respectively, that allow them to reach the lysosome independent of the interaction partner (see 3.5.1.5). Given the interaction between MFSD1 and GLMP, I decided to investigate whether the interaction of the cell surface mutants MFSD1 LL/AA and GLMP Y400A with GLMP or MFSD1, respectively, would rescue the lysosomal localization of MFSD1 LL/AA and GLMP Y400A.

In order to answer this question, the tyrosine of the previously described lysosomal targeting motif of GLMP (Schieweck et al. 2009) was mutated into an alanine in a plasmid containing GLMP with an HA tag at the C-terminus (GLMPY400A-HA). The immunofluorescence analysis of MEF cells after transfection with GLMPY400A-HA using the anti-HA antibody and an anti-CD63 antibody, a late endosome/lysosomal marker, revealed little co-localization of GLMPY400A-HA with CD63 positive vesicles. In contrast to the ER localization of GLMPY400A described previously (Schieweck et al. 2009) the majority of GLMPY400A-HA was localized at the cell surface (Figure 47A). Interestingly, the co-transfection of GLMPY400A-HA with MFSD1-GFP revealed the co-localization of GLMPY400A-HA with the late/endosome lysosome marker CD63, while it was absent at the cell surface. This result indicates that the mutation of the tyrosine based sorting motif of GLMP leads to a plasma membrane localization, and that the co-transfection with MFSD1 can overcome the missorting of GLMP Y400A to the plasma membrane.

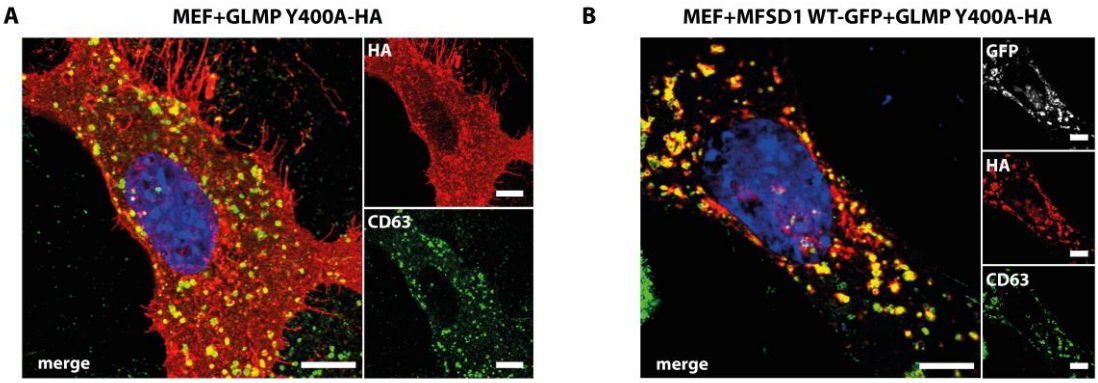

Figure 47. Co-transfection of MFSD1 restores the lysosomal localization of the plasma membrane localized mutant GLMPY400A. (A) MEF cells were transiently transfected with a plasmid coding for GLMPY400A-HA, fixed 24 hours post-transfection, permeabilized and analysed by immunofluorescence with anti-HA and anti-CD63 antibodies. (B) MEF cells were transiently transfected with plasmids coding for GLMPY400A-HA and MFSD1-GFP, fixed 24 hours post-transfection, permeabilized and analysed by immunofluorescence with anti-HA and anti-CD63 antibodies. Scale bars, 10 µm.

The mutation of two leucines to alanines from the lysosomal transport motif of MFSD1 leads to the missorting of MFSD1 LL/AA-GFP to the plasma membrane (Figure 48A). The analysis of MEFs co-transfected with MFSD1 LL/AA-GFP and GLMP-HA after staining with anti-HA and anti-CD63 antibodies revealed that MFSD1 was partially co-localizing with CD63 positive cells. However, MFSD1 was still present at the plasma membrane (Figure 48B).

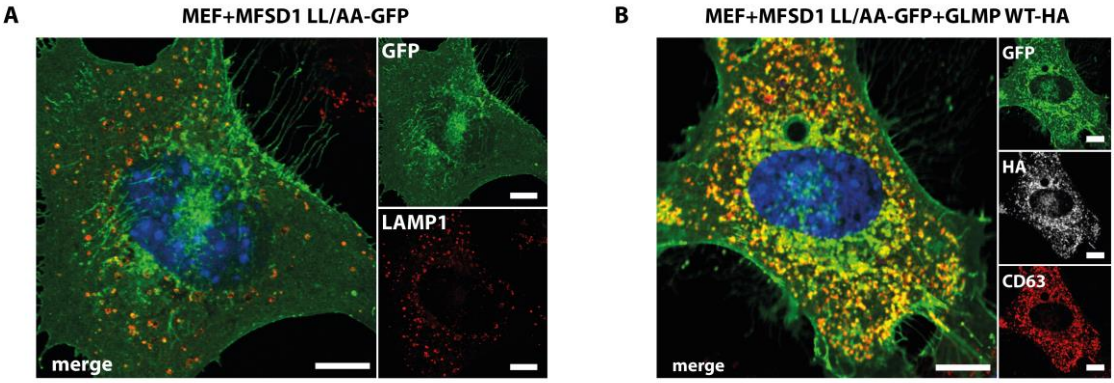

Figure 48. MFSD1 LL/AA is redirected to the lysosome when co-expressed with GLMP. (A) MEF cells were transiently transfected with a plasmid coding for MFSD1 LL/AA-HA, fixed 24 hours post-transfection, permeabilized and analysed by immunofluorescence with anti-LAMP2 antibody. (B) MEF cells were transiently transfected with plasmids coding for MFSD1 LL/AA-GFP and GLMP-HA, fixed 24 hours post-transfection, permeabilized and analysed by immunofluorescence with anti-HA and anti-CD63 antibodies. Scale bars, 10 µm.

Despite the clear partial co-localization of MFSD1 LL/AA with CD63 after co-expression with GLMP in contrast to the exclusive plasma membrane localization of MFSD1 LL/AA after single transfection, this result does not answer whether GLMP is able to redirect MFSD1 LL/AA to

the lysosome. It can be speculated that each MFSD1 molecule might interact with two or more GLMP molecules, and therefore the amount of GLMP molecules needed to redirect MFSD1 to the lysosome is limiting under overexpression conditions.

In order to obtain quantitative data, MFSD1 LL/AA TMD1-HA-TMD2 (Figure 49A) was co-expressed in HeLa cells together with GLMP or together with LAMP1 and the cell surface

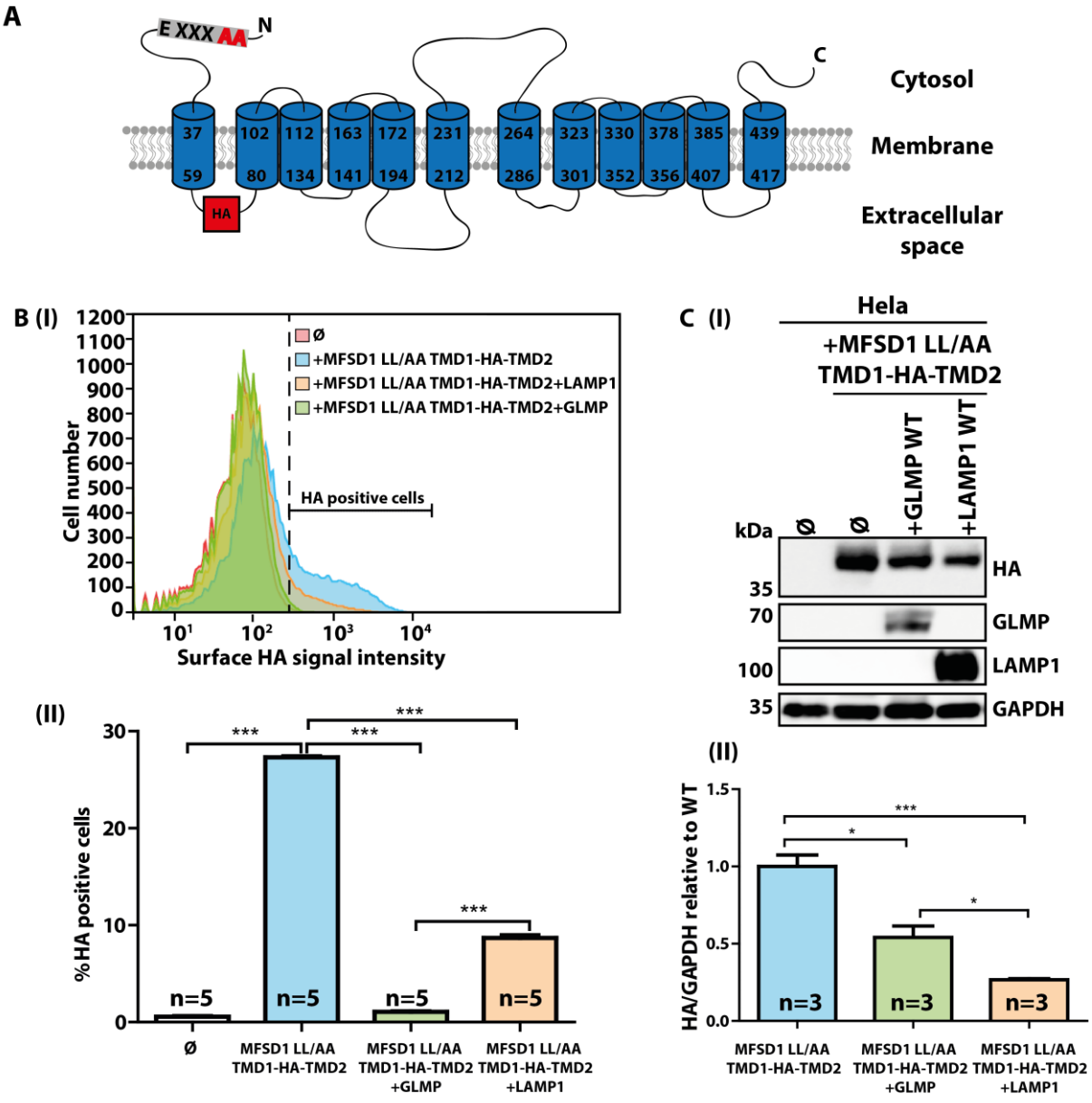

Figure 49 Mutation of the dileucine motif of MFSD1 leads to a plasma membrane localization. (A) Scheme of MFSD1 with EDRALL motif mutated into EDRAAA with an HA tag between TMD1 and TMD2. (B) HeLa cells were transfected with a plasmid coding for MFSD1 LL/AA TMD1-HA-TMD2, MFSD1 LL/AA TMD1-HA-TMD2 and GLMP or MFSD1 LL/AA TMD1-HA-TMD2 and LAMP1, collected 24 hours after transfection and analysed by flow cytometry with an HA antibody coupled to phycoerythrin (PE)(I). The percentage of HA positive cells was quantified (II) (C) HeLa cells were transiently transfected with plasmids coding for MFSD1 LL/AA TMD1-HA-TMD2, MFSD1 LL/AA TMD1-HA-TMD2 and GLMP or MFSD1 LL/AA TMD1-HA-TMD2 and LAMP1, collected 24 hours after transfection and the lysates were analysed by Western Blotting using anti-HA and anti-GAPDH antibodies (I) and the signals were quantified (II).

localization of MFSD1 was analysed by flow cytometry using an HA antibody coupled to phycoerythrin (PE). MFSD1 LL/AA TMD1-HA-TMD2 was localized in the cell surface in approximately 9% of the HeLa cells that co-expressed LAMP1 while only in 1% of the cells co-expressing GLMP (Figure 49BI,II). The expression levels of MFSD1 LL/AA TMD1-HA-TMD2 in HeLa cells after single expression or co-expression with GLMP or LAMP1 were analysed by Western blotting using anti-HA and anti-GAPDH antibodies. The results revealed that when MFSD1 LL/AA TMD1-HA-TMD2 was co-expressed with LAMP1, MFSD1 LL/AA TMD1-HA-TMD2 protein levels were approximately 25% of the protein levels in HeLa cells single transfected with the plasmid coding for MFSD1 LL/AA TMD1-HA-TMD2 (Figure 49CI,II). This reduction in MFSD1 LL/AA TMD1-HA-TMD2 protein levels could explain the reduction in the percentage of cells with cell surface expression of MFSD1 LL/AA TMD1-HA-TMD2 when co-expressed with LAMP1 in comparison to HeLa cells single transfected with MFSD1 LL/AA TMD1-HA-TMD2.
These results show that the interaction between MFSD1 and GLMP can partially redirect GLMP Y400A or MFSD1 LL/AA to the lysosomes when co-expressed with MFSD1 and GLMP, respectively.

3.5.2 Study of MFSD1-GLMP interaction *in vivo*

After the study of the interaction between MFSD1 and GLMP in cell-based assays, the interdependence between the two proteins was investigated *in vivo*.

3.5.2.1 The highest GLMP expression in mouse tissues is in kidney

Due to the lack of an anti-GLMP antibody that recognizes GLMP at an endogenous level, the expression of GLMP in tissues has so far only been assessed at a mRNA level using Northern blot (Schieweck et al. 2009). GLMP was found to have the highest expression in kidney, lower expression in intestine, testis, brain, liver, spleen, heart and lung, and no expression in skeletal muscle (Schieweck et al. 2009). The newly generated anti-GLMP antibody was used to analyse the expression of GLMP in tissues at a protein level.
In order to validate the specificity of the newly generated anti-GLMP antibody in tissue lysates, tissue membrane proteins of $GLMP^{wt/wt}$ and $GLMP^{gt/gt}$ mice were analysed. Briefly, membrane proteins were separated from soluble proteins using ultracentrifugation, and the proteins were further analysed by Western blotting using the anti-GLMP antibody and the anti-Na^+/K^+ ATPase antibody as a loading control for membrane fractions. GLMP was detected in kidney,

liver, lung and spleen of GLMP$^{wt/wt}$ mice at an approximate molecular weight of 70kDa, while it was absent in the same organs of GLMP$^{gt/gt}$ mice, and the highest expression was found in kidney (Figure 50, arrows). No specific signal for GLMP was observed in brain and heart lysates.

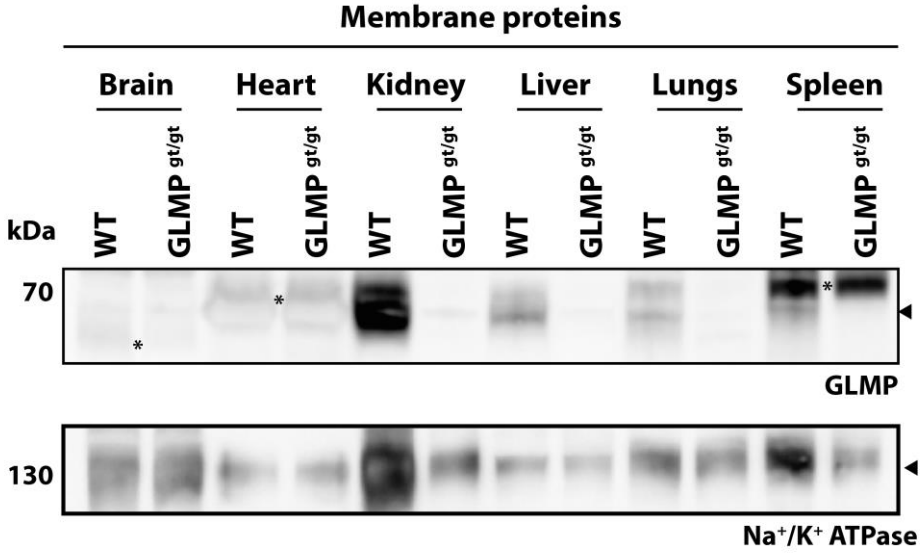

Figure 50. Highest expression of GLMP is found in kidney. The indicated tissues were collected and the membrane proteins were separated from the soluble proteins using ultracentrifugation. The membrane proteins were analysed by Western blotting with anti-GLMP antibody and anti-Na^+/K^+-ATPase as a membrane loading control.

Interestingly, the pattern of expression of GLMP through the tissues analysed resembles to the expression pattern of MFSD1, that is highest expressed in kidney, liver, lung and spleen, while low expression was detected in brain and heart (Figure 19). These results demonstrate that the newly generated anti-GLMP antibody can detect efficiently the protein in crude membrane fractions.

3.5.2.2 MFSD1 deficiency leads to strongly reduced GLMP levels in all tissues

Our data has shown that MFSD1 deficiency leads to a decrease of GLMP levels in liver lysosomes and MEF cells. The newly generated anti-GLMP antibody was used to investigate whether GLMP tissue levels were altered in the absence of MFSD1.

Tissues of MFSD1$^{wt/wt}$ and MFSD1$^{tm1a/tm1a}$ mice were collected and the membrane proteins were separated from soluble proteins using ultracentrifugation. The membrane proteins were further analysed by Western blotting using the anti-GLMP antibody, revealing that GLMP levels were strongly decreased, almost not detected, in kidney, liver, lung and spleen membrane fractions of MFSD1$^{tm1a/tm1a}$ mice (Figure 51A). In order to obtain quantitative data about how the lack or decrease of MFSD1 levels affected GLMP levels, liver membrane

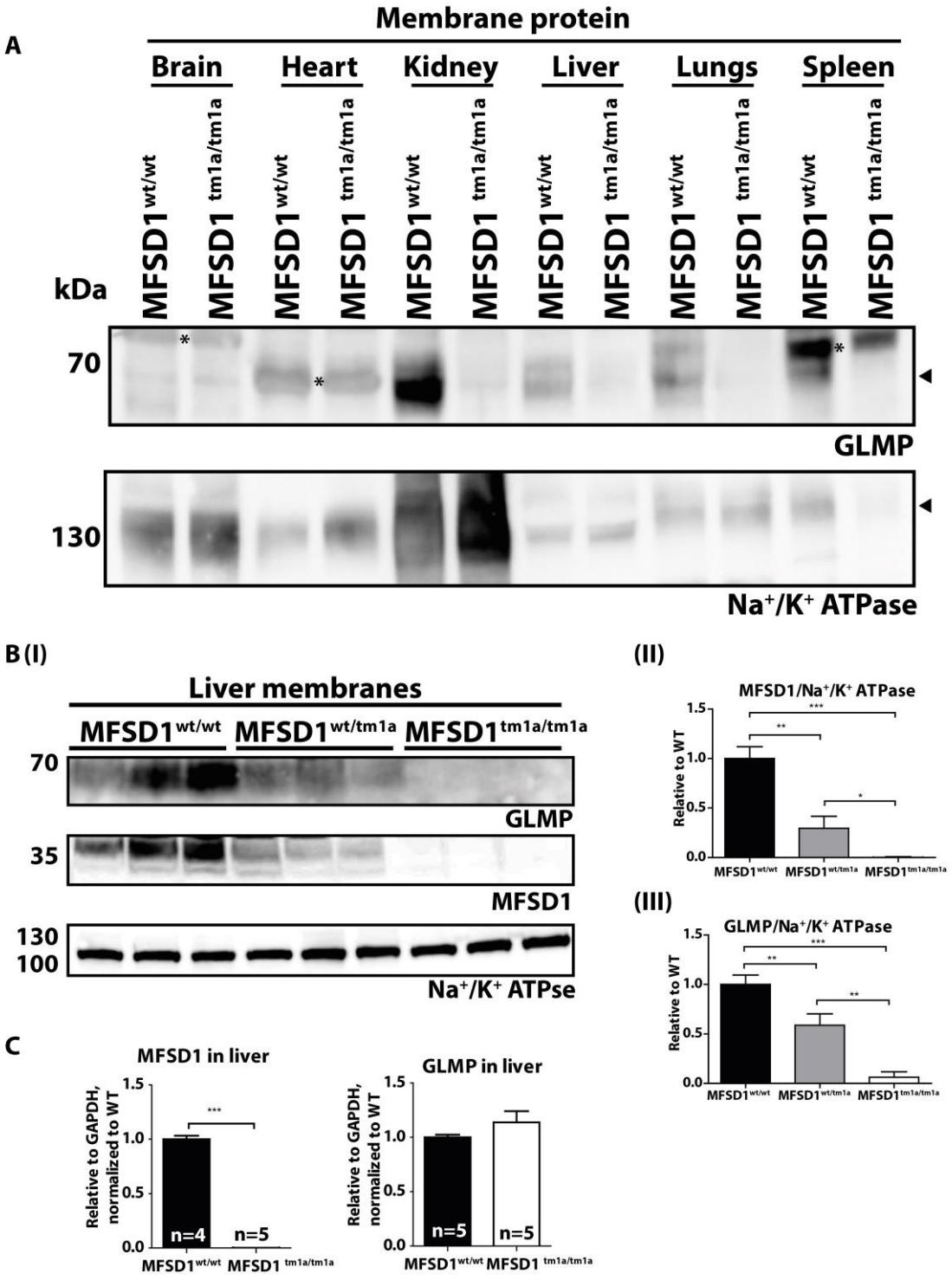

Figure 51. The deficiency of MFSD1 leads to a dramatic decrease of GLMP in all tissues. (A) The indicated tissues from MFSD1$^{wt/wt}$ and MFSD1$^{tm1a/tm1a}$ mice were collected and the membrane proteins were separated from the soluble proteins using ultracentrifugation. The membrane proteins were analysed by Western blotting with anti-GLMP antibody and anti-Na$^+$/K$^+$-ATPase antibody as a membrane loading control. (B) Liver membrane fractions from MFSD1$^{wt/wt}$, MFSD1$^{wt/tm1a}$ and MFSD1$^{tm1a/tm1a}$ mice were analysed by Western blotting with anti-GLMP, anti-MFSD1 and anti-Na$^+$/K$^+$-ATPase antibodies (I) and the signals were quantified (II and III). (C) MFSD1$^{wt/wt}$, MFSD1$^{wt/tm1a}$ and MFSD1$^{tm1a/tm1a}$ livers were collected, the total RNA was extracted and it was used to generate cDNA, which afterwards was used to analyse the transcription of *MFSD1* and *GLMP* genes by qRT-PCR. Values are given as mean±SEM. Asterisks indicate statistically significant differences between the two groups (*p<0.05; **p<0.01; ***p<0.005).

fractions of MFSD1$^{wt/wt}$, MFSD1$^{wt/tm1a}$ and MFSD1$^{tm1a/tm1a}$ mice were analysed by Western blotting using anti-GLMP, anti-MFSD1 and anti-Na^+/K^+-ATPase antibodies. The results revealed that the lack of MFSD1 in liver leads to a decrease of GLMP levels of approximately 5% of the GLMP levels found in MFSD1$^{wt/wt}$ livers (Figure 51B). Interestingly, when MFSD1 levels where decreased in MFSD1$^{wt/tm1a}$ to 30% of the MFSD1 levels found in MFSD1$^{wt/wt}$ livers, GLMP levels were also decreased in heterozygote livers to approximately 60% of the GLMP levels found in MFSD1$^{wt/wt}$ livers (Figure 51B). Finally, the mRNA levels of MFSD1$^{wt/wt}$ and MFSD1$^{tm1a/tm1a}$ livers were analysed by qRT-PCR in order to exclude that the decreased GLMP protein levels were due to a decrease in the transcription of *GLMP*, finding comparable GLMP mRNA levels in MFSD1$^{tm1a/tm1a}$ livers to MFSD1$^{wt/wt}$ livers (Figure 51C).

These results demonstrate that the deficiency of MFSD1 leads to decreased GLMP levels in the analysed tissues. The results also indicate that the decrease of MFSD1 levels also leads to decreased GLMP levels, suggesting that GLMP is stable in a complex with MFSD1, but unstable without its interaction partner.

3.5.2.3 MFSD1 levels are strongly reduced in GLMP $^{gt/gt}$ tissues

Our results have demonstrated that MFSD1 levels are decreased in the absence of GLMP in MEF cells. In order to test if the absence of GLMP was affecting MFSD1 levels *in vivo*, membrane fractions from tissues of GLMP$^{wt/wt}$ and GLMP$^{gt/gt}$ mice were analysed by western blotting using anti-MFSD1 antibody. The results revealed that the deficiency of GLMP in

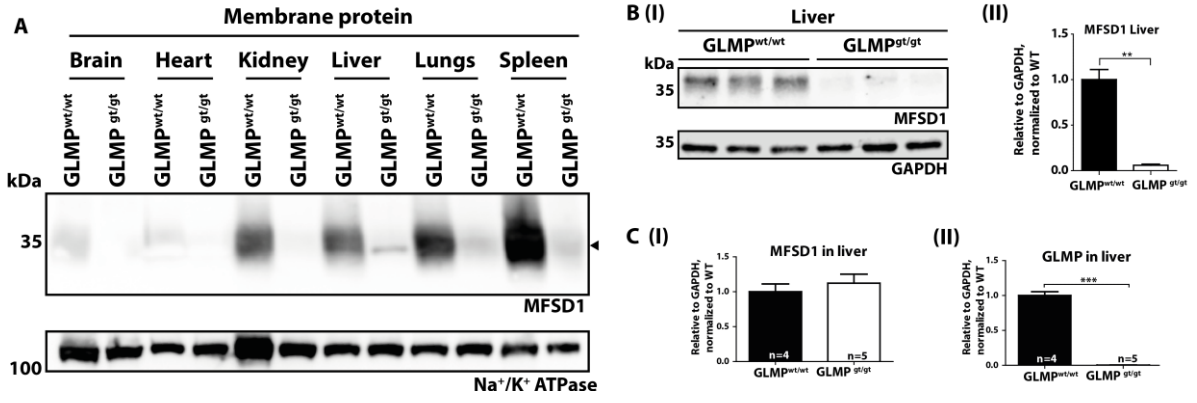

Figure 52. The deficiency of GLMP leads to a dramatic decrease of MFSD1 in all tissues. (A) The indicated tissues from GLMP$^{/wt}$ and GLMP$^{gt/gt}$ mice were collected and the membrane proteins were separated from the soluble proteins using ultracentrifugation. The membrane proteins were analysed by Western blotting with anti-MFSD1 antibody and anti-Na^+/K^+-ATPase antibody as a membrane loading control. (B) Liver lysates from GLMP$^{/wt}$ and GLMP$^{gt/gt}$ mice were analysed by Western blotting with anti-MFSD1 and anti-GAPDH antibodies (I) and the signals were quantified (II). (C) GLMP$^{/wt}$ and GLMP$^{gt/gt}$ livers were collected, the total RNA was extracted and it was used to generate cDNA, which afterwards was used to analyse the transcription of *MFSD1* and *GLMP* genes. Values are given as mean±SEM. Asterisks indicate statistically significant differences between the two groups (*p<0.05; **p<0.01; ***p<0.005).

tissues leads to decreased MFSD1 levels in all the tissues (Figure 52A). Interestingly, despite no GLMP expression was detected in brain and heart with the anti-GLMP antibody (Figure 50), MFSD1 levels were decreased in brain and heart of $GLMP^{gt/gt}$ mice compared to $GLMP^{wt/wt}$ mice (Figure 52A), suggesting that GLMP is expressed in those tissues below the limit of detection of the anti-GLMP antibody. In order to obtain quantitative data about the decrease of MFSD1 levels in the absence of GLMP, liver lysates of $GLMP^{wt/wt}$ and $GLMP^{gt/gt}$ mice were analysed by Western blotting using anti-MFSD1 and anti-GAPDH antibodies (Figure 52BI). The quantification of the signals exposed that in the absence of GLMP, MFSD1 levels in liver were reduced to approximately 5% of the MFSD1 levels found in liver of $GLMP^{wt/wt}$ mice (Figure 52BII). In order to rule out that the decreased MFSD1 protein levels found in $GLMP^{gt/gt}$ liver were due to a decrease in the transcript levels of *MFSD1,* the MFSD1 mRNA levels of $GLMP^{wt/wt}$ and $GLMP^{gt/gt}$ livers were analysed by qRT-PCR, revealing comparable MFSD1 mRNA levels in $GLMP^{wt/wt}$ liver to $GLMP^{gt/gt}$ liver (Figure 52C).

Since the deficiency of GLMP in MEF cells leads to a redistribution of MFSD1 to the Golgi apparatus, the subcellular distribution of MFSD1 in the tissues of GLMP deficient mice was investigated. Sections of kidney, liver, spleen and thymus of $GLMP^{wt/wt}$ and $GLMP^{gt/gt}$ mice were prepared and analysed by immunofluorescence using anti-MFSD1 and anti-LAMP1 antibodies. The experiments show that while MFSD1 was localized in lysosomes of kidney, liver, spleen and thymus of $GLMP^{wt/wt}$ mice, MFSD1 was below the limit of detection in the same organs of GLMP deficient mice (Figure 53).

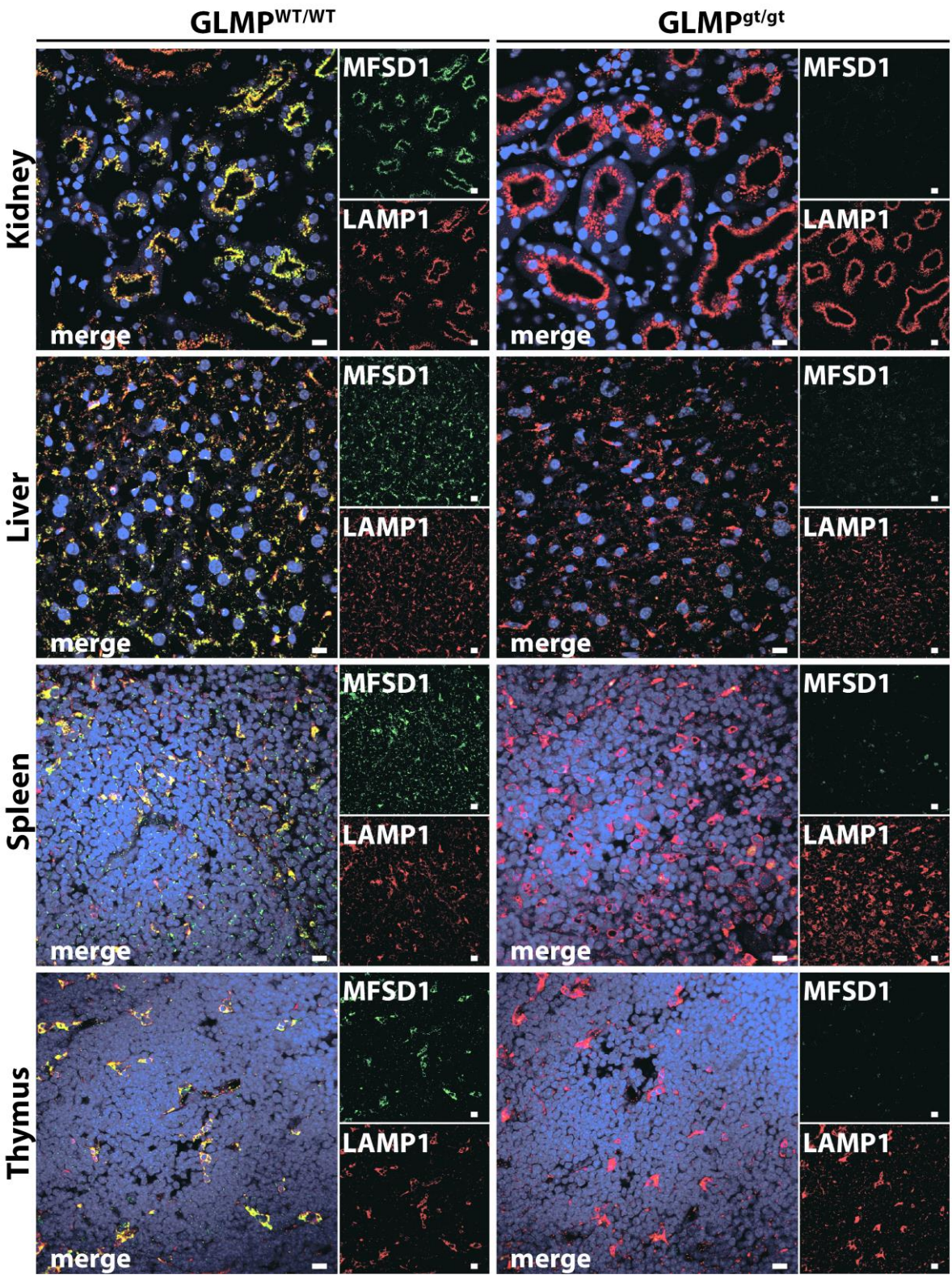

Figure 53. GLMP deficiency leads to undetectable MFSD1 levels in lysosomes of tissues. MFSD1$^{tm1a/tm1a}$ and MFSD1$^{wt/wt}$ kidney, liver, spleen and thymus sections were prepared after mice perfusion with 4% PFA and were stained with anti-MFSD1 and anti-LAMP1 antibodies. Scale bars, 10 µm.

3.5.3 Study of the GLMP KO mouse liver phenotype

The previous results showed that the absence of MFSD1 triggers the death of LSECs, which lead to a liver insult with extravasation of erythrocytes in the tissue, inflammation, neovascularization, fibrosis and finally the generation of tumors (see 3.3.2). The analysis of GLMP-deficient membrane fractions of tissues demonstrated that the lack of GLMP in all the tissues leads to a strong decrease of MFSD1 levels. Therefore, the phenotype of GLMP$^{gt/gt}$ liver from three months old mice were analysed and compared with the MFSD1$^{tm1a/tm1a}$ liver phenotype. H&E analysis of GLMP$^{gt/gt}$ liver sections displayed affected areas with sinusoidal obstruction and hepatocyte atrophy (Figure 54A, white arrow), and areas with extravasation of leukocytes and erythrocytes (Figure 54A yellow and green arrow, respectively), while no hepatocyte atrophy, leukocyte extravasation or erythrocyte extravasation was observed in GLMP$^{wt/wt}$ liver. Toluidine blue staining confirmed the extravasation of erythrocytes and the

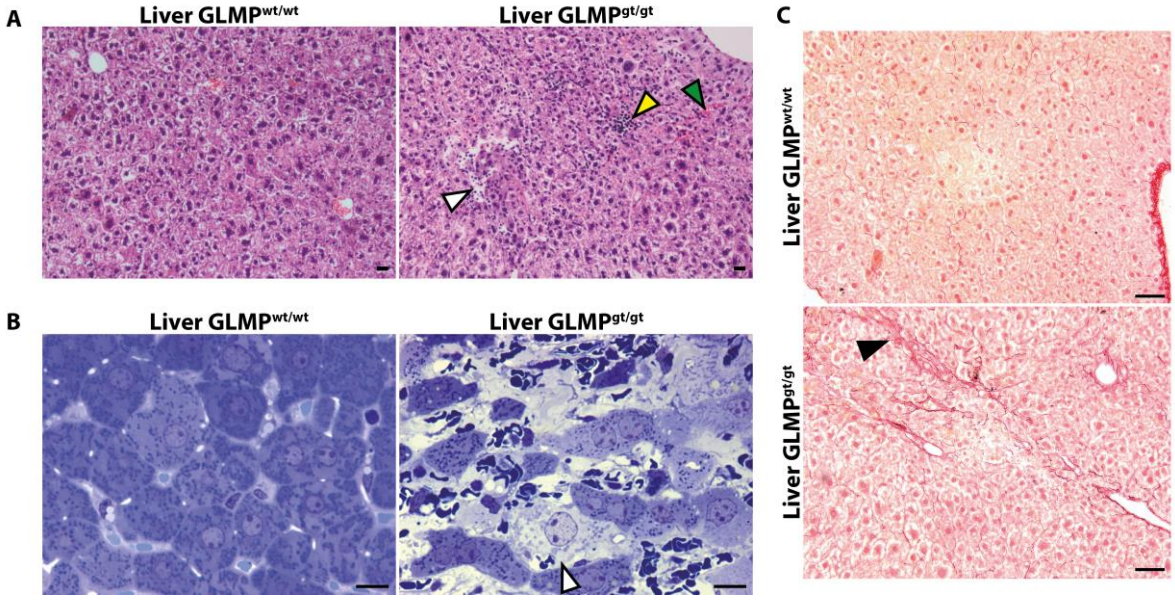

Figure 54. GLMP deficiency leads to sinusoidal obstruction and erythrocyte extravasation in liver. GLMP$^{gt/gt}$ and GLMP$^{wt/wt}$ liver sections of three months old mice were prepared after fixation with 4% PFA O/N at 4°C and were stained with haematoxylin and eosin (A), toluidine blue (B) and Sirius red (C). Scale bars (A) and (B), 10 µm; Scale bars (C), 50 µm. The stainings were performed by R. Lüllmann-Rauch and D. Niemeier.

atrophy of hepatocytes (Figure 54B, white arrow). Sirius red staining of liver sections allowed to identify the presence of fibrotic collagen fibers in liver of GLMP$^{gt/gt}$ mice (Figure 54C, black arrow), while no fibrotic collagen was observed in GLMP$^{gt/gt}$ mice liver. The analysis of proinflammatory cytokine mRNA levels by qRT-PCR revealed a significant increase of MCP1 and an increase in CXCL1 levels, that did not reach statistical significance, in GLMP$^{gt/gt}$ liver

compared to GLMP$^{wt/wt}$ liver (Figure 55C). The analysis of the transcript levels of genes involved in matrix remodeling revealed a statistically significant increase of MMP9 levels and an increase of TIMP1 and MMP2, that didn´t reach statistical significance in GLMP$^{gt/gt}$ liver compared to GLMP$^{wt/wt}$ liver but followed a similar trend (Figure 55E). qRT-PCR analysis also revealed higher levels of CD31 and CD34 mRNA in GLMP$^{gt/gt}$ liver compared to GLMP$^{wt/wt}$ liver (Figure 55D). CD31 and vWF levels in liver were also analysed by immunofluorescence, revealing an accumulation of vWF staining in the injuried areas of GLMP$^{gt/gt}$ liver and an increase of CD31 staining in GLMP$^{gt/gt}$ liver compared to GLMP$^{wt/wt}$ liver (Figure 55A), similar to the increase of vWF and CD31 staining observed in MFSD1$^{tm1a/tm1a}$ liver.

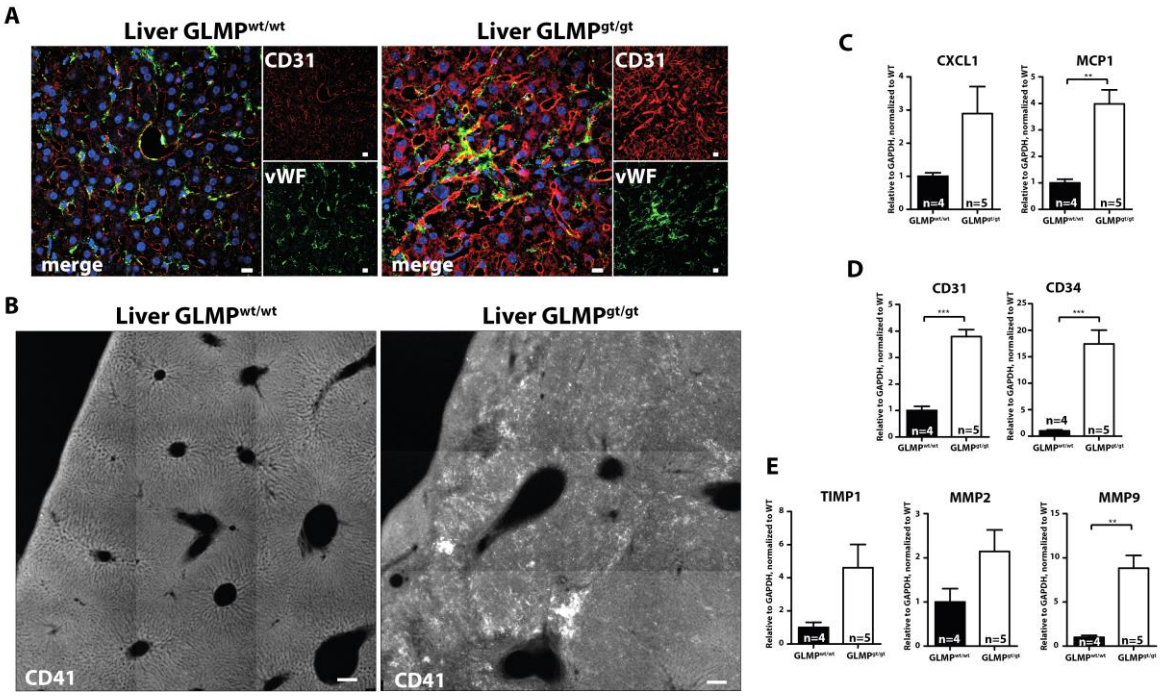

Figure 55. GLMP$^{gt/gt}$ liver suffer of inflammation and neovascularization. GLMP$^{gt/gt}$ and GLMP$^{wt/wt}$ liver sections were prepared after mice perfusion with 4% PFA and were stained with antibodies against CD31 and vWF (A) or with anti-CD41 antibody (B). (C), (D) and (E) Livers of GLMP$^{gt/gt}$ and GLMP$^{wt/wt}$ mice were collected, the total RNA was extracted and retrotranscribed to cDNA, which afterwards was used to analyse the transcript levels of the mentioned genes by qRT-PCR. Scale bars (A), 10 µm; Scale bars (B), 100 µm.

In order to analyse the recruitment of platelets to the injured areas in the liver of GLMP$^{gt/gt}$ mice, immunofluorescence staining using the anti-CD41 antibody was performed on liver sections, showing an increased staining in GLMP$^{gt/gt}$ liver compared to GLMP$^{wt/wt}$ liver (Figure 55B).

Altogether these results demonstrate the close similarity between the liver phenotype of GLMP-deficient mice and the liver phenotype of MFSD1-deficient mice.

The levels of CD41 in spleen were also analysed by immunofluorescence, revealing an increase of the CD41 staining in GLMP$^{gt/gt}$ spleen compared to GLMP$^{wt/wt}$ spleen (Figure 56A) similar to the high CD41 levels observed in MFSD1$^{tm1a/tm1a}$ spleen. The increase in CD41 staining corresponds to increased numbers of platelets and megakaryocytes. In order to investigate whether GLMP deficient mice also suffer of immunodeficiency, the immunoglobulin levels in serum were analysed in collaboration with K.Dittmann (Institute for cellular and Molecular Immunology, University of Göttingen), revealing a decrease of all the immunoglobulins analysed, IgG1, IgG2a, IgG2b, IgG3, IgA and IgM, in serum of GLMP$^{gt/gt}$ mice compared to the serum of GLMP$^{wt/wt}$ mice (Figure 56B). This result indicates that similar to MFSD1 deficient mice, GLMP deficient mice are immunodeficient.

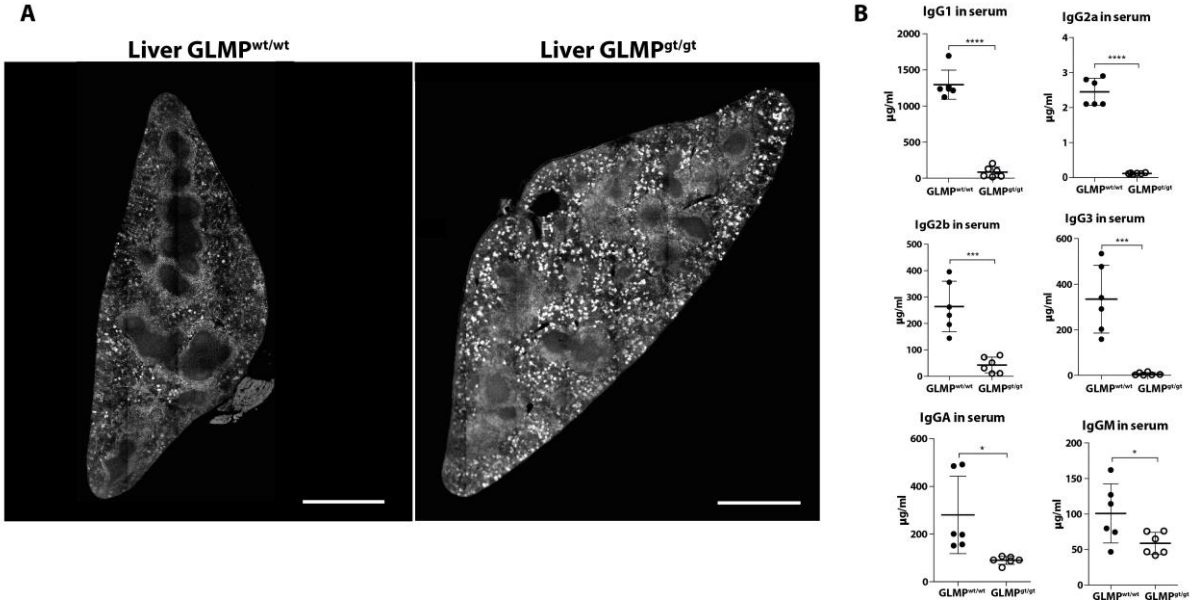

Figure 56. GLMP$^{gt/gt}$ mice have increased megakaryocytes in spleen and suffer immunodeficiency. (A) GLMP$^{gt/gt}$ and GLMP$^{wt/wt}$ spleen sections were prepared after mice perfusion with 4% PFA and were stained with an anti-CD41 antibody. (B) Serum from GLMP$^{gt/gt}$ and GLMP$^{wt/wt}$ mice was collected and the immunoglobulin levels were analysed. Scale bars, 1mm. The immunoglobulins analysis was performed by K. Dittmann (Institute for Cellular and Molecular Immunology, University of Göttingen).

3.6 Study of MFSD1 function

MFSD1 is a member of the MFS superfamily of transporters, that can transport a broad range of substrates, including amino acids (aa), small peptides, phosphate, nitrates, drugs, xenobiotics and even lipids (Law, Maloney, and Wang 2009; Nguyen et al. 2014b; Quistgaard et al. 2016; Vu et al. 2017). According to the transporter classification database (TCDB), MFSD1 is predicted to be an aa transporter that belongs to the Proteobacterial Intraphagosomal Aa

Transporter family (Pht,2.A.1.52), and has an homology with the threonine transporter, PhtA, and the valine transporter, PhtJ, of 20.4% and 21.1%, respectively.

3.6.1 MFSD1 is not an amino acid transporter

The loss of function of lysosomal transporters can lead to an accumulation of the specific substrates in lysosomes, tissues or urine. For instance, sialic acid storage disease is primarily caused by transport defects across the lysosomal membrane, that leads to increased levels of free sialic acid in tissues, fibroblasts and urine. The disease is caused by mutations in the gene coding for sialin transporter, *SLC17A5*, that affect the transport of sialic acid out of lysosomes (Valianpour et al. 2004).

In order to indirectly get a hint towards putative substrate/s transported by MFSD1, the aa levels in urine and serum of MFSD1 deficient mice were analysed in collaboration with C. Thiel (Universitätsklinikum Heidelberg). The levels of tyrosine and argininosuccinate were slightly

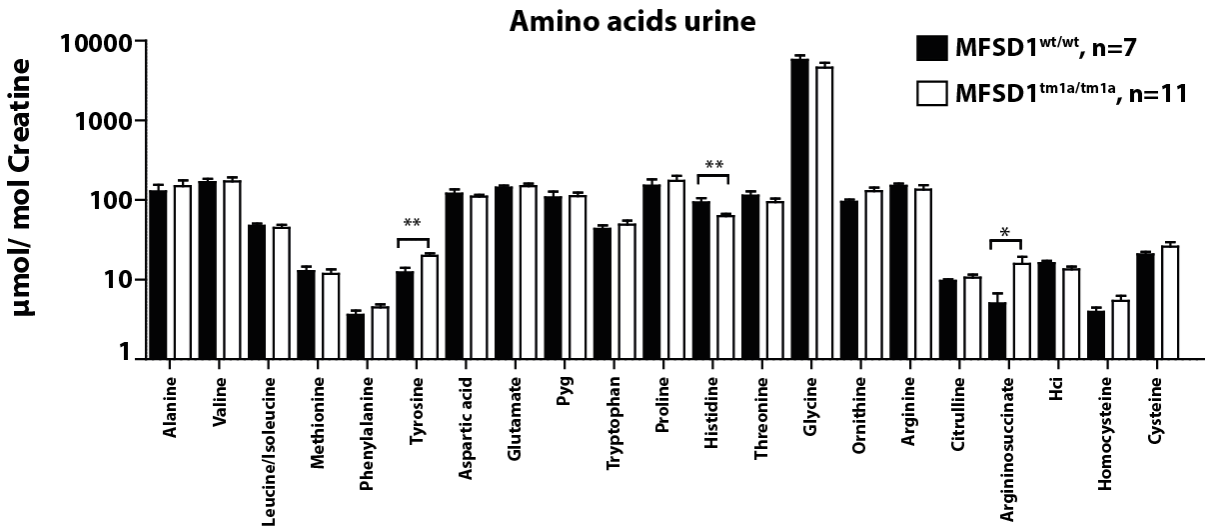

Figure 57. No major change of the aa levels in urine of MFSD1 deficient mice compared to wild type mice. The urine of MFSD1$^{tm1a/tm1a}$ and MFSD1$^{wt/wt}$ mice was collected and the aa levels were analysed by mass spectrometry. The analysis was performed by C. Thiel (Universitätsklinikum Heidelberg).

but significantly increased in urine of MFSD1$^{tm1a/tm1a}$ mice compared to MFSD1$^{wt/wt}$ mice, while the histidine levels were decreased (Figure 57). In contrast to the urine data, the analysis of the serum revealed no differences of the levels of tyrosine, argininosuccinate or histidine between MFSD1$^{tm1a/tm1a}$ mice and MFSD1$^{wt/wt}$ mice (Figure 58). In serum, the levels of glycine and citrulline of MFSD1$^{tm1a/tm1a}$ mice were increased in comparison to MFSD1$^{wt/wt}$ mice (Figure 58).

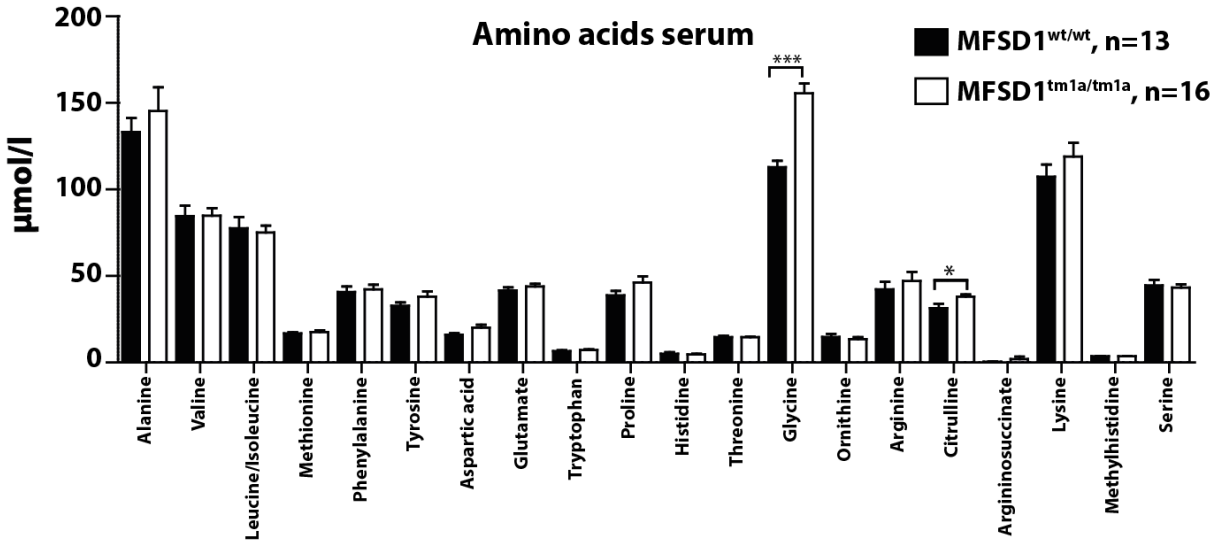

Figure 58. No major change of the aa levels in serum of MFSD1 deficient mice. The serum of MFSD1$^{tm1a/tm1a}$ and MFSD1$^{wt/wt}$ mice was collected and the aa levels were analysed by mass spectrometry. The analysis was performed by C. Thiel (Universitätsklinikum Heidelberg).

The analysis of free sialic acid levels in urine of Salla disease patients revealed that all the patients had at least a threefold higher concentration of sialic acid than the controls (Valianpour et al. 2004). The analysis of the aa concentrations in urine and serum did not reveal a hit with a difference higher than twofold between MFSD1$^{tm1a/tm1a}$ mice and MFSD1$^{wt/wt}$ mice, with the exception of argininosuccinate. In order to test more specifically whether MFSD1 was an aa transporter, an aa uptake assay using radiolabelled aa was designed.

Human embryonic kidney cells (HEKs) were transfected either with a plasmid coding for MFSD1 LL/AA, that localizes at the plasma membrane, or with a plasmid coding for LYAAT1, a lysosomal transporter that transports alanine, glycine and proline (Sagné et al. 2001), as a positive control of the experimental set up. As the subunit of lysosomal transporters can be necessary for the function of the transporter, like OSTM1 affects the chloride transport by CLC-7 (Leisle et al. 2011), HEKs cells were co-transfected with plasmids coding for MFSD1 LL/AA and GLMP Y400A-HA, that both localize at the plasma membrane. 24 hours post-transfection, radioactively labelled aa were offered in a medium with a pH=5.5 in order to mimic the acidic lysosomal lumen. After several washing steps, the cells were collected and the radiation accumulated in the cells was measured with liquid scintillation and normalized to the protein concentration (Figure 59).

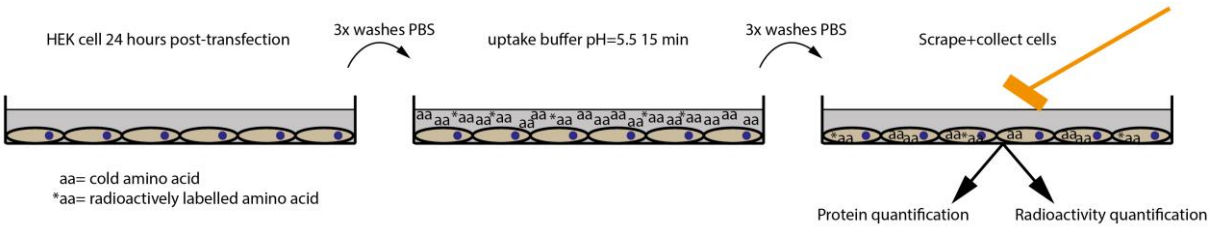

Figure 59. Scheme of radioactive amino acid uptake assay.

[^{3}H] labelled glutamine, threonine, valine, glycine and proline were analysed independently. Also an aa mix including [^{3}H] labelled alanine, arginine, aspartic acid, glutamic acid, glycine, histidine, isoleucine, leucine, lysine, phenylalanine, proline, serine, threonine, tyrosine and valine was tested. Additionally, the transport of a mix of [^{35}S] labelled cysteine and methionine was analysed.

The analysis of the [^{3}H] labelled aa mix revealed that the cells transfected with LYAAT-1 accumulated more than twofold radioactivity compared to the untransfected HEKs, indicating that LYAAT-1 transported aa from the mix into the cell. In contrast, there was no such an increase of the radioactive signal in the cells transfected either with MFSD1 LL/AA or with MFSD1 LL/AA and GLMPY400A-HA compared to the untransfected cells (Figure 60).

As a positive control for the uptake of a single radiolabelled aa by HEKs overexpressing a known transporter, the import of [^{3}H] labelled proline by HEKs transfected with a plasmid coding for LYAAT-1 was analysed. The results revealed a sevenfold increase in the cells transfected with LYAAT-1 compared to untransfected HEKs (Figure 60A).

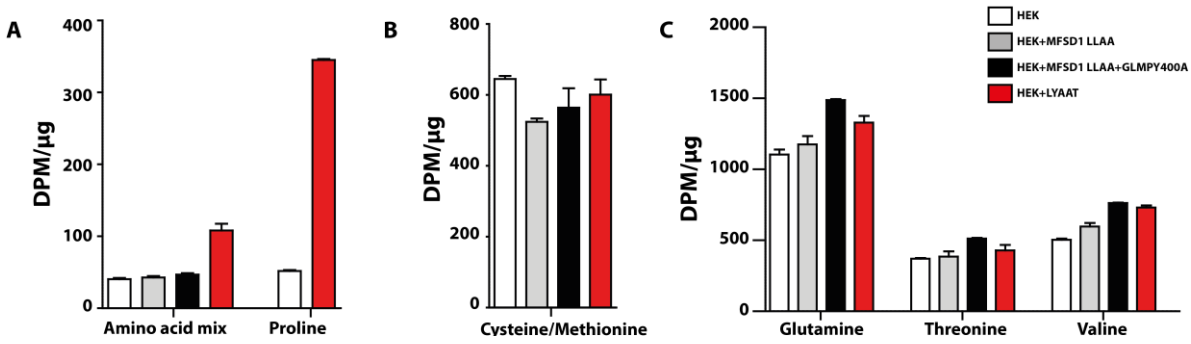

Figure 60. No aa transport at pH=5.5 by MFSD1 was detected. HEKs were transfected with plasmids coding for MFSD1 LL/AA, MFSD1 LL/AA and GLMP Y400A and LYAAT-1. 24 hours post-transfection, buffer with a pH=5.5 containing a mix of [^{3}H] labelled aa or [^{3}H] labelled proline (A), a mix of [^{35}S] labelled cysteine and methionine (B) and [^{3}H] labelled glutamine, threonine or valine (C) was added to the transfected cells and untransfected HEKs for 15 min at room temperature. After several washes, the radioactivity of the cells was measured with liquid scintillation. The radioactive measurements were performed by Christoph Gelhaus. The values are represented as the mean corrected by the protein concentration.

The transport of [^{3}H] labelled glutamine, threonine or valine by MFSD1 LL/AA, MFSD1 LL/AA and GLMPY400A-HA and LYAAT-1 was analysed, revealing a slight increase in the signal for the three aa in all the transfected cells compared to the untransfected cells (Figure 60C). This increase of the radioactivity is not comparable to the sevenfold increase found in the cells transfected with LYAAT-1 for the transport of proline, that was used as positive control (Figure 60A). Since additional experiments did not confirm the tendency observed (data not shown), the increase in the signal was interpreted as variability.

Finally, the transport of cysteine and methionine in HEKs transfected with MFSD1 LL/AA, MFSD1 LL/AA and GLMPY400A-HA or LYAAT-1 was analysed by offering a mix of [^{35}S] labelled cysteine and methionine in the buffer. The results revealed no increase in the radioactive signal of any of the transfected cells compared to the untransfected HEKs (Figure 60).

As a summary, the analysis of the transport of 18 of the standard aa (asparagine and tryptophan were not tested) by MFSD1, with and without its interaction partner GLMP, did not provide conclusive evidence for a specific aa transport, strongly suggesting that MFSD1 is not transporting any of the aa analysed under the conditions used for the assay, or that the sensitivity of the assay is not enough to detect such a transport.

3.6.2 MFSD1$^{tm1a/tm1a}$ spleen and liver have altered sugars levels

Some members of MFS superfamily are known to transport sugars, and some of them are found intracellularly in vesicles, like the lysosomal transporter of sialic acid, sialin, or the vesicular transporters of glutamate, vGLUT1, vGLUT2 and vGLUT3 (Bellocchio et al. 2000; El Mestikawy et al. 2011; Morin, Sagné, and Gasnier 2004; Takamori et al. 2002). In order to investigate whether the deficiency of MFSD1 leads to an increase of monosaccharides in the tissues, the liver and spleen sugar levels of MFSD1$^{tm1a/tm1a}$ and MFSD1$^{wt/wt}$ mice were analysed in collaboration with C. Thiel (Universitätsklinikum Heidelberg). The results revealed an increase in the levels of glucose, fructose and inositol in MFSD1$^{tm1a/tm1a}$ liver compared to MFSD1$^{wt/wt}$ liver (Figure 61A). The levels of fructose were also increased in spleen of MFSD1$^{tm1a/tm1a}$ mice compared to MFSD1$^{wt/wt}$ mice, while the levels of mannose, saccharose and sorbitol were decreased in MFSD1$^{tm1a/tm1a}$ spleen in comparison to MFSD1$^{wt/wt}$ spleen (Figure 61B).

These results demonstrate that the levels of all the sugars analysed are changed in liver or spleen of MFSD1$^{tm1a/tm1a}$ mice compared to MFSD1$^{wt/wt}$ mice, but only fructose is increased

consistently in both tissues. The increase of fructose levels in liver and spleen is moderate, approximately twofold, and could be due to metabolic changes.

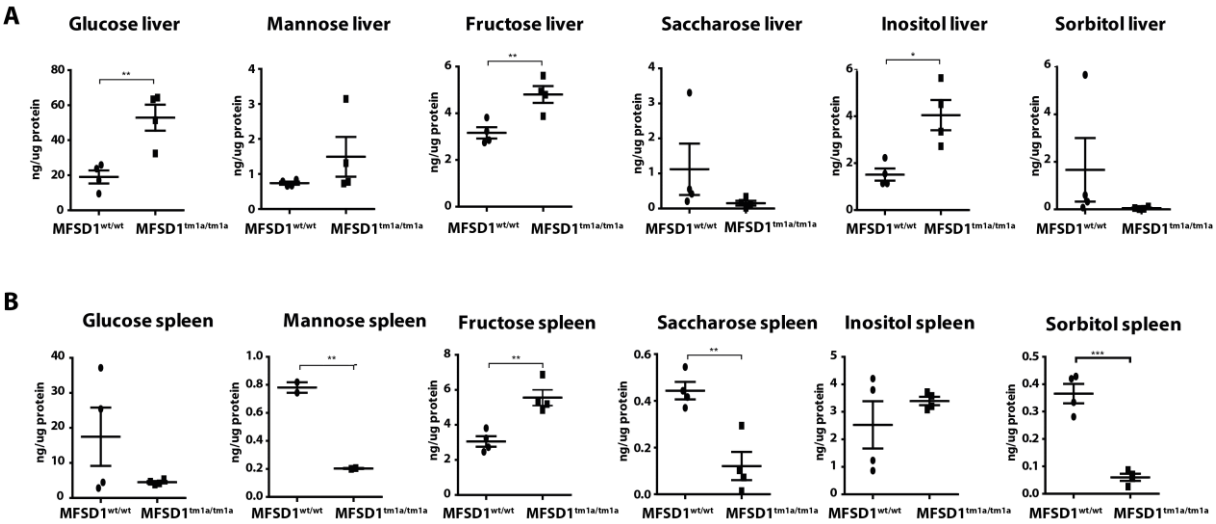

Figure 61. Several changes in the sugar levels of MFSD1$^{tm1a/tm1a}$ liver and spleen. The liver (A) and spleen (B) of MFSD1$^{tm1a/tm1a}$ and MFSD1$^{wt/wt}$ mice was collected and the mentioned sugars levels were analysed by mass spectrometry. The analysis was performed by C. Thiel (Universitätsklinikum Heidelberg).

3.6.3 Metabolomics analysis reveals no dramatic increase of metabolites in MFSD1$^{tm1a/tm1a}$ liver

The deficiency of lysosomal transporters can lead to accumulation of the substrate in tissues, like in the case of cystinosin deficient mice, which have increased cystine levels in tissues, ranging from tenfold in spleen to 350-fold in liver compared to WT mice (Cherqui et al. 2002). The liver of MFSD1$^{tm1a/tm1a}$ and MFSD1$^{wt/wt}$ mice were analysed by metabolomics (including steroids, bile acids, amino acids, carnitines, hexoses and several lipids) in order to investigate whether the levels of a possible substrate were dramatically changed in MFSD1$^{tm1a/tm1a}$ mice. The results revealed mild differences in many metabolites between MFSD1$^{tm1a/tm1a}$ and MFSD1$^{wt/wt}$ liver (Figure 62). Several of the differences found in metabolite levels between MFSD1$^{wt/wt}$ and MFSD1$^{tm1a/tm1a}$ liver can possibly be explained by the liver insult that MFSD1$^{tm1a/tm1a}$ mice suffer from. For instance, serotonin is known to play a role inducing fibrosis (Mann and Oakley 2013; Ruddell, Mann, and Ramm 2008), and creatinine and phosphoethanolamine levels are increased in patients with non-alcoholic fatty liver disease (NAFLD) and with liver cirrhosis, respectively (Safaei et al. 2016). In conclusion, the

metabolomics assay of the liver did not reveal an overt accumulation of a potential substrate transported by MFSD1 in liver with deficient expression of MFSD1.

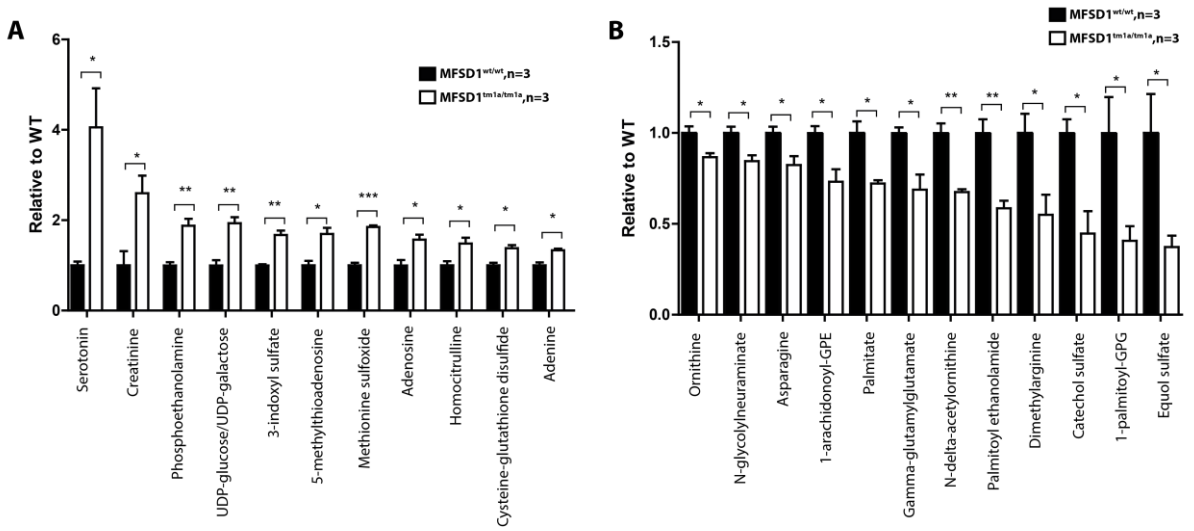

Figure 62. Changes in several metabolites in liver of MFSD1$^{tm1a/tm1a}$ mice. The livers of MFSD1$^{tm1a/tm1a}$ and MFSD1$^{wt/wt}$ mice were collected and a metabolomics analysis was performed. (A) shows increased metabolites in MFSD1$^{tm1a/tm1a}$ liver. (B) shows decreased metabolites in MFSD1$^{tm1a/tm1a}$ liver. All the metabolites identified are represented in Supplementary Table 3.

3.6.4 Sphingosine and S1P levels are unaltered in MFSD1$^{tm1a/tm1a}$ kidney and plasma

Spns2 and MFSD2b are members of the MFS superfamily of transporters described to export sphingosine-1-phosphate (S1P) from the endothelial cells and erythrocytes and platelets, respectively (Fukuhara et al. 2012; Vu et al. 2017). S1P levels in blood are important for the lymphocyte egression from lymphoid organs, and Spns2 deficient mice have decreased number of lymphocytes in circulation, a reduction of the mature B cells in spleen and bone marrow and decreased IgGs levels after antigen challenge immunization (Nijnik et al. 2012). Interestingly, like MFSD1 KO mice, MFSD2b-deficient mice have decreased levels of red blood cells and white blood cells in serum, and suffer of splenomegaly (Vu et al. 2017).

The source of cytosolic S1P is cytosolic sphingosine that is phosphorylated by sphingosine kinases 1 and 2. The source of cytosolic sphingosine is the degradation of complex sphingolipids and ceramide in the lysosome, ER and other membranes and there is not *de novo* synthesis of sphingosine (Kunkel et al. 2013). Lysosomal sphingosine export mechanism from lysosomes is not known and the cellular export of S1P, produced by phosphorylation of cytosolic sphingosine, from endothelial cells is important for the homeostasis of serum S1P levels. MFSD1 deficient mice exhibit degeneration of liver sinusoidal endothelial cells and have

an immunologic phenotype that resembles the immunologic phenotype observed in mice deficient for the expression of cell surface S1P exporters Spns2 and MFSD2b, independently. Additionally, lipid-like structures were accumulated in vesicles of the proximal convoluted tubules of MFSD1 deficient kidneys. Altogether, lead to the hypothesis that MFSD1 might be a lysosomal exporter of sphingosine.

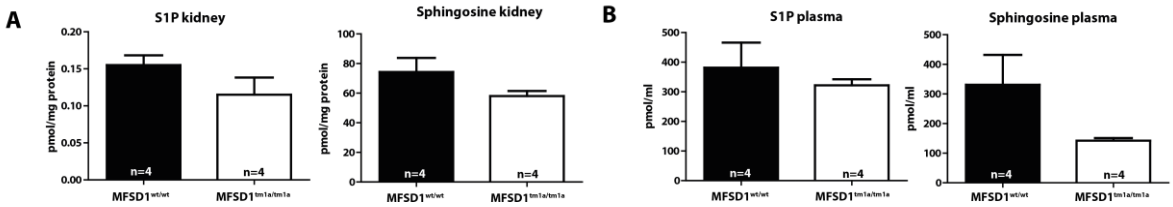

Figure 63. S1P and sphingosine levels are not changed in MFSD1$^{tm1a/tm1a}$ kidneys and plasma. The sphingosine and sphingosine-1-phosphate (S1P) levels of MFSD1$^{tm1a/tm1a}$ and MFSD1$^{wt/wt}$ mice (A) and plasma (B) were analysed by mass spectrometry. The analysis was performed by H. Aerts and M. Mirzaian.

In order to test this hypothesis, sphingosine and S1P levels in serum and kidney extracts of MFSD1$^{tm1a/tm1a}$ and MFSD1$^{wt/wt}$ mice were analysed in collaboration with H. Aerts and M. Mirzaian (University of Leiden), revealing no striking differences between MFSD1$^{tm1a/tm1a}$ and MFSD1$^{wt/wt}$ kidneys or serum (Figure 63).

4 Discussion

MFSD1 is a member of the MFS superfamily of transporters. The *MFSD1* gene was identified in 2011 as a member of the CLEAR network (coordinated lysosomal expression and regulation). The CLEAR network is formed by a group of lysosomal genes, which expression is promoted by the transcription factor TFEB (Sardiello et al. 2009). In 2013, the MFSD1 protein was detected in a proteomics assay in lysosomes (Chapel et al., 2013; Palmieri et al., 2011). However, a thorough biochemical or functional analysis of MFSD1 was lacking so far.

In the course of this work a detailed biochemical characterization of MFSD1 has been performed. The lysosomal localization of MFSD1 as well as the expression pattern in different mouse tissues has been analysed. A MFSD1-deficient mouse strain was generated and used as a tool to investigate possible substrate(s) transported by MFSD1. MFSD1-deficient mice display a complex phenotype that has been extensively characterized. During the course of this study, an interaction partner of MFSD1, GLMP, has been identified and the relation between both proteins has been investigated *in vitro* and *in vivo.*

4.1 MFSD1 is a lysosomal protein

A new anti-MFSD1 antibody recognizing the N-terminus of mouse MFSD1 was generated. Before using the anti-MFSD1 antibody for analysis, its specificity was confirmed using MFSD1-deficient tissues and cells by immunoblotting and immunofluorescence analysis. A prior study interpreted that a commercial antibody was specific because it detected a protein at a similar molecular weight to the predicted molecular weight of MFSD1 by immunoblotting (Perland, Hellsten, et al. 2017). Since our anti-MFSD1 antibody detected MFSD1 at a clearly different molecular weight than the predicted one and lacked a signal in knockout tissues, the previous published data seems questionable.

Despite MFSD1 has a predicted molecular mass of 51 kDa, our results showed that after SDS-PAGE electrophoresis it migrates at approximately 37 kDa. The migration of membrane proteins on SDS-PAGE usually does not correlate with their predicted molecular weight as their detergent loading ratio is variable (Rath et al. 2009). Hence, the migration pattern of MFSD1 can be explained by its hydrophobic transmembrane domains.

The immunofluorescence analysis of MEF cells validated the lysosomal localization of MFSD1. Additional staining of MFSD1 at the ER/Golgi compartments was observed after transfection,

but not endogenously in MEFs, suggesting that the ER/Golgi localization might be an artefact due to overexpression.

The analysis of tissue sections by immunofluorescence confirmed that MFSD1 is localized in lysosomes in liver, kidney, spleen and thymus. Partial co-fractionation of MFSD1 with β-hexosaminidase in liver and kidney after Percoll gradient centrifugation further supports the lysosomal localization of MFSD1. However, MFSD1 co-fractionated with only one of the two peaks of β-hexosaminidase activity in the kidney. Two lysosomal subpopulations with different densities have been described in kidney, which likely correspond with the two peaks of β-hexosaminidase fractions obtained by Percoll fractionation (Andersen, Haga, and Dobrota 1987; Harikumar et al. 1989). MFSD1 is only expressed in the less dense kidney lysosomes subpopulation. These two lysosomal fractions could correspond to different lysosomal subpopulations of one cell type or to lysosomes from different cell populations. The specific localization of MFSD1 in the less dense lysosomal subpopulation is likely related to its function.

Additional evidence for establishing MFSD1 as a lysosomal protein is that it is subjected to the tyloxapol-induced buoyant density shift that leads to a selective decrease in the density of lysosomes (Wattiaux et al. 1996). The validation of other putative lysosomal proteins has been described using this technique (Boonen et al. 2006; Schieweck et al. 2009; Della Valle et al. 2006).

Finally, it has been experimentally proven that the transport of MFSD1 to lysosomes requires a dileucine motif localized in its N-terminus that was identified in this study. It is well established that the dileucine motif is used for the internalization of membrane proteins from the plasma membrane or for the direct transport from the Golgi to lysosomes by AP-2 and AP-1 complexes, respectively (Bonifacino and Traub 2003). The study of the subcellular localization of MFSD1 in AP-1- or AP-2-deficient cells, or after knockdown of AP-1 or AP-2, would help to elucidate whether MFSD1 is transported via the direct pathway, the indirect pathway or using both pathways.

Both C and N-terminus of MFSD1 are facing the cytosol. According to the transmembrane domains (TMD) predictions, MFSD1 could have 10 or 12 TMD. Taking in account that the vast majority of MFS transporters bear 12 TMD, it is tempting to speculate that MFSD1 is also formed by 12 TMD (Marger and Saier 1993; Quistgaard et al. 2016; Yan 2015).

Lysosomal membrane proteins can be proteolytically cleaved in acidic compartments, like MFSD8 and DIRC2 (Savalas et al. 2011; Steenhuis et al. 2012). Potential proteolytic cleavage products of MFSD1 were detected after overexpression in HeLa cells and endogenously in lysosomal fractions of liver. However, no fragments were detected in MEF cells, whole liver lysates or fractions of liver containing both mitochondria and lysosomes. These results suggest that the MFSD1 fragments observed are not produced *in vivo*, or that only minor amounts undergo proteolytic cleavage as initiation of degradation. The fragments observed after transfection could be explained as an artefact of overexpression, while the fragment in liver lysosomal fractions could be originated during the sample preparation. After lysis of the lysosomal fraction of the liver, the cytosolic domains of membrane proteins are accessible to high concentrations of luminal proteases that might cleave MFSD1 *in vitro*.

As determined by immunofluorescence, Western blotting and LacZ expression analysis with tissues of MFSD1$^{wt/wt}$, MFSD1$^{wt/tm1a}$ and MFSD1$^{tm1a/tm1a}$, MFSD1 is expressed in all tissues and in a wide range of cell populations. The widespread presence of MFSD1 in cells and tissues leads to the speculation that the substrate transported by MFSD1 might be present in those tissues, and that its transport across the lysosomal membrane by MFSD1 is necessary to preserve the physiological homeostasis.

4.2 Lack of MFSD1 leads to a complex phenotype in mice

All the experiments shown in this thesis were performed using a knockout first MFSD1$^{tm1a/tm1a}$ mouse strain (See 2.2.5.2). The splice acceptor site located at the lacZ gene of tm1a allele can be exceptionally skipped as an ineffective usage by the spliceosome, leading to hypomorphic expression of the targeted gene, like in the case of MFSD8 $^{tm1a/tm1a}$ mice that suffer from a milder phenotype than MFSD8 $^{tm1d/tm1d}$ mice (Brandenstein et al. 2016; Damme et al. 2014). No MFSD1 protein was detected in cells, tissue lysates nor highly enriched liver lysosomal fractions using a sensitive anti-MFSD1 antibody, suggesting that the protein expression of MFSD1 is completely abolished in MFSD1$^{tm1a/tm1a}$ mice. Nevertheless, MFSD1$^{tm1d/tm1d}$ mice, which has a deletion of exon 2 leading to a frameshift mutation in exon 3, were produced in order to analyse whether they had a more severe phenotype than MFSD1$^{tm1a/tm1a}$ mice. No differences were observed between the liver phenotype of both mouse strains, leading to the assumption that functional MFSD1 was absent in MFSD1$^{tm1a/tm1a}$ mice.

The importance of MFSD1 function *in vivo* is highlighted by the complex phenotype that MFSD1-deficient mice suffer from. Additionally, the phenotype of MFSD1-deficient mice described indicates that MFSD1 is unique in its lysosomal function and that the lack of MFSD1 function can not be compensated by other proteins.

4.2.1 The liver phenotype of MFSD1-deficient mice resembles sinusoidal obstructive syndrome in man

MFSD1-deficient mice suffer from a liver phenotype characterized by death of sinusoidal endothelial cells, extravasation of erythrocytes, hepatocyte damage, obstruction of the sinusoids, recruitment of lymphocytes, neutrophils and platelets to the injured areas followed by new capillarization, fibrosis and at a late stage, tumour development.

The maintenance of a fibrotic reaction state can lead to cirrhosis and hepatocellular carcinoma (Hernandez-Gea and Friedman 2011; Pinzani, Rosselli, and Zuckermann 2011). Therefore, it is likely that MFSD1-deficient mice suffer from cancer as a consequence of the liver pathology, rendering a direct role of MFSD1 in cancer development unlikely.

The liver pathology resembles in several regards a human disease named Sinusoidal Obstructive Syndrome (SOS) or hepatic veno-occlusive disease (VOD). SOS is a focal liver disease characterized by damage in liver sinusoidal endothelial cells and hepatocytes (Mohty et al. 2015). The incidence of SOS is primarily in the setting of hematopoietic cell transplantation, but it can also be triggered by other causes (C. Q. Fan and Crawford 2014). For instance, SOS can appear after liver hepatectomy followed by oxaliplatin-containing chemotherapy or in patients taking pyrrolizidine alkaloid-containing herbal remedies. Liver sinusoidal endothelial cells (LSEC) are known to have a high endocytic/pynocytic activity, and play an important role in the detoxification of blood compounds (Sørensen et al. 2015). It has also been shown that LSECs are more sensitive to toxic compounds than other cells like hepatocytes or vascular endothelial cells (DeLeve et al. 1996). A rat model of SOS is based on the administration of monocrotaline, a pyrrolizidine alkaloid found in some herbs. The concentration of glutathione, a protein involved in the detoxification process, in LSECs is decreased one day after the administration of monocrotaline, but not the glutathione level of whole liver (Wang, Kanel, and DeLeve 2000). LSECs are damaged and start to die 24-48 hours post-administration. It is believed that the death of LSECs is the trigger of the following sinusoidal obstruction and hemorrhage by days 3-5 that leads to fibrosis by day 6-7 (DeLeve

et al. 1999). Another animal model of SOS are mice treated with FOLFOX (chemotherapy regimen containing Folinic acid, 5-Fluorouracil, and Oxaliplatin), which suffer from sinusoidal dilatation and hepatocyte atrophy. These mice have a pro-thrombotic state, with upregulation of von Willebrand Factor (vWF) among others characteristics (Robinson et al. 2013). Some members of the MFS superfamily transport drugs (Pao, Paulsen, and Saier 1998). The similarities between the liver phenotype of MFSD1-deficient mice and patients and animal models of SOS suggest that MFSD1 is involved in the transport of the drugs leading to the disease, like oxaliplatin, pyrrolizidine alkaloids or related compounds. Alternatively, MFSD1 could transport a substrate necessary for the detoxification processes, like an amino acid precursor of glutathione or Fe^{3+}, which is coupled to cytochrome P450.

To date, only a monogenetic disease associated with SOS has been identified (Roscioli et al. 2006). This disease is accompanied by immunodeficiency (VODI). In those cases the gene SP110, which is an immunoregulatory gene expressed in B and T lymphocytes within lymph nodes, spleen and liver, is mutated (C. Q. Fan and Crawford 2014). Patients with mutations in SP110 suffer from hypogammaglobulinemia, and the ability of B cells to respond to T cell stimuli is compromised (Cliffe et al. 2012). Since MFSD1-deficient mice also suffer from immunodeficiency, it can not be excluded that also the expression of MFSD1 is downregulated in those patients. The expression analysis pattern of MFSD1 and the sequencing of *MFSD1* of those patients would elucidate whether MFSD1 is involved in the VODI pathology.

MFSD1-deficient mice at three months of age share most of the characteristics displayed by SOS animal models and human patients. Additionally, the results obtained with the Tie2 conditional MFSD1 KO mice supports the hypothesis that the liver pathology of MFSD1-deficient mice is triggered by the death of LSECs, as it happens in the case of SOS animal models (DeLeve et al. 1999; Robinson et al. 2013).

MFSD1-deficient mice also suffer from splenomegaly. Since SOS and liver fibrosis and cirrhosis are commonly associated to splenomegaly, one can speculate that the splenomegaly in MFSD1-deficient mice is secondary to the liver pathology (Kim et al. 2016; Li et al. 2017; Overman et al. 2010). However, since the mice suffer from immunodeficiency and the spleen is an immune competent organ, it can not be ruled out that the splenomegaly might be directly and primarily related to the immune phenotype.

The death of LSECs in MFSD1-deficient mice as an initial step triggering the liver pathology observed, hints towards a role of MFSD1 transporting a substrate involved in the

detoxification of LSECs. No consistent enlargement of lysosomes was observed by immunofluorescence or electron microscopy in MFSD1-deficient liver or spleen, unlike in mice deficient for the lysosomal cystine exporter, cystinosin (Cherqui et al. 2002). Therefore, one possible explanation is that MFSD1 is a lysosomal importer. Or it might be an exporter of a substrate present at very low concentrations, so low that its accumulation would not lead to a change in the morphology of lysosomes.

4.2.2 MFSD1-deficient mice present a ''Hyper IgM syndrome'' phenotype

Lysosomal proteins are important for B lymphocyte maturation. For instance, the lysosomal intramembrane protease SPPL2A is responsible of cleaving the invariant chain of the histocompatibility class II complex (MHCII), also named CD74. In the absence of SPPL2A, the N-terminal fragment of CD74 is accumulated in lysosomes impairing endocytic traffic and leading to altered response to B-cell receptor stimulation (Schneppenheim et al. 2013). Moreover, several LSD are associated with immune system irregularities, like in the case of patients suffering from Gaucher disease, α-mannosidosis and mucopolysaccharidosis VII (Castaneda et al. 2008).

The analysis of MFSD1 expression by Western blotting showed that MFSD1 is highly expressed in thymus, spleen and bone marrow, the main immune competent organs in mouse. Immunofluorescence studies of spleen sections revealed the lysosomal localization of MFSD1 in B and T lymphocytes, both highly specialized immune cell types. Additionally, splenic macrophages also express MFSD1 in lysosomes.

The deficiency of MFSD1 in mice at three months of age leads to a decrease of the lymphocyte number in serum, a decrease of the relative number of B lymphocytes in spleen and a dramatic reduction of the IgG levels in spleen. The concentrations of IgG and IgA in serum are also reduced, while the levels of IgM are unchanged. IgM are produced by mature and immature B lymphocytes, while the soluble IgG and IgA are produced by mature B lymphocytes after class switch recombination, suggesting that the maturation of B lymphocytes in MFSD1-deficient mice is impaired (Hoffman, Lakkis, and Chalasani 2016). The impaired maturation of B lymphocytes is a common characteristic of patients suffering from Hyper IgM syndrome (HIGM) (Etzioni and Ochs 2004). HIGM is a human disease caused by a defective B cell activation secondary to fail in class-switch recombination (de la Morena 2016). To date, mutations in at least 12 genes have been described to be causative for different subtypes of

HIGM. The majority of the genes mutated in HIGM are directly involved in the process of class-switch recombination or B cell function (de la Morena 2016). However, there are many cases of patients suffering of HIGM without a causative gene identified.

The clinical features vary among the different types of HIGM. A general clinical trait of patients with Hyper IgM are reduced levels of IgA, IgE and IgG in serum and normal or increased concentrations of IgM. Some patients have normal levels of B and T lymphocytes, while some other patients suffer from lymphopenia (Etzioni and Ochs 2004; de la Morena 2016). The immune phenotype observed in MFSD1-deficient mice fits into the description of HIGM with lymphocytopenia. The fact that the IgG levels in spleen of MFSD1 after one month of live are indistinguishable between MFSD1-deficient and WT mice indicates that HIGM in MFSD1 knockout mice is acquired. The age of onset of HIGM symptoms in human patients varies from 0 to 10 years (Etzioni and Ochs 2004). Therefore, it is plausible that the age of onset of the immunodeficiency symptoms of MFSD1-deficient mice is after one month of age, and that it is independent of the liver phenotype. It is also possible that the liver pathology and the immune deficiency are related to each other, as patients suffering from veno-occlusive disease with immunodeficiency (VODI) have decreased levels of B and T lymphocytes in serum. Furthermore, B lymphocytes isolated from patients fail to produce IgG, IgA and IgM upon stimulation with CD40L (Cliffe et al. 2012). Therefore, it is needed to investigate the relation or the independence of the liver pathology and the immune deficiency of MFSD1-deficient mice.

The deletion of MFSD1 in LSECs and macrophages of the liver driven by Tie2 promoter, which leads to a slight reduction of whole liver MFSD1 levels, is enough for the development of the described liver pathology. Unfortunately, Tie2 promoter is also active in the hematopoietic lineage during development affecting B and T lymphocytes (Tang et al. 2010). Hence, the Tie2 conditional MFSD1 KO mouse model is not suitable to analyse the independence of the immune phenotype from the liver pathology observed in MFSD1-deficient mice. In order to investigate the primary cell responsible of the immune deficiency of MFSD1-deficient mice it will be valuable to analyse mice deficient for MFSD1 expression specifically in B or T lymphocytes. It is difficult to speculate how the lack of MFSD1 can affect the maturation of B lymphocytes without knowing the substrate transported by MFSD1. In any case, unravelling the cell responsible for the failure in the maturation of B cells in MFSD1-deficient mice would help to further investigate the putative substrate(s) of MFSD1.

4.2.3 Decreased osteoblast activity in vertebrae of MFSD1-deficient mice

The deficiency of some lysosomal membrane proteins leads to bone abnormalities. For instance, mice deficient for the lysosomal intramembrane protease SPPL2A suffer from hypomineralization of the teeth enamel, but the role of SPPL2A in the mentioned process is not fully understood (Bronckers et al. 2013). The deficiency of the lysosomal membrane proteins CLC7 and its β-subunit, OSTM1, leads to increased bone mineral density (osteopetrosis) due to defective bone resorption by osteoclasts (Kornak et al. 2001; Pangrazio et al. 2006).

Femur and tibia of MFSD1-deficient mice are paler than usual due to an increase of the adipocyte area in the bone marrow space, and their cortical and trabecular bone mineral density is unchanged. Our data revealed that the bone volume and the trabecular number is decreased in vertebrae of MFSD1-deficient mice, which is translated into decreased stiffness. The number of osteoblasts in vertebrae of MFSD1-deficient mice is increased two-fold when compared to wild type mice, but their mineralization ability is impaired. Additionally, despite the number of osteoclasts in vertebrae is unchanged, the bone resorption activity in MFSD1-deficient mice is increased. The increased osteoclast activity and the impaired osteoblast bone formation rate in vertebrae leads to a decreased bone volume in MFSD1-deficient vertebrae.

Osteoblasts are known to be one of the main sources of RANKL, a cytokine that stimulates osteoclast activation by cell-to-cell contact (Boyce and Xing 2007; Jimi et al. 1996; Udagawa et al. 1999). It is likely that the higher osteoblast number in vertebrae of MFSD1-deficient mice is accompanied by an increase in RANKL levels that would activate osteoclast activity. Such is the case in mice lacking the protein Arl6ip5, that is involved in calcium regulation in osteoblasts. Arl6ip5-deficient osteoblasts fail to differentiate, and activate osteoclast activity through RANKL expression, resulting in decreased bone formation parameters (Wu et al. 2014). Therefore, it would be of interest to measure the RANKL levels in vertebrae of MFSD1-deficient mice. Other factors than RANKL can modulate the activity and differentiation of osteoclasts, like MCSF, IL-1, IL-6, EGF, TGF-α or TNF-α (Amarasekara et al. 2018; Roodman 1993). Additionally, it has been reported that patients with chronic liver injuries, like non-alcoholic fatty liver disease (NAFLD), also show a decrease in the bone mineral density (Wang et al. 2016; Chung et al. 2016; Pardee et al. 2012; Yang et al. 2016). Therefore, it can not be ruled out that the loss of bone mineral density in MFSD1-deficient mice is related to the liver pathology. It would be of interest to analyse the serum cytokine levels in MFSD1-deficient

mice, as the concentrations of osteoclast activating cytokines might be increased. It is puzzling that the bone parameters of tibia and femur are unaffected in MFSD1-deficient mice. A more detailed characterization of MFSD1 expression in the different osteoblast populations would be necessary. Whether the lack of MFSD1 in osteoblast is directly involved in the decreased mineralization activity of osteoblasts remains to be investigated.

4.2.4 Enlarged LAMP1 vesicles in proximal tubules of MFSD1-deficient kidneys

The malfunction of lysosomes can lead to lysosomal storage diseases (LSD) that are characterized by accumulation of material in lysosomes. The accumulation of undigested material or accumulation of non-exported material in lysosomes can lead to such an enlargement of lysosomes that they become dysfunctional (Walkley and Vanier 2009).

At 6 months of age, MFSD1-deficient mice accumulate material in lysosomes of the proximal tubule cells of the kidney, a cell type in which the expression of MFSD1 is highest in kidney. There is variability in the number of vesicles that accumulate material, and vacuoles are found only in small areas of the kidney. However, the size of the lysosomes in the proximal tubules is increased as it has been shown by immunofluorescence and supported by the increased expression of LAMP1. At earlier stages there is already a tendency towards increased LAMP1 expression in kidney. The nature of the material accumulating in lysosomes of the kidney of MFSD1-deficient mice has not yet been identified. It is also not well understood why the material is not accumulating at earlier stages of life, or why the enlargement of lysosomes is only observed in the proximal tubules of the kidney and not in other organs where MFSD1 is also highly expressed.

Proximal tubule cells (PTC) recover many substrates from the filtered blood by endocytosis, that is mediated by megalin and cubilin receptor proteins. (Erik Ilsø Christensen, Verroust, and Nielsen 2009). For instance, Vitamin D-binding protein, retinol-binding protein or folate-binding protein are endocytosed in PTC, but the mechanism by how Vitamin D, retinol or folate escape from endo-lysosomal vesicles is unknown (E. I. Christensen et al. 2012). Drugs and toxins like cisplatin and aminoglycosides are also found in lysosomes of PTC (Camano et al. 2010; Olbricht, Fink, and Gutjahr 1991). Additionally, accumulation of aminoglycosides in lysosomes of PTC lead to enlarged lysosomal size (Tulkens 1999; Watanabe 1978). Therefore, a plausible explanation is that MFSD1 is involved in the lysosomal export of substrate(s) endocytosed by megalin and cubilin. In most cases, however, the connection between the

primary lysosomal defect and the secondary accumulation of material in lysosomes is not well understood (Walkley and Vanier 2009).

4.3 MFSD1 and GLMP are interaction partners

The data generated during this study shows how a member of the MFS superfamily, MFSD1, is tightly associated with GLMP. Many transport proteins have auxiliary subunits that can modulate their transport activity, their subcellular localization or can act as a chaperone (Barrallo-Gimeno et al. 2015; Jansen et al. 2008; Kirk et al. 2000; Ohno et al. 2011). However, in the subgroup of MFS transporters, only a few members interact with auxiliary proteins. For instance, CD98 heavy chain, a 529 amino acid transmembrane protein, interacts with the amino acid transporters LAT1 and LAT2, members of the APC superfamily, and with the glucose transporter GLUT1, a member of the MFS superfamily. CD98 heavy chain increases the glucose transport activity of GLUT1 (Ohno et al. 2011; Pineda et al. 1999; Y Kanai, H Segawa, Miyamoto K, Uchino H, Takeda E 1998). Also BASIGIN, a single transmembrane glycoprotein with two immunoglobulin-like domains localized in the plasma membrane, facilitates the cell surface localization of the monocarboxylate transporters MCT1 and MCT4, members of the MFS superfamily, indicating that auxiliary subunits can modulate both trafficking and activity (Kirk et al. 2000).

An interaction between a transport protein and its auxiliary subunit can have a different outcome in regard to stability, subcellular localization and transport activity. For instance, three out of the nine members of the chloride channels and transporters family are associated with an auxiliary subunit, but the role of the interaction in each couple of proteins is different. Barttin is a two transmembrane domain containing protein essential for the membrane localization of CLC-K and for its activity (Estévez et al. 2001). CLC-2 is active on its own, but GlialCAM, a transmembrane protein, regulates its subcellular localization and its activity in glial cells (Jeworutzki et al. 2012). OSTM1 is a highly glycosylated type I transmembrane protein localized in lysosomes and the ruffled border of osteoclasts, and it is the beta subunit of CLC-7, the only CLC channel that is not glycosylated (Barrallo-Gimeno et al. 2015). The stability of CLC-7 and OSTM1 depends on each other, and the subcellular localization of OSTM1 depends on CLC-7. Additionally, the transport activity of CLC-7 relies on OSTM1 (Barrallo-Gimeno et al. 2015; Lange et al. 2006; Leisle et al. 2011). The interdependence between CLC-7 and OSTM1 is demonstrated by a striking reduction of CLC-7 protein levels in

OSMT1 KO mice, which are below 10 % of normal levels, and the reduction of OSTM1 protein in CLC-7 KO mice (Lange et al. 2006). In addition, both KO mice share a very similar bone phenotype, which is caused by the decreased bone resorption activity of osteoclasts due to the impaired chloride ion pumping into the resorption lacunae (Lange et al. 2006). Interestingly, the relationship between MFSD1 and GLMP strongly resembles that of the lysosomal CLC-7 channel and OSTM1.

4.3.1 The protein stability of MFSD1 depends on GLMP and *vice-versa*

Our results revealed that the deficiency of MFSD1 leads to a decrease of the protein levels of GLMP, a highly glycosylated type I transmembrane protein also localized in lysosomes, in both MEF cells and mouse tissues. GLMP protein was not detected in liver lysosomes of MFSD1 KO mice, indicating that the residual GLMP protein is localized in a different subcellular compartment. In the absence of GLMP, MFSD1 protein levels are reduced to less than 10% of the normal levels found in mouse tissues, as it is the case for CLC-7 in OSTM1-deficient tissues and cells (Lange et al. 2006). Interestingly, in liver of *MFSD1* heterozygote mice, where the expression of MFSD1 proteins is 50 % of normal levels, GLMP protein levels are also reduced to half, supporting the hypothesis that the GLMP stability directly depends on the interaction with MFSD1, independent of the function of MFSD1. This results also implicates that a specific MFSD1:GLMP stoichiometry is necessary for the stability of both proteins and that MFSD1 is a limiting factor. No data is yet available about the stoichiometry CLC-7:OSTM1. Using a FRET based assay it has been shown that the stoichiometry MCT1:BASIGIN is at least 1:2 (Wilson, Meredith, and Halestrap 2002). Such an assay would also be of interest to investigate the stoichiometry of the complex MFSD1-GLMP.

4.3.2 Co-immunoprecipitation assays support the direct physical interaction between MFSD1 and GLMP

The interdependence between MFSD1 and GLMP requires a physical interaction between both proteins. The detergent used for the solubilisation of membrane proteins can irreversibly denature them affecting their function and the interaction with other proteins (Garavito and Ferguson-Miller 2001). For instance, Triton X-100, a detergent widely used to lyse samples, disrupts the interaction between mTOR and its interaction partners (Sabatini 2017). While the interaction between CLC-7 and Ostm1 is stable after lysis of samples with TX-100, in order to

keep the interaction between BASIGIN and the MFS transporter MCT-1, the samples have to be solubilized using the detergent Brij97 (Kirk et al. 2000; Lange et al. 2006). Our results have confirmed the physical interaction between MFSD1 and GLMP. Such interaction is not stable when the samples are solubilized with many detergents. Only after solubilisation with the zwitterionic detergent CHAPS or the non-ionic detergent Brij78 the interaction MFSD1-GLMP remains intact, emphasizing the importance of the solubilisation detergent used for co-immunoprecipitation studies.

It is puzzling that the interaction MFSD1-GLMP has not been detected when precipitating both proteins with an anti-HA antibody, but only precipitating MFSD1 with the MFSD1-specific antibody. The cytosolic domain of GLMP, where the HA tag is fused to, is very short (12 aa). It is likely that the interaction between the HA tag and the anti-HA antibody disrupts the association between GLMP and MFSD1. In order to test this hypothesis, co-immunoprecipitation analysis should be done with a GLMP construct bearing the tag at a different position, for instance within the N-terminus.

Attempts to precipitate GLMP with our novel antibody failed, indicating that it is not suitable for immunoprecipitation of GLMP protein. The antibody was raised against a peptide located in its luminal domain. Since GLMP is highly glycosylated, it is likely that the epitope is not accessible under native conditions.

4.3.3 GLMP protects MFSD1 from the activity of lysosomal hydrolases

In MEF cells deficient for GLMP, MFSD1 protein is absent in lysosomes, but remaining MFSD1 is found in the Golgi apparatus. The reintroduction of GLMP into GLMP knockout cells restores the lysosomal localization of MFSD1, demonstrating that the lack of lysosomal MFSD1 in GLMP-deficient MEFs is a direct consequence of the absence of GLMP. This experiment raises the question whether MFSD1 needs GLMP for its transport to lysosomes, for protection from lysosomal proteases or for both. Since OSTM1 is a highly glycosylated protein and CLC-7 is not glycosylated, it has been speculated that OSTM1 protects CLC-7 from lysosomal hydrolases (Lange et al. 2006). Such interpretation could be also translated in the case of MFSD1-GLMP, since MFSD1 is not N-glycosylated and GLMP is highly glycosylated. MFSD1 protein levels in GLMP KO cells were restored to wild type levels after the use of lysosomal inhibitors, supporting the protective role of GLMP for MFSD1. Additionally, the highly glycosylated luminal domain of GLMP is necessary and sufficient to restore the lysosomal localization of

MFSD1 in GLMP-deficient MEFs, as shown by a rescue experiment using GLMP-LAMP1 chimeric proteins. This result suggests that the luminal domain of GLMP interacts with MFSD1. The MFSD1-GLMP interaction differs from the interaction CLC7-OSTM1, since the transmembrane domain of OSTM1 interacts with CLC-7 (Leisle et al. 2011). Also the transmembrane domain and the cytoplasmic domain of CD147 are important for the interaction with MCT-1, but not the extracellular domain, which would be the equivalent to the luminal domain of a vesicular single transmembrane protein (Kirk et al. 2000). In contrast, the experiments shown here provide evidence that the luminal domain of GLMP interacts with MFSD1.

4.3.4 The interaction MFSD1-GLMP ensures the lysosomal localization of the complex

MFSD1 and GLMP can be transported to lysosomes even in the absence of each other, at least after overexpression. In the case of CLC-7 and its β-subunit, OSTM1, the subcellular localization of OSTM1 fully depends on CLC-7. When CLC-7 bears a mutation within its lysosomal transport motif leading to a cell surface localization, OSTM1 is also redirected to the plasma membrane (Stauber and Jentsch 2010). In the case of MFSD1 and GLMP, their transport to lysosomes does not depend on the interaction with its partner protein under physiological conditions. If GLMP bears a mutation within its tyrosine lysosomal sorting motif, it is localized to the cell surface. However, the cell surface mutant of GLMP is localized to lysosomes after co-expression with MFSD1. In the same way, the cell surface mutant of MFSD1 is partially localized to lysosomes after co-expression with GLMP. Therefore, in case of mutations leading to an incorrect subcellular transport, the interaction between both proteins can be used for the redirection to lysosomes (Figure 64).

Since MFSD1 and GLMP stability depends on each other, it is tempting to speculate that the described relation between both proteins regarding the lysosomal transport is a ´back-up plan´ for both proteins to localize to lysosomes and stay stable together. The importance of the lysosomal localization of both MFSD1 and GLMP is highlighted by the complex phenotype developed by both KO mouse models (See 3.3 and 3.5.3). Therefore, it is reasonable that the interaction between MFSD1 and GLMP is used to ensure their lysosomal localization.

The ability of MFSD1 and GLMP of redirecting the respective interaction partner to lysosomes raises also the question in which subcellular compartment the interaction between MFSD1

and GLMP starts and the complex is formed. It could be in the ER or Golgi apparatus during the direct transport pathway, or at the cell plasma membrane during the indirect transport pathway. In order to answer this question, it would be of interest to perform co-transfection experiments using MFSD1 fused to ER retention motifs and the WT version of GLMP to analyse its subcellular localization, and *vice-versa*.

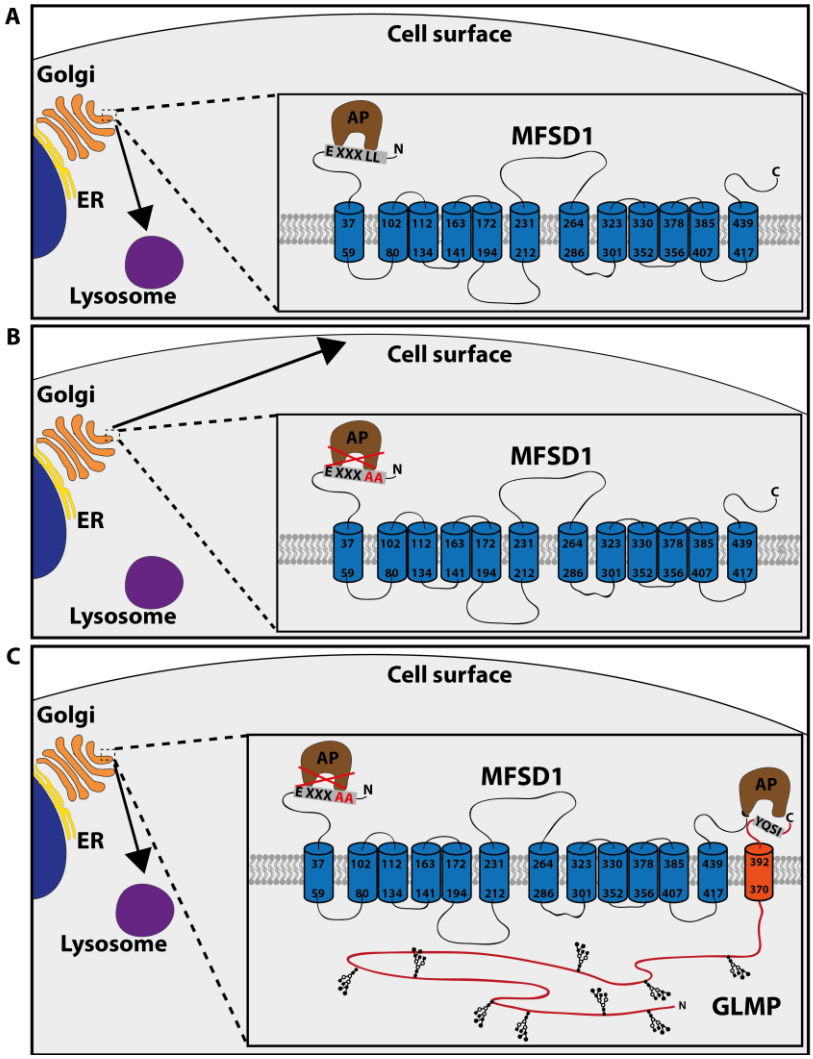

Figure 64. (A) Scheme of the interaction between MFSD1 and the adaptor proteins during the transport of MFSD1 to the lysosome. (B) Scheme of the disruption of the interaction between MFSD1 LL/AA and the adaptor proteins due to the mutation of the dileucine motif. As a result, MFSD1 LL/AA is transported to the cellular surface. (C) Scheme of how the interaction of GLMP with MFSD1 LL/AA prevents the transport of MFSD1 LL/AA to the cellular surface, and how it is finally localized to the lysosome.

4.3.5 The phenotype of GLMP-deficient mice is a phenocopy of MFSD1-deficient mice

The levels of GLMP in different tissues have been analysed only at the transcriptional level (Schieweck et al. 2009). Our results showed that the expression of GLMP protein is highest in kidney, approving the initial description of GLMP as ''kidney predominant protein NCU-G1'' (Steffensen et al. 2007). Additionally, GLMP expression has been detected in liver, lung and spleen. Interestingly, the expression of MFSD1 is highest in the tissues where GLMP expression was detected, kidney, liver, lung and spleen, strengthening the interdependence between MFSD1 and GLMP. However, the expression of GLMP in kidney is considerably higher than in liver, lung and spleen, while the difference in the expression of MFSD1 among these four tissues is minor. It has been shown that an auxiliary subunit can interact with more than one transport protein. For instance, CD147 interacts with the MFS transporters MCT1 and MCT4 (Kirk et al. 2000). Therefore, it can not be excluded that GLMP also interacts with other proteins.

Our data revealed that the deficiency of GLMP in mice, which is accompanied by a strong reduction of MFSD1 protein levels, leads to sinusoidal obstruction, hepatocyte atrophy, erythrocyte and leukocyte extravasation, neo-vascularization and fibrosis (See 3.5.3). Some of these features were previously described (Kong et al. 2014; Nesset et al. 2016). The liver phenotype of GLMP-deficient mice has remarkable similarities to the liver pathology observed in MFSD1-deficient mice (See 3.3.2). Similarly, the bone phenotype of CLC-7-deficient mice resembles to that of mice with mutations in the gene coding for its auxiliary subunit, *OSTM1* (Kornak et al. 2001; Pangrazio et al. 2006). Additionally, GLMP-deficient mice and MFSD1-deficient mice also share a strong reduction in serum of the lgGs and lgA levels.

Despite the high expression of GLMP in the kidney, GLMP-deficient kidney appeared to be normal but this tissue was not analysed in detail (Kong et al. 2014). Preliminary analysis of 6 months old GLMP-deficient mice suggests that the lysosomes of the proximal tubule of the kidney are enlarged (data not shown).

These results indicate that the remaining MFSD1 protein levels detected in GLMP-deficient mice are not enough to prevent the development of the liver pathology or the immunodeficiency that is present in the complete absence of MFSD1. Our results lead to the assumption that the remaining MFSD1 in GLMP-deficient tissues is localized to the Golgi

apparatus. However, it can not be ruled out that some protein might reach lysosomes, where it would be most likely rapidly degraded. In any case, since GLMP-deficient mice do not have a milder phenotype than MFSD1 knockout mice, it is tempting to speculate that GLMP has a dual role protecting MFSD1 from proteolysis and regulating its transport activity, as it is the case for CLC-7 and OSMT1 (Leisle et al. 2011).

4.4 MFSD1 transport function remains unknown

Members of the MFS superfamily can transport monosaccharides, oligosaccharides, amino acids, peptides, vitamins, enzyme cofactors, drugs, chromophores, nucleosides, nucleotides, anions, cations, etc. (Reddy et al. 2013). According to the transporter classification database (TCDB), MFSD1 belongs to an amino acid transporter family. MFSD1 has approximately 20 % homology with a threonine transporter and a valine transporter. The analysis of the amino acid levels in urine and serum of MFSD1-deficient mice revealed changes for the level of some amino acids like tyrosine, histidine and argininosuccinate (in urine) or glycine and citrulline (in serum). An abnormal functioning of liver or kidney can also contribute to changes in the amino acid levels in serum and urine (Duranton et al. 2014; Morgan et al. 1982). Since the changes in the levels of the mentioned amino acids were rather minor (1.2 fold to 3 fold), it is likely that they are secondary to the liver and/or kidney phenotypes.

However, the lysosomal export of radioactive amino acids was tested. Despite the results did not reveal the transport of any of the analysed amino acids by MFSD1-GLMP, it can not be ruled out that the methodology used is not sensitive enough to detect the export of a specific amino acid, or that MFSD1 acts as an amino acid importer.

Even though the analysis of monosaccharides levels in liver and spleen revealed several changes, only the levels of fructose were consistently increased in spleen and liver of MFSD1-deficient mice. GLUT8 is a trehalose transporter localized in lysosomes in testis (Augustin, Riley, and Moley 2005; Chen, Nagpal, and Lin 2003). It is present in other tissues like liver, where its localization is mainly at the plasma membrane (Mayer et al. 2016). Therefore, a role of MFSD1 in sugar transport seems possible.

Patients suffering from Salla disease, which is caused by a defective export of sialic acid from lysosomes, have swollen lysosomes which accumulate free sialic acid (Morin, Sagné, and Gasnier 2004). The increased size of lysosomes in proximal tubules of MFSD1-deficient mice indicates a potential accumulation of substrate(s) of MFSD1. The proximal tubule reabsorbs

major fractions of nutrients such as glucose, amino acids, ions and phosphates among other molecules, through apical transporters (Nakhoul and Batuman 2011). Additionally, proximal tubule cells (PTC) recover many molecules by endocytosis mediated by megalin and cubilin proteins from the blood filtrate (Erik Ilsø Christensen, Verroust, and Nielsen 2009). In Table 20, a list of the identified ligands of megalin and cubilin is shown. Amino acids and sugars are catabolic products of the degradation of proteins and glycoproteins which have to be exported from the lysosome (Winchester 2005). Also vitamins, like Vitamin B12, Vitamin D, retinol and folate need to exit from the lysosomal lumen. Only ABCD4 and LMBD1 have been identified to export a vitamin from lysosomes, Vitamin B12 (Coelho et al. 2012; Rutsch et al. 2009). Therefore, vitamins could be considered as potential substrates of MFSD1.

Ligand type	Ligands
Vitamin carrier porters	Transcobalamin-Vitamin B_{12}, Vitamin D-binding factor, Retinol-binding protein, Folate-binding protein, Intrinsic factor-Vitamin B_{12}
Other carrier proteins	Albumin, Myoglobin, Hemoglobin, Transferrin, Lactoferrin, Selenoprotein P, Metallothionein, Neutrophil-Associated lipocalin, Oderant-binding protein, Transthyretin, Liver-type fatty acid-binding protein, Sex hormone-binding globulin
Lipoproteins	Apolipoprotein A1, Apolipoprotein B, Apolipoprotein E, Apolipoprotein H, Apolipoprotein J/clusterin, Apolipoprotein M, High-density lipoprotein
Hormones, hormone precursors, and signalling proteins	Parathyroid hormone, Insulin, Epidermal growth factor, Prolactin, Thyroglobulin, Hedgehog protein, Angiotensin II, Leptin, Bone morphogenic protein 4
Enzymes and enzymes inhibitors	Plasminogen activator inhibitor (PAI)-type 1, PAI-type 1-urokinase, PAI-type 1-tissue plasminogen activator, Pro-urokinase, Lipoprotein lipase, Plasminogen, α-Amylase, α_1-Microglobulin, Lysozyme, Cathepsin B, α-Galactosidase A
Immune and stress-response related proteins	Immunoglobulin light chains, Pancreatitis-associated protein 1, Clara cell secretory protein, Advanced glycation end products, α_2-Microglobulin
Receptors and transmembrane proteins	Heavy metallothionein, Cation-independent mannopse-6-phosphate receptor, TCII-B_{12} receptor
Drugs and toxins	Aminoglycosides, Polymyxin B, Aprotinin, Trichosantin
Others	Ca^{2+},Cytochrome C, Receptor-associated protein, Receptor for seminal vesicle secretory protein II, Coagulation factor VIII

Table 20. List of ligands recognized and endocytosed by megalin and/or cubilin in proximal tubule cells (Adapted from Erik Ilsø Christensen, Verroust, and Nielsen 2009).

Several heme-containing proteins are endocytosed by megalin and cubilin, like myoglobin, haemoglobin or cytochrome C. HRG-1, a four transmembrane domain protein, has been suggested to be a endosomal heme exporter (White et al. 2013). Human membrane heme transporters FLVCR1 and FLVCR2 are members of the MFS superfamily and contain 12

transmembrane domains (Quigley 2014). Despite the regulation of the expression of HRG-1 is dependent on heme levels, the direct transport of heme has not been proven (Quigley 2014). A role of MFSD1 in heme transport can therefore not be ruled out.

Finally, drugs and toxins, like aminoglycosides or cisplatin, are found in lysosomes of PTC (Camano et al. 2010; Olbricht, Fink, and Gutjahr 1991). Additionally, aminoglycoside treatment lead to enlarged lysosomes (Tulkens 1999; Watanabe 1978). Interestingly, an animal model for SOS, the liver pathology resembling the phenotype of MFSD1-deficient mice, is induced after the administration of oxaliplatin, a drug from the same family as cisplatin (Robinson et al. 2013). Therefore, and since drugs are substrates of some members of the MFS superfamily, a role of MFSD1 transporting aminoglycosides, cisplatin or related proteins is conceivable.

4.5 Outlook

During the course of this study, it was shown that MFSD1 is transported to lysosomes through a dileucine motif identified within its N-terminus. Lysosomal membrane proteins can be transported to lysosomes via the direct pathway, from the trans-Golgi network to lysosomes, and/or the indirect pathway, from the trans-Golgi network to the plasma membrane and further endocytosis to lysosomes. The transport of lysosomal membrane proteins through the direct or indirect pathways depends on the binding of AP-1 or AP-2 complexes, respectively, to lysosomal sorting motifs. In order to investigate the transport pathway(s) used by MFSD1 for its transport to lysosomes in more detail, additional experiments using cells with decreased or depleted AP-1 or AP-2 complexes, using siRNA-treated cells or knockout cells, respectively, should be performed.

GLMP was identified as an interaction partner of MFSD1. GLMP protects MFSD1 from the activity of lysosomal hydrolases. Additionally, the FACS data after co-expression, revealed that the interaction of the plasma membrane GLMP mutant with MFSD1 redirects GLMP to lysosomes and *vice-versa*, indicating that the interaction MFSD1-GLMP starts in earlier subcellular compartments than lysosomes. In order to figure out in which organelle of the endocytic pathway the interaction starts, experiments using chimeric proteins containing ER retention motifs are of major interest. With the aim to increase the knowledge about the stoichiometry of the complex MFSD1-GLMP, additional co-immunoprecipitation, FRET and

blue native PAGE experiments are planned. Since the function of MFSD1 has not yet been unraveled, a possible regulation of its transport activity by GLMP can only be speculated. Therefore, future transport activity assays should be carried out by expressing MFSD1 alone and co-expressed with GLMP.

The similarities between the liver and immune system phenotypes of MFSD1-deficient mice with that of patients suffering veno-occlusive disease with immunodeficiency (VODI) suggest a potential role of MFSD1 in such a disease. Therefore, in order to address a possible implication of MFSD1 in the development of VODI, the expression of MFSD1 and the genomic sequences of *MFSD1* in VODI patients should be investigated. The immunologic data indicated that the maturation of B lymphocytes in MFSD1-deficient mice was impaired. Since several cells are involved in the maturation of B lymphocytes, like B and T lymphocytes or antigen presenting cells, attempts to unravel which is the primary cell responsible for the immunodeficiency of MFSD1-deficient mice are planned. Hence, mouse strains with conditional depletion of MFSD1 expression in B lymphocytes or T lymphocytes will be generated and analysed.

Furthermore, even though MFSD1-deficient mice had higher osteoblast number in vertebrae, their mineralization activity was impaired, the osteoclast activity was increased and the bone mineral density was decreased. Therefore, the cell type(s) which ultimately trigger(s) the bone phenotype remains to be determined. Also, the expression of MFSD1 in the different bone cells should be analysed and compared. Since high RANKL concentrations can lead to increased osteoclastic activity, the analysis of RANKL mRNA levels in vertebrae and cortical bone of femur is planned. Additionally, the mineralization of MFSD1-deficient osteoblasts *in vitro* will be addressed.

Despite considerable experimental efforts to unravel the substrate(s) transported by MFSD1 were made, it/they have not been identified. However, the phenotypic data from MFSD1-deficient mice generated might help to elucidate the nature of the substrate(s) transported. The liver phenotype data hinted towards the transport of molecules involved in the detoxification process, which might be in accordance with the kidney findings of enlarged vesicles. The isolation of proximal tubule cells and/or isolation of lysosomal fractions and further metabolomics analysis would possibly help to identify the substrate(s) accumulated in MFSD1-deficient kidneys. Special attention should be paid to xenobiotics, drugs and

substrates recognized by megalin/cubilin. Transport assays for these substrates are of interest.

5 References

Abramson, J., Smirnova, I., Kasho, V., Verner, G., Kaback, H. R., & Iwata, S. (2003). Structure and Mechanism of the Lactose Permease of Escherichia coli. *Science*, *301*(5633), 610–616.

Abu-Remaileh, M., Wyant, G. A., Kim, C., Laqtom, N. N., Abbasi, M., Chan, S. H., Sabatini, D. M., et al. (2017). Lysosomal metabolomics reveals V-ATPase- and mTOR-dependent regulation of amino acid efflux from lysosomes. *Science*, *358*(6364), 807–813.

Adams, D., & Gahl, W. A. (1993). Free Sialic Acid Storage Disorders. *GeneReviews(®)*, 1–13.

Agre, P. (2006). The Aquaporin Water Channels. Proceedings of the american thoracic society, 3(1), 5-13.

Aiello, C., Terracciano, A., Simonati, A., Discepoli, G., Cannelli, N., Claps, D., Santorelli, F. M., et al. (2009). Mutations in MFSD8/CLN7 are a frequent cause of variant-late infantile neuronal ceroid lipofuscinosis. *Human Mutation*, *30*(3).

Aihara, Y., Mashima, H., Onda, H., Hisano, S., Kasuya, H., Hori, T., Takeda, J., et al. (2000). Molecular cloning of a novel brain-type Na+-dependent inorganic phosphate cotransporter. *Journal of Neurochemistry*, *74*(6), 2622–2625.

Amarasekara, D. S., Yun, H., Kim, S., Lee, N., Kim, H., & Rho, J. (2018). Regulation of Osteoclast Differentiation by Cytokine Networks. *Immune Network*, *18*(1), 1–18.

Andersen, K. J., Haga, H. J., & Dobrota, M. (1987). Lysosomes of the renal cortex: heterogeneity and role in protein handling. *Kidney International*, *31*(4), 886–97.

Augustin, R., Riley, J., & Moley, K. H. (2005). GLUT8 contains [DE]XXXL[LI] sorting motif and localizes to a late endomosal/lysosomal compartment. *Traffic*, *6*(12), 1196–1212.

Bach, G. (2005). Mucolipin 1: Endocytosis and cation channel - A review. *Pflugers Archiv European Journal of Physiology*, *451*(1), 313–317.

Bame, K. J., & Rome, L. H. (1985). Acetyl coenzyme A:α-glucosaminide N-acetyltransferase. Evidence for a transmembrane acetylation mechanism. *Journal of Biological Chemistry*, *260*(20), 11293–11299.

Barrallo-Gimeno, A., Gradogna, A., Zanardi, I., Pusch, M., & Estévez, R. (2015). Regulatory/Auxiliary subunits of CLC chloride channel/transport proteins. *The Journal of Physiology*, *18*, 4111–4127.

Bassi, M. T., Manzoni, M., Monti, E., Pizzo, M. T., Ballabio, A., & Borsani, G. (2000). Cloning of

the gene encoding a novel integral membrane protein, mucolipidin-and identification of the two major founder mutations causing mucolipidosis type IV. *American Journal of Human Genetics*, *67*(5), 1110–1120.

Bataller, R., & Brenner, D. (2005). Liver fibrosis. *The Journal of Clinical Investigation*, *115*(2), 209–218.

Bellocchio, E. E., Reimer, R. J., Fremeau, J., & Edwards, R. H. (2000). Uptake of glutamate into synaptic vesicles by an inorganic phosphate transporter. *Science*, *289*(5481), 957–960.

Berman, E. R., Livni, N., Shapira, E., Merin, S., & Levij, I. S. (1974). Congenital corneal clouding with abnormal systemic storage bodies: A new variant of mucolipidosis. *The Journal of Pediatrics*, *84*(4), 519–526.

Bhunchet, E., & Fujieda, K. (1993). Capillarization and venularization of hepatic sinusoids in porcine serum-induced rat liver fibrosis: A mechanism to maintain liver blood flow. *Hepatology*, *18*(6), 1450–1458.

Boers, W., Aarrass, S., Linthorst, C., Pinzani, M., Elferink, R. O., & Bosma, P. (2006). Transcriptional profiling reveals novel markers of liver fibrogenesis: Gremlin and insulin-like growth factor-binding proteins. *Journal of Biological Chemistry*, *281*(24), 16289–16295.

Bonifacino, J. S., & Traub, L. M. (2003). Signals for Sorting of Transmembrane Proteins to Endosomes and Lysosomes. *Annual Review of Biochemistry*, *72*(1), 395–447.

Boonen, M., Hamer, I., Boussac, M., Delsaute, A.-F., Flamion, B., Garin, J., & Jadot, M. (2006). Intracellular localization of p40, a protein identified in a preparation of lysosomal membranes. *Biochemical Journal*, *395*(1), 39–47.

Boyce, B. F., & Xing, L. (2007). Biology of RANK, RANKL, and osteoprotegerin. *Arthritis Research and Therapy*, *9*(SUPPL.1).

Brandenstein, L., Schweizer, M., Sedlacik, J., Fiehler, J., & Storch, S. (2016). Lysosomal dysfunction and impaired autophagy in a novel mouse model deficient for the lysosomal membrane protein Cln7. *Human Molecular Genetics*, *25*(4), 777–791.

Braulke, T., & Bonifacino, J. S. (2009). Sorting of lysosomal proteins. *Biochimica et Biophysica Acta*, *1793*(4), 605–14.

Bronckers, A. L. J. J., Gueneli, N., Lüllmann-Rauch, R., Schneppenheim, J., Moraru, A. P., Himmerkus, N., Schröder, B et al. (2013). The intramembrane protease SPPL2A is critical for tooth enamel formation. *Journal of Bone and Mineral Research*, *28*(7), 1622–1630.

Budak, Y. U., Polat, M., & Huysal, K. (2016). The use of platelet indices, plateletcrit, mean platelet volume and platelet distribution width in emergency non-traumatic abdominal surgery: A systematic review. *Biochemia Medica*, *26*(2), 178–193.

Burant, C. F. (1992). Fructose transporter in human spermatozoa and small intestine is GLUTS. *Journal of Biological Chemistry*, *267*(21), 14523–14526.

Camano, S., Lazaro, A., Moreno-Gordaliza, E., Torres, A. M., de Lucas, C., Humanes, B., … Tejedor, A. (2010). Cilastatin attenuates cisplatin-induced proximal tubular cell damage. *The Journal of Pharmacology and Experimental Therapeutics*, *334*(2), 419–429.

Cang, C., Aranda, K., Seo, Y., Gasnier, B., & Ren, D. (2015). TMEM175 Is an Organelle K+ Channel Regulating Lysosomal Function. *Cell*, *162*(5), 1101–1112.

Cantiello, H. F., Montalbetti, N., Goldmann, W. H., Raychowdhury, M. K., González-Perrett, S., Timpanaro, G. A., & Chasan, B. (2005). Cation channel activity of mucolipin-1: The effect of calcium. *Pflugers Archiv European Journal of Physiology*, *451*(1), 304–312.

Carstea, E. D., Morris, J. A., Coleman, K. G., Loftus, S. K., Zhang, D., Cummings, C., Tagle, D. A. et al. (1997). Niemann-Pick C1 Disease Gene : Homology to Mediators of Cholesterol Homeostasis. *Science*, *228*.

Castaneda, J. A., Lim, M. J., Cooper, J. D., & Pearce, D. A. (2008). Immune system irregularities in lysosomal storage disorders. *Acta Neuropathologica*, *115*(2), 159–174.

Chapel, A., Kieffer-Jaquinod, S., Sagné, C., Verdon, Q., Ivaldi, C., Mellal, M., Journet, A. et al. (2013). An extended proteome map of the lysosomal membrane reveals novel potential transporters. *Molecular & Cellular Proteomics : MCP*, *12*(6), 1572–88.

Chen, Y., Nagpal, M. L., & Lin, T. (2003). Expression and regulation of glucose transporter 8 in rat Leydig cells. *The Journal of Endocrinology*, *179*(1), 63–72.

Cherqui, S., Sevin, C., Hamard, G., Kalatzis, V., Sich, M., Pequignot, M. O., Antignac, C. et al. (2002). Intralysosomal cystine accumulation in mice lacking cystinosin, the protein defective in cystinosis. *Molecular and Cellular Biology*, *22*(21), 7622–7632.

Christensen, E. I., Birn, H., Storm, T., Weyer, K., & Nielsen, R. (2012). Endocytic Receptors in the Renal Proximal Tubule. *Physiology*, *27*(4), 223–236.

Christensen, E. I., Verroust, P. J., & Nielsen, R. (2009). Receptor-mediated endocytosis in renal proximal tubule. *Pflugers Archiv European Journal of Physiology*, *458*(6), 1039–1048.

Chung C., & Insogna, K. L. (2016). The liver throws the skeleton a bone (Resorption factor). *Hepathology*, 64(3), 977-979.

Cliffe, S. T., Bloch, D. B., Suryani, S., Kamsteeg, E. J., Avery, D. T., Palendira, U., Roscioli, T. et al. (2012). Clinical, molecular, and cellular immunologic findings in patients with SP110-associated veno-occlusive disease with immunodeficiency syndrome. *Journal of Allergy and Clinical Immunology*, *130*(3).

Coelho, D., Kim, J. C., Miousse, I. R., Fung, S., du Moulin, M., Buers, I., … Baumgartner, M. R. (2012). Mutations in ABCD4 cause a new inborn error of vitamin B12 metabolism. *Nature Genetics*, *44*(10), 1152–1155.

Cotman, S. L., & Staropoli, J. F. (2012). The juvenile Batten disease protein, CLN3, and its role in regulating anterograde and retrograde post-Golgi trafficking. *Clinical Lipidology*, *7*(1), 79–91.

Damme, M., Brandenstein, L., Fehr, S., Jankowiak, W., Bartsch, U., Schweizer, M., … Storch, S. (2014). Gene disruption of Mfsd8 in mice provides the first animal model for CLN7 disease. *Neurobiology of Disease*, *65*, 12–24.

de Duve, C., Pressman, B. C., Gianetto, R., Wattiaux, R., & Appelmans, F. (1955). Tissue fractionation studies. 6. Intracellular distribution patterns of enzymes in rat-liver tissue. *Biochemical Journal*, *60*(4), 604–617.

de la Morena, M. T. (2016). Clinical Phenotypes of Hyper-IgM Syndromes. *Journal of Allergy and Clinical Immunology: In Practice*, *4*(6), 1023–1036.

DeLeve, L. D., McCuskey, R. S., Wang, X., Hu, L., McCuskey, M. K., Epstein, R. B., & Kanel, G. C. (1999). Characterization of a reproducible rat model of hepatic veno-occlusive disease. *Hepatology*, *29*(6), 1779–1791.

DeLeve, L. D., Wang, X., Kuhlenkamp, J. F., & Kaplowitz, N. (1996). Toxicity of azathioprine and monocrotaline in murine sinusoidal endothelial cells and hepatocytes: the role of glutathione and relevance to hepatic venoocclusive disease. *Hepatology*, *23*(3), 589–99.

Della Valle, M. C., Sleat, D. E., Sohar, I., Wen, T., Pintar, J. E., Jadot, M., & Lobel, P. (2006). Demonstration of lysosomal localization for the mammalian ependymin-related protein using classical approaches combined with a novel density shift method. *Journal of Biological Chemistry*, *281*(46), 35436–35445.

Di Daniel, E., Mok, M. H. S., Mead, E., Mutinelli, C., Zambello, E., Caberlotto, L. L., Maycox, P. R. et al. (2009). Evaluation of expression and function of the H+/myo-inositol transporter HMIT. *BMC Cell Biology*, *10*, 1–12.

Dong, X. P., Cheng, X., Mills, E., Delling, M., Wang, F., Kurz, T., & Xu, H. (2008). The type IV

mucolipidosis-associated protein TRPML1 is an endolysosomal iron release channel. *Nature*, *455*(7215), 992–996.

Duranton, F., Lundin, U., Gayrard, N., Mischak, H., Aparicio, M., Mourad, G., Argilés, À. et al. (2014). Plasma and urinary amino acid metabolomic profiling in patients with different levels of kidney function. *Clinical Journal of the American Society of Nephrology*, *9*(1), 37–45.

El Mestikawy, S., Wallén-Mackenzie, Å., Fortin, G. M., Descarries, L., & Trudeau, L. E. (2011). From glutamate co-release to vesicular synergy: Vesicular glutamate transporters. *Nature Reviews Neuroscience*, *12*(4), 204–216.

Erickson, J. D., Varoqui, H., Schafer, M. K. H., Modi, W., Diebler, M. F., Weihe, E., … Usdin, T. B. (1994). Functional identification of a vesicular acetylcholine transporter and its expression from a "cholinergic" gene locus. *Journal of Biological Chemistry*, *269*(35), 21929–21932.

Eskelinen, E.L., Schmidt, C.K., Neu, S., Willenborg, M., Fuertes, G., Salvador, N. et al. (2004). Disturbed cholesterol traffic but normal proteolytic function in LAMP-1/LAMP-2 double-deficient fibroblasts. *Molecular Biology of the Cell*, *15*, 3132-3145.

Estévez, R., Boettger, T., Stein, V., Birkenhäger, R., Otto, E., Hildebrandt, F., & Jentsch, T. J. (2001). Barttin is a Cl- channel β-subunit crucial for renal Cl- reabsorption and inner ear K+ secretion. *Nature*, *414*(6863), 558–561.

Etzioni, A., & Ochs, H. D. (2004). The hyper IgM syndrome - An evolving story. *Pediatric Research*, *56*(4), 519–525.

Fahs, S. a, Hille, M. T., Shi, Q., Weiler, H., & Montgomery, R. R. (2014). A conditional knockout mouse model reveals endothelial cells as the predominant and possibly exclusive source of plasma factor VIII. *Blood*, *123*(24), 3706–3713.

Fan, C. Q., & Crawford, J. M. (2014). Sinusoidal Obstruction Syndrome (Hepatic Veno-Occlusive Disease). *Journal of Clinical and Experimental Hepatology*, *4*(4), 332–346.

Fan, X., Zhang, H., Zhang, S., Bagshaw, R. D., Tropak, M. B., Callahan, J. W., & Mahuran, D. J. (2006). Identification of the Gene Encoding the Enzyme Deficient in Mucopolysaccharidosis IIIC (Sanfilippo Disease Type C). *The American Journal of Human Genetics*, *79*(4), 738–744.

Fettelschoss, V., Burda, P., Sagné, C., Coelho, D., De Laet, C., Lutz, S., … Baumgartner, M. R. (2017). Clinical or ATPase domain mutations in ABCD4 disrupt the interaction between

the Vitamin B12-trafficking proteins ABCD4 and LMBD1. *Journal of Biological Chemistry*, *292*(28), 11980–11991.

Fina, B. L., Molgaard, H. V, Robertson, D., Bradley, N. J., Monaghan, P., Delia, D., Greaves, M. F. et al. (1990). Expression of the CD34 gene in vascular endothelial cells. *Blood*, *75*(12), 2417–2426.

Forgac, M. (1999). Structure and properties of the vacuolar (H^+)-ATPases *. The Journal of Biological Chemistry, 274(19), 12951-12954.

Frattini, A., Pangrazio, A., Susani, L., Sobacchi, C., Mirolo, M., Abinun, M., Teti, A. et al. (2003). Chloride channel ClCN7 mutations are responsible for severe recessive, dominant and intermediate osteopetrosis. Journal of Bone and Mineral Research, 18(10), 1740-1747.

Friedman, S. L. (2008). Hepatic fibrosis-Overview. *Toxicology*, *254*(3), 120–129.

Froissart, R., Cheillan, D., Bouvier, R., Tourret, S., Bonnet, V., Piraud, M., & Maire, I. (2005). Clinical, morphological, and molecular aspects of sialic acid storage disease manifesting in utero. *Journal of Medical Genetics*, *42*(11), 829–836.

Fukuhara, S., Simmons, S., Kawamura, S., Inoue, A., Orba, Y., Tokudome, T., Moriwaki, K. et al. (2012). The sphingosine-1-phosphate transporter Spns2 expressed on endothelial cells regulates lymphocyte trafficking in mice. *Journal of Clinical Investigation*, *122*(4), 21–28.

Gahl, W. a, Bashan, N., Tietze, F., Bernardini, I., & Schulman, J. D. (1982). Cystine transport is defective in isolated leukocyte lysosomes from patients with cystinosis. *Science*, *217*(4566), 1263–5.

Garavito, R. M., & Ferguson-Miller, S. (2001). Detergents as Tools in Membrane Biochemistry. *Journal of Biological Chemistry*, *276*(35), 32403–32406.

Goberdhan, D. C. I., Wilson, C., & Harris, A. L. (2016). Amino Acid Sensing by mTORC1: Intracellular Transporters Mark the Spot. *Cell Metabolism*, *23*(4), 580–589.

Graves, A. R., Curran, P. K., Smith, C. L., & Mindell, J. A. (2008). The Cl-/H+antiporter ClC-7 is the primary chloride permeation pathway in lysosomes. *Nature*, *453*(7196), 788–792.

Harikumar, P., Darshini, T., Dutt, A., & Ninjoor, V. (1989). A rapid procedure for the isolation of lysosomes from kidney cortex by Percoll density gradient centrifugation. *Enzyme Engineering*, *14*(3), 269–277.

Hayashi, H., Shitara, M., Yamasaki, F. (1982). The Origin of lipid accumulated in liver lysosomes after administration of Triton WR-1339. *The Journal of Biochemistry*, *92*(5), 1585–1590.

Hayashi, H., Niinobe, S., Matsumoto, Y., Suga, T. et al. (1981). Effects of Triton WR-1339 on

lipoprotein lipolytic activity and lipid content of rat liver lysosomes. *The Journal of Biochemistry*, *89*(2), 573–579.

Hernandez-Gea, V., & Friedman, S. L. (2011). Pathogenesis of Liver Fibrosis. *Annual Review of Pathology: Mechanisms of Disease*, *6*(1), 425–456.

Higgins, M. E., Davies, J. P., Chen, F. W., & Ioannou, Y. A. (1999). Niemann-pick C1 is a late endosome-resident protein that transiently associates with lysosomes and the trans-Golgi network. *Molecular Genetics and Metabolism*, *68*(1), 1–13.

Hirabayashi, Y., Nomura, K. H., & Nomura, K. (2013). The acetyl-CoA transporter family SLC33. *Molecular Aspects of Medicine*, *34*(2–3), 586–589.

Hoffman, W., Lakkis, F. G., & Chalasani, G. (2016). B cells, antibodies, and more. *Clinical Journal of the American Society of Nephrology*, *11*(1), 137–154.

Hřebíček, M., Mrázová, L., Seyrantepe, V., Durand, S., Roslin, N. M., Nosková, L., Pshezhetsky, A. V. et al. (2006). Mutations in TMEM76* Cause Mucopolysaccharidosis IIIC (Sanfilippo C Syndrome). *The American Journal of Human Genetics*, *79*(5), 807–819.

Huang, X. Y., Morielli, A. D., & Peralta, E. G. (1993). Tyrosine kinase-dependent suppression of a potassium channel by the G protein-coupled m1 muscarinic acetylcholine receptor. *Cell*, *75*(6), 1145–1156.

Ivanova, E., De Leo, M. G., De Matteis, M. A., & Levtchenko, E. (2014). Cystinosis: Clinical presentation, pathogenesis and treatment. *Pediatric Endocrinology Reviews*, *12*, 176–184.

Jansen, E. J. R., Scheenen, W. J. J. M., Hafmans, T. G. M., & Martens, G. J. M. (2008). Accessory subunit Ac45 controls the V-ATPase in the regulated secretory pathway. *Biochimica et Biophysica Acta - Molecular Cell Research*, *1783*(12), 2301–2310.

Jardetzky, O. (1966). Simple allosteric model for membrane pumps [27]. *Nature*, *211*(5052), 969–970.

Jeworutzki, E., López-Hernández, T., Capdevila-Nortes, X., Sirisi, S., Bengtsson, L., Montolio, M., Estévez, R.et al. (2012). GlialCAM, a Protein Defective in a Leukodystrophy, Serves as a ClC-2 Cl - Channel Auxiliary Subunit. *Neuron*, *73*(5), 951–961.

Jimi, E., Nakamura, I., Amano, H., Taguchi, Y., Tsurukai, T., Tamura, M. et al. (1996). Osteoclast function is activated by osteoblastic cells through a mechanism involving cell-to-cell contact. *Endocrinology*, 137(5), 2187-2190.

Jonas, A. J., Greene, A. A., Smith, M. L., & Schneider, J. A. (1982). Cystine accumulation and loss in normal, heterozygous, and cystinotic fibroblasts. *Proceedings of the National Academy of Sciences of the United States of America*, *79*(14), 4442–4445.

Kalatzis, V., Cherqui, S., Antignac, C., & Gasnier, B. (2001). Cystinosin, the protein defective in cystinosis, is a H+-driven lysosomal cystine transporter. *EMBO Journal*, *20*(21), 5940–5949.

Kalipatnapu, S., & Chattopadhyay, A. (2005). Membrane protein solubilization: Recent advances and challenges in solubilization of serotonin1A receptors. *IUBMB Life*, *57*(7), 505–512.

Kanai, Y., Segawa, H., Miyamoto K., Uchino H., Takeda E., Endou, H. (1998). Expression Cloning and Characterization of a Transporter for Large Neutral Amino Acids Activated by the Heavy Chain of 4F2 Antigen (CD98)*. The Journal of Biological Chemistry, 273(37), 23629-23632.

Kasper, D., Planells-Cases, R., Fuhrmann, J. C., Scheel, O., Zeitz, O., Ruether, K., Jentsch, T. J. et al. (2005). Loss of the chloride channel CIC-7 leads to lysosomal storage disease and neurodegeneration. *EMBO Journal*, *24*(5), 1079–1091.

Kawaguchi, K., Okamoto, T., Morita, M., & Imanaka, T. (2016). Translocation of the ABC transporter ABCD4 from the endoplasmic reticulum to lysosomes requires the escort protein LMBD1. *Scientific Reports*, *6*(1), 30183.

Kim, M.-J., Han, S.-W., Lee, D.-W., Cha, Y., Lee, K.-H., Kim, T.-Y., Kim, T.-Y. et al. (2016). Splenomegaly and Its Associations with Genetic Polymorphisms and Treatment Outcome in Colorectal Cancer Patients Treated with Adjuvant FOLFOX. *Cancer Research and Treatment*, *48*(3), 990–997.

Kirk, P., Wilson, M. C., Heddle, C., Brown, M. H., Barclay, a. N., & Halestrap, a. P. (2000). CD147 is tightly associated with lactate transporters MCT1 and MCT4 and facilitates their cell surface expression. *The EMBO Journal*, *19*(15), 3896–3904.

Knittel, T., Neubauer, K., Armbrust, T., & Ramadori, G. (1995). Expression of von Willebrand factor in normal and diseased rat livers and in cultivated liver cells. *Hepatology*, *21*(2), 470–6.

Koltzscher, M., Neumann, C., Kö, S., & Gerke, V. (2003). Ca 2⁺ -dependent Binding and Activation of Dormant Ezrin by Dimeric S100P. *Molecular Biology of the Cell*, *14*(February), 2372–2384.

Kong, X. Y., Nesset, C. K., Damme, M., Løberg, E.-M., Lübke, T., Mæhlen, J., Eskild, W. et al. (2014). Loss of lysosomal membrane protein NCU-G1 in mice results in spontaneous liver fibrosis with accumulation of lipofuscin and iron in Kupffer cells. *Disease Models & Mechanisms*, *7*(3), 351–62.

Koni, P. A., Joshi, S. K., Temann, U. A., Olson, D., Burkly, L., & Flavell, R. A. (2001). Conditional vascular cell adhesion molecule 1 deletion in mice: impaired lymphocyte migration to bone marrow. *The Journal of Experimental Medicine*, *193*(6), 741–54.

Kornak, U., Kasper, D., Bösl, M. R., Kaiser, E., Schweizer, M., Schulz, a, Jentsch, T. J. et al. (2001). Loss of the ClC-7 chloride channel leads to osteopetrosis in mice and man. *Cell*, *104*(2), 205–15.

Kousi, M., Siintola, E., Dvorakova, L., Vlaskova, H., Turnbull, J., Topcu, M., … Lehesjoki, A. E. (2009). Mutations in CLN7/MFSD8 are a common cause of variant late-infantile neuronal ceroid lipofuscinosis. *Brain*, *132*(3), 810–819.

Kovacs, A. D., & Pearce, D. A. (2015). Finding the most appropriate mouse model of juvenile CLN3 (Batten) disease for therapeutic studies: the importance of genetic background and gender. *Disease Models & Mechanisms*, *8*(4), 351–361.

Kresse, H., Von Figura, K., & Klein, U. (1978). A New Biochemical Subtype of the Sanfilippo Syndrome: Characterization of the Storage Material in Cultured Fibroblasts of Sanfilippo C Patients. *European Journal of Biochemistry*, *92*(2), 333–339.

Kunkel, G. T., MacEyka, M., Milstien, S., & Spiegel, S. (2013). Targeting the sphingosine-1-phosphate axis in cancer, inflammation and beyond. *Nature Reviews Drug Discovery*, *12*(9), 688–702.

Kuo, T.-R., & Chen, C.-H. (2017). Bone biomarker for the clinical assessment of osteoporosis: recent developments and future perspectives. *Biomarker Research*, *5*(1), 18.

Lange, P. F., Wartosch, L., Jentsch, T. J., & Fuhrmann, J. C. (2006). ClC-7 requires Ostm1 as a beta-subunit to support bone resorption and lysosomal function. *Nature*, *440*(7081), 220–3.

Laplante, J. M., Falardeau, J., Sun, M., Kanazirska, M., Brown, E. M., Slaugenhaupt, S. A., & Vassilev, P. M. (2002). Identification and characterization of the single channel function of human mucolipin-1 implicated in mucolipidosis type IV , a disorder affecting the lysosomal pathway. *FEBS Letters*, *532*, 183–187.

Law, C. J., Maloney, P. C., & Wang, D. (2009). Ins and outs of Major Facilitator Superfamily

antiporters. *Annual Review of Microbiology*, (67), 289–305.

Leisle, L., Ludwig, C. F., Wagner, F. a, Jentsch, T. J., & Stauber, T. (2011). ClC-7 is a slowly voltage-gated 2Cl(-)/1H(+)-exchanger and requires Ostm1 for transport activity. *The EMBO Journal*, *30*(11), 2140–2152.

Li, L., Duan, M., Chen, W., Jiang, A., Li, X., Yang, J., & Li, Z. (2017). The spleen in liver cirrhosis: Revisiting an old enemy with novel targets. *Journal of Translational Medicine*, *15*(1), 1–10.

Liu, B., Du, H., Rutkowski, R., Gartner, A., & Wang, X. (2013). LAAT-1 is the lysosomal Lysine/Arginine transporter that maintains amino acid homeostasis. *Science*, *337*(6092), 351–354.

Malm, D. (2001). Alpha-Mannosidosis. *GeneReviews* , 1–19.

Mancini, G. M. S., Havelaar, A. C., & Verheijen, F. W. (2000). Lysosomal transport disorders. *Journal of Inherited Metabolic Disease*, *23*(3), 278–292.

Mann, D. A., & Oakley, F. (2013). Serotonin paracrine signaling in tissue fibrosis. *Biochimica et Biophysica Acta - Molecular Basis of Disease*, *1832*(7), 905–910.

Marger, M. D., & Saier, M. H. (1993). A major superfamily of transmembrane facilitators that catalyse uniport, symport and antiport. *Trends in Biochemical Sciences*, *18*(1), 13–20.

Marsh, M., Schmid, S., Kern, H., Harms, E., Male, P., Mellman, I., & Helenius, A. (1987). Rapid analytical and preparative isolation of functional endosomes by free flow electrophoresis. *Journal of Cell Biology*, *104*(4), 875–886.

Martinez-Hernandez, A., & Martinez, J. (1991). The role of capillarization in hepatic failure: Studies in carbon tetrachloride-induced cirrhosis. *Hepatology*, *14*(5), 864–874.

Mayer, A. L., Higgins, C. B., Heitmeier, M. R., Kraft, T. E., Qian, X., Crowley, J. R., Debosch, B. J. et al. (2016). SLC2A8 (GLUT8) is a mammalian trehalose transporter required for trehalose-induced autophagy. *Scientific Reports*, *6*(May), 1–15.

Mitchison, H. M., Bernard, D. J., Greene, N. D., Cooper, J. D., Junaid, M. A., Pullarkat, R. K., Nussbaum, R. L. et al. (1999). Targeted disruption of the Cln3 gene provides a mouse model for Batten disease. *Neurobiology of Disease*, 6, 321-334.

Mohty, M., Malard, F., Abecassis, M., Aerts, E., Alaskar, A. S., Aljurf, M., Carreras, E. et al. (2015). Sinusoidal obstruction syndrome/veno-occlusive disease: Current situation and perspectives - a position statement from the European Society for Blood and Marrow Transplantation (EBMT). *Bone Marrow Transplantation*, *50*(6), 781–789.

Morgan, M. Y., Marshall, A. W., Milsom, J. P., & Sherlock, S. (1982). Plasma amino-acid patterns in liver disease. *Gut*, *23*(5), 362–370.

Mori, T., Okanoue, T., Sawa, Y., Hori, N., Ohta, M., & Kagawa, K. (1993). Defenestration of the Sinusoidal Endothelial-Cell in a Rat Model of Cirrhosis. *Hepatology*, *17*(5), 891–897.

Morin, P., Sagné, C., & Gasnier, B. (2004). Functional characterization of wild-type and mutant human sialin. *The EMBO Journal*, *23*(23), 4560–4570.

Munroe, P. B., Mitchison, H. M., O'Rawe, A. M., Anderson, J. W., Boustany, R. M., Lerner, T. J., Mole, S. E. et al. (1997). Spectrum of mutations in the Batten disease gene, CLN3. *Am J Hum Genet.*, *61*(2), 310–316.

Nakhoul, N., & Batuman, V. (2011). Role of proximal tubules in the pathogenesis of kidney disease. *Experimental Models for Renal Diseases: Pathogenesis and Diagnosis*, *169*(1), 37–50.

Nesset, C. K., Kong, X. Y., Damme, M., Schjalm, C., Roos, N., Løberg, E. M., & Eskild, W. (2016). Age-dependent development of liver fibrosis in Glmp gt/gt mice. *Fibrogenesis & Tissue Repair*, *9*(1), 5.

Neufeld, E. B., Wastney, M., Patel, S., Suresh, S., Cooney, A. M., Dwyer, N. K., Blanchette-Mackie, E. J. et al. (1999). The Niemann-Pick C1 protein resides in a vesicular compartment linked to retrograde transport of multiple lysosomal cargo. *Journal of Biological Chemistry*, *274*(14), 9627–9635.

Nguyen, L. N., Ma, D., Shui, G., Wong, P., Cazenave-Gassiot, A., Zhang, X., Silver, D. L. et al. (2014a). Mfsd2a is a transporter for the essential omega-3 fatty acid docosahexaenoic acid. *Nature*, *509*(7501), 503–506.

Nguyen, L. N., Ma, D., Shui, G., Wong, P., Cazenave-Gassiot, A., Zhang, X., Silver, D. L. et al. (2014b). Mfsd2a is a transporter for the essential omega-3 fatty acid docosahexaenoic acid. *Nature*, *509*(7501), 503–506.

Nijnik, a., Clare, S., Hale, C., Chen, J., Raisen, C., Mottram, L., Hancock, R. E. W. et al. (2012). The Role of Sphingosine-1-Phosphate Transporter Spns2 in Immune System Function. *The Journal of Immunology*, *189*(1), 102–111.

Nishino, I., Fu, J., Tanji, K., Yamada, T., Shimojo, S., Koori, T., Hirano, M. et al. (2000). Primary LAMP-2 deficiency causes X-linked vacuolar cardiomyopathy and\nmyopathy (Danon disease). *Nature*, *406*(6798), 906–910.

Ohno, H., Nakatsu, Y., Sakoda, H., Kushiyama, A., Ono, H., Fujishiro, M., Asano, T. et al. (2011).

4F2hc stabilizes GLUT1 protein and increases glucose transport activity. *American journal of physiology-cell physiology* 300, 1047–1054.

Olbricht, C. J., Fink, M., & Gutjahr, E. (1991). Alterations in lysosomal enzymes of the proximal tubule in gentamicin nephrotoxicity. *Kidney International*, *39*(4), 639–646.

Overman, M. J., Maru, D. M., Charnsangavej, C., Loyer, E. M., Wang, H., Pathak, P., Kopetz, S. et al. (2010). Oxaliplatin-mediated increase in spleen size as a biomarker for the development of hepatic sinusoidal injury. *Journal of Clinical Oncology*, *28*(15), 2549–2555.

Palmieri, M., Impey, S., Kang, H., di Ronza, A., Pelz, C., Sardiello, M., & Ballabio, A. (2011). Characterization of the CLEAR network reveals an integrated control of cellular clearance pathways. *Human Molecular Genetics*, *20*(19), 3852–66.

Pangrazio, A., Poliani, P. L., Megarbane, A., Lefranc, G., Lanino, E., Di Rocco, M., Frattini, A. et al. (2006). Mutations in OSTM1 (grey lethal) define a particularly severe form of autosomal recessive osteopetrosis with neural involvement. *Journal of Bone and Mineral Research*, *21*(7), 1098–1105.

Pao, S. S., Paulsen, I. A. N. T., & Saier, M. H. (1998). Major Facilitator Superfamily. *Microbiology and molecular biology reviews*, *62*(1), 1–34.

Pardee, P. E., Dunn, W., Schwimmer, J. B. (2012). Nonalcoholic fatty liver disease is associated with low bone mineral density in obese children. *Alimentary pharmacology & Therapeutics*, 35(2), 248-254.

Parenti, G., Andria, G., & Ballabio, A. (2015). Lysosomal Storage Diseases: From Pathophysiology to Therapy. *Annual Review of Medicine*, *66*(1), 471–486.

Perland, E., Bagchi, S., Klaesson, A., & Fredriksson, R. (2017). Characteristics of 29 novel atypical solute carriers of major facilitator superfamily type: evolutionary conservation, predicted structure and neuronal co-expression. *Open Biology*, *7*(9), 170142.

Perland, E., Hellsten, S. V., Lekholm, E., Eriksson, M. M., Arapi, V., & Fredriksson, R. (2017). The Novel Membrane-Bound Proteins MFSD1 and MFSD3 are Putative SLC Transporters Affected by Altered Nutrient Intake. *Journal of Molecular Neuroscience*, *61*(2), 199–214.

Peters, C., & von Figura, K. (1994). Biogenesis of lysosomal membranes. *FEBS Letters*, *346*(1), 108–114.

Pineda, M., Fernández, E., Torrents, D., Estévez, R., López, C., Camps, M., … Palacín, M. (1999). Identification of a membrane protein, LAT-2, that co-expresses with 4F2 heavy chain, an

L-type amino acid transport activity with broad specificity for small and large zwitterionic amino acids. *Journal of Biological Chemistry*, *274*(28), 19738–19744.

Pinzani, M., Rosselli, M., & Zuckermann, M. (2011). Liver cirrhosis. *Best Practice and Research: Clinical Gastroenterology*, *25*(2), 281–290.

Pisoni, R. L., & Thoene, J. G. (1991). The transport systems of mammalian lysosomes. *BBA - Reviews on Biomembranes*, *1071*(4), 351–373.

Platt, F. M., Boland, B., & van der Spoel, A. C. (2012). Lysosomal storage disorders: The cellular impact of lysosomal dysfunction. *Journal of Cell Biology*, *199*(5), 723–734.

Pohorille, A., Schweighofer, K., Wilson, M. A. (2005). *Astrobiology*, 5(1), 1-17.

Poisson, J., Lemoinne, S., Boulanger, C., Durand, F., Moreau, R., Valla, D., & Rautou, P. E. (2017). Liver sinusoidal endothelial cells: Physiology and role in liver diseases. *Journal of Hepatology*, *66*(1), 212–227.

Quigley, J. G. & Khan, A. A. (2014). Heme and FLVCR-related transporter families SLC48 and SLC49. *Molecular aspects of medicine*, *34*, 669–682.

Quigley, J. G., Yang, Z., Worthington, M. T., Phillips, J. D., Sabo, K. M., Sabath, D. E., Abkowitz, J. L. et al. (2004). Identification of a human heme exporter that is essential for erythropoiesis. *Cell*, *118*(6), 757–766.

Quistgaard, E. M., Löw, C., Guettou, F., & Nordlund, P. (2016). Understanding transport by the major facilitator superfamily (MFS): structures pave the way. *Nature Reviews Molecular Cell Biology*, *17*, 123-132.

Ramirez-Montealegre, D., & Pearce, D. A. (2005). Defective lysosomal arginine transport in juvenile Batten disease. *Human Molecular Genetics*, *14*(23), 3759–3773.

Rath, A., Glibowicka, M., Nadeau, V. G., Chen, G., & Deber, C. M. (2009). Detergent binding explains anomalous SDS-PAGE migration of membrane proteins. *Proceedings of the National Academy of Sciences*, *106*(6), 1760–1765.

Reddy, V. S., Shlykov, M. a, Castillo, R., Sun, E. I., & Saier, M. H. (2013). The Major Facilitator Superfamily (Revisited). *The FEBS Journal*, *279*(11), 2022–2035.

Renlund, M., Tietze, F., Gahl, W. A., & Edwards, R. H. (1986). Defective sialic acid egress from isolated fibroblast lysosomes of patients with Salla disease. *Science*, *232*(4751), 759–62.

Robinson, S. M., Mann, J., Vasilaki, A., Mathers, J., Burt, A. D., Oakley, F., Mann, D. A. et al. (2013). Pathogenesis of FOLFOX induced sinusoidal obstruction syndrome in a murine chemotherapy model. *Journal of Hepatology*, *59*(2), 318–326.

Rodríguez, C. I., Buchholz, F., Galloway, J., Sequerra, R., Kasper, J., Ayala, R., Dymecki, S. M. et al. (2000). High-efficiency deleter mice show that FLPe is an alternative to Cre- loxP. *Nature Genetics*, *25*(2), 139–140.

Rome, L. H., Hill, D. F., Bame, K. J., & Crain, L. R. (1983). Utilization of exogenously added acetyl coenzyme A by intact isolated lysosomes. *Journal of Biological Chemistry*, *258*(5), 3006–3011.

Roodman, G. D. (1993). Role of cytokines in the regulation of bone resorption. *Calcified Tissue International*, *53*(1 Supplement), 94–98.

Roscioli, T., Cliffe, S. T., Bloch, D. B., Bell, C. G., Mullan, G., Taylor, P. J., Buckley, M. F. et al. (2006). Mutations in the gene encoding the PML nuclear body protein Sp110 are associated with immunodeficiency and hepatic veno-occlusive disease. *Nature Genetics*, *38*(6), 620–622.

Rosen, H. N., Moses, A. C., Garber, J., Iloputaife, I. D., Ross, D. S., Lee, S. L., & Greenspan, S. L. (2000). Serum CTX: A new marker of bone resorption that shows treatment effect more often than other markers because of low coefficient of variability and large changes with bisphosphonate therapy. *Calcified Tissue International*, *66*(2), 100–103.

Rosenblatt, D., Hosack, A., Matiaszuk, N., Cooper, B., & Laframboise, R. (1985). Defect in vitamin B12 release from lysosomes: newly described inborn error of vitamin B12 metabolism. *Science*, *228*(4705), 1319–1321.

Ruddell, R. G., Mann, D. A., & Ramm, G. A. (2008). The function of serotonin within the liver. *Journal of Hepatology*, *48*(4), 666–675.

Ruivo, R., Anne, C., Sagné, C., & Gasnier, B. (2009). Molecular and cellular basis of lysosomal transmembrane protein dysfunction. *Biochimica et Biophysica Acta - Molecular Cell Research*, *1793*(4), 636–649.

Rutsch, F., Gailus, S., Miousse, I. R., Suormala, T., Sagné, C., Toliat, M. R., Nürnberg, P. et al. (2009). Identification of a putative lysosomal cobalamin exporter altered in the cblF defect of vitamin B12 metabolism. *Nature Genetics*, *41*(2), 234–239.

Sabatini, D. M. (2017). Twenty-five years of mTOR: Uncovering the link from nutrients to growth. *Proceedings of the National Academy of Sciences*, *0*, 201716173.

Sadée, W., Drübbisch, V., & Amidon, G. (1995). Biology of membrane transport proteins. *Pharmaceutical Research*, 12(12), 1823-1837.

Safaei, A., Oskouie, A. A., Mohebbi, S. R., Rezaei-Tavirani, M., Mahboubi, M., Peyvandi, M.,

Zamanian-Azodi, M. et al. (2016). Metabolomic analysis of human cirrhosis, hepatocellular carcinoma, non-alcoholic fatty liver disease and non-alcoholic steatohepatitis diseases. *Gastroenterology and Hepatology from Bed to Bench*, *9*(3), 158–173.

Saftig, P., & Klumperman, J. (2009). Lysosome biogenesis and lysosomal membrane proteins: trafficking meets function. *Nature Reviews. Molecular Cell Biology*, *10*(9), 623–635.

Sagné, C., Agulhon, C., Ravassard, P., Darmon, M., Hamon, M., El Mestikawy, S., Giros, B. et al. (2001). Identification and characterization of a lysosomal transporter for small neutral amino acids. *Proceedings of the National Academy of Sciences of the United States of America*, *98*(13), 7206–11.

Sardiello, M., Palmieri, M., di Ronza, A., Medina, D. L., Valenza, M., Gennarino, V.A. et al. (2009). A gene network regulating lysosomal biogenesis and function. *Science*, 325(5939):473-477.

Savalas, L. R. T., Gasnier, B., Damme, M., Lübke, T., Wrocklage, C., Debacker, C., Schröder, B. et al. (2011). Disrupted in renal carcinoma 2 (DIRC2), a novel transporter of the lysosomal membrane, is proteolytically processed by cathepsin L. *Biochemical Journal*, *439*(1), 113–128.

Schieweck, O., Damme, M., Schröder, B., Hasilik, A., Schmidt, B., & Lübke, T. (2009). NCU-G1 is a highly glycosylated integral membrane protein of the lysosome. *Biochemical Journal*, *422*(1), 83–90.

Schlaeger, T. M., Bartunkova, S., Lawitts, J. A., Teichmann, G., Risau, W., Deutsch, U., & Sato, T. N. (1997). Uniform vascular-endothelial-cell-specific gene expression in both embryonic and adult transgenic mice. *Proceedings of the National Academy of Sciences of the United States of America*, *94*(7), 3058–63.

Schmidt, S., Joost, H.-G., & Schurmann, A. (2009). GLUT8, the enigmatic intracellular hexose transporter. *AJP: Endocrinology and Metabolism*, *296*(4), E614–E618.

Schneppenheim, J., Dressel, R., Hüttl, S., Lüllmann-Rauch, R., Engelke, M., Dittmann, K., Schröder, B. et al. (2013). The intramembrane protease SPPL2a promotes B cell development and controls endosomal traffic by cleavage of the invariant chain. *The Journal of Experimental Medicine*, *210*(1), 41–58.

Schwenk, F., Baron, U., & Rajewsky, K. (1995). A cre-transgenic mouse strain for the ubiquitous deletion of loxP-flanked gene segments including deletion in germ cells. *Nucleic Acids*

Research, *23*(24), 5080–5081.

Settembre, C., Fraldi, A., Medina, D. L., Ballabio, A., & Children, T. (2015). Signals for the lysosome: a control center for cellular clearance and energy metabolism. *Nature Reviews. Molecular Cell Biology*, *14*(5), 283–296.

Shahani, T., Covens, K., Lavend'homme, R., Jazouli, N., Sokal, E., Peerlinck, K., & Jacquemin, M. (2014). Human liver sinusoidal endothelial cells but not hepatocytes contain factor? VIII. *Journal of Thrombosis and Haemostasis*, *12*(1), 36–42.

Siintola, E., Topcu, M., Aula, N., Lohi, H., Minassian, B. A., Paterson, A. D., Lehesjoki, A.-E. et al. (2007). The Novel Neuronal Ceroid Lipofuscinosis Gene MFSD8 Encodes a Putative Lysosomal Transporter. *The American Journal of Human Genetics*, *81*(1), 136–146.

Sørensen, K. K., Simon-Santamaria, J., McCuskey, R. S., & Smedsrød, B. (2015). Liver sinusoidal endothelial cells. *Comprehensive Physiology*, *5*(4), 1751–1774.

Sreedharan, S., Stephansson, O., Schiöth, H. B., & Fredriksson, R. (2011). Long evolutionary conservation and considerable tissue specificity of several atypical solute carrier transporters. *Gene*, *478*(1–2), 11–18.

Srinivas, S., Watanabe, T., Lin, C. S., William, C. M., Tanabe, Y., Jessell, T. M., & Costantini, F. (2001). Cre reporter strains produced by targeted insertion of EYFP and ECFP into the ROSA26 locus. *BMC Developmental Biology*, *1*, 1–8.

Stauber, T., & Jentsch, T. J. (2010). Sorting motifs of the endosomal/lysosomal CLC chloride transporters. *Journal of Biological Chemistry*, *285*(45), 34537–34548.

Steenhuis, P., Froemming, J., Reinheckel, T., & Storch, S. (2012). Proteolytic cleavage of the disease-related lysosomal membrane glycoprotein CLN7. *Biochimica et Biophysica Acta - Molecular Basis of Disease*, *1822*(10), 1617–1628.

Steffensen, K. R., Bouzga, M., Skjeldal, F., Kasi, C., Karahasan, A., Matre, V., Eskild, W. et al. (2007). Human NCU-G1 can function as a transcription factor and as a nuclear receptor co-activator. *BMC Molecular Biology*, *8*, 1–15.

Steinberg, B. E., Huynh, K. K., Brodovitch, A., Jabs, S., Stauber, T., Jentsch, T. J., & Grinstein, S. (2010). A cation counterflux supports lysosomal acidification. *Journal of Cell Biology*, *189*(7), 1171–1186.

Sternberg, N. (1981). Bacteriophage P1 site-specific recombination. *Journal of Molecular Biology*, *150*(4), 603–608.

Stogmann, E., El Tawil, S., Wagenstaller, J., Gaber, A., Edris, S., Abdelhady, A., … Zimprich, A.

(2009). A novel mutation in the MFSD8 gene in late infantile neuronal ceroid lipofuscinosis. *Neurogenetics*, *10*(1), 73–77.

Sun, M., Goldin, E., Stahl, S., Falardeau, J. L., Kennedy, J. C., Acierno, J. S., Slaugenhaupt, S. A. et al. (2000). Mucolipidosis type IV is caused by mutations in a gene encoding a novel transient receptor potential channel. *Human Molecular Genetics*, *9*(17), 2471–2478.

Susca, M., Grassi, A., Zauli, D., Volta, U., Lenzi, M., Marchesini, G., et al. (2001). Liver inflammatory cells, apoptosis, regeneration and stellate cell activation in NASH. *Digestive and Liver Disease*, *33*, 768–777.

Takamori, S., Malherbe, P., Broger, C., & Jahn, R. (2002). Molecular cloning and functional characterization of human vesicular glutamate transporter 3. *EMBO Reports*, *3*(8), 798–803.

Takanaga, H., & Frommer, W. B. (2010). Facilitative plasma membrane transporters function during ER transit. *The FASEB Journal*, *24*(8), 2849–2858.

Tanaka, Y., Guhde, G., Suter, A., Eskelinen, E. L., Hartmann, D., Lüllmann-Rauch, R., Saftig, P. et al. (2000). Accumulation of autophagic vacuoles and cardiomyopathy LAMP-2-deficient mice. *Nature*, *406*(6798), 902–906.

Tang, Y., Harrington, A., Yang, X., Friesel, R. E., & Liaw, L. (2010). The contribution of the Tie2+ lineage to primitive and definitive hematopoietic cells. *Genesis*, *48*(9), 563–567.

Town, M., Jean, G., Cherqui, S., Attard, M., Forestier, L., Whitmore S. A. et al. (1998). A novel gene encoding an integral membrane protein is mutated in nephropatic cystinosis. *Nature Genetics*, *18*, 319-324.

Tripp, R. A., Topham, D. J., Watson, S. R., & Doherty, P. C. (1997). Bone marrow can function as a lymphoid organ during a primary immune response under conditions of disrupted lymphocyte trafficking. *Journal of Immunology*, *158*(8), 3716–20.

Tulkens, P. M. (1999). Aminoglycosides : Nephrotoxicity. *Antimicrobial agents and chemotherapy*, *43*(5), 1003–1012.

Turner, N. A., & Moake, J. L. (2015). Factor VIII is synthesized in human endothelial cells, packaged in weibel-palade bodies and secreted bound to ULVWF strings. *PLoS ONE*, *10*(10), 1–28.

Udagawa, N., Takahashi, N., Jimi, E., Matsuzaki, K., Tsurukai, T., Itoh, K., Suda, T. et al. (1999). Osteoblasts/stromal cells stimulate osteoclast activation through expression of osteoclast differentiation factor/RANKL but not macrophage colony-stimulating factor.

Bone, *25*(5), 517–523.

Valianpour, F., Abeling, N. G. G. M., Duran, M., Huijmans, J. G. M., & Kulik, W. (2004). Quantification of Free Sialic Acid in Urine by HPLC-Electrospray Tandem Mass Spectrometry: A Tool for the Diagnosis of Sialic Acid Storage Disease. *Clinical Chemistry*, *50*(2), 403–409.

Walkley, S. U., & Vanier, M. T. (2009). Secondary lipid accumulation in lysosomal disease. *Biochimica et Biophysica Acta - Molecular Cell Research*, *1793*(4), 726–736.

Wang, X., Wei, W., Krzenszinski, J. Y., Wang, Y., Wan, Y., (2015). A liver-bone endocrine relay by IGFBP1 promotes osteoclastogenesis and mediates FGF21-induced bone resorption. *Cell metabolism*, 22(5), 811-824.

Wang, X., Kanel, G. C., & DeLeve, L. D. (2000). Support of sinusoidal endothelial cell glutathione prevents hepatic veno-occlusive disease in the rat. *Hepatology*, *31*(2), 428–34.

Watanabe, M. (1978). Drug-induced lysosomal changes and nephrotoxicity i n rats Mitsutoshi. *Acta pathology Japan*, *28*(6), 867–889.

Wattiaux, R., Wibo, M., Baudhuin, P., (1963). Effect of the injection of Triton WR 1339 on the hepatic lysosomes of the rat. Arch Int Physiol Biochim, 71, 140-142.

Wattiaux, R., Jadot, M., Dubois, F., & Wattiaux-De Coninck, S. (1996). Phagocytosis by rat liver: Relationships between phagosomes and lysosomes. *Biochemical and Biophysical Research Communications*, *220*(3), 569–574.

White, C., Yuan, X., Schmidt, P., Bresciani, E., Samuel, T., Campagna, D., Hall, C., et al. (2013). *Cell metabolism*, 17(2) 261-270.

Wilke, S., Krausze, J., & Büssow, K. (2012). Crystal structure of the conserved domain of the DC lysosomal associated membrane protein: implications for the lysosomal glycocalyx. *BMC Biology*, *10*(1), 62.

Wilson, M. C., Meredith, D., & Halestrap, A. P. (2002). Fluorescence resonance energy transfer studies on the interaction between the lactate transporter MCT1 and CD147 provide information on the topology and stoichiometry of the complex in Situ. *Journal of Biological Chemistry*, *277*(5), 3666–3672.

Winchester, B. (2005). Lysosomal metabolism of glycoproteins. *Glycobiology*, *15*(6), 1–15.

Wisse, E., de Zanger, R. B., Charels, K., van der Smissen, P., & McCuskey, R. S. (1985). The liver sieve: Considerations concerning the structure and function of endothelial fenestrae, the sinusoidal wall and the space of disse. *Hepatology*, *5*(4), 683–692.

Wu, Y., Yang, M., Fan, J., Peng, Y., Deng, L., Ding, Y., Fu, Q. et al. (2014). Deficiency of osteoblastic Arl6ip5 impaired osteoblast differentiation and enhanced osteoclastogenesis via disturbance of ER calcium homeostasis and induction of ER stress-mediated apoptosis. *Cell Death and Disease*, *5*(10).

Wyant, G. A., Abu-Remaileh, M., Wolfson, R. L., Chen, W. W., Freinkman, E., Danai, L. V., … Sabatini, D. M. (2017). mTORC1 Activator SLC38A9 Is Required to Efflux Essential Amino Acids from Lysosomes and Use Protein as a Nutrient. *Cell*, *171*(3), 642–654.e12.

Yamayoshi, S., Yamashita, Y., Li, J., Hanagata, N., Minowa, T., Takemura, T., & Koike, S. (2009). Scavenger receptor B2 is a cellular receptor for enterovirus 71. *Nature Medicine*, *15*(7), 798–801.

Yan, N. (2015). Structural Biology of the Major Facilitator Superfamily Transporters. *Annual Review of Biophysics*, *44*(1), 257–283.

Yang, H. J., Shim, S. G., Ma, B. O., & Kwak, J. Y. (2016). Association of nonalcoholic fatty liver disease with bone mineral density and serum osteocalcin levels in Korean men. *European Journal of Gastroenterology & Hepatology*, *28*(3), 338–344.

Yang, T. T., Sinai, P., Green, G., Kitts, P. A., Chen, Y. T., Lybarger, L., Kain, S. R. et al. (1998). Improved fluorescence and dual color detection with enhanced blue and green variants of the green fluorescent protein. *Journal of Biological Chemistry*, *273*(14), 8212–8216.

Yin, T., & Li, L. (2006). Review series The stem cell niches in bone. *Journal of Clinical Investigation*, *116*(5), 1195–1201.

Zhao, E., Xu, H., Wang, L., Kryczek, I., Wu, K., Hu, Y., Zou, W. et al. (2012). Bone marrow and the control of immunity. *Cellular and Molecular Immunology*, *9*(1), 11–19.

6 Supplement

6.1 Supplemental tables

UniProt Accession Number	Gene ID	Description	Fold change KO/WT	p-value
P31725	S100a9	Protein S100-A9	4,853	0,006
P10107	Anxa1	Annexin A1	4,373	0,000
P20152	Vim	Vimentin	3,466	0,000
Q80X19	Col14a1	Collagen alpha-1(XIV) chain	3,257	0,001
Q8BTM8	Flna	Filamin-A	3,254	0,008
P19324	Serpinh1	Serpin H1	3,016	0,003
P04117	Fabp4	Fatty acid-binding protein, adipocyte	2,581	0,011
P15331	Prph	Peripherin	2,552	0,000
Q63836	Selenbp2	Selenium-binding protein 2	2,405	0,029
Q6IRU2	Tpm4	Tropomyosin alpha-4 chain	2,369	0,005
Q05144	Rac2	Ras-related C3 botulinum toxin substrate 2	2,294	0,001
P16110	Lgals3	Galectin-3	2,262	0,000
P19639	Gstm3	Glutathione S-transferase Mu 3	2,186	0,010
Q8QZR1	Tat	Tyrosine aminotransferase	2,183	0,020
P07356	Anxa2	Annexin A2	2,159	0,005
Q91VC3	Eif4a3	Eukaryotic initiation factor 4A-III	2,116	0,000
P51885	Lum	Lumican	2,115	0,001
P31001	Des	Desmin	2,104	0,001
P52480	Pkm	Pyruvate kinase PKM	2,091	0,000
P21107	Tpm3	Tropomyosin alpha-3 chain	2,040	0,030
P43275	Hist1h1a	Histone H1.1	1,993	0,010
Q8R0W0	Eppk1	Epiplakin	1,980	0,009
O08638	Myh11	Myosin-11	1,899	0,002
Q923B6	Steap4	Metalloreductase STEAP4	1,874	0,002
P26041	Msn	Moesin	1,870	0,005
P43276	Hist1h1b	Histone H1.5	1,867	0,003
Q61879	Myh10	Myosin-10	1,863	0,029
Q61646	Hp	Haptoglobin	1,857	0,017
Q9DAK9	Phpt1	14 kDa phosphohistidine phosphatase	1,851	0,048
P42225	Stat1	Signal transducer and activator of transcription 1	1,847	0,006
Q6URW6	Myh14	Myosin-14	1,829	0,001
Q91X72	Hpx	Hemopexin	1,828	0,006
P11276	Fn1	Fibronectin	1,789	0,002
O08553	Dpysl2	Dihydropyrimidinase-related protein 2	1,788	0,008
A6X935	Itih4	Inter alpha-trypsin inhibitor, heavy chain 4	1,709	0,004
Q9Z1Q5	Clic1	Chloride intracellular channel protein 1	1,706	0,004
P99024	Tubb5	Tubulin beta-5 chain	1,703	0,000
P48036	Anxa5	Annexin A5	1,693	0,014
P13020	Gsn	Gelsolin	1,689	0,005
P28661	Sept4	Septin-4	1,656	0,004
Q99JI6	Rap1b	Ras-related protein Rap-1b	1,645	0,018
O35639	Anxa3	Annexin A3	1,637	0,011
P08752	Gnai2	Guanine nucleotide-binding protein G(i) subunit alpha-2	1,628	0,002
Q61207	Psap	Prosaposin	1,628	0,007
Q02788	Col6a2	Collagen alpha-2(VI) chain	1,621	0,009
P05064	Aldoa	Fructose-bisphosphate aldolase A	1,608	0,011
P47753	Capza1	F-actin-capping protein subunit alpha-1	1,607	0,001
P26039	Tln1	Talin-1	1,605	0,003
P07724	Alb	Serum albumin	1,593	0,012
O70400	Pdlim1	PDZ and LIM domain protein 1	1,592	0,049
Q8VDD5	Myh9	Myosin-9	1,589	0,001
Q8K0E8	Fgb	Fibrinogen beta chain	1,587	0,001
Q61233	Lcp1	Plastin-2	1,584	0,005
Q9Z2V4	Pck1	Phosphoenolpyruvate carboxykinase, cytosolic [GTP]	1,578	0,003
Q08857	Cd36	Platelet glycoprotein 4	1,571	0,002

P68510	Ywhah	14-3-3 protein eta	1,568	0,012
Q8VCI0	Plbd1	Phospholipase B-like 1	1,562	0,009
Q4KML4	3110003A17Rik; Abracl	Costars family protein ABRACL	1,553	0,028
Q8CI94	Pygb	Glycogen phosphorylase, brain form	1,539	0,000
Q64727	Vcl	Vinculin	1,538	0,003
Q60605	Myl6	Myosin light polypeptide 6	1,531	0,003
P40124	Cap1	Adenylyl cyclase-associated protein 1	1,519	0,001
P18760	Cfl1	Cofilin-1	1,514	0,001
P45376	Akr1b3	Aldose reductase	1,513	0,001
P09055	Itgb1	Integrin beta-1	1,510	0,000
Q9WVJ3	Cpq; Pgcp	Carboxypeptidase Q	1,504	0,002
Q9D662	Sec23b	Protein transport protein Sec23B	1,501	0,002
Q00623	Apoa1	Apolipoprotein A-I	1,496	0,012
P39061	Col18a1	Collagen alpha-1(XVIII) chain	1,492	0,006
Q61147	Cp	Ceruloplasmin	1,488	0,007
Q9JJU8	Sh3bgrl	SH3 domain-binding glutamic acid-rich-like protein	1,481	0,002
Q9QXC1	Fetub	Fetuin-B	1,469	0,003
Q8C1B7	Sept11	Septin-11	1,467	0,004
Q8CHH9	Sept8	Septin-8	1,467	0,004
Q9WV32	Arpc1b	Actin-related protein 2/3 complex subunit 1B	1,462	0,009
P21981	Tgm2	Protein-glutamine gamma-glutamyltransferase 2	1,453	0,021
P60710	Actb	Actin, cytoplasmic 1	1,453	0,050
P63260	Actg1	Actin, cytoplasmic 2	1,453	0,050
Q62465	Vat1	Synaptic vesicle membrane protein VAT-1 homolog	1,449	0,004
O55222	Ilk	Integrin-linked protein kinase	1,448	0,007
O08677	Kng1	Kininogen-1	1,447	0,003
P68369	Tuba1a	Tubulin alpha-1A chain	1,438	0,007
P68373	Tuba1c	Tubulin alpha-1C chain	1,438	0,007
P05214	Tuba3b; Tuba3a	Tubulin alpha-3 chain	1,438	0,007
Q5SWU9	Acaca	Acetyl-CoA carboxylase 1	1,436	0,002
Q62318	Trim28	Transcription intermediary factor 1-beta	1,431	0,013
Q61235	Sntb2	Beta-2-syntrophin	1,431	0,002
P62962	Pfn1	Profilin-1	1,426	0,007
Q60854	Serpinb6a	Serpin B6	1,407	0,002
Q6PDN3	Mylk	Myosin light chain kinase, smooth muscle	1,404	0,002
P04186	Cfb	Complement factor B	1,402	0,001
P68433	Hist1h3i; Hist1h3a; Hist1h3g; Hist1h3h	Histone H3.1	1,397	0,034
P84228	Hist1h3d; Hist1h3f; Hist2h3c1; Hist2h3b; Hist2h3c2; Hist1h3c; Hist1h3e; Hist1h3b	Histone H3.2	1,397	0,034
Q9QXS1	Plec	Plectin	1,386	0,001
O89020	Afm	Afamin	1,382	0,044
P14733	Lmnb1	Lamin-B1	1,380	0,026
P58044	Idi1; LOC102635781; Gm38481	Isopentenyl-diphosphate Delta-isomerase 1	1,379	0,010
P10649	Gstm1	Glutathione S-transferase Mu 1	1,376	0,011
Q01279	Egfr	Epidermal growth factor receptor	1,369	0,045
Q3UTJ2	Sorbs2	Sorbin and SH3 domain-containing protein 2	1,367	0,002
P60122	Ruvbl1	RuvB-like 1	1,366	0,006
Q9QXG4	Acss2	Acetyl-coenzyme A synthetase, cytoplasmic	1,358	0,046
P70333	Hnrnph2	Heterogeneous nuclear ribonucleoprotein H2	1,357	0,007
Q9JIK5	Ddx21	Nucleolar RNA helicase 2	1,357	0,012
P63001	Rac1	Ras-related C3 botulinum toxin substrate 1	1,357	0,046
P62874	Gnb1	Guanine nucleotide-binding protein G(I)/G(S)/G(T) subunit beta-1	1,356	0,002
O35660	Gstm6	Glutathione S-transferase Mu 6	1,353	0,010
Q61838	Pzp	Pregnancy zone protein	1,349	0,031
P06728	Apoa4	Apolipoprotein A-IV	1,348	0,045
P11679	Krt8	Keratin, type II cytoskeletal 8	1,347	0,012
P50516	Atp6v1a	V-type proton ATPase catalytic subunit A	1,346	0,005
O55131	Sept7	Septin-7	1,345	0,034
Q921I1	Trf	Serotransferrin	1,345	0,015
Q62261	Spnb2; Sptbn1	Spectrin beta chain, non-erythrocytic 1	1,343	0,004
Q00896	Serpina1c	Alpha-1-antitrypsin 1-3	1,341	0,032
P07758	Serpina1a	Alpha-1-antitrypsin 1-1	1,341	0,032

E9PV24	Fga	Fibrinogen alpha chain	1,336	0,003
P10605	Ctsb	Cathepsin B	1,335	0,010
Q9WTI7	Myo1c	Unconventional myosin-Ic	1,330	0,006
O09159	Man2b1	Lysosomal alpha-mannosidase	1,329	0,004
P68254	Ywhaq;	14-3-3 protein theta	1,323	0,005
Q9CY64	Blvra	Biliverdin reductase A	1,323	0,037
Q9JLQ0	Cd2ap	CD2-associated protein	1,319	0,007
P63101	Ywhaz	14-3-3 protein zeta/delta	1,319	0,008
Q9DCD0	Pgd	6-phosphogluconate dehydrogenase, decarboxylating	1,317	0,008
Q9Z1F9	Uba2	SUMO-activating enzyme subunit 2	1,316	0,003
O88342	Wdr1	WD repeat-containing protein 1	1,314	0,000
P06909	Cfh	Complement factor H	1,311	0,010
P47757	Capzb	F-actin-capping protein subunit beta	1,310	0,014
P83940	Tceb1; Eloc;	Transcription elongation factor B polypeptide 1	1,306	0,002
Q80UG5	Sept9	Septin-9	1,304	0,007
P46425	Gstp2	Glutathione S-transferase P 2	1,303	0,036
P19157	Gstp1	Glutathione S-transferase P 1	1,298	0,028
Q9DCP2	Slc38a3	Sodium-coupled neutral amino acid transporter 3	1,296	0,036
Q8C650	Sept10	Septin-10	1,293	0,046
Q80X90	Flnb	Filamin-B	1,289	0,000
Q64459	Cyp3a11	Cytochrome P450 3A11	1,283	0,046
Q07076	Anxa7	Annexin A7	1,279	0,004
P62880	Gnb2	Guanine nucleotide-binding protein G(I)/G(S)/G(T) subunit beta-2	1,278	0,027
Q91V92	Acly	ATP-citrate synthase	1,275	0,024
Q93092	Taldo1	Transaldolase	1,275	0,017
P54071	Idh2	Isocitrate dehydrogenase [NADP], mitochondrial	1,274	0,023
P00493	Hprt	Hypoxanthine-guanine phosphoribosyltransferase	1,270	0,001
P22599	Serpina1b	Alpha-1-antitrypsin 1-2	1,270	0,049
P05784	Krt18	Keratin, type I cytoskeletal 18	1,263	0,021
P27046	Man2a1	Alpha-mannosidase 2	1,262	0,048
O70492	Snx3	Sorting nexin-3	1,261	0,038
P19096	Fasn	Fatty acid synthase	1,258	0,001
P47754	Capza2	F-actin-capping protein subunit alpha-2	1,251	0,002
P39054	Dnm2	Dynamin-2	1,251	0,000
Q99JY9	Actr3	Actin-related protein 3	1,246	0,010
Q3B7Z2	Osbp	Oxysterol-binding protein 1	1,246	0,036
P70168	Kpnb1	Importin subunit beta-1	1,245	0,013
Q921F2	Tardbp	TAR DNA-binding protein 43	1,242	0,018
Q9QXK3	Copg2	Coatomer subunit gamma-2	1,241	0,022
O70133	Dhx9	ATP-dependent RNA helicase A	1,241	0,001
P61290	Psme3	Proteasome activator complex subunit 3	1,235	0,005
Q8BP47	Nars	Asparagine--tRNA ligase, cytoplasmic	1,233	0,012
P17751	Tpi1	Triosephosphate isomerase	1,229	0,017
P53810	Pitpna	Phosphatidylinositol transfer protein alpha isoform	1,215	0,007
Q9JHJ0	Tmod3	Tropomodulin-3	1,212	0,015
Q9WU78	Pdcd6ip	Programmed cell death 6-interacting protein	1,210	0,049
P22892	Ap1g1	AP-1 complex subunit gamma-1	1,210	0,035
Q9JHU4	Dync1h1	Cytoplasmic dynein 1 heavy chain 1	1,206	0,005
P51855	Gss	Glutathione synthetase	1,203	0,048
Q61990	Pcbp2	Poly(rC)-binding protein 2	1,202	0,039
P21278	Gna11	Guanine nucleotide-binding protein subunit alpha-11	1,197	0,016
P32883	Kras	GTPase KRas	1,196	0,023
P63085	Mapk1	Mitogen-activated protein kinase 1	1,193	0,007
Q99LM2	Cdk5rap3	CDK5 regulatory subunit-associated protein 3	1,191	0,028
Q9CZE3	Rab32	Ras-related protein Rab-32	1,191	0,015
P68037	Ube2l3; Gm10705	Ubiquitin-conjugating enzyme E2 L3	1,190	0,049
Q9D0E1	Hnrnpm	Heterogeneous nuclear ribonucleoprotein M	1,189	0,024
P70398	Usp9x	Probable ubiquitin carboxyl-terminal hydrolase FAF-X	1,189	0,003
P09405	Ncl	Nucleolin	1,187	0,047
Q9CYR6	Pgm3	Phosphoacetylglucosamine mutase	1,182	0,029
Q9JJ28	Flii	Protein flightless-1 homolog	1,178	0,009
P68368	Tuba4a	Tubulin alpha-4A chain	1,175	0,039
P46735	Myo1b	Unconventional myosin-Ib	1,174	0,001
P62827	LOC100045999; Ran;	GTP-binding nuclear protein Ran	1,172	0,045
P97384	Anxa11	Annexin A11	1,167	0,015
Q6ZQI3	Mlec	Malectin	1,166	0,033
P59999	Arpc4	Actin-related protein 2/3 complex subunit 4	1,163	0,000

Q9DBJ1	Pgam1	Phosphoglycerate mutase 1	1,163	0,024
Q60930	Vdac2	Voltage-dependent anion-selective channel protein 2	1,161	0,004
P10648	Gsta2	Glutathione S-transferase A2	1,161	0,029
P13745	Gsta1	Glutathione S-transferase A1	1,161	0,029
P47791	Gsr	Glutathione reductase, mitochondrial	1,160	0,039
O55023	Impa1	Inositol monophosphatase 1	1,158	0,031
O70250	Pgam2	Phosphoglycerate mutase 2	1,153	0,029
Q8CHR6	Dpyd	Dihydropyrimidine dehydrogenase [NADP(+)]	1,147	0,028
Q9JIF7	Copb1	Coatomer subunit beta	1,143	0,023
Q9QZE5	Copg; Copg1	Coatomer subunit gamma-1	1,141	0,047
Q6P1B1	Xpnpep1	Xaa-Pro aminopeptidase 1	1,139	0,044
Q80W21	Gstm7	Glutathione S-transferase Mu 7	1,137	0,020
Q9D358	Acp1; LOC631286;	Low molecular weight phosphotyrosine protein phosphatase	1,127	0,016
Q9Z1Z0	Uso1	General vesicular transport factor p115	1,118	0,001
P09411	Pgk1	Phosphoglycerate kinase 1	1,114	0,033
P06745	Gpi1	Glucose-6-phosphate isomerase	1,107	0,029
Q922E4	Pcyt2	Ethanolamine-phosphate cytidylyltransferase	1,102	0,035
P40142	Tkt	Transketolase	1,095	0,001
P80318	Cct3	T-complex protein 1 subunit gamma	1,094	0,029
P35278	Rab5c	Ras-related protein Rab-5C	1,092	0,032
Q91VI7	Rnh1	Ribonuclease inhibitor	1,082	0,035
Q61176	Arg1	Arginase-1	1,071	0,015
Q8VBW8	Ttc36	Tetratricopeptide repeat protein 36	-1,056	0,011
Q64133	Maoa	Amine oxidase [flavin-containing] A	-1,070	0,027
P50580	Pa2g4	Proliferation-associated protein 2G4	-1,099	0,039
Q8CGK3	Lonp1	Lon protease homolog, mitochondrial	-1,099	0,015
Q9QY30	Abcb11	Bile salt export pump	-1,108	0,029
Q9WVD5	Slc25a15	Mitochondrial ornithine transporter 1	-1,122	0,042
Q9Z2I0	Letm1	LETM1 and EF-hand domain-containing protein 1, mitochondrial	-1,127	0,042
Q9QYG0	Ndrg2	Protein NDRG2	-1,128	0,007
P50295	Nat2	Arylamine N-acetyltransferase 2	-1,139	0,039
Q9Z2I8	Suclg2	Succinate--CoA ligase [GDP-forming] subunit beta, mitochondrial	-1,141	0,036
Q60759	Gcdh	Glutaryl-CoA dehydrogenase, mitochondrial	-1,149	0,024
Q9EQ20	Aldh6a1	Methylmalonate-semialdehyde dehydrogenase [acylating], mitochondrial	-1,160	0,003
P06801	Me1	NADP-dependent malic enzyme	-1,161	0,024
Q8VCZ9	Prodh2	Probable proline dehydrogenase 2	-1,173	0,029
Q06185	Atp5k	ATP synthase subunit e, mitochondrial	-1,182	0,032
Q8BMS1	Hadha	Trifunctional enzyme subunit alpha, mitochondrial	-1,184	0,004
Q99JW2	Acy1	Aminoacylase-1	-1,231	0,049
P53808	Pctp	Phosphatidylcholine transfer protein	-1,232	0,029
O88451	Rdh7	Retinol dehydrogenase 7	-1,234	0,010
Q60936	Adck3; Coq8a	Atypical kinase COQ8A, mitochondrial	-1,238	0,010
O09172	Gclm	Glutamate--cysteine ligase regulatory subunit	-1,248	0,008
Q9QZ85	Iigp1; Iigp1b	Interferon-inducible GTPase 1	-1,248	0,007
Q99L20	Gstt3	Glutathione S-transferase theta-3	-1,252	0,037
Q9WTP6	Ak2	Adenylate kinase 2, mitochondrial	-1,271	0,031
P52760	Hrsp12; Rida	Ribonuclease UK114	-1,278	0,018
O08601	Mttp	Microsomal triglyceride transfer protein large subunit	-1,292	0,049
Q8BWQ1	Ugt2a3	UDP-glucuronosyltransferase 2A3	-1,303	0,044
Q9WUR2	Eci2	Enoyl-CoA delta isomerase 2, mitochondrial	-1,303	0,034
Q63880	Ces3a	Carboxylesterase 3A	-1,304	0,015
Q9ERK4	Cse1l	Exportin-2	-1,310	0,018
Q8CC88	Vwa8	von Willebrand factor A domain-containing protein 8	-1,311	0,032
P56657	Cyp2c40	Cytochrome P450 2C40	-1,337	0,024
P35492	Hal	Histidine ammonia-lyase	-1,344	0,018
Q64464	Cyp3a13	Cytochrome P450 3A13	-1,344	0,050
P41216	Acsl1	Long-chain-fatty-acid--CoA ligase 1	-1,408	0,009
Q8VCC1	Hpgd	15-hydroxyprostaglandin dehydrogenase [NAD(+)]	-1,429	0,005
Q9D0S9	Hint2	Histidine triad nucleotide-binding protein 2, mitochondrial	-1,439	0,001
P55050	Fabp2	Fatty acid-binding protein, intestinal	-1,446	0,013
Q6XVG2	Cyp2c54	Cytochrome P450 2C54	-1,447	0,009
Q91W43	Gldc	Glycine dehydrogenase (decarboxylating), mitochondrial	-1,456	0,001
P16015	Car3	Carbonic anhydrase 3	-1,459	0,039
Q8CIM7	Cyp2d26	Cytochrome P450 2D26	-1,470	0,003
P46664	Adss	Adenylosuccinate synthetase isozyme 2	-1,604	0,004

P17717	Ugt2b5	UDP-glucuronosyltransferase 2B17	-1,624	0,048
Q5FW57	Gm4952	Glycine N-acyltransferase-like protein	-1,632	0,006
Q9D1L0	Chchd2	Coiled-coil-helix-coiled-coil-helix domain-containing protein 2	-1,642	0,044
P15105	Glul	Glutamine synthetase	-1,659	0,018
Q9QYR9	Acot2	Acyl-coenzyme A thioesterase 2, mitochondrial	-1,684	0,009
O55137	Acot1	Acyl-coenzyme A thioesterase 1	-1,684	0,009
P47740	Aldh3a2	Fatty aldehyde dehydrogenase	-1,694	0,031
P97501	Fmo3	Dimethylaniline monooxygenase [N-oxide-forming] 3	-1,876	0,023
P56654	Cyp2c37	Cytochrome P450 2C37	-2,177	0,004

Supplementary Table 1. List of the proteins detected by proteomics analysis of liver. A two-tailed unpaired Student's t-test was applied.

UniProt Accession Number	Gene ID	Description	Fold change KO/WT	p-value
P28654	Dcn	Decorin	2,908	0,039
O09164	Sod3	Extracellular superoxide dismutase [Cu-Zn]	2,868	0,004
Q9DCG2	Cd302	CD302 antigen	2,794	0,046
Q8CG16	C1ra	Complement C1r-A subcomponent	2,490	0,030
Q8CFG9	C1rb	Complement C1r-B subcomponent	2,490	0,030
O08692	Ngp	Neutrophilic granule protein	2,428	0,009
P08207	S100a10	Protein S100-A10	2,373	0,017
P19324	Serpinh1	Serpin H1	2,334	0,029
Q9ET30	Tm9sf3	Transmembrane 9 superfamily member 3	2,258	0,038
P12023	App	Amyloid beta A4 protein	2,141	0,049
P06728	Apoa4	Apolipoprotein A-IV	2,042	0,002
P46935	Nedd4	E3 ubiquitin-protein ligase NEDD4	1,987	0,024
P02463	Col4a1	Collagen alpha-1(IV) chain	1,896	0,050
O70370	Ctss	Cathepsin S	1,870	0,004
E9Q414	Apob	Apolipoprotein B-100	1,869	0,033
Q61646	Hp	Haptoglobin	1,841	0,009
Q9R0Q3	Tmed2; Gm21540;	Transmembrane emp24 domain-containing protein 2	1,837	0,033
P06909	Cfh	Complement factor H	1,836	0,031
Q8VEH3	Arl8a	ADP-ribosylation factor-like protein 8A	1,826	0,014
Q06890	Clu	Clusterin	1,758	0,008
P01899	H2-D1	H-2 class I histocompatibility antigen, D-B alpha chain	1,753	0,049
Q60634	Flot2	Flotillin-2	1,725	0,029
Q8C7G5	Apoa5	Apolipoprotein A-V	1,705	0,043
Q9CQW9	Ifitm3	Interferon-induced transmembrane protein 3	1,687	0,005
Q9D1D4	Tmed10	Transmembrane emp24 domain-containing protein 10	1,677	0,029
P02088	Hbb-b1	Hemoglobin subunit beta-1	1,664	0,008
O08917	Flot1	Flotillin-1	1,648	0,035
P01942	Hba-a1; Hba-a2	Hemoglobin subunit alpha	1,645	0,005
Q61581	Igfbp7	Insulin-like growth factor-binding protein 7	1,641	0,007
P02089	Hbb-b2	Hemoglobin subunit beta-2	1,631	0,012
Q9QZ85	Iigp1; Iigp1b	Interferon-inducible GTPase 1	1,619	0,014
P19221	F2	Prothrombin	1,599	0,031
Q05793	Hspg2	Basement membrane-specific heparan sulfate proteoglycan core protein	1,591	0,006
P08226	Apoe	Apolipoprotein E	1,583	0,042
Q91X72	Hpx	Hemopexin	1,552	0,027
P33622	Apoc3	Apolipoprotein C-III	1,528	0,002
Q9D0F3	Lman1	Protein ERGIC-53	1,523	0,047
Q5KU39	Vps41	Vacuolar protein sorting-associated protein 41 homolog	1,521	0,047
Q08857	Cd36	Platelet glycoprotein 4	1,507	0,016
Q01405	Sec23a	Protein transport protein Sec23A	1,491	0,037
P04186	Cfb	Complement factor B	1,462	0,014
Q91W98	Slc15a4	Solute carrier family 15 member 4	1,459	0,038
Q9ESY9	Ifi30	Gamma-interferon-inducible lysosomal thiol reductase	1,441	0,020
P62821	Rab1; Rab1a	Ras-related protein Rab-1A	1,432	0,017
P54116	Stom	Erythrocyte band 7 integral membrane protein	1,411	0,003
Q99J93	Ifitm2	Interferon-induced transmembrane protein 2	1,403	0,043
Q9D1G1	Rab1b	Ras-related protein Rab-1B	1,397	0,016
E9PV24	Fga	Fibrinogen alpha chain	1,390	0,038
Q99MB1	Tlr3	Toll-like receptor 3	1,380	0,010
Q9DBH5	Lman2	Vesicular integral-membrane protein VIP36	1,380	0,019

Q8BRF7	Scfd1	Sec1 family domain-containing protein 1	1,368	0,018
Q6YGZ1	Hpse	Heparanase	1,357	0,006
Q07797	Lgals3bp	Galectin-3-binding protein	1,303	0,007
Q8BGD6	Slc38a9	Sodium-coupled neutral amino acid transporter 9	1,296	0,010
P57746	Atp6v1d	V-type proton ATPase subunit D	1,295	0,027
Q6PGD0	Atraid	All-trans retinoic acid-induced differentiation factor	1,281	0,023
Q9Z1G3	Atp6v1c1	V-type proton ATPase subunit C 1	1,270	0,005
P52503	Ndufs6	NADH dehydrogenase [ubiquinone] iron-sulfur protein 6, mitochondrial	1,259	0,001
Q8BVE3	Atp6v1h	V-type proton ATPase subunit H	1,259	0,003
O35609	Scamp3	Secretory carrier-associated membrane protein 3	1,255	0,018
Q9DBD0	1300017J02Rik	Inhibitor of carbonic anhydrase	1,237	0,040
Q61207	Psap	Prosaposin	1,236	0,017
Q62192	Cd180	CD180 antigen	1,226	0,007
Q9D593	Atp6v1e2	V-type proton ATPase subunit E 2	1,203	0,002
P28798	Grn	Granulins	1,203	0,035
P51863	Atp6v0d1	V-type proton ATPase subunit d 1	1,181	0,007
A6X935	Itih4	Inter alpha-trypsin inhibitor, heavy chain 4	1,160	0,048
O88783	F5	Coagulation factor V	1,157	0,045
Q60590	Orm1	Alpha-1-acid glycoprotein 1	1,153	0,036
P51569	Gla	Alpha-galactosidase A	1,145	0,009
P62814	Atp6v1b2	V-type proton ATPase subunit B, brain isoform	1,124	0,049
Q8BMQ8	Mon1b	Vacuolar fusion protein MON1 homolog B	-1,115	0,035
Q3TAA7	Stk11ip	Serine/threonine-protein kinase 11-interacting protein	-1,148	0,032
P49935	Ctsh	Pro-cathepsin H	-1,164	0,005
O70404	Vamp8	Vesicle-associated membrane protein 8	-1,185	0,039
O35604	Npc1	Niemann-Pick C1 protein	-1,189	0,025
Q3TB48	Tmem104	Transmembrane protein 104	-1,192	0,003
Q3UMW8	Cln5	Ceroid-lipofuscinosis neuronal protein 5 homolog	-1,198	0,012
P10605	Ctsb	Cathepsin B	-1,202	0,025
Q9CQ01	Rnaset2a; Rnaset2b	Ribonuclease T2	-1,202	0,007
Q9CQC7	Gm3244; Ndufb4; Gm3873	NADH dehydrogenase [ubiquinone] 1 beta subcomplex subunit 4	-1,203	0,044
Q9Z1G4	Atp6v0a1	V-type proton ATPase 116 kDa subunit a isoform 1	-1,213	0,048
Q6PDG8	Mon1a	Vacuolar fusion protein MON1 homolog A	-1,215	0,009
Q80XH1	Kxd1	KxDL motif-containing protein 1	-1,229	0,019
Q64191	Aga	N(4)-(beta-N-acetylglucosaminyl)-L-asparaginase	-1,265	0,021
Q64446	Atp7b	Copper-transporting ATPase 2	-1,269	0,044
Q8R0G7	Spns1	Protein spinster homolog 1	-1,285	0,013
Q9JIF3	Slc2a8	Solute carrier family 2, facilitated glucose transporter member 8	-1,297	0,020
Q2TBE6	Pi4k2a	Phosphatidylinositol 4-kinase type 2-alpha	-1,301	0,010
P57716	Ncstn	Nicastrin	-1,302	0,035
Q9Z0L8	Ggh	Gamma-glutamyl hydrolase	-1,309	0,002
O70496	Clcn7	H(+)/Cl(-) exchange transporter 7	-1,318	0,032
Q8K4D3	Slc36a1	Proton-coupled amino acid transporter 1	-1,322	0,042
Q04519	Smpd1	Sphingomyelin phosphodiesterase	-1,337	0,040
O54782	Man2b2	Epididymis-specific alpha-mannosidase	-1,342	0,007
Q8R242	Ctbs	Di-N-acetylchitobiase	-1,363	0,012
P26041	Msn	Moesin	-1,369	0,030
P63001	Rac1	Ras-related C3 botulinum toxin substrate 1	-1,371	0,022
Q3UDW8	Hgsnat	Heparan-alpha-glucosaminide N-acetyltransferase	-1,373	0,048
P60764	Rac3	Ras-related C3 botulinum toxin substrate 3	-1,385	0,019
Q05144	Rac2	Ras-related C3 botulinum toxin substrate 2	-1,390	0,018
Q9D2L1	Arsk	Arylsulfatase K	-1,430	0,029
Q61176	Arg1	Arginase-1	-1,435	0,004
O88983	Stx8	Syntaxin-8	-1,435	0,018
P55258	Rab8a	Ras-related protein Rab-8A	-1,437	0,038
P17426	Ap2a1	AP-2 complex subunit alpha-1	-1,446	0,006
P61021	Rab5b	Ras-related protein Rab-5B	-1,461	0,011
P35278	Rab5c	Ras-related protein Rab-5C	-1,467	0,034
Q6NVG5	Mreg	Melanoregulin	-1,492	0,012
Q8CF66	Lamtor4	Ragulator complex protein LAMTOR4	-1,516	0,002
Q99LJ1	Fuca1	Tissue alpha-L-fucosidase	-1,526	0,025
P23780	Glb1	Beta-galactosidase	-1,567	0,049
P70665	Siae	Sialate O-acetylesterase	-1,588	0,033
Q9CQD1	Rab5a	Ras-related protein Rab-5A	-1,625	0,010
P04938	Mup11; Mup18	Major urinary protein 11	-1,700	0,040
B5X0G2	Mup17	Major urinary protein 17	-1,700	0,040

P02762	Mup1; Mup19; Mup16; Mup18; Mup9	Major urinary protein 6	-1,700	0,040
Q9D1L9	Hbxip; Lamtor5	Ragulator complex protein LAMTOR5	-1,708	0,022
O55125	Nipsnap1	Protein NipSnap homolog 1	-1,756	0,034
Q05117	Acp5	Tartrate-resistant acid phosphatase type 5	-1,763	0,034
Q8VDG7	Pafah2	Platelet-activating factor acetylhydrolase 2, cytoplasmic	-1,779	0,031
Q91WS4	Bhmt2	S-methylmethionine--homocysteine S-methyltransferase BHMT2	-1,980	0,045
P06330	IghmAC38.205.12	Ig heavy chain V region AC38 205.12	-2,158	0,026
P97384	Anxa11	Annexin A11	-2,391	0,009
Q64458	Cyp2c29	Cytochrome P450 2C29	-2,601	0,030
P01633	Igkv6-17	Ig kappa chain V19-	-4,767	0,021
Q9JHJ3	0610031J06Rik; Glmp	Glycosylated lysosomal membrane protein	-6,909	0,000
Q9DC37	Mfsd1	Major facilitator superfamily domain-containing protein 1	-7,865	0,000

Supplementary Table 2. List of the proteins detected by proteomics analysis of tritosomes. A two-tailed unpaired Student's t-test was applied.

Biochemical	Pathway	CAS	Fold change KO/WT	p-value
methionine sulfoxide	Amino Acid	3226-65-1	1,797	0,002
3-indoxyl sulfate	Amino Acid	2642-37-7	1,672	0,003
N-delta-acetylornithine*	Amino Acid		0,674	0,004
UDP-glucose/UDP-galactose	Carbohydrate		1,934	0,006
phosphoethanolamine	Lipid	1071-23-4	1,877	0,007
palmitoyl ethanolamide	Lipid	544-31-0	0,586	0,009
adenine	Nucleotide	73-24-5	1,335	0,011
cysteine-glutathione disulfide	Amino Acid	13081-14-6	1,380	0,014
palmitate (16:0)	Lipid	57-10-3	0,722	0,014
5-methylthioadenosine (MTA)	Amino Acid	2457-80-9	1,695	0,015
catechol sulfate	Xenobiotics	4918-96-1	0,446	0,019
adenosine	Nucleotide	58-61-7	1,571	0,024
serotonin	Amino Acid	153-98-0	4,054	0,024
gamma-glutamylglutamate	Peptide	1116-22-9	0,688	0,025
gamma-glutamylphenylalanine	Peptide	7432-24-8	0,694	0,025
1-arachidonoyl-GPE (20:4n6)*	Lipid		0,732	0,026
N-glycolylneuraminate	Xenobiotics	1113-83-3	0,845	0,031
creatinine	Amino Acid	60-27-5	2,597	0,034
ornithine	Amino Acid	3184-13-2	0,867	0,036
homocitrulline	Amino Acid	1190-49-4	1,482	0,040
dimethylarginine (SDMA + ADMA)	Amino Acid	102783-24-4	0,549	0,042
asparagine	Amino Acid	70-47-3	0,824	0,043
equol sulfate	Xenobiotics		0,373	0,048
1-palmitoyl-GPG (16:0)*	Lipid		0,407	0,050
ketamine	Xenobiotics	6740-88-1	0,640	0,057
1-stearoyl-GPS (18:0)*	Lipid		0,583	0,060
margarate (17:0)	Lipid	506-12-7	0,585	0,063
1-palmitoyl-GPS (16:0)*	Lipid		0,550	0,068
histidine	Amino Acid	5934-29-2	1,221	0,069
caprate (10:0)	Lipid	112-37-8	0,634	0,070
stearoylcarnitine	Lipid	18822-91-8	0,657	0,070
adenosine 3'-monophosphate (3'-AMP)	Nucleotide	84-21-9	1,955	0,073
thiamin (Vitamin B1)	Cofactors and Vitamins	59-43-8	0,540	0,074
1-palmitoyl-GPE (16:0)	Lipid		0,654	0,075
beta-hydroxyisovaleroylcarnitine	Amino Acid	99159-87-2	0,832	0,076
6-phosphogluconate	Carbohydrate	921-62-0;53411-70-4	0,609	0,078
succinate	Energy	110-15-6	0,689	0,078
1-palmitoyl-GPC (16:0)	Lipid	17364-16-8	0,709	0,082
pyroglutamine*	Amino Acid	2353-44-8	0,537	0,085
choline phosphate	Lipid	72556-74-2	0,758	0,086
maltotriose	Carbohydrate	1109-28-0	0,534	0,086
stearate (18:0)	Lipid	57-11-4	0,798	0,092
lysine	Amino Acid	56-87-1	0,765	0,093
myristate (14:0)	Lipid	544-63-8	0,742	0,094
choline	Lipid	67-48-1	0,845	0,095
riboflavin (Vitamin B2)	Cofactors and Vitamins	83-88-5	0,742	0,099
serine	Amino Acid	56-45-1	0,807	0,099
glutarylcarnitine (C5)	Amino Acid	102636-82-8	1,154	0,100

spermidine	Amino Acid	124-20-9	0,363	0,108
creatine	Amino Acid	57-00-1	1,211	0,112
maltohexaose	Carbohydrate	34620-77-4	0,527	0,115
maltopentaose	Carbohydrate	34620-76-3	0,490	0,115
3-methylglutarylcarnitine (C6)	Amino Acid	102673-95-0	1,242	0,115
oleate (18:1n9)	Lipid	112-80-1	0,767	0,118
1-stearoyl-GPI (18:0)	Lipid	796963-93-4	0,534	0,119
glycerol	Lipid	56-81-5	0,763	0,125
hypotaurine	Amino Acid	300-84-5	0,779	0,130
linolenate [alpha or gamma; (18:3n3 or 6)]	Lipid		0,620	0,132
tauroursodeoxycholate	Lipid	14605-22-2	0,505	0,140
taurine	Amino Acid	107-35-7	0,901	0,140
maltotetraose	Carbohydrate	34612-38-9	0,519	0,142
S-adenosylhomocysteine (SAH)	Amino Acid	979-92-0	0,798	0,145
N-stearoyltaurine	Lipid	63155-80-6	0,742	0,148
kynurenine	Amino Acid	2922-83-0	0,478	0,153
nicotinamide	Cofactors and Vitamins	98-92-0	0,817	0,153
7-alpha-hydroxy-3-oxo-4-cholestenoate (7-Hoca)	Lipid	115538-85-7	0,684	0,153
guanosine	Nucleotide	118-00-3	1,346	0,156
laurate (12:0)	Lipid	143-07-7	0,739	0,158
succinylcarnitine	Energy		1,540	0,159
arachidonate (20:4n6)	Lipid	506-32-1	0,722	0,159
trigonelline (N'-methylnicotinate)	Cofactors and Vitamins	535-83-1	0,517	0,168
lactate	Carbohydrate	79-33-4	0,620	0,174
eicosapentaenoate (EPA; 20:5n3)	Lipid	10-2005-9;10417-94-4	0,577	0,185
2-arachidonoylglycerol (20:4)	Lipid	53847-30-6	0,606	0,185
cis-aconitate	Energy	585-84-2	0,601	0,186
pro-hydroxy-pro	Amino Acid	18684-24-7	1,445	0,188
arachidate (20:0)	Lipid	506-30-9	0,580	0,197
linoleate (18:2n6)	Lipid	60-33-3	0,756	0,198
1-stearoyl-GPE (18:0)	Lipid	69747-55-3	0,494	0,201
docosahexaenoate (DHA; 22:6n3)	Lipid	6217-54-5	0,714	0,202
C-glycosyltryptophan	Amino Acid	180509-18-6	0,774	0,204
malate	Energy	6915-15-7	0,729	0,206
tetradecanedioate	Lipid	821-38-5	1,276	0,217
stearidonate (18:4n3)	Lipid	111174-40-4	0,571	0,218
S-adenosylmethionine (SAM)	Amino Acid	24346-00-7;86867-01-8;86867-0108	1,604	0,221
xanthosine	Nucleotide	146-80-5	0,790	0,226
1-palmitoyl-GPI (16:0)*	Lipid		0,442	0,230
cytidine 5'-monophosphate (5'-CMP)	Nucleotide	63-37-6	1,349	0,237
tauro(alpha + beta)muricholate	Lipid		0,422	0,239
10-heptadecenoate (17:1n7)	Lipid	29743-97-3	0,739	0,249
dihomo-linoleate (20:2n6)	Lipid	2091-39-6	0,786	0,256
sphinganine	Lipid	3102-56-5	1,295	0,259
2-stearoyl-GPC (18:0)*	Lipid		1,569	0,262
glycerophosphorylcholine (GPC)	Lipid	28319-77-9	0,698	0,265
hypoxanthine	Nucleotide	68-94-0	0,714	0,267
citrate	Energy	77-92-9	0,375	0,272
phenol sulfate	Amino Acid	937-34-8	1,562	0,275
coenzyme A	Cofactors and Vitamins	85-61-0;18439-24-2	1,441	0,276
glycylisoleucine	Peptide	19461-38-2	1,324	0,285
taurocholate	Lipid	145-42-6	0,461	0,292
pantothenate	Cofactors and Vitamins	137-08-6	0,881	0,295
phenylalanine	Amino Acid	63-91-2	0,915	0,295
hippurate	Xenobiotics	495-69-2	0,612	0,301
N-octanoylglycine	Lipid	14246-53-8	0,694	0,302
nicotinamide adenine dinucleotide (NAD+)	Cofactors and Vitamins	53-84-9	1,218	0,304
daidzein	Xenobiotics	486-66-8	0,757	0,318
gamma-glutamylvaline	Peptide	2746-34-1	0,695	0,321
17-methylstearate	Lipid	2724-59-6	0,790	0,322
docosapentaenoate (n6 DPA; 22:5n6)	Lipid	25182-74-5	0,850	0,330
1-linoleoyl-GPE (18:2)*	Lipid		0,765	0,334
pyridoxate	Cofactors and Vitamins	82-82-6	0,597	0,337
phosphate	Energy	7664-38-2	0,817	0,341
cholate	Lipid	81-25-4	0,311	0,351
adrenate (22:4n6)	Lipid	2091-25-0	0,840	0,352

uridine	Nucleotide	58-96-8	0,820	0,354
gamma-glutamylthreonine*	Peptide	5652-48-2	0,810	0,354
nonadecanoate (19:0)	Lipid	646-30-0	0,616	0,356
ergothioneine	Xenobiotics	58511-63-0	0,734	0,356
caprylate (8:0)	Lipid	124-07-2	0,646	0,362
palmitoleate (16:1n7)	Lipid	373-49-9	0,695	0,365
uracil	Nucleotide	66-22-8	1,342	0,367
isobutyrylcarnitine	Amino Acid	25518-49-4	0,167	0,368
deoxycarnitine	Lipid	6249-56-5	0,887	0,373
5-methyltetrahydrofolate (5MeTHF)	Cofactors and Vitamins	68703-91-3;68792-52-9	1,331	0,376
3-ureidopropionate	Nucleotide	462-88-4	1,160	0,377
2-methylbutyrylcarnitine (C5)	Amino Acid	31023-25-3	0,318	0,380
10-nonadecenoate (19:1n9)	Lipid	73033-09-7	0,821	0,386
xanthine	Nucleotide	69-89-6	0,886	0,388
beta-muricholate	Lipid	2393-59-1	0,332	0,393
4-hydroxy-nonenal-glutathione	Amino Acid	99927-70-5	1,526	0,394
spermine	Amino Acid	71-44-3	0,416	0,399
myristoleate (14:1n5)	Lipid	544-64-9	0,682	0,410
ethyl glucuronide	Xenobiotics	17685-04-0	0,617	0,416
N-oleoyltaurine	Lipid	52514-04-2	0,686	0,419
corticosterone	Lipid	50-22-6	0,780	0,425
butyrylglycine	Lipid	20208-73-5	0,429	0,426
glutamine	Amino Acid	56-85-9	1,124	0,428
pseudouridine	Nucleotide	1445-07-4	1,167	0,429
N-acetylmethionine	Amino Acid	65-82-7	0,894	0,432
N-acetylleucine	Amino Acid	1188-21-2	1,217	0,447
urea	Amino Acid	57-13-6	0,813	0,453
1-stearoyl-GPC (18:0)	Lipid	19420-57-6	0,903	0,463
propionylcarnitine	Lipid	17298-37-2	0,702	0,463
docosapentaenoate (n3 DPA; 22:5n3)	Lipid	2234-74-4	0,771	0,469
trans-4-hydroxyproline	Amino Acid	51-35-4	1,283	0,471
heme	Cofactors and Vitamins	14875-96-8	0,696	0,473
1-oleoylglycerol (18:1)	Lipid	111-03-5	1,255	0,477
leucine	Amino Acid	61-90-5	0,929	0,488
taurodeoxycholate	Lipid	207737-97-1	0,514	0,490
dihydrobiopterin	Cofactors and Vitamins	6779-87-9	0,840	0,494
isoleucine	Amino Acid	73-32-5	1,092	0,501
S-nitrosoglutathione (GSNO)	Amino Acid	57564-91-7	1,578	0,503
3-hydroxybutyrylcarnitine (1)	Lipid		1,418	0,506
erucate (22:1n9)	Lipid	112-86-7	0,713	0,506
2-hydroxystearate	Lipid	629-22-1	0,871	0,506
methionine	Amino Acid	63-68-3	0,872	0,515
Isobar: betaine aldehyde, N-methyldiethanolamine	Amino Acid		0,800	0,517
gamma-glutamylisoleucine*	Peptide		0,871	0,522
gamma-glutamylleucine	Peptide	2566-39-4	0,808	0,523
1-palmitoleoyl-GPC (16:1)*	Lipid		1,226	0,527
1-oleoyl-GPI (18:1)*	Lipid		0,742	0,527
alanine	Amino Acid	56-41-7	0,900	0,529
4-guanidinobutanoate	Amino Acid	463-003;463-00-3	0,701	0,529
citrulline	Amino Acid	372-75-8	0,924	0,537
1-arachidonoyl-GPC (20:4n6)*	Lipid		1,276	0,555
allantoin	Nucleotide	97-59-6	1,137	0,559
threonine	Amino Acid	72-19-5	0,952	0,575
adenosine 5'-diphosphoribose (ADP-ribose)	Cofactors and Vitamins	68414-18-6	1,208	0,578
aspartate	Amino Acid	56-84-8	0,900	0,591
methyl-4-hydroxybenzoate sulfate	Xenobiotics		1,121	0,591
ascorbate (Vitamin C)	Cofactors and Vitamins	134-03-2	1,129	0,597
dihomo-linolenate (20:3n3 or n6)	Lipid	17046-59-2	0,922	0,599
thymidine	Nucleotide	50-89-5	1,139	0,610
S-methylglutathione	Amino Acid	2922-56-7	1,090	0,615
1-arachidonoyl-GPI (20:4)*	Lipid		0,899	0,616
glutathione, oxidized (GSSG)	Amino Acid	103239-24-3	0,856	0,622
pipecolate	Amino Acid	4043-87-2	0,892	0,630
adenosine 3',5'-diphosphate	Nucleotide	75431-54-8	1,556	0,632
12-dehydrocholate	Lipid	2458-08-4;2458-08-4	1,333	0,634
isoleucylglycine	Peptide	868-28-0	0,940	0,635
N2-acetyllysine	Amino Acid	1946-82-3	0,943	0,639

imidazole propionate	Amino Acid	1074-59-5	0,813	0,643
hexanoylglycine	Lipid	24003-67-6	0,744	0,655
caproate (6:0)	Lipid	142-62-1	1,187	0,655
1-methylimidazoleacetate	Amino Acid	2625-49-2	1,056	0,657
docosadienoate (22:2n6)	Lipid	7370-49-2	0,821	0,663
5-oxoproline	Amino Acid	98-79-3	0,866	0,673
nicotinate	Cofactors and Vitamins	59-67-6	0,717	0,674
valine	Amino Acid	72-18-4	0,952	0,684
glutamate	Amino Acid	56-86-0	1,116	0,695
cytidine 5'-diphosphocholine	Lipid	33818-15-4	1,105	0,696
N-acetylasparagine	Amino Acid	4033-40-3	1,058	0,696
adenosine 5'-monophosphate (AMP)	Nucleotide	149022-20-8	1,167	0,698
tyrosine	Amino Acid	60-18-4	0,953	0,702
eicosenoate (20:1)	Lipid		0,877	0,704
tryptophan	Amino Acid	73-22-3	0,961	0,712
adenosine 2'-monophosphate (2'-AMP)	Nucleotide	130-49-4	0,778	0,722
stachydrine	Xenobiotics	4136-37-2	1,049	0,733
UDP-N-acetylglucosamine/galactosamine	Carbohydrate		1,054	0,735
isovalerylcarnitine	Amino Acid	31023-24-2	0,900	0,758
flavin mononucleotide (FMN)	Cofactors and Vitamins	130-40-5	1,044	0,760
12-HETE	Lipid	71030-37-0;73837-14-6	0,807	0,762
2-palmitoleoyl-GPC (16:1)*	Lipid		0,865	0,764
carnitine	Lipid	461-05-2	0,976	0,765
glutathione, reduced (GSH)	Amino Acid	70-18-8	1,035	0,768
phosphopantetheine	Cofactors and Vitamins	NA	0,902	0,780
cytidine	Nucleotide	65-46-3	0,882	0,781
inosine 5'-monophosphate (IMP)	Nucleotide	4691-65-0	1,119	0,790
2-hydroxypalmitate	Lipid	764-67-0	0,929	0,803
guanosine 5'- monophosphate (5'-GMP)	Nucleotide	09/12/5550	1,114	0,806
N-acetylglucosamine 6-phosphate	Carbohydrate	102029-88-9	0,882	0,808
N-acetylglutamate	Amino Acid	03/08/5817	0,941	0,816
N-acetylglutamine	Amino Acid	2490-97-3	0,950	0,817
ophthalmate	Amino Acid	495-27-2	0,892	0,817
1-oleoyl-GPE (18:1)	Lipid	89576-29-4	0,979	0,818
16-hydroxypalmitate	Lipid	506-13-8	1,102	0,824
13-HODE + 9-HODE	Lipid		0,928	0,828
N1-methyladenosine	Nucleotide	15763-06-1	1,084	0,829
inosine	Nucleotide	58-63-9	1,017	0,850
uridine monophosphate (5' or 3')	Nucleotide	58-97-9	0,924	0,853
betaine	Amino Acid	107-43-7	1,075	0,854
flavin adenine dinucleotide (FAD)	Cofactors and Vitamins	146-14-5;84366-81-4	0,985	0,855
1-palmitoylglycerol (16:0)	Lipid	542-44-9	0,927	0,858
nicotinamide adenine dinucleotide reduced (NADH)	Cofactors and Vitamins	58-68-4;606-68-8	0,948	0,859
3-(4-hydroxyphenyl)lactate	Amino Acid	6482-98-0	1,053	0,877
3'-dephosphocoenzyme A	Cofactors and Vitamins	3633-59-8	0,982	0,890
valerylglycine	Lipid	24003-66-5	1,039	0,897
hexadecanedioate	Lipid	505-54-4	0,968	0,910
Isobar: fructose 1,6-diphosphate, glucose 1,6-diphosphate, myo-inositol 1,4 or 1,3-diphosphate	Carbohydrate		1,034	0,925
1-oleoyl-GPC (18:1)	Lipid	19420-56-5	1,024	0,925
proline	Amino Acid	147-85-3	0,989	0,927
nicotinamide riboside	Cofactors and Vitamins	1341-23-7	0,986	0,933
taurohyodeoxycholic acid	Lipid	38411-85-7	0,954	0,938
2-palmitoyl-GPC (16:0)	Lipid		1,020	0,946
1-linoleoyl-GPC (18:2)	Lipid		0,986	0,957
docosatrienoate (22:3n3)	Lipid	59708-86-0	1,007	0,965
acetylcarnitine	Lipid	5080-50-2	0,979	0,969
sphingosine	Lipid	123-78-4	1,005	0,974
S-lactoylglutathione	Amino Acid	54398-03-7	0,984	0,982

Supplementary Table 3. List of the metabolites detected by metabolomics analysis of the liver . A two-tailed unpaired Student's t-test was applied.

6.2 List of figures

6.3 List of tables

6.4 List of supplementary tables

7 Declaration

Herewith I declare that:

I. Apart from the supervisor's guidance, the content of this dissertation is my own work.

II. This thesis has not been submitted partially or wholly as a part of a doctoral degree to another examining body.

III. This thesis has been prepared according to the Rules of Good Scientific Practice of the German Research Foundation.

Kiel, July 2018 David Massa Lopez

8 Acknowledgements

Four and a half years ago I changed Barcelona for Kiel, and during the adaptation period to north Germany, its language, its culture and its weather it was hard to imagine that today I would be sad to write the last sentences of this Thesis, since they represent the end of this stage of my life. Therefore, I would like to thank the people that accompanied and supported me during this time.

I want to specially thank my PhD supervisors Dr. Markus Damme and Dr. Prof. Paul Saftig. Thank you for giving me the opportunity to do the PhD in your lab and for the scientific and personal discussions, advices and ideas. You always found the time to discuss and I deeply appreciate it. I have learned a lot during this process from both of you.

Thanks to Prof. Dr. Eric Beitz for being the second reviewer of this Thesis.

I thank all the members of the EUROCLAST network. Special thanks to Miep and Vincent for their tremendous organisation work. Additional thanks to Vincent for the mentoring, every time that we talked it was helpful. And thanks to all the students for the moments shared, for the support and for the scientific chats. I feel a privileged to have been part of this network.

I want to thank all the collaboration partners with whom I have worked: Prof. Dr. Renate Lüllmann-Rauch, Dagmar Niemeier, Dr. Petra Henning, Prof. Dr. Ulf Lernern, Viktė Lionikaitė, Daniella Wiegmann, Dr. Thorsten Schinke, Mona Neven, Dr. Kai Dittmann, Dr. Catherine Meyer-Schwesinger and Dr. Juha Tuukkannen.

Thanks to all the members from the AG Saftig for their help to integrate me into the group and for the daily moments and laughs shared. Arne, Chama, Marlies Seba an Lea you made very light and easy to work at the lab. Basti, Lisa, Marlies and Niklas, I will remember with a smile on my face the time spent at the office, specially after 4 pm, time to get schwifty!

8.Acknowledgements

I would like to remember and thank my friends from the University of Barcelona, Ferran, Gonzalo, Joan, Lucia, Marti and Miquel. Gràcies pels riures i per l'aire fresc que sempre heu aportat!

Also I want to thank my partner, Kathrin, for understanding me and supporting me during this rollcoaster writing time.

Finally, I want to thank to my family, specially my mother Araceli and my father Moises, so they have always supported me and they have given me everything that I needed to arrive where I am today.